

---

UNIVERSITÀ DEGLI STUDI DI PADOVA  
DIPARTIMENTO DI FISICA E ASTRONOMIA “GALILEO GALILEI”

CORSO DI DOTTORATO DI RICERCA IN ASTRONOMIA  
Ciclo XXXVI

THE IMPACT OF CHAOTIC DYNAMICS AND BINARY  
EVOLUTION ON THE FORMATION OF COMPACT BINARY  
SYSTEMS

**Coordinator:** Prof. Giovanni Carraro  
**Supervisor:** Prof. Michela Mapelli  
**Co-supervisor:** Dott. Giuliano Iorio  
**Co-supervisor:** Dott. Sara Rastello

**Ph.D. Candidate:** Marco Dall’Amico

---



*"Magic mirror in my hand  
who's the fairest in the land?"  
"You're the fairest here so true  
'cause no one is here with you"*

*Mirrorwatcher - The Old Knights*



# Contents

<b>Abstract</b>	<b>I</b>
<b>Symbols and abbreviations</b>	<b>IV</b>
<b>1 Formation channels of compact binary mergers</b>	<b>1</b>
1.1 Where we are and where we are going . . . . .	1
1.2 Where do black holes and neutron stars come from? . . . . .	4
1.2.1 Black Holes and Neutron Stars . . . . .	4
1.2.2 From a single star to a compact object . . . . .	5
1.3 Two is better than one: the Isolated Channel . . . . .	10
1.3.1 Mass transfer . . . . .	10
1.3.2 Common Envelope . . . . .	12
1.3.3 Chemically Homogeneous Evolution . . . . .	14
1.3.4 Compact binary merger formation . . . . .	14
1.4 Too many stars in a crowded place: the Dynamical Channel . . . . .	17
1.4.1 Star clusters: properties and evolution . . . . .	17
1.4.2 Different flavors of star clusters . . . . .	21
1.4.3 Dynamical encounters in star clusters . . . . .	22
1.4.4 Three-Body interactions &hard binaries . . . . .	23
1.4.5 Dynamical hardening &gravitational wave emission . . . . .	25
1.4.6 Exchanges . . . . .	26
1.4.7 Ionizations . . . . .	28
1.4.8 Hierarchical mergers . . . . .	29
1.4.9 Stellar collisions &runaway mergers . . . . .	30
<b>2 GW190521 formation via three-body encounters in young massive star clusters</b>	<b>34</b>
2.1 Introduction . . . . .	34
2.2 Methods . . . . .	36
2.2.1 $N$ -body simulations with ARWV . . . . .	36
2.2.2 Initial Conditions . . . . .	37
2.3 Results . . . . .	39
2.3.1 Flybys, exchanges and ionizations . . . . .	39
2.3.2 Component masses . . . . .	40
2.3.3 Effective and precessing spins . . . . .	43
2.3.4 Merger remnants . . . . .	46
2.4 Discussion . . . . .	48
2.4.1 Dynamical origin of GW190521 and merger rate density . . . . .	48

2.4.2	Caveats . . . . .	50
2.5	Summary . . . . .	51
<b>3</b>	<b>Eccentric black hole mergers via three-body interactions in young, globular and nuclear star clusters</b>	<b>54</b>
3.1	Introduction . . . . .	54
3.2	Methods . . . . .	58
3.2.1	Direct $N$ -Body simulations . . . . .	58
3.2.2	Initial conditions . . . . .	59
3.3	Results . . . . .	61
3.3.1	Outcomes . . . . .	61
3.3.2	BBH mergers . . . . .	61
3.3.3	Eccentric mergers . . . . .	66
3.3.4	Dynamical ejections . . . . .	69
3.3.5	Orbital plane tilt . . . . .	72
3.4	Discussion and caveats . . . . .	72
3.4.1	Merger rate density of eccentric mergers . . . . .	72
3.4.2	Single vs multiple three-body interactions . . . . .	73
3.5	Summary . . . . .	74
3.6	Appendix: Impact of the maximum impact parameter . . . . .	75
<b>4</b>	<b>Chemically Homogeneous Evolution: Impact on Stellar and Compact Binary Populations</b>	<b>82</b>
4.1	Introduction . . . . .	82
4.1.1	Population synthesis with SEVN . . . . .	84
4.1.2	Chemically Quasi-Homogeneous Simulations . . . . .	85
4.1.3	Initial conditions . . . . .	86
4.2	Results: Stellar populations . . . . .	87
4.2.1	Wolf-Rayet & red supergiant stars . . . . .	87
4.2.2	Single stellar evolution . . . . .	88
4.2.3	Binary stellar evolution . . . . .	88
4.2.4	RSG to WR ratio . . . . .	89
4.2.5	WR luminosity . . . . .	91
4.2.6	From Wolf-Rayet and red supergiant stars to compact objects . . . . .	91
4.3	Results: Compact object binaries . . . . .	93
4.3.1	Binary black holes . . . . .	96
4.3.2	Black Hole - Neutron Star binaries . . . . .	96
4.4	Discussions . . . . .	98
4.4.1	Accretion vs tidally-induced CHE . . . . .	98
4.5	Summary . . . . .	100
4.6	Appendix: The CHE20zams model . . . . .	101
<b>5</b>	<b>Conclusions and outlook</b>	<b>108</b>
<b>List of Figures</b>		<b>113</b>
<b>List of Tables</b>		<b>114</b>





---

## Abstract

Compact binary mergers stand out among the most energetic events in the Universe. These phenomena are driven by the emission of gravitational waves from two inspiraling compact objects, such as black holes (BHs) and neutron stars (NSs), which gradually draw closer and ultimately collide. Their groundbreaking discovery in 2015 has opened a new frontier in astrophysical research. The inspiraling dance of compact binary systems, observable through gravitational wave detectors like the LIGO, Virgo, and KAGRA, provides us with a unique window to probe the fundamental processes governing the evolution and interactions of these dense stellar remnants. Despite the observation of nearly 90 of these exotic systems to date, understanding their formation pathways still remains an ongoing challenge.

In this thesis, I delved into the intricate interplay of diverse formation channels and their role in the production of compact binary mergers. This work is specifically centered on the two most important astrophysical processes that lead to the production of gravitational wave sources: chaotic dynamical interactions and binary stellar evolution. The former represents the fundamental building block of the dynamical formation channel in dense stellar environments. The latter drives the evolution of massive stars into compact binaries through the isolated formation channel. My research aims to analyze the physical properties of compact binary mergers and to establish connections to potential observables that can serve as evidence for reconstructing their formation history.

In the first part of this work, I have focused on the gravitational wave event GW190521, which detains the record as the most massive binary black hole (BBH) merger observed to date. GW190521 allowed us to witness for the first time the formation of an intermediate-mass black hole, i.e. a BH exceeding  $100 M_{\odot}$ , arising from the merger of two smaller BHs. Here, I present a possible explanation for the formation of this peculiar BH merger event. This has been achieved through direct  $N$ -body simulations of three-body encounters between a binary and a single BH within young massive star clusters. My results indicate that the GW190521 origin may be attributed to a merger triggered by three-body encounters within young star clusters, compatible with a second-generation BBH merger. The substantial masses involved in this event, coupled with the significant precession of the spin parameter, support its dynamical formation.

In the second part of this thesis, I have extended my study to other stellar environments, exploring the formation of eccentric BH mergers produced by chaotic dynamical encounters within young, globular, and nuclear star clusters. I discuss how dynamics might leave some major fingerprints in the physical properties of these dynamically assembled mergers, and how these can be used as a tool to disentangle their formation channel based

on observations. My analysis suggests that three-body interactions can be a significant source of eccentric mergers detectable with gravitational wave signals. Eccentricity, combined with large masses and misaligned spins, can serve as compelling evidence for the dynamical origin of these gravitational wave sources.

Finally, I conducted an innovative study using population-synthesis simulations to explore the isolated formation channels of compact binary mergers through binary evolution. In this part of my thesis, I have specifically explored the effects of rotational mixing and chemically homogeneous evolution (CHE) on the production of massive stars and the subsequent compact merger population. My results show that CHE strongly affects not only the observable stellar populations of star clusters, but also the compact binary mergers population produced by these stars. CHE quenches the formation of red supergiant stars (RSGs) in favour of the production of Wolf-Rayet stars (WRs). WRs produced by CHE are, on average, more numerous, more massive, and more luminous than their non-CHE counterparts. This promotes the creation of more massive BHs while concurrently halting the formation of NSs. If, on the one hand, with CHE the population of mergers becomes more massive, on the other, CHE strongly suppresses the formation of all types of compact binary mergers. My findings further show that accretion-induced CHE is a valid formation pathway to produce compact binary mergers with asymmetric mass ratio without involving any dynamical interaction.



---

## Symbols

$M_{\odot}$	solar mass	$1.98892 \times 10^{33}$ g
$R_{\odot}$	solar radius	$6.957 \times 10^{10}$ cm
AU	astronomical unit	$1.495978707 \times 10^{12}$ cm
pc	parsec	$3.08567758149137 \times 10^{18}$ cm
Myr	megayear	$3.1536 \times 10^{13}$ s
c	speed of light in vacuum	$2.99792458 \times 10^{10}$ cm s <sup>-1</sup>
$G$	gravitational constant	$6.6743 \times 10^{-8}$ cm <sup>3</sup> g <sup>-1</sup> s <sup>-2</sup>

## Acronyms

<b>BBH</b>	Binary black hole
<b>BHNS</b>	Black hole-neutron star binary
<b>BNS</b>	Binary neutron star
<b>BH</b>	Black hole
<b>IMBH</b>	Intermediate-mass black hole
<b>GW</b>	Gravitational wave
<b>NS</b>	Neutron star
<b>CE</b>	Common envelope
<b>NSC</b>	Nuclear star cluster
<b>GC</b>	Globular cluster
<b>YSC</b>	Young star cluster
<b>OC</b>	Open cluster
<b>PI</b>	Pair instability
<b>PPI</b>	Pulsational pair instability
<b>SN</b>	Supernova
<b>CHE</b>	Chemically homogeneous evolution
<b>WR</b>	Wolf-Rayet star
<b>RSG</b>	Red supergiant star



# Chapter 1

## Formation channels of compact binary mergers

### 1.1 Where we are and where we are going

September 14, 2015, marked a historic event for Astrophysics. On that day gravitational waves, ripples in space-time produced by the inspiraling merger process of a binary black hole, were measured for the first time in human history (Abbott &al. 2016). This discovery closed a chapter opened nearly 100 years ago by Albert Einstein, who first theorized them (Einstein 1916). The measurement of gravitational waves ultimately confirms not only the existence of black holes but also their presence in binary systems and their capability to merge within the age of the Universe through the emission of gravitational waves. But as on September 14 a chapter was closed, a new one opened. With the first detection GW150914 (Abbott et al. 2016), the gravitational waves era was just at its beginning, and now, 8 years later, we can count almost 90 compact binary mergers detected with gravitational wave interferometers (Abbott et al. 2019, 2021c; Abbott &et al. 2021a; The LIGO Scientific Collaboration et al. 2021), with this number set to triple by the end of 2024 (Borhanian &Sathyaprakash 2022). Of these merger events, 86 originated from binary black holes, 2 from binary neutron stars (GW170817 & GW190425, Abbott et al. 2017; Abbott &et al. 2020), and 2 from black hole-neutron star systems (GW200105 & GW200115, Abbott et al. 2021a). All the compact binary merger candidates reported by the LIGO-Virgo-KAGRA collaboration in Abbott et al. (2023) are depicted in Figure 1.1, along with other electromagnetic candidates of black holes and neutron stars.

This growing population of detected gravitational wave sources has led the astrophysical community to gain new insights into the physical properties of these compact objects. For instance, the black hole masses of the observed gravitational wave mergers range from a few to several tens of solar masses, with the mass distribution of the primary black hole  $m_1$  - the most massive component of the binary - matching a power law plus peak distribution (Abbott et al. 2023). In the upper part of the mass spectrum lies GW190521, which, with a primary black hole of approximately  $85 M_\odot$ , holds the record for the most massive black hole in the gravitational wave population, challenging the stellar evolutionary models of massive stars (Abbott &et al. 2020; Abbott et al. 2020a). Two other events stand out due to their large masses at the top of the spectrum, namely GW190426 and GW200220. However, these events have a low probability of being of astrophysical origin. On the other end of the spectrum, the least massive black hole belongs to the GW190814 event, which with a secondary mass  $m_2$  of approximately  $2.6 M_\odot$  might also be compatible with the most massive neutron star ever detected (Abbott et al. 2020b). GW190814 is also one of the few events, along

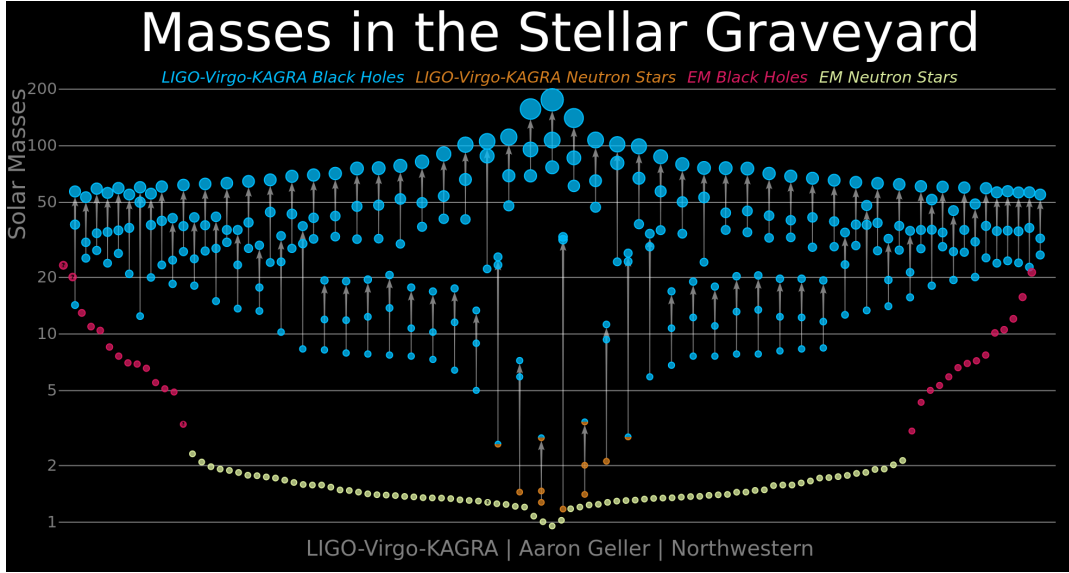


Figure 1.1: Masses of all the black hole (blue) and neutron star (orange) candidates detected by the ground interferometer of the Ligo-Virgo-Kagra collaboration. Half-blue and half-orange circles are compact objects whose nature remains uncertain. The arrows mark the connection between the progenitor compact objects in the merging binary with the compact object remnant. Red (Orange) circles refer to black hole (neutron star) candidates detected through electromagnetic surveys. An interactive version of this plot is available at this link.

with the two black hole-neutron star mergers GW200105 & GW200115, exhibiting a significant mass difference between their primary and secondary components. These systems are characterized by small mass ratios ( $q = m_2/m_1$ ) of approximately 0.1, 0.2, and 0.3, respectively (Abbott et al. 2021a). Additionally, a binary black hole merger event, named GW190412, has been observed with an asymmetric mass ratio of 0.3 (Abbott & et al. 2020).

Gravitational wave signals encode information also on the spin magnitude and orientation of these black hole mergers. Observations tell us that a non-negligible fraction of black holes have misaligned spins at the moment of the merger, and that most of the black holes in the population have relatively low spins with a dimensionless spin  $\chi$  distribution that peaks at  $\lesssim 0.2$  (Abbott et al. 2023). This is in strong contrast with previous electromagnetic observations of black holes hosted in X-ray binaries, which on the other hand favor the existence of mildly rapidly rotating ( $\chi \lesssim 0.3\text{--}0.9$ ), aligned ( $i < 10^\circ$ ) black holes (e.g., Zhang et al. 1997; Fragos & McClintock 2015).

Finally, the first detected binary neutron star merger event GW170817, conclusively established that such mergers function as sources of short gamma-ray bursts (Abbott et al. 2017; Abbott et al. 2017). These events also give rise to an electromagnetic counterpart known as a kilonova, which, through its interaction with the surrounding medium, makes neutron star mergers the most efficient heavy elements factories in the Universe (Rosswog et al. 2014).

All these features were inferred from the past 8 years of observations conducted by the Advanced Laser Interferometer Gravitational-Wave Observatory (LIGO, Aasi et al. 2015), the Advanced Virgo (Acernese 2015), and the Kamioka Gravitational Wave Detector (KAGRA, Aso et al. 2013) interferometers. Nevertheless, the compact binary merger population just discussed is likely to be updated soon. A new observation run is currently underway as of the date of writing, with plans for significant enhancements to the current detectors in the near future (e.g. LIGO Voyager, Adhikari et al. 2020).

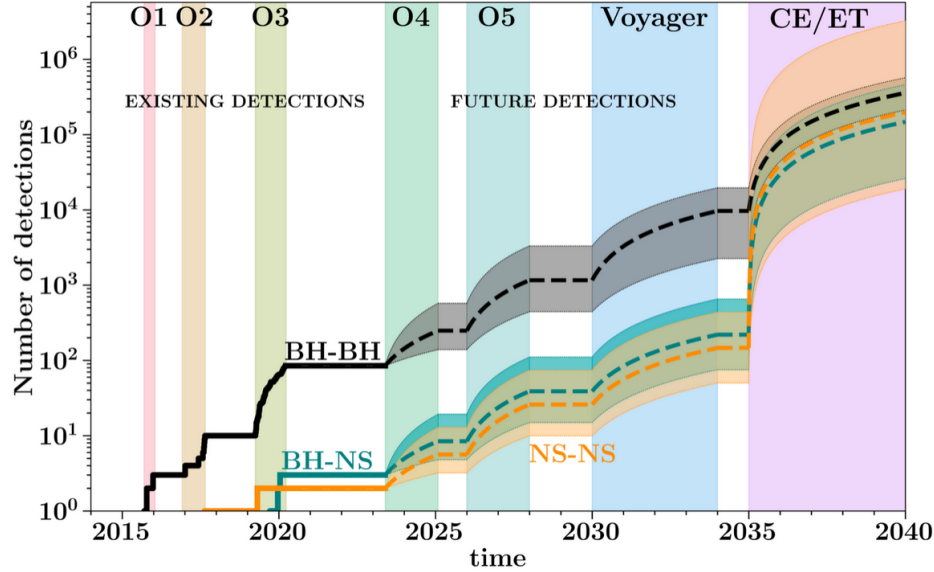


Figure 1.2: Number of expected detections of binary black holes (BH-BH; black), black hole-neutron stars (BH-NS; teal), and binary neutron stars (NS-NS; orange) mergers with their uncertainties as a function of past (O1 - Abbott et al. 2019, O2 - Abbott et al. 2021c, O3 - The LIGO Scientific Collaboration et al. 2021), ongoing (O4), and future observation runs (Voyager, CE/ET) performed with ground-based gravitational wave detectors. Predictions for future detected mergers were calculated by Borhanian & Sathyaprakash 2022. Plot Credit: Floor Broekgaarden.

Additionally, a new family of third-generation gravitational wave detectors is expected to become operative in the next decades, joining forces with the current network of detectors. The Einstein Telescope (ET, Punturo et al. 2010) and the Cosmic Explorer (CE, Reitze et al. 2019) are among these new detectors, designed specifically to push the observational horizon of stellar-mass black holes up and beyond redshift  $z = 100$  (Maggiore et al. 2020; Ng et al. 2021, 2022). Figure 1.2 shows the observed number of mergers over time alongside the predicted detections in future observational runs using upgraded gravitational wave interferometers.

As the number of detections continues to grow, we uncover fresh data regarding the unique characteristics of these events such as their masses, spins, and eccentricities. This will provide new insights into how these properties are distributed across the entire population of mergers, while addressing the question of whether and how they are correlated with each other. These properties act as fingerprints of the formation channels of these binary mergers and encode the evolutionary history of these binaries. If studying the observed properties of a merger is crucial for tracing back its formation, the reverse is also true: studying a stellar population and its surrounding environment is essential to predict the compact merger population to compare with gravitational wave observations. This is precisely the method employed to study the formation channels of compact binary mergers, which is the focus of this thesis. In the following sections, I will present the main formation channels of compact binary mergers that are commonly discussed in the literature.

## 1.2 Where do black holes and neutron stars come from?

Black holes and neutron stars are the first and second most compact objects in the Universe. Their density is so high that when they are part of a tight binary system, their motion strongly affects the binary's quadrupole moment—i.e., the measure of the system's mass distribution—and efficiently generates gravitational wave emission. Black hole and neutron star binaries are the only gravitational wave sources detected by LIGO-Virgo-Kagra to date. Other theorized gravitational wave sources include binaries of white dwarfs, supernovae, continuous gravitational wave background produced by asymmetric single neutron stars, cosmic strings, and inflation. Below, I outline the main properties of black holes and neutron stars, along with their formation process through the evolution from a single star.

### 1.2.1 Black Holes and Neutron Stars

Black holes are the simplest objects existing in nature. Defined as purely geometric objects, black holes are classically described by just five degrees of freedom: their mass, their spin components, and their electric charge. They were first theorized in 1916 by Karl Schwarzschild as the spherically symmetric, non-rotating solution of the Einstein field equations. In principle, any object with mass  $M$  could become a black hole if squeezed below the limit known as the Schwarzschild radius:

$$r_s = \frac{2GM}{c^2} \sim 3 \left( \frac{M}{M_\odot} \right) \text{ km.} \quad (1.1)$$

Here,  $G$  is the gravitational constant,  $c$  is the speed of light and  $M_\odot \simeq 1.989 \times 10^{33} \text{ g}$  is the mass of the sun. The Schwarzschild radius defines the boundary of a non-rotating black hole, known as the event horizon, or the limit beyond which events cannot affect any external observer. Equation 1.1 implies that, if we could compress the Sun to a radius of 3 km, we would create a black hole. In spite of their purely geometric nature, the processes leading to the formation of a black hole are anything but straightforward. Depending on their mass, black holes can form through different channels and are therefore categorized in 3+1 groups. *Stellar-mass black holes* include all black holes with a mass below  $100 M_\odot$  and represent the final stage in the evolution of stars with a mass greater than  $\sim 25 M_\odot$  (Maeder 1992; Heger et al. 2003). These black holes can also be created if a neutron star accretes enough mass by a nearby stellar companion or through a merger with another compact object. *Intermediate-mass black holes* cover the mass range  $100 - 10^5 M_\odot$ . Their formation is associated with the evolution of very massive, metal-free Population III stars (Madau & Rees 2001), runaway collisions among stars (Portegies Zwart & McMillan 2002a), or repeated multiple mergers of lighter black holes (Miller & Hamilton 2002). They are considered the seeds of supermassive black holes and one of the primary candidates for tidal disruption events (Greene et al. 2020). *Super-massive black holes* are a class of black holes with a mass larger than  $\sim 10^5 M_\odot$ : they reside in the core of galactic nuclei, playing a crucial role in shaping the structure and evolution of galaxies (Ferrarese & Ford 2005; Kormendy & Ho 2013). Finally, the last category are the *primordial black holes*. These are also known as non-astrophysical black holes as they are theorized to have formed in the early universe shortly after the Big Bang from the direct collapse of high-density regions (Khlopov 2010). Hence, their mass is not constrained by any stellar evolution model and can thus cover the entire mass spectrum (Carr 1975). In this thesis, we treat only stellar- and intermediate-mass black holes.

Neutron stars, on the contrary, are one of the most complex objects existing in nature. They exhibit extreme physical conditions, with densities reaching  $\rho \sim 10^{15} \text{ g cm}^{-3}$  enclosed within a radius

of  $r \sim 12$  km. Phenomena such as superfluidity and superconductivity, with critical temperatures near  $10^{10}$  K, occur in their core at birth. Neutron stars also demonstrate opaqueness to neutrinos and may be composed of strange matter in their inner layers. Additionally, they undergo rapid rotation with periods as low as milliseconds, possess magnetic fields exceeding  $10^{13}$  Gauss, and exhibit surface temperatures that can range up to  $\sim 10^6$  K (Lattimer & Prakash 2004). The mass range of a neutron star is set to be in the range between  $1.4 M_{\odot}$  and  $\lesssim 3 M_{\odot}$ . The lower limit is known as the Chandrasekhar limit (Chandrasekhar 1931), beyond which electron degeneracy pressure is insufficient to counteract gravitational forces, leading to the collapse of a white dwarf and the formation of a neutron star. The upper limit is the Tolman-Oppenheimer-Volkoff limit (Tolman 1939; Oppenheimer & Volkoff 1939), which is still poorly constrained due to its strong dependency on the equation-of-state of neutron stars (Akmal et al. 1998). Above this limit, the neutron degeneracy pressure and repulsive nuclear forces are not enough to compensate for the self-gravity of the star, which collapses into a black hole. As a consequence of their nature, only two processes can form neutron stars. Most neutron stars born from the ashes of a supernova event in stars with masses ranging from approximately  $\sim 8 M_{\odot}$  to  $\sim 25 M_{\odot}$  Heger et al. (2003). Less commonly, neutron stars can also originate from an accretion-induced collapse event of a white dwarf (Nomoto & Kondo 1991; Fryer et al. 1999). With respect to black holes, neutron stars have the advantage of being visible in the electromagnetic spectrum. Furthermore, if the magnetic poles of the star are misaligned with respect to the rotational axis, the neutron star will appear as a pulsar: highly magnetized, rotating neutron stars that emit beams of electromagnetic radiation out of their magnetic poles. These beams of radiation are observed as regular pulses of light when the rotation of the neutron star causes the beams to sweep across the observer's line of sight, much like a lighthouse beam. To date, more than 3400 radio pulsars are known (Manchester et al. 2005)

### 1.2.2 From a single star to a compact object

Both black holes and neutron stars are the final byproducts of the evolution of massive stars, i.e. stars with mass  $> 8 - 10 M_{\odot}$ . However, not all massive stars follow the same evolutionary path. The evolution of a star is generally determined by three factors: primarily by its initial mass at the onset of the main sequence, denoted as  $M_{\text{ZAMS}}$ , and secondarily by its metallicity fraction,  $Z$ , and its rotation rate,  $\omega$ . Even though their evolution is regulated almost solely by these three parameters, all stars progressively burn chemical elements from lighter to heavier ones during their lifetime. Stars spend most of their life (85 – 90%) in the main sequence burning hydrogen in their core. After the main sequence, the second longest phase in the lifetime of a star is the core helium burning sequence (10 – 15%). Whether a star continues burning heavier elements in its core depends on its initial mass. Low- and intermediate-mass stars are not massive enough to ignite carbon in their cores, and after the core helium burning, they conclude their lives as white dwarf stars. In contrast, massive stars have cores that reach the conditions necessary to ignite and burn heavier elements than helium. The final stages of the evolution in these stars cover only approximately  $\sim 0.001$  of the total lifetime, and range from the carbon-burning phase to the neon-, oxygen- and silicon-burning, up to the formation of iron-group elements and the subsequent explosion/implosion event (Maeder & Meynet 2000a; Kippenhahn et al. 2013). The duration of each of these phases, as well as the compact remnant left at the end of a star's evolution, are summarized in Figure 1.3 as functions of the star's initial mass.

The evolution of a massive star is strongly affected by its metallicity. At the beginning of the main sequence, low metallicity stars are more compact than their metal-rich counterparts, primarily

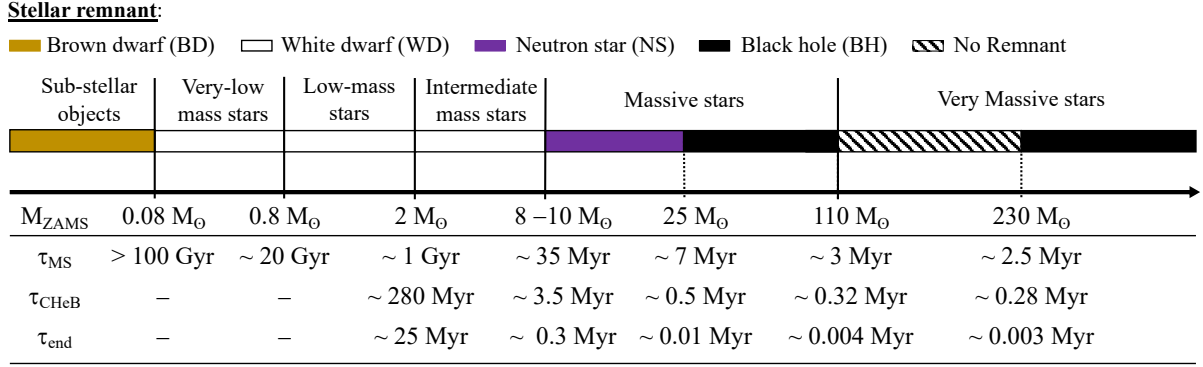


Figure 1.3: The colors show the remnant type left from a star at the end of its lifetime as a function of its initial mass ( $M_{ZAMS}$ ), the time spent in the main sequence ( $\tau_{MS}$ ), the time spent in the core helium burning phase ( $\tau_{CHeB}$ ), and the time spent from the end of the core helium burning phase to the formation of the compact object ( $\tau_{end}$ ). Low-mass and intermediate-mass star limits are taken from Nguyen et al. (2022), neutron stars-black holes transition mass from Fryer et al. (2012), and limits for the no remnant region from Spera & Mapelli (2017). Plot credit: Costa et al. (2023a).

due to lower opacity in the envelope. Additionally, they develop larger cores at the end of the main sequence and during the core helium burning phases. Furthermore, metallicity plays a key role in shaping the winds of massive stars. Throughout their life, stars experience mass loss episodes under the form of stellar winds, which are outflows of matter ejected from the upper atmosphere of the star. Massive and very massive stars have their evolutionary tracks completely shaped by winds, as shown in Figure 1.4. Stellar winds play a crucial role in the mass-loss process during the star lifetime, and drastically decrease the initial mass of the star along its evolutionary path influencing the star's overall evolution. Additionally, stellar winds contribute to the enrichment of the interstellar medium with heavy elements, affecting the chemical evolution of galaxies. Stellar winds exhibit distinct behaviors not only based on metallicity but also during different phases of stellar evolution. For evolved cold stars (e.g. red giant, asymptotic giant branch stars) winds are produced by the interaction between radiation pressure and dust particles in the colder outer layers of the atmosphere. For these stars, a commonly used approach is to adopt a wind prescription in which the mass loss is modeled using empirical interpolation equations developed by de Jager et al. (1988). These equations are a function of the star's luminosity and effective temperature. In massive hot stars (e.g. O, B, Wolf-Rayet, luminous blue variable stars), winds are driven by radiation pressure on the resonance absorption lines of atmospherical metal ions. Massive star winds, and the relative mass loss rate  $\dot{M}$ , are therefore strictly related to the star metallicity  $Z$ . For O-B stars, this dependence can be expressed with the relation found by Vink et al. (2001):

$$\dot{M} \propto Z^{0.85} v_\infty^p \quad \begin{cases} p = -1.23 & \text{if } T_{\text{eff}} \gtrsim 25000K \\ p = -1.60 & \text{if } 12000K \lesssim T_{\text{eff}} \lesssim 25000K \end{cases} \quad (1.2)$$

where  $T_{\text{eff}}$  is the effective temperature of the star and  $v_\infty$  is the terminal velocity of the wind which corresponds to its maximum velocity. These stellar winds can strip away substantial amounts of the hydrogen envelope in an O-B star, leading to the star to evolve into a Wolf-Rayet star (also known as the Conti-scenario, Conti 1975a; Abbott & Conti 1987). Eventually, if stellar winds are extremely effective, the H-rich envelope can be completely peeled off, and the star becomes a naked

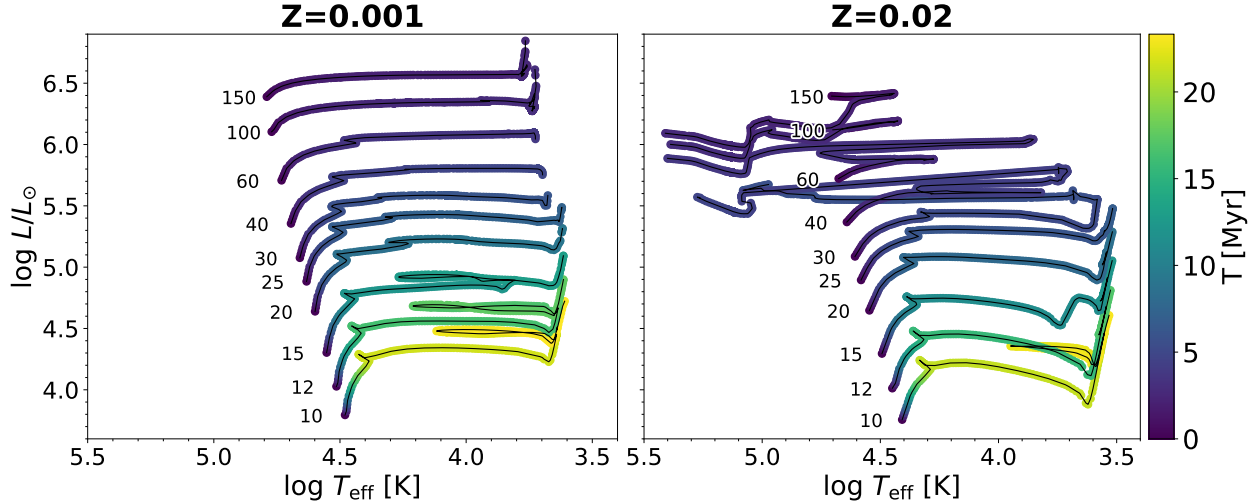


Figure 1.4: Evolutionary tracks in the Hertzsprung-Russell diagram for single stars in the mass range  $10 - 150 M_\odot$ . The left (right) panel shows the effective temperature and luminosity evolution of the stars at metallicity  $Z = 0.001$  ( $Z = 0.02 \simeq Z_\odot$ ). The color bar shows the time spent by the stars at any point of the evolutionary tracks. The evolutionary tracks are computed by Nguyen et al. (2022) with the PARSEC stellar evolution code (Bressan et al. 2012).

pure He star. Even in Wolf-Rayet stars, mass loss through wind emission strongly depends on stellar metallicity. A commonly used prescription for modeling Wolf-Rayet winds, while also considering the Eddington factor  $\Gamma_{Edd}$ , is the one introduced by Tang et al. (2014) and Chen et al. (2015)

$$\dot{M} \propto Z^\alpha \quad \begin{cases} \alpha = 0.85 & \text{if } \Gamma_{Edd} < 2/3 \\ \alpha = 2.45 - 2.4\Gamma_{Edd} & \text{if } 2/3 \leq \Gamma_{Edd} \leq 1 \end{cases} \quad (1.3)$$

The Eddington factor is defined as the ratio between the star luminosity and the Eddington luminosity  $L_{Edd} = 4\pi cGM/k$ . It keeps into account the maximum luminosity that a star in hydrostatic equilibrium with mass  $M$  can reach due to the electron-scattering process, defined by the cross-section  $k$ . Stellar winds increase strongly when stars approach the Eddington limit (Gräfener & Hamann 2008; Vink et al. 2011).

The initial mass of a star, combined with its mass loss history, determines the final mass during the star's last evolutionary phases and the corresponding supernova mechanism. Stars with zero-age main sequence mass in the range  $10 \lesssim M_{\text{ZAMS}}/M_\odot \lesssim 30$  experience an iron core-collapse supernova. In the last stages of these stars, when temperatures in the core reach  $\sim 10^{10}$  K, energy can no longer be produced by fusion. The photo-disintegration of Fe-group nuclei and electron capture by inverse beta-decay become highly efficient, leading to the effective production of alpha particles, neutrons, and neutrinos (Janka 2012). Ultimately, the degenerate iron-nickel core collapses when it reaches the Chandrasekhar mass limit ( $\sim 1.4, M_\odot$ , Chandrasekhar 1931). This causes an outgoing bounce shock that reverses the supersonic infalling material of the outer envelopes. Neutrino energy possibly contributes to the reverse blastwave, which leads the outer layers of the star to explode. Since part of the total mass is ejected in the explosion, core-collapse SNe produces low-mass compact objects such as neutron stars or stellar-mass black holes in the range  $\sim 3 - 15 M_\odot$  (Fryer et al. 1999). In some cases, neutrino energy contribution is not sufficient to re-ignite the outgoing blastwave,

and the shock stalls leading a great part of the star layers to fall and accrete the proto-neutron star. If degeneracy neutron pressure is not sufficient to overcome the infalling material pressure, the proto-neutron star can become a black hole by fallback with slightly larger masses in the range  $\sim 15 - 30 M_{\odot}$ <sup>1</sup>. The asymmetric explosion of a core-collapse supernova can induce large recoil velocities, called natal kick, to the newborn compact object (Fryer et al. 2012). The natal kick is expected to be larger on neutron stars, and can range from a few  $\text{km s}^{-1}$  to  $\sim 1000 \text{ km s}^{-1}$  (Wongwathanarat et al. 2013). Stars in the mass range  $8 - 10 M_{\odot}$  are massive enough to ignite carbon in a shell surrounding a degenerate oxygen-neon-magnesium core. If the core remains less massive than the critical limit  $\sim 1.37 M_{\odot}$  (Nomoto 1984), the star will end its life as a neon-oxygen white dwarf. Above this threshold, electron capture on magnesium and neon nuclei becomes efficient, removing part of the pressure support against gravity and driving the core collapse. In these stars, the bounce-back shock does not stall and leads to a successful explosion of the outer layers, known as an electron-capture supernova (Jones et al. 2019). Electron-capture supernovae produce lighter neutron stars with moderately low natal kicks (Gessner & Janka 2018).

More massive stars  $M_{\text{ZAMS}} \gtrsim 30 M_{\odot}$  can build up a carbon-oxygen core of  $M_{CO} > 7.6 M_{\odot}$  ending their life via the direct collapse mechanism to form a black hole with  $M_{\text{BH}} \geq 20 M_{\odot}$  (Fryer et al. 2012). Direct collapse SNe are failed supernovae and differ from the core-collapse mechanism because the outgoing shock wave generated by the core contraction fails to unbind mass, therefore all the star envelopes keep falling and no ejecta are produced. All the mass is accreted by the central compact object, and if the pre-SN star is massive enough an intermediate-mass black hole can be left. Furthermore, due to the nearly spherical symmetry of the process, kick velocities are highly reduced with respect to the core-collapse case.

When massive stars develop a helium core  $M_{\text{He}} \sim 30 M_{\odot}$ , pair production becomes extremely efficient. In the core, electron-positron pairs make oxygen/silicon ignite in a thermal runaway reaction which exerts a pulse outwards. This process can repeat several times and, if the star is able to restore the equilibrium after these instabilities, the phenomenon is defined as a pulsational pair-instability supernova. This induces a severe mass loss to the star, which will eventually end its life by core-collapse, leaving a lighter black hole  $M_{\text{BH}} \sim 30 - 55 M_{\odot}$  compared to the expected values of  $M_{\text{BH}} \sim 50 - 100 M_{\odot}$  without pulsations. On the other hand, if the star cannot survive this explosive burning phase, it explodes in a pair-instability supernova leaving no remnant. Pair-instability becomes more efficient at low metallicities  $Z \simeq 0.1 Z_{\odot}$ : when  $70 \lesssim M_{\text{ZAMS}}/M_{\odot} \lesssim 150$  (i.e.  $32 \lesssim M_{\text{He}}/M_{\odot} \lesssim 64$ ) a star possibly evolves into a pulsational pair-instability supernova, while if  $150 \lesssim M_{\text{ZAMS}}/M_{\odot} \lesssim 260$  (i.e.  $64 \lesssim M_{\text{He}}/M_{\odot} \lesssim 135$ ) a star can explode as a pair-instability supernova (Woosley 2017; Spera & Mapelli 2017). Pulsational and pair-instability supernovae cause the pair-instability mass gap in the range  $60 \lesssim M_{\text{BH}}/M_{\odot} \lesssim 120$  shown in Figure 1.5, where no black holes are expected to be formed by the evolution of single stars of any mass and metallicity.

In addition to the initial mass and metallicity, rotation also plays a crucial role in influencing the evolution of all stars. Rotation primarily reduces gravity at any point of the star, except on the rotation axis, due to centrifugal force. This alters the star's shape, transforming it from a spherical to an oblate form, with a polar radius smaller than the equatorial one. Since the local surface brightness of a star is proportional to the local effective gravity, a rotating star will have lower

---

<sup>1</sup>The mass ranges in which a supernova gives birth to a neutron star by core-collapse or a black hole by fallback are still a matter of discussion. O'Connor & Ott (2011), for example, proposed an "island of explodability" scenario derived from their 1D hydrodynamical simulations in which SN explosion mechanisms do not behave monotonically with the mass of the progenitor star.

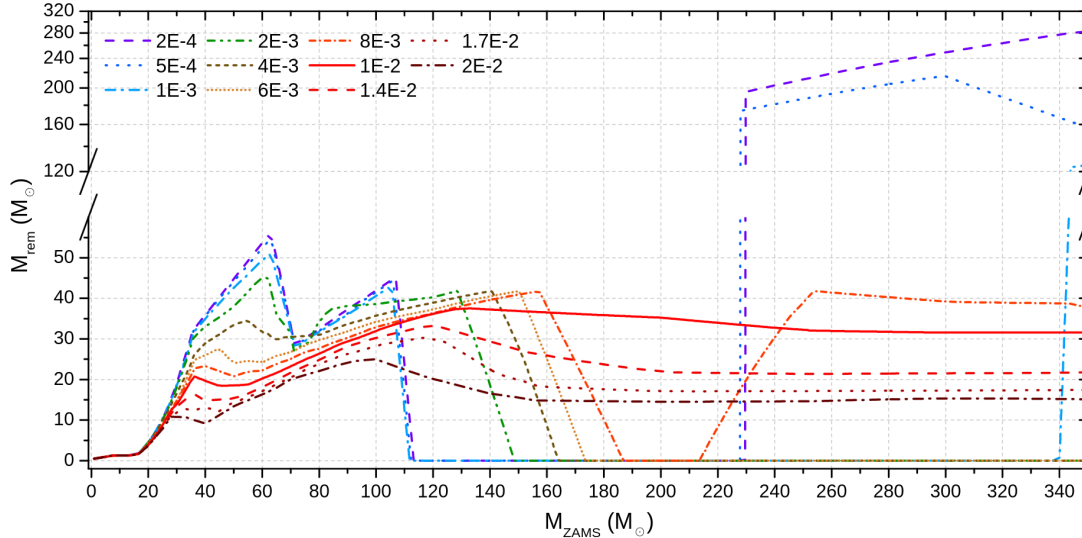


Figure 1.5: Remnant mass ( $M_{\text{rem}}$ ) as a function of the zero-age main sequence mass ( $M_{\text{ZAMS}}$ ) from different metallicities (colors) from Spera & Mapelli (2017). The y-axis is broken in the range  $60 \lesssim M_{\text{rem}}/M_{\odot} \lesssim 120$  due to the lack of black holes caused by pulsational and pair-instability supernovae. This is the so-called pair-instability mass gap in the black hole mass spectrum. The plot shows that only stars with low metallicity experience pair-instability, while being also the only ones to form intermediate-mass black holes by direct collapse due to the weaker winds.

temperatures closer to the equator (known as Von Zeipel effect, von Zeipel 1924). Since luminosity is proportional to the effective temperature of a star (Stefan-Boltzmann law), this implies that the luminosity is not constant across the stellar surface and it is larger at the poles where gravity and temperature are higher (known as gravity darkening effect, Maeder 1999; Espinosa Lara & Rieutord 2011). A first primary consequence of the reduced gravity is that rotation also enhances the mass loss rates by stellar winds. This is particularly important for massive stars, which have been observed to exhibit higher rotational velocities compared to low-mass stars (Hunter et al. 2007; McQuillan et al. 2014). Finally, rotation causes rotational mixing in the star under the form of meridional currents, also known as Eddington-Sweet circulation, and shear mixing. Meridional currents are a direct consequence of the von Zeipel effect and manifest as large-scale flows that transport material and angular momentum within the star along the meridional direction (Eddington 1925a; Sweet 1950a). Shear mixing occurs when the star does not rotate as a solid body, but its inner shells rotate with different angular velocities, causing friction (Zahn 1974). In general, rotational mixing redistributes the chemical abundances within the stellar structure, providing fresh hydrogen to the core from the outer layers and carrying the ashes of nuclear fusion up to the star's envelope. This contributes to increase the lifetime of a star from 25% (for a  $9 M_{\odot}$  star) to 15% (for a  $120 M_{\odot}$  star, Maeder & Meynet 2000a; Costa et al. 2023a). Stellar rotation is particularly relevant if the star is part of a binary system, as it can be triggered by binary processes as tides and mass transfer episodes.

### 1.3 Two is better than one: the Isolated Channel

The vast majority of massive stars live in binary or higher-order multiple systems (Sana et al. 2012; Moe & Di Stefano 2017). More than 85% of O-type stars, the progenitors of compact objects, are found in binary systems, with this fraction decreasing for lower mass stars. While the majority of massive stars exist in binaries, only a small fraction of them are capable of producing a compact binary merger. When a star is part of a binary system, its evolution is significantly influenced by interactions with its companion. Binary processes such as mass transfer, common envelope events, tidal interactions, collisions, and the loss of mass and angular momentum can profoundly impact the evolution of both stars in the system, and of the binary. The intricate interplay between these binary processes and the individual evolution of the two stars within the binary will determine whether the system evolves into a compact binary merger. The following chapter summarizes the effects of the most significant binary processes and their impact on the formation of compact binary mergers.

#### 1.3.1 Mass transfer

When two stars are part of a binary system, they can exchange mass and angular momentum through mass transfer episodes. Two main processes of mass transfer exist: the wind mass transfer through Bondi-Hoyle accretion, and the Roche lobe overflow. In Section 1.2.2 we have seen that massive stars lose a large amount of mass due to the wind mass loss episodes experienced along their lifetime. If the massive star is in a binary system, the mass lost can be accreted from the companion star or compact object at a rate:

$$\dot{M}_{\text{acc}} = \frac{1}{\sqrt{q - e^2}} \left( \frac{G M_{\text{acc}}}{v_w^2} \right)^2 \frac{\alpha_w}{2 a^2} \frac{1}{[1 + (v_{\text{orb}}/v_w)^2]^{3/2}} |\dot{M}_{\text{don}}|. \quad (1.4)$$

Equation 1.4 describes the accretion rate, i.e. the amount of matter accreted by the accretor star over time, according to the Bondi-Hoyle formalism (Bondi & Hoyle 1944) updated by Hurley et al. (2002). The accretion rate depends on the semi-major axis  $a$  and the eccentricity  $e$  of the binary, on the orbital velocity  $v_{\text{orb}} = \sqrt{G(M_{\text{acc}} + M_{\text{don}})/a}$ , on the efficiency parameter  $\alpha_w \sim 3/2$  and on the mass lost by the donor star over time  $\dot{M}_{\text{don}}$  and the wind velocity  $v_w$ . These latter terms strongly depend on the stellar phase of the donor. When the star is an O-B type supergiant, stellar winds can reach supersonic velocities of  $\gtrsim 10^3 \text{ km s}^{-1}$  with mass loss rates of the order of  $\sim 10^3 \text{ M}_\odot \text{ yr}^{-1}$  (Crowther et al. 2002). These numbers, combined with the fact that winds are ejected almost isotropically (dependent on stellar rotation, as discussed in Section 1.2.2), and considering the relatively small cross-section of the companion star, indicate that only a small fraction of the lost mass is accreted by the companion. Consequently, the wind-accretion mechanism is an inefficient form of mass transfer in binary systems. Nevertheless, winds still play a significant role as they carry away angular momentum from the system, leading to the widening of the binary orbit. This implies that binaries with large metallicities are expected to exhibit larger orbital separations compared to their counterparts with lower metallicity. Finally, wind accretion is the mechanism that powers X-ray emission in high-mass X-ray binary systems (Tauris & van den Heuvel 2006).

A more efficient mechanism of mass transfer in a binary is the Roche lobe overflow. In a binary system, the gravitational potential is given by the combination of the gravitational potentials of the two stars, and it depends not only on the masses of the stars but also on the geometry of the system. This potential is depicted in Figure 1.6, and takes the name of Roche potential. When one of the two stars expands its radius up to the inner Lagrangian point L1, its matter starts to flow and is

accreted by the companion star. Analytically, the Roche lobe overflow starts when the radius of the donor star is equal or larger with respect to the Roche lobe radius (Eggleton 1983):

$$\frac{R_L}{a} = \frac{0.49 q^{2/3}}{0.6 q^{2/3} + \ln(1 + q^{1/3})}. \quad (1.5)$$

The equation depends on the semi-major axis of the binary  $a$  and on the mass ratio  $q = M_{\text{don}}/M_{\text{acc}}$ . The Roche lobe radius is defined as the radius of a sphere enclosing the same volume as the volume of the Roche lobe. Equation 1.5 is solely valid for binaries with  $e = 0$ , as systems entering the Roche lobe overflow regime have typically already been circularized by tidal interactions between the two stars. The Roche lobe overflow is generally triggered by the expansion of the donor star along its evolution. This can happen in various phases of the stellar evolution history, and it depends on the properties of the star but also of the binary system. For very tight binaries with periods  $< 10$  days, the Roche lobe overflow can be triggered even when the primary is in its main sequence. This is more likely for massive ( $\geq 40 M_\odot$ ) metal-rich stars, where gravity and radiation pressure on their surface are comparable, leading to the formation of an inflated envelope (Brott et al. 2011a; Klencki et al. 2020). The mass transfer is then more likely to take place when the stars cross the Hertzsprung gap, i.e. the evolutionary phase after the core-hydrogen burning, where the star can expand as twice its radius before igniting helium in its core. In this phase, the expansion once again depends on metallicity, with substantial expansion observed for stars with high  $Z$ , while low-metallicity stars remain compact during this transitioning phase (Brunish & Truran 1982). Finally, when the star reaches the red supergiant branch, its outer envelope can expand reaching a few thousand solar radii triggering the Roche lobe overflow. In general, metallicity plays a crucial role in the expansion of star radii. Stars with low  $Z$  expand later in their evolutionary history and are more prone to initiating mass transfer in the later stages of their evolution. Consequently, a binary with the same initial parameters formed at different metallicities is likely to enter mass transfer at different ages (Anders et al. 2022).

Roche lobe overflow not only alters the mass distribution of the binary system but also affects the radii of the stars, the orbital period, and the overall conservation of angular momentum and matter within the system, depending on whether it is conservative or not. The stability of the mass transfer is set by the interplay between the evolution of these parameters and the evolution of the Roche lobe radius of the donor star. More specifically, it is commonly assumed that if the Roche lobe radius of the donor star shrinks faster than the radius of the star, the process is considered unstable. Assuming that the stellar radius and its mass are connected through a relation  $R \propto M^\zeta$ , the variation of the donor star radius undergoing a Roche lobe overflow can be described as (Mapelli et al. 2019)

$$\frac{dR_{\text{don}}}{dt} = \frac{\partial R_{\text{don}}}{\partial t} + \zeta_{\text{don}} \frac{R_{\text{don}}}{M_{\text{don}}} \frac{dM_{\text{don}}}{dt}, \quad (1.6)$$

where  $\frac{\partial R_{\text{don}}}{\partial t}$  denotes the radial evolution of the star because of the nuclear burning processes,  $\frac{dM_{\text{don}}}{dt}$  is the mass loss rate of the donor star, and  $\zeta_{\text{don}} = d\log R_{\text{don}}/d\log M_{\text{don}}$  measures the adiabatic or thermal response of the donor star to mass loss. The evolution of the Roche lobe radius of the donor star is described as

$$\frac{dR_L}{dt} = \frac{\partial R_L}{\partial t} + \zeta_L \frac{R_L}{M_L} \frac{dM_L}{dt}, \quad (1.7)$$

with  $\frac{\partial R_L}{\partial t}$  depending on the evolution of the semi-major axis of the binary, which in turn depends on tides, gravitational-wave emission, and wind mass loss. The term  $\zeta_L = d\log R_L/d\log M_{\text{don}}$  encodes the response of  $R_L$  to the mass transfer process. The mass transfer is assumed to become unstable

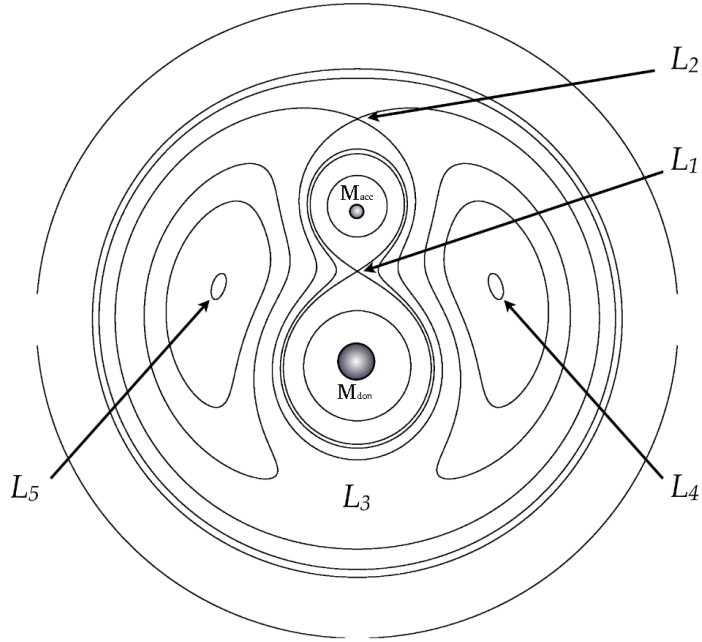


Figure 1.6: Equipotential surfaces of the Roche potential of a binary with a donor,  $M_{\text{don}}$ , and an accretor  $M_{\text{acc}}$  star. The plot highlights also the Lagrangian points, i.e. the region in the potential where the gravitational forces from the two stars acting on a point mass co-rotating with the system cancel out. Image credit: Benacquista & Downing (2013).

when  $\zeta_L > \zeta_{\text{don}}$ , i.e. when the Roche radius evolves faster toward smaller radii than the donor radius. This stability criterion can be expressed also in the form of a critical mass ratio  $q_{\text{crit}}$ , such that if the binary reaches  $q > q_{\text{crit}}$  due to mass transfer, the process becomes unstable. Stars with different types of stellar structures tend to respond differently to mass transfer, exhibiting different values of  $\zeta_{\text{don}}$ . Stars with a convective envelope and a flat entropy profile tend to expand, while radiative-envelope stars, with a steep entropy gradient, shrink in response to mass loss (Costa et al. 2023a). As a result, mass transfer from convective-envelope donors is much more likely to become dynamically unstable (Soberman et al. 1997). In general, low mass ratios<sup>2</sup> and stellar donors with radiative envelopes trigger more likely a stable mass transfer.

### 1.3.2 Common Envelope

The Roche lobe overflow can be unstable either on a dynamical timescale or on a thermal timescale. If the process of mass transfer is dynamically unstable, or if both stars exceed their Roche lobes, then two possible outcomes may occur. In cases where the donor lacks a steep density gradient between the core and the envelope, the binary is expected to undergo a merger. Alternatively, if the donor exhibits a clear distinction between the core and the envelope, the binary may enter a common envelope phase. When a common envelope phase is triggered, the binary system evolves in a configuration composed by the core of the donor and the companion star embedded in the

<sup>2</sup>In the context of Roche lobe overflow, the definition of mass ratio takes the form of  $q = M_{\text{don}}/M_{\text{acc}}$  such that  $q$  can be larger than 1. In binary stellar evolution, as in the rest of this thesis, the common definition of mass ratio is  $q = M_2/M_1$ , where  $M_1$  and  $M_2$  are the primary and secondary component of the binary, respectively, such that  $M_1 > M_2$ .

same non-corotating envelope. The companion star can also be a compact object or the core of a stripped star. During a common envelope phase the embedded binary system is subject to drag forces from the envelope which cause the separation of the two stars to decrease. The loss of orbital energy is assumed to heat up and expand the envelope, and the whole common-envelope phase ends when either the envelope is completely expelled, or the two objects inside the envelope merge and no more energy is available to expel the envelope. Mergers driven by unstable mass transfer are expected to produce exotic objects as blue stragglers (Lombardi et al. 1996; Wang et al. 2022), Thorne-Zytkov objects (Thorne & Zytkow 1977; Wei et al. 2023), and massive black holes falling inside the pair-instability mass gap (Di Carlo et al. 2019; Ballone et al. 2023). On the other hand, if the system is capable of ejecting the envelope, the post-common envelope binary will be composed of two naked stellar cores, or of a compact object and a naked stellar core. A binary that has survived a common envelope event is typically characterized by a smaller orbital separation compared to its initial state. This is a consequence of the spiral-in process experienced due to the drag force exerted by the envelope. The survivability of a binary system through a common envelope phase remains one of the most significant open questions in astrophysics (Taam & Sandquist 2000; Zorotovic et al. 2010; Ricker & Taam 2012; Ivanova et al. 2013; Claeys et al. 2014a; Klencki et al. 2021). The most commonly used prescription to analytically describe the common envelope is the energy formalism (Webbink 1984), also known as the  $\alpha - \lambda$  formalism, which allows obtaining a first-order approximation of the survivability of the system and its orbital properties post-envelope ejection. This prescription works under the assumption that the sole source of energy required to unbind the envelope is exclusively provided by the loss of orbital energy of the two cores during the spiral-in process. In this framework, the orbital energy variation is expressed as:

$$\Delta E = \alpha(E_{b,f} - E_{b,i}) = \alpha \frac{G M_{c,1} M_{c,2}}{2} \left( \frac{1}{a_f} - \frac{1}{a_i} \right) \quad (1.8)$$

The parameter  $\alpha$  represents the fraction of orbital energy converted into kinetic energy to remove the envelope during the evolution. Here,  $E_{b,i}$  and  $a_i$  represent the binding energy and the semi-major axis at the onset ( $i = b$ ) and after ( $i = f$ ) the common envelope event. Meanwhile,  $M_{c,1}$  and  $M_{c,2}$  denote the mass of the core of the two stars, or their total mass if they are compact objects. This energy variation, is to be set equal to the binding energy of the envelope, defined as

$$E_{b,env} = \frac{G}{\lambda} \left[ \frac{M_{env,1} M_1}{R_1} + \frac{M_{env,2} M_2}{R_2} \right], \quad (1.9)$$

where  $M_1$  and  $M_2$  are the masses,  $M_{env,1}$  and  $M_{env,2}$  the masses of the envelopes, and  $R_1$  and  $R_2$  the radii of the two components of the binary. The  $\lambda$  parameter measures the concentration of the envelope and incorporates all the uncertainties related to the envelope structure. If we set  $\Delta E = E_{b,env}$  it is possible to derive the final semi-major axis  $a_f$  post envelope ejection. If  $a_f$  is smaller than the sum of the radii of the two cores, the binary has successfully ejected the envelope and survives as a tight binary, composed either of pure helium stars, Wolf-Rayet stars, or compact objects. The common envelope process is extremely important to produce binary black hole mergers, as it represents an efficient mechanism to shrink the semi-major axis of a binary before gravitational wave emission becomes efficient (Dominik et al. 2012; Giacobbo & Mapelli 2018a). Some authors have found that  $\alpha \geq 1$  (e.g. Fragos et al. 2019; Iorio et al. 2023) is necessary to produce a successful population of compact binary mergers. This unphysical value is justified by the fact that the orbital binding energy is not the only source of energy available in the system to eject the envelope. Other sources may participate, such as the thermal energy of the envelope (e.g. Han et al. 1994), the

recombination energy of the envelope medium (e.g. Kruckow et al. 2016), tidal heating/cooling from stellar spin up/spin down (e.g. Ivanova et al. 2013), nuclear fusion energy (e.g. Ivanova et al. 2002), the enthalpy of the envelope (e.g. Ivanova & Chaichenets 2011), and the accretion energy, which might produce outflow and jets (e.g. MacLeod & Ramirez-Ruiz 2015).

### 1.3.3 Chemically Homogeneous Evolution

The necessary ingredient for a star to trigger a common envelope phase is the requirement of a steep density gradient between its inner and outer parts, with a net distinction between the core and the envelope. However, when the rotational velocity of a star is sufficiently large, this net distinction vanishes as chemical abundances are redistributed along the radial direction of the stellar structure, such as the star becomes chemically homogeneous (de Mink et al. 2009, 2013; Brott et al. 2011a). Rotation transports heavy elements produced in the core toward the surface due to the centrifugal force, while mixing currents carry fresh hydrogen from the star’s envelope toward the core, beyond the limit of convection. This allows the star to burn in its core the hydrogen present in the stellar envelope, increasing the lifetime of the star along its main sequence (see section 1.2.2). Simultaneously, as heavier elements are transported to the outer layers, the opacity of the star changes, and the star moves towards larger temperatures and luminosities along its evolution. The star eventually becomes a pure helium star or a Wolf-Rayet star, with a larger core produced by the overabundance of nuclear fuel transported by rotational mixing (Limongi & Chieffi 2018). These larger cores lead the star to produce larger compact objects. The chemically homogeneous evolution is one of the possible formation mechanisms of the isolated channel used to explain the formation of binary black hole mergers with black holes  $\geq 20 M_{\odot}$  (Eldridge et al. 2017; Riley et al. 2021). Rapid rotation can be achieved only at low metallicities, typically  $Z < 0.004$ , as winds are weaker, and the escape of angular momentum through mass loss is limited. Stars born as rapid rotators are generally massive, i.e.,  $> 10 - 20 M_{\odot}$ , but they require an external mechanism to maintain their rotation sufficiently large to counteract wind momentum loss and become chemically homogeneous.

Two possible mechanisms exist in the literature: accretion-induced spin-up (Eldridge et al. 2008) and tidal spin-up (Song et al. 2016a). In the first scenario, the primary star expands and triggers a Roche-Lobe overflow. If the mass loss by the donor star is sufficiently large, the secondary star can accrete enough angular momentum to become a rapid rotator and evolve as a chemically homogeneous star. In the second scenario, a tight binary system can experience significant tidal interactions that lead the binary to become tidally locked. When the two stars are tidally locked, their rotational velocity becomes synchronized with the orbital period, and the two stars become rapid rotators, reaching chemical homogeneity. If the tidal forces are strong enough, chemical homogeneity can be achieved even before a Roche lobe overflow is triggered, and the binary may become an overcontact binary (Marchant et al. 2016).

### 1.3.4 Compact binary merger formation

Binary evolution is one of the main formation channels of gravitational wave mergers. However, not all binary systems are able to successfully produce a compact object binary that can reach the merger within the age of the Universe, i.e. the Hubble time  $t_H \simeq 13.8$  Gyr. Along its evolution, a binary system can experience some of the processes described in this chapter, which in turn may favor or halt the production of compact objects. Figure 1.7 shows the most common evolutionary path that a binary system faces to successfully produce a compact binary merger. The evolution depicted in the plot proceeds as follows:

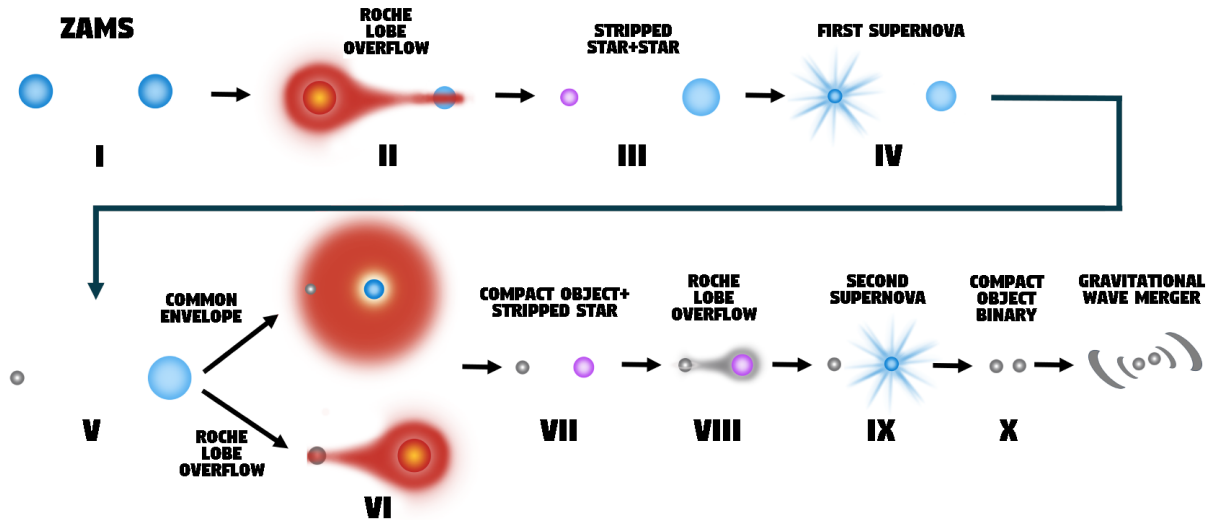


Figure 1.7: Phases of the binary evolution in the isolated formation channel of a compact object binary. Plot adaptation from Costa et al. (2023a) and Vigna-Gómez et al. (2020).

- I. To form a binary of compact objects, the initial system must consist of two massive stars with relatively low metallicity. This ensures that wind emissions do not halt the formation of compact objects while also preventing excessive widening of the mutual separation. The initial semi-major axis must be in the range  $a \sim 100 - 1000 R_{\odot}$ . At lower orbital separation, when  $a \sim 10 R_{\odot}$ , tidal interactions force the binary to become tidally locked, and the stars become chemically homogeneous (see section 1.3.3). The system becomes a binary of pure helium or Wolf-Rayet stars, and after the first supernova event, proceeds its evolution as in point VII onward.
- II. The primary star ends its main sequence and enters in the Hertzsprung-gap phase. Here, the core starts contracting, and the hydrogen keeps burning in a shell surrounding the core. The star expands its outer envelope up to  $\sim 10 - 100 R_{\odot}$ , possibly overcoming its Roche lobe radius. If this happens, the system enters a Roche lobe overflow phase. If the Roche limit is not reached during this evolutionary phase, stable mass transfer can also be initiated in later stages of the primary star's evolution, such as when the star evolves into a red supergiant star. Either ways, almost  $\sim 70\%$  of the observed massive star binaries are expected to experience this Roche lobe overflow phase (Sana et al. 2012). The Roche lobe overflow can proceed stably, lasting the equivalent of a few thermal timescales of the primary. If the mass transfer becomes unstable, a common envelope might be triggered. This can either lead to a merger, halting the formation of a compact object binary, or result in a binary of two stripped stars if the envelope is successfully ejected. In this latter case the evolution proceeds with a supernova explosion triggered by the primary, skipping its evolution to point VII.
- III. After the conclusion of the Roche lobe overflow, the system is composed of a stripped star, either a pure helium or a Wolf-Rayet star, and a secondary star, likely still in its zero-age main sequence stage, that has accreted hydrogen from the mass transfer episode. In this framework, the secondary star can be efficiently spun up by the accretion process. If its metallicity is sufficiently low, the star might become a rapid rotator and become chemically homogeneous. In this case, the two stars will likely become massive black holes without interacting anymore.

Their mutual separation remains quite large as no common envelope events are possible, given that both stars have lost their envelopes. On the other hand, if the binary system is sufficiently small, the evolution proceeds as described in point VII, after the first supernova event of the primary.

- IV. The primary star eventually ends its life as a stripped Type Ib or ultra-stripped Type Ic supernova. If massive enough, the star produces a black hole or a neutron star. Depending on the supernova mechanism, the compact object remnant may receive a natal kick that can reach a few hundreds of  $\text{km s}^{-1}$ . The natal kick not only is capable of tearing apart the binary, but it possibly ejects the compact object from the hosting environment (as a star cluster, see Section 1.4).
- V. If the secondary star has not evolved into a chemically homogeneous star and the binary has not been torn apart from the supernova kick, the binary is now composed by a compact object and a star. This system may appear as a high-mass X-ray binary (Remillard & McClintock 2006; Corral-Santana et al. 2016) or as a dormant black hole system in Gaia (Tanikawa et al. 2023; El-Badry et al. 2023).
- VI. As the secondary star evolves, the system enters once again a Roche lobe overflow phase. In this phase, the mass transfer is typically considered non-conservative, as the compact object can accrete only up to a finite amount of matter, determined by its Eddington limit. The non-accreted matter is then lost by the system, carrying away angular momentum. This leads the binary to rapidly reduce the orbital separation, triggering a runaway process: the more the semi-major axis decreases, the more also the Roche radius of the donor decreases (see Equation 1.5). At this point, the mass transfer might become dynamically unstable, evolving into a common-envelope phase. If this happens, the compact object starts to spiral in because of the envelope drag force, while the orbital binding energy is transformed into kinetic energy of the envelope. If the system is not capable of ejecting the envelope, the compact object and the core of the secondary star merge, as described in Section 1.3.2; otherwise, the binary proceeds with its evolution.
- VII. The post-mass transfer system is composed of a compact object and a stripped star, i.e. a pure helium or a Wolf-Rayet star. Because of the mass transfer episode, the orbital separation of the binary is significantly reduced.
- VIII. In some cases the binary might experience a further Roche lobe overflow caused by the expansion of the pure helium star. This is more likely if the secondary star is a low-mass pure helium star, progenitor of a neutron star Dewi & Pols (2003); Tauris et al. (2015).
- IX. The secondary star explodes as a Type Ib or Type Ic supernova. The natal kick can once again tear apart the binary, although in this case, the disruption is less likely than in the first kick, given the larger binding energy of the system.
- X. The system is now a binary of compact objects. If the orbital separation is small enough, the binary begins emitting gravitational waves, causing the two compact objects to spiral in. Eventually, the binary merges within the age of the Universe.

## 1.4 Too many stars in a crowded place: the Dynamical Channel

In the previous chapter, we have considered the evolution only of isolated single and binary stars. Nevertheless, the evolution of stars and binaries can be significantly impacted by their surrounding environment, particularly if it is considered collisional. In a collisional environment, dynamical interactions occur on a timescale much shorter than the evolutionary timescale of the cluster. Dynamical interactions govern the evolution of collisional systems, such as star clusters, and serve as an efficient mechanism to produce compact binary mergers. The upcoming sections will delve into the characteristics of star clusters and the primary dynamical processes responsible for the formation of gravitational wave events.

### 1.4.1 Star clusters: properties and evolution

The vast majority of massive stars are born inside star clusters (Lada & Lada 2003). Star clusters are self-gravitating collisional systems composed of a coeval stellar population born from the same molecular cloud (Portegies Zwart et al. 2010a). The stellar densities inside star clusters are sufficiently high that dynamical encounters between cluster components take place frequently. The combination of these interactions with the stellar evolution processes of its population, such as winds and supernovae, shapes the properties and the evolution of the cluster while also defining its observational features.

The dimensions of a star cluster are typically measured through its Lagrangian radii, defined as the distances from the cluster's center containing specific fractions of the total cluster mass. The half-mass radius,  $r_{\text{hm}}$ , is the most commonly used among the Lagrangian radii and represents the distance from the center of the cluster that contains half of its total mass. Similarly, in astronomical observations, it is common to define a cluster's dimension through isophotes, specifying the effective radius,  $r_{\text{eff}}$ , or the spatial extent that encompasses half of the total luminosity of the cluster from its center. Another practical definition of a cluster spatial extension is given by the tidal radius  $r_t$ , i.e. the distance where the gravitational acceleration of the cluster equals the tidal acceleration of the parent galaxy. The tidal radius roughly corresponds to the distance where the density of stars drops to a value comparable to the background. A star can escape from the gravitational influence of the cluster if its velocity is larger than the escape velocity of the cluster (Georgiev et al. 2009)

$$v_{\text{esc}} = 40 \text{ km s}^{-1} \left( \frac{M_{\text{cl}}}{10^5 M_{\odot}} \right)^{1/3} \left( \frac{\rho_{\text{hm}}}{10^5 M_{\odot} \text{ pc}^{-3}} \right)^{1/6}, \quad (1.10)$$

where  $M_{\text{cl}}$  is the cluster mass and  $\rho_{\text{hm}}$  is its density at the half-mass radius. The mass loss due to stellar escapers from a star cluster is called cluster evaporation<sup>3</sup>.

Star clusters can exhibit complex, non-spherical geometries. Generally, they are structured with a dense core at the center and a looser envelope encompassing the outer regions of the cluster. The core of the cluster can reach densities 20 times larger than the average cluster density and is typically confined at a distance

$$r_c = \sqrt{\frac{3\sigma_0^2}{4\pi G\rho_0}} \quad (1.11)$$

known as the core radius. The quantities  $\sigma_0$  and  $\rho_0$  are the velocity dispersion and the core density, respectively. The core radius corresponds to the distance at which the three-dimensional stellar

---

<sup>3</sup>Other processes can contribute to cluster evaporation, such as tidal stripping induced by an external gravitational potential, as seen in interactions with a galaxy (Gieles et al. 2011) or a giant molecular cloud (Gieles et al. 2006).

density drops by a factor of  $\sim 3$ , and the projected density (or surface density) by  $\sim 2$  (King 1966).

Star clusters are complex systems whose evolution strictly depends on the evolution of their stellar population. Their evolution is generally divided in three phases:

- I. The initial phase is marked by intense episodes of star formation while the cluster is still rich in gas. During this stage, the evolution of the cluster is dominated by the complex interplay of gas dynamics, stellar dynamics, stellar evolution, and radiative transfer. This phase ends  $\sim 3$  Myr after the formation, when the first supernova events start to take place and sweep the gas from the cluster with the help of stellar winds and radiation of OB stars.
- II. In the second stage, the cluster is predominantly gas-free, and stellar mass loss becomes a significant factor in the overall dynamics. During this phase, gas loss removes potential energy from the cluster, leading to the loss of some stars or potentially causing the cluster to completely dissolve (referred to as "infant mortality," Lada & Lada 2003). The conclusion of this stage and the survivability of the cluster depend strictly on the initial properties of the cluster, and this phase could last anywhere from  $\sim 100$  Myr years to  $\sim 1$  Gyr.
- III. In the final phase, if the cluster has survived, the gas is completely expelled and the evolution is solely governed by dynamical interactions.

The primary driver of star cluster dynamical evolution is two-body relaxation. In a particle system dominated by gravity, the long-range interactions between particles lead to the redistribution of energy, causing the system to approach energy equipartition. In this framework, the cluster tends to reach the thermodynamical equilibrium where the kinetic energy of every particle is equal<sup>4</sup>, i.e.  $m_i \sigma_i^2 = m_j \sigma_j^2$ , with  $m_{i,j}$  and  $\sigma_{i,j}$  representing the masses and velocity dispersions of each cluster particle  $i, j$  (Spitzer 1969). This process is characterized by the two-body relaxation timescale  $t_{\text{rlx}}$ , defined as the time it takes for the stars in a cluster to lose the memory of their initial velocities due to mutual gravitational interactions. The expression for this timescale is (Spitzer 1987)

$$t_{\text{rlx}} = 0.138 \frac{M_{\text{cl}} r_{\text{hm}}^{3/2}}{m^{1/2} G^{1/2} \ln(\Lambda)}. \quad (1.12)$$

Here,  $M_{\text{cl}}$  is the total mass of the cluster,  $r_{\text{hm}}$  is its half-mass radius,  $m$  the average mass of a star in the cluster,  $G$  is the gravitational constant and  $\ln(\Lambda) \sim 10$  is the Coulomb logarithm (Giersz et al. 2008). The relaxation time is longer for stellar systems with a larger number of stars. In galaxies,  $t_{\text{rlx}}$  is longer than the age of the Universe, implying that galaxies are collisionless systems. In clusters, on the other hand,  $t_{\text{rlx}}$  spans from a few Myr to a few Gyr, meaning that close encounters can take place frequently.

Another important timescale is the dynamical timescale, defined as the time in which a particle crosses the system from part to part. This can be expressed as (Portegies Zwart et al. 2010a)

---

<sup>4</sup>In a real star cluster, energy equipartition is never achieved due to factors such as the initial stellar mass function following a power-law (e.g.,  $N(m) \propto m^{-2.3}$ , Kroupa 2001), and the mass loss episodes that the cluster might experience, for instance, due to tidal stripping by the external potential of a galaxy. A direct consequence of a cluster's evolution towards energy equipartition is the formation of a dynamically decoupled sub-core, consisting of the most massive particles, at the center of the star cluster. Once formed, the sub-core evolves independently from the cluster and may be composed of massive stars and black holes (Spitzer 1969). This is crucial for the formation of hierarchical mergers (section 1.4.8) and stellar collisions (section 1.4.9).

$$t_{\text{dyn}} = \frac{GM_{\text{cl}}^{5/2}}{(-4E)^{3/2}} \sim 2 \times 10^5 \text{ yr} \left( \frac{M_{\text{cl}}}{10^4 M_{\odot}} \right)^{-1/2} \left( \frac{r_{\text{vir}}}{1 \text{ pc}} \right)^{3/2}. \quad (1.13)$$

In the left expression,  $E = T + U$  is the total energy, and  $M_{\text{cl}}$  the total mass of the cluster. The right expression has been derived assuming that the cluster satisfy the virial theorem, i.e. that  $2T + U = 0$  with  $T$  and  $U$  kinetic and potential energy of the cluster, with the virial radius defined as  $r_{\text{vir}} = GM_{\text{cl}}^2/2|U|$ . The dynamical timescale determines also the time that the system takes to reach the dynamical equilibrium.

A star cluster is in equilibrium as long as the virial theorem  $2T + U = 0$  holds. However, during its life, a cluster evolves out of this stable configuration in a dynamical process known as the core collapse or gravothermal instability. For a star cluster with a realistic mass function, this is directly related to the two-body relaxation timescale and can be expressed as (Portegies Zwart & McMillan 2002a)

$$t_{\text{cc}} \sim 0.2 t_{\text{rlx}}. \quad (1.14)$$

Core collapse occurs even before two-body relaxation. Two-body relaxation acts as a mechanism to transfer kinetic energy from the inner to the outer regions of the cluster. In the inner regions, high-velocity stars are expelled through the evaporation process. This reduces the potential energy and, more significantly, the kinetic energy, as these stars belong to the high-velocity tail of the velocity distribution in the central regions. This leads to a violation of virial equilibrium ( $2T + U < 0$ ) in the core and triggers its collapse, initiating a runaway scenario known as gravothermal instability. Since star clusters exhibit negative heat capacity, the contraction causes the core to heat up while the outer regions expand. Consequently, the dispersion velocity of stars in the core drastically increases, leading to more escapers and a further reduction in kinetic energy. This accelerates the collapse toward infinite density in a runaway process. To counteract the core collapse and restore virial equilibrium, a source of energy is required. This energy is provided by three-body interactions between stars. As the density increases during the core collapse, the probability of encounters between binaries and single bodies rises. In these encounters, energy is extracted from the internal energy of binaries and redistributed in the form of kinetic energy in a process called hardening. These binaries, defined as hard binaries (see section 1.4.4), are tight binaries that, as a consequence of interactions with other bodies, tend to reduce their internal energy, favoring an increase in the kinetic energy of the three-body center-of-mass. They therefore represent a source of heating for the core, which can finally stop collapse process and restore the virial equilibrium.

Core collapse is a phenomenon that occurs even if the system is composed of particles with equal mass. In a real star cluster, particles exhibit a spread mass spectrum. This diversity in mass accelerates the dynamical evolution and the core-collapse phase of the cluster. The more massive objects in a cluster experience a drag force exerted by lighter objects in their surroundings. This drag force that causes massive objects to decelerate is known as dynamical friction (Chandrasekhar 1943), and acts on a star of mass  $m$  in a timescale given by the following equation:

$$t_{\text{DF}} = \frac{3}{4(2\pi)^{1/2} G^2 \ln(\Lambda)} \frac{\sigma^3}{m \rho}. \quad (1.15)$$

A consequence of dynamical friction is that once massive stars have decelerated, losing memory of their initial velocity, they start sinking toward the cluster core, attracted by the center of the potential well. This means that, at a given age of the cluster evolution, the most massive elements

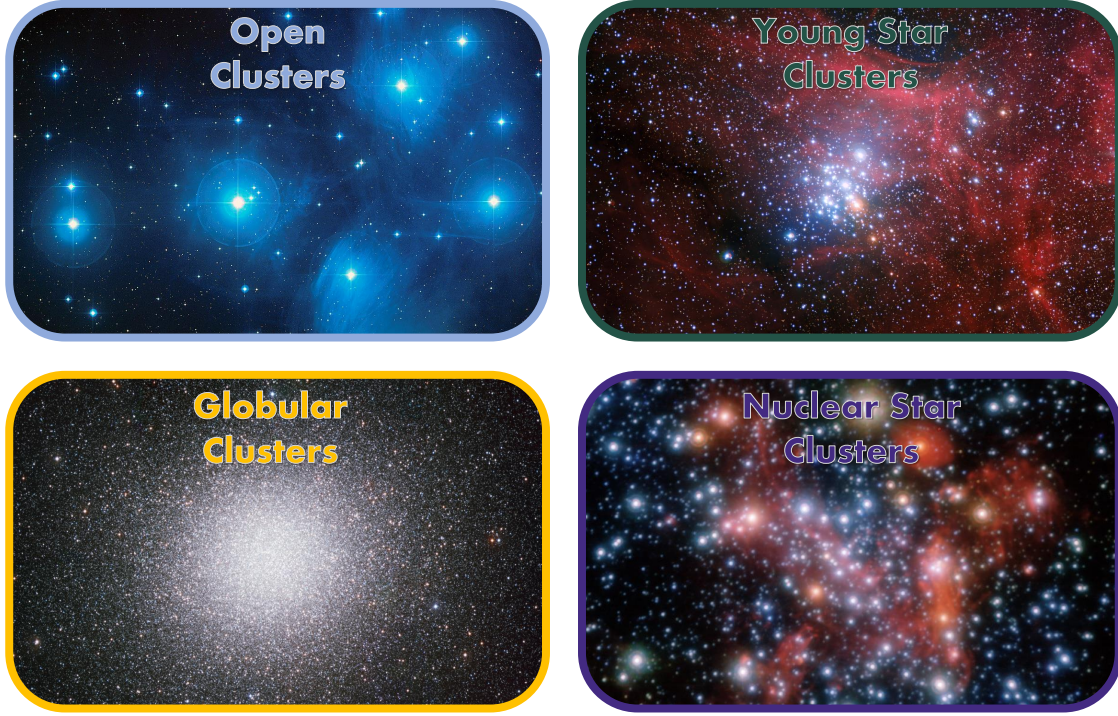


Figure 1.8: Example of four kind of star clusters. From the upper left clockwise: Pleiades open cluster (credit: D. Soderblom, NASA), young star cluster NGC 3293 (credit: G. Beccari, ESO), Milky Way Nuclear cluster (credit: S. Gillessen, ESO), and Omega centauri globular cluster (credit: ESO).

of a star cluster will reach the core of the cluster. This process is known as mass segregation and occurs on a dynamical friction timescale

$$t_{\text{MS}} = t_{\text{DF}} = \frac{\langle m \rangle}{m} t_{\text{rlx}}. \quad (1.16)$$

that is exactly equation 1.15 rewritten as a function of the relaxation timescale of the cluster. This equation gives the time necessary for all objects of mass  $m$  to reach the core of a cluster composed of stars with an average mass of  $\langle m \rangle$ . The mass segregation timescale varies with the properties of the cluster, and it is critical to determine if massive stars can reach the core of the cluster before they evolve into compact objects, i.e. within their lifetime  $t_{\text{lifetime}}$ <sup>5</sup>. If  $t_{\text{MS}} < t_{\text{lifetime}}$ , massive stars can reach the core and interact with each other through repeated mergers, possibly leading to runaway collisions (section 1.4.9). On the other hand, if  $t_{\text{MS}} > t_{\text{lifetime}}$ , the stars reach the core in the form of compact objects (if not expelled by the natal kick). This is extremely important for black holes, as in the core they might grow through hierarchical mergers (section 1.4.8).

<sup>5</sup>Some young and globular clusters have shown evidence of primordial mass segregation, i.e. a mass stratification with more massive stars in the core and lighter stars in the outskirts (Sirianni et al. 2002; Baumgardt et al. 2008). Primordial mass segregation is a feature inherited from their birth and is not connected to dynamical processes. It speeds up the cluster's dynamical evolution and results in a stronger expansion than for unsegregated clusters, leading to a more likely dissolution of the cluster (Vesperini et al. 2009).

### 1.4.2 Different flavors of star clusters

Star clusters are classified based on their properties, including the presence of gas, the stellar population and its age, density, and mass. This classification gives rise to four families of star clusters, depicted in Figure 1.8:

- **Open clusters (OCs)** are young clusters with an age of a few hundred Myr, composed of tens to a few thousand Population I stars loosely bound together. There are more than  $\sim 3000$  observed open clusters only in the Milky Way by date (Scholz et al. 2015). They represent what remains of a young star cluster that has survived infant mortality and lost its gas, halting further star formation. Open clusters are, therefore, the end products of recent star formation episodes, and their stars have nearly the same age, chemical composition, and Earth distance. Their lifetime is typically short, as tidal interactions with the galactic disc tend to dissolve them, populating the galactic field.
- **Young star clusters (YSCs)** are extremely young systems with an age of  $\lesssim 100$  Myr, where star formation is still active. They are the most common family of star clusters in the Universe and constitute the primary forges of massive stars (Kroupa &Boily 2002; Lada &Lada 2003). Young star clusters are typically embedded in a molecular cloud of gas, which provides the main fuel for star formation, and they are characterized by fractal geometry. Their masses can vary from a few hundred  $M_{\odot}$  to tens of thousands of  $M_{\odot}$ , with the most massive systems reaching densities comparable to those of globular clusters. These latter clusters are known as young massive star clusters, and they are dense enough to survive infant mortality and live up to  $\sim 10$  Gyr, i.e. the typical age of globular clusters. Twelve clusters in the Milky Way satisfy these conditions and are considered young massive star clusters, while many others are observed in the local group and beyond. (e.g. for a catalog see Portegies Zwart et al. 2010a).
- **Globular clusters (GCs)** are old, metal-poor clusters hosting Population II stars, and they originated approximately 12 Gyr ago. They are characterized by a spheroidal shape and have masses ranging from approximately  $10^3 M_{\odot}$  (e.g., AM4, a member of the Sagittarius dwarf spheroidal galaxy) to  $2.2 \times 10^6 M_{\odot}$  (e.g., NGC5139 Omega Centauri). Nearly 150 globular clusters are known in the Milky Way, and they are typically found orbiting the halo of the Galaxy (Harris 2010). Globular clusters are depleted of gas and dust. Their evolution is solely governed by stellar dynamics, and due to large densities in their cores, they can host strong dynamical interactions contributing to the formation of compact binary mergers (Portegies Zwart &McMillan 2000a).
- **Nuclear star clusters (NSCs)** are luminous and massive clusters with  $M_{cl} \sim 10^6 - 10^8 M_{\odot}$  and effective radii  $2 - 5 pc$ . They are characterized by extremely high densities  $\sim 10^6 M_{\odot} pc^{-3}$  such that the escape velocities in their cores reach values up to  $\sim 100 km s^{-1}$  (Neumayer et al. 2020a). Nuclear clusters undergo multiple epochs of star formation and are present in almost all types of galaxies, with a fraction exceeding  $\gtrsim 80\%$  for galaxies more massive than  $10^8 M_{\odot}$  and decreasing to 0% for galaxies less massive than  $10^6 M_{\odot}$  (Böker 2010; Sánchez-Janssen et al. 2019). They are typically situated in the galaxy core, orbiting in the vicinity of a supermassive black hole. Finally, nuclear star clusters represent the most efficient environment where black holes can grow through hierarchical mergers (section 1.4.8).

The main properties of these families of star clusters are reported in Table 1.1

cluster	age [Gyr]	$M$ [ $M_{\odot}$ ]	$r_{\text{hm}}$ [pc]	$\rho_c$ [ $M_{\odot}/pc^3$ ]	$t_{\text{rlx}}$ [Myr]	$t_{\text{dyn}}$ [Myr]	$v_{\text{esc}}$ [km s $^{-1}$ ]	location
OC	$\lesssim 0.3$	$\lesssim 10^3$	$\lesssim 10$	$\lesssim 10^3$	$\lesssim 100$	$\sim 1$	$\lesssim 1$	disc
YSC	$\lesssim 0.1$	$\gtrsim 10^3$	$\lesssim 10$	$\gtrsim 10^3$	$\lesssim 100$	$\lesssim 1$	$\sim 1$	disc
GC	$\gtrsim 10$	$\gtrsim 10^5$	$\lesssim 50$	$\gtrsim 10^3$	$\gtrsim 10^4$	$\gtrsim 1$	$\gtrsim 10$	halo
NSC	$\gtrsim 10$	$10^6 - 10^9$	$\lesssim 50$	$10^6 - 10^7$	$\gtrsim 10^5$	$\gtrsim 1$ check	$\gtrsim 100$	galactic bulge

Table 1.1: Indicative properties of open clusters (OC), globular clusters (GC), nuclear clusters (NSC), and young massive star clusters (YSC). The first column is the cluster type, the second is the age of the cluster, followed by the total cluster mass, the half-mass radius, the core density, the relaxation timescale, the dynamical timescale, the escape velocity, and the typical location where they can be found in a galaxy. Table credit: Portegies Zwart et al. (2010a) and Neumayer et al. (2020a).

### 1.4.3 Dynamical encounters in star clusters

In massive star clusters, such as nuclear clusters, the densities are sufficiently large to allow frequent dynamical interactions. The questions here are: what cluster components are involved in these interactions? and how do these bodies interact? In general, the larger the mass of the cluster is, the longer the relaxation timescale (Eq.1.12) and the longer it takes for a star to reach the core by mass segregation (Eq.1.16). In massive clusters, the timescales for mass segregation can extend beyond a few hundred Myr, meaning that only compact objects can reach the core<sup>6</sup>. Typically, neutron stars are ejected from the cluster either by their natal kicks or the dynamical recoil experienced during these interactions (Eq. 1.23). On the other hand, black holes receive softer kicks (due to the direct collapse mechanism, see section 1.2.2) and are more likely to drift into the cluster core (as their mass is large and the segregation timescale is lower). When most of the massive stars in the cluster have evolved into compact objects, black holes become the most massive objects in the cluster. As a consequence of the cluster evolving asymptotically toward energy equipartition, once segregated in the core, black holes create a dynamically decoupled sub-core in which they start interacting with each other. These interactions become even more frequent when the star cluster enters its core collapse phase. Black holes can then form binaries and give rise to binary black hole mergers. One mechanism to produce a binary is the gravitational capture of two single black holes. This takes place on a timescale (Quinlan & Shapiro 1990):

$$t_{\text{cap}} \sim 10 \text{ Gyr} \left( \frac{m_{\text{BH}}}{10 M_{\odot}} \right)^{-2} \left( \frac{n_c}{10^8 \text{ pc}^{-3}} \right)^{-1} \left( \frac{\sigma}{50 \text{ km s}^{-1}} \right)^{11/7}, \quad (1.17)$$

where  $m_{\text{BH}}$  is the black hole mass,  $\sigma$  is the 3d velocity dispersion of the cluster,  $n_c \simeq \rho_c/\langle m \rangle$  is the number density of the core with  $\langle m \rangle$  the average mass of a star in the core, and  $\rho_c$  the mass density of the cluster core.

Another mechanism to form a binary is the gravitational encounter of three single black holes, where one black hole carries away the excess energy needed to create a binary. This process occurs in a timescale (Goodman & Hut 1993; Lee 1995; Antonini & Rasio 2016):

<sup>6</sup>If the cluster is primordially segregated, a large fraction of massive stars may already populate the core (Section 1.4.1). However, by the time dynamical mass segregation has become efficient, and the core has become denser due to its collapse, these stars have already evolved into compact objects.

$$t_{3\text{bb}} \sim 30 \text{ Myr} \left( \frac{n}{10^6 \text{ pc}^{-3}} \right)^{-2} \left( \zeta^{-1} \frac{\sigma}{50 \text{ km s}^{-1}} \right)^9 \left( 10 \frac{\langle m \rangle}{m_{\text{BH}}} \right)^{9/2} \left( \frac{m_{\text{BH}}}{10 M_{\odot}} \right)^{-5}, \quad (1.18)$$

where  $n$  is the number density of stars in the cluster, while  $\zeta = (\langle m \rangle \sigma^2) / (m_{\text{BH}} \sigma_{\text{BH}}^2) \leq 1$  is a parameter that measures the departure of the cluster from equipartition.

The binary fraction of a cluster is defined as  $f_{\text{bin}} = N_{\text{bin}}/N$ , where  $N_{\text{bin}}$  and  $N$  are, respectively, the total number of binaries and stars in the cluster. If the binary fraction in a cluster is non-negligible, the formation of a binary black hole can occur through a three-body interaction between a binary system and a single black hole. This can happen through multiple exchange events, each taking place in a timescale (Miller & Lauburg 2009)

$$t_{12} \sim 300 \text{ Myr} \left( \frac{0.1}{f_{\text{bin}}} \right) \left( \frac{n_c}{10^6 \text{ pc}^{-3}} \right)^{-1} \left( \frac{\sigma}{50 \text{ km s}^{-1}} \right) \left( \frac{m_{\text{BH}} + 2\langle m \rangle}{12 M_{\odot}} \right)^{-1} \left( \frac{a_{\text{hard}}}{1 \text{ AU}} \right)^{-1} \quad (1.19)$$

where  $a_{\text{hard}} = G \langle m \rangle / \sigma^2$  is the minimum semi-major axis to consider a binary as a hard binary (see next section).

Finally, if the binary fraction is large, dynamics can trigger the formation of black hole binaries and mergers through the interaction of two binary systems. These are called binary-binary interactions, and take place in a timescale Zevin et al. (2019):

$$t_{\text{bin}} \sim 10 - 100 t_{12}. \quad (1.20)$$

Binary black holes are created dynamically mostly through the encounters of three single black holes during the core collapse phase of a star cluster. Once most of the black holes are set in binary systems, three-body interactions start dominating the encounters between black holes in the core of the cluster. These interactions are fundamental for halting the core collapse (section 1.4.1), as single stars or black holes can extract energy from hard binaries in a process called dynamical hardening (section 1.4.5). Dynamical hardening is a fundamental process for reducing the orbital separation of binary black holes, bringing them into the regime of gravitational wave emission. Figure 1.9 summarizes the mass segregation phase of a massive star, and the dynamical interactions that its black hole remnant undergo when it reaches the cluster core.

#### 1.4.4 Three-Body interactions & hard binaries

Three-body encounters are dynamical interactions involving a binary system and a single object, referred to as the intruder. The primary distinction from the two-body encounter scenario lies in the fact that, in this case, the interaction involves a binary system, and energy exchanges between the internal energy of the binary and the kinetic energy of the single object are allowed. The total energy of a binary system is defined as

$$E_{\text{tot}} = \frac{1}{2} \mu v^2 - \frac{G m_1 m_2}{r}. \quad (1.21)$$

If the system is bound the total energy is negative  $E_{\text{tot}<0}$ , and the binary system has an elliptical orbit with semi-major axis  $a$  and eccentricity  $e$ . In the equation, the first term is the kinetic energy of the system center-of-mass  $E_k$  defined as a function of the reduced mass of the system  $\mu = (m_1 m_2) / (m_1 + m_2)$ , with  $m_1$  and  $m_2$  the primary and secondary components of the binary, respectively. The second term represents instead the internal energy of the system  $E_i$ , which is

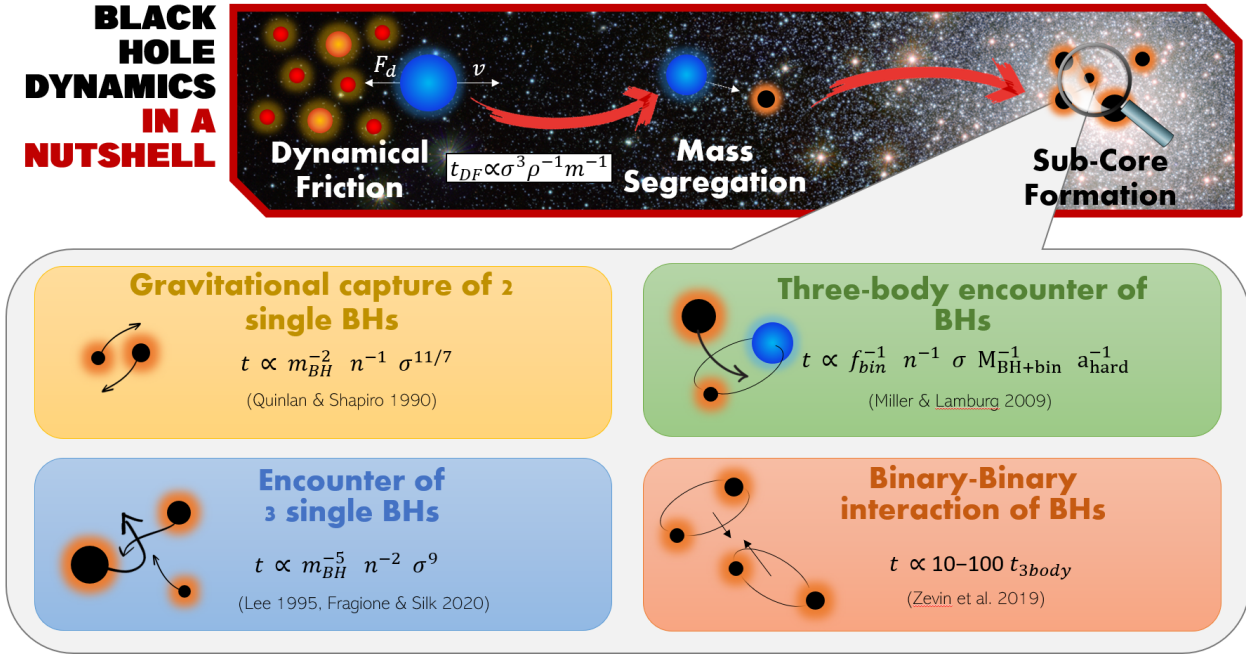


Figure 1.9: Summary of the dynamical evolution of a massive star and its remnant inside a star cluster.

related to the binding energy of the system as  $E_b = Gm_1m_2/(2a) = -E_i$ . The internal energy serves as the energy reservoir for the binary and can be exchanged with the single object during the dynamical encounter. As a result of these energy exchanges, various outcomes are possible in a three-body interaction: *hardening*, *dynamical ejection*, *exchange*, and *ionization*. Three-body interaction lacks an exact solution due to the chaotic nature of the three-body problem (Poincaré 1892; Valtonen & Karttunen 2006). Nevertheless, we can statistically predict the outcome of a three-body interaction from the properties of the encounter and the binary system. One crucial factor determining the amount of energy exchanged in a three-body interaction is whether the binary can be classified as hard or soft:

- *Hard binaries* are defined as binaries whose binding energy is higher with respect to the average star  $\langle m \rangle$  kinetic energy, i.e.

$$\frac{Gm_1m_2}{2a} > \frac{1}{2}\langle m \rangle \sigma^2$$

- *Soft binaries* are defined as binaries whose binding energy is lower with respect to the average star  $\langle m \rangle$  kinetic energy, i.e.

$$\frac{Gm_1m_2}{2a} < \frac{1}{2}\langle m \rangle \sigma^2$$

The outcomes of a three-body interaction strictly depend on the energy exchanges of the process, and whether a binary will gain or lose binding energy can be predicted only in a statistical sense. Heggie (1975) developed the analytical formalism with the first numerical simulations to find the following important result known as Heggie's law:

**Heggie's law -** Hard binaries statistically tend to harden, meaning that in a dynamical encounter they will likely increase their binding energy (e.g. the intruder can extract internal energy from the binary which causes a decrease of the semi-major axis of the system, or an exchange event can introduce a more massive body in the binary increasing  $E_b$ ). Soft binaries statistically tend to soften, or in other words they will likely decrease their binding energy as a result of a dynamical interaction (this happens if the binary gains internal energy at the expense of the kinetic energy of the intruder).

### 1.4.5 Dynamical hardening & gravitational wave emission

The hardening process occurs during a three-body interaction, where an intruder object extracts energy from the internal energy  $E_i$  of the binary system in a flyby encounter. Due to energy conservation, the extracted energy is utilized to increase the initial center-of-mass kinetic energy  $E_{k,i}$  of both the binary and the single object, resulting in  $E_{k,i} < E_{k,f}$ . In this process, the internal energy of the binary becomes more negative, while its initial binding energy  $E_{b,i}$ , grows. Consequently,

$$E_{b,i} = \frac{Gm_1m_2}{2a_i} < \frac{Gm_1m_2}{2a_f} = E_{b,f} \quad (1.22)$$

In the absence of mass transfer, this implies that  $a_f < a_i$ , indicating that the final orbital separation between the two components of the binary has decreased due to energy exchanges with the third object during the flyby process. In other words, this means that the binary has "hardened". As the kinetic energy of the three-body center-of-mass increases after the encounter, both the binary and the intruder experience a recoil. Sigurdsson & Phinney (1993) computed the recoil velocity of the binary system, which can be expressed as

$$v_{\text{rec}} = \frac{m'_3}{(m_1 + m_2 + m_3)} \sqrt{\frac{m_3(m_1 + m_2)}{m'_3(m'_1 + m'_2)} v_\infty^2 + \frac{2(m_1 + m_2 + m_3)}{m'_3(m'_1 + m'_2)} \Delta E_b} \quad (1.23)$$

where  $m'_1$ ,  $m'_2$  and  $m'_3$  are respectively the masses of the primary, secondary and intruder after the interaction (they may change in the process, e.g. for an exchange),  $v_\infty \sim \sigma$  and  $\Delta E_b = E_{b,f} - E_{b,i}$  is the energy exchanged in the encounter. This recoil velocity may vary from a few  $\text{km s}^{-1}$  up to several hundreds of  $\text{km s}^{-1}$ , and it can cause the ejection of the binary if it exceeds the escape velocity of the cluster. This process is known as dynamical ejection. When a binary is ejected into the field, it can no longer participate in the dynamic of the cluster.

Hardening is a crucial process for the formation of binary black hole mergers. Binary black holes are hard binaries, as they are the most massive elements in a star cluster. As hard binaries, binary black holes undergo multiple three-body interactions throughout their lifetime, and each of these interactions contributes to further hardening the binary. The evolution of the orbital parameters of binary black holes, caused by an arbitrary number of three-body interactions occurring within a given amount of time, can be estimated as (Heggie 1975; Mapelli et al. 2019)

$$\left( \frac{da}{dt} \right)_{\text{hard}} = -2\pi G \xi \frac{\rho_c}{\sigma} a^2, \quad (1.24)$$

$$\left( \frac{de}{dt} \right)_{\text{hard}} = 2\pi \xi \kappa \frac{G \rho_c}{\sigma} a. \quad (1.25)$$

The hardening rate strongly depends on the properties of the environment in which the binary is embedded, as the core density  $\rho_c$  and the velocity dispersion  $\sigma$ . The parameters  $\xi$  and  $\kappa = de/d \ln(1/a)$  can be calibrated numerically from simulations; typical values are  $\xi \sim 0.01 - 0.1$  (Hills 1983a) and  $\xi \sim 0.2 - 3$  (Quinlan 1996; Sesana et al. 2006). The right-hand term in equation 1.24 is negative as hardening decreases the binary orbital separation. Furthermore, its strong dependence on  $a$  implies that the smaller the semi-major axis is, the smaller the cross-section of the binary, and the less efficient the hardening process becomes. Below a particular value of  $a$ , gravitational wave emission becomes the primary mechanism of orbit-tightening. Gravitational waves extract energy and momentum from the orbit of the two black holes, which as a consequence keep reducing their mutual distance, spiraling in to eventually merge. The description of the orbital evolution has been derived by Peters (Peters 1964) as

$$\left(\frac{da}{dt}\right)_{\text{gw}} = -\frac{64}{5} \frac{G^3 m_1 m_2 M_{\text{tot}}}{a^3 c^5} \frac{(1 + 73e^2/24 + 37e^4/96)}{(1 - e^2)^{7/2}} \quad (1.26)$$

$$\left(\frac{de}{dt}\right)_{\text{gw}} = -\frac{304}{15} \frac{G^3 m_1 m_2 M_{\text{tot}}}{a^4 c^5} \frac{e(1 + 121e^2/304)}{(1 - e^2)^{5/2}} \quad (1.27)$$

where  $M_{\text{tot}} = m_1 + m_2$  and  $c$  is the speed of light. In summary, both hardening and gravitational wave emission contribute to reducing the orbital separation of a binary black hole, ultimately leading to its merger. The efficiency of the former is notable when the orbital separation and impact parameter of the binary are large. In contrast, the latter becomes effective only when the semi-major axis of the binary has already been sufficiently reduced by dynamical hardening. Figure 1.10 shows the two separate regimes where hardening and gravitational wave emission operate.

#### 1.4.6 Exchanges

Three-body interactions can lead to an exchange, a process in which the intruder replaces either the primary or the secondary component in the binary. Whether an exchange follows a three-body interaction depends on the properties of the system and the encounter. However, exchanges are more likely to occur if the intruder is more massive than one of the two binary components. Exchanges, therefore, represent another mechanism contributing to the production of binaries with a higher binding energy. Hills & Fullerton (1980a), exploiting the analytical approach of Heggie Heggie (1975), demonstrated with numerical simulations that the probability for an exchange event in a three-body interaction between a single object and the secondary component of the binary (i.e the less massive component) is higher ( $\sim 1$ ) if the intruder is more massive than one of the binary members. The probability is instead lower ( $\sim 0$ ) if the intruder is less massive than both the components of the binary.

Black holes stand out as among the most massive objects in a star cluster, making them likely candidates to undergo multiple exchanges. A stellar binary system can initially undergo an exchange event in which one of the two stars is replaced by a black hole. Subsequently, a second exchange can occur, wherein another black hole takes the place of the second star in the binary, resulting in the formation of a binary black hole. As long as the newly formed binary black hole resides in a dynamically active environment, its growth in mass does not cease. Exchange processes can persist even after the formation of a binary black hole, allowing heavier single black holes to be introduced into the binary while the lighter one is ejected. This scenario, depicted in Figure 1.11, has been explored through direct N-body simulations by various authors in the literature (e.g. Ziosi et al.

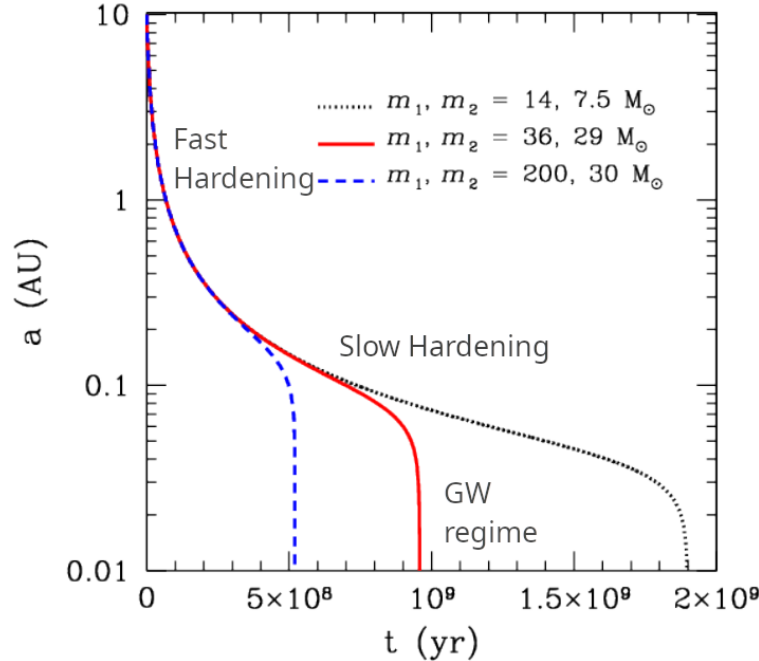


Figure 1.10: Semi-major axis evolution over time caused by hardening and gravitational wave emission from Mapelli et al. (2019). The plot shows the numerical results of equation 1.24 considering three different binaries and  $\xi = 1$ ,  $\rho = 10^5 M_\odot$ ,  $\sigma = 10 km s^{-1}$ ,  $e = 0$ ,  $a_0 = 10 AU$  ( $\sigma$ ,  $\rho$ ,  $e$  are assumed constant in time).

2014; Torniamenti et al. 2022; Rastello et al. 2021a), who concur that up to approximately 90% of binary black holes in young star clusters are formed through dynamical exchanges.

Exchanges not only produce more massive systems, but the members of binary black holes born via exchanges will likely have misaligned or nearly isotropic spins, as dynamical processes tend to completely reset the values of the original spins. This implies that a binary consisting of two components with spins parallel to the orbital angular momentum vector, following an exchange event, will probably exhibit misaligned spins. This is because the replaced member of the binary will not have any preferential direction of spin orientation due to the chaotic nature of the three-body interaction. The opposite is true for binary black holes formed through the isolated channel, where the binary is circularized by tides and mass transfer episodes tend to align the spins of the two stars (Hurley et al. 2002). Even if a clear relation between the magnitudes of the progenitor-BH spins still does not exist, it is, however, reasonable to assume that the spin orientation is conserved<sup>7</sup> (Mapelli et al. 2019).

Binary black holes formed through exchanges, and more generally, dynamically formed binary black holes, may exhibit another orbital property that distinguishes them from compact binaries created by the isolated formation channel. Dynamical interactions, such as three-body encounters, generally increase the eccentricity of a binary. These interactions can occur rapidly enough to prevent gravitational wave emission from having sufficient time to circularize the orbit by dissipating orbital angular momentum. As a result, a dynamically-assembled binary may reach the merger with a non-

<sup>7</sup>Natal kicks might impart partial misalignment on the black holes spins with the fallback mechanism. When a black hole is born through direct collapse, the kick is milder and it is generally assumed that the spin orientation is coherent with the spin orientation of the stellar progenitor.

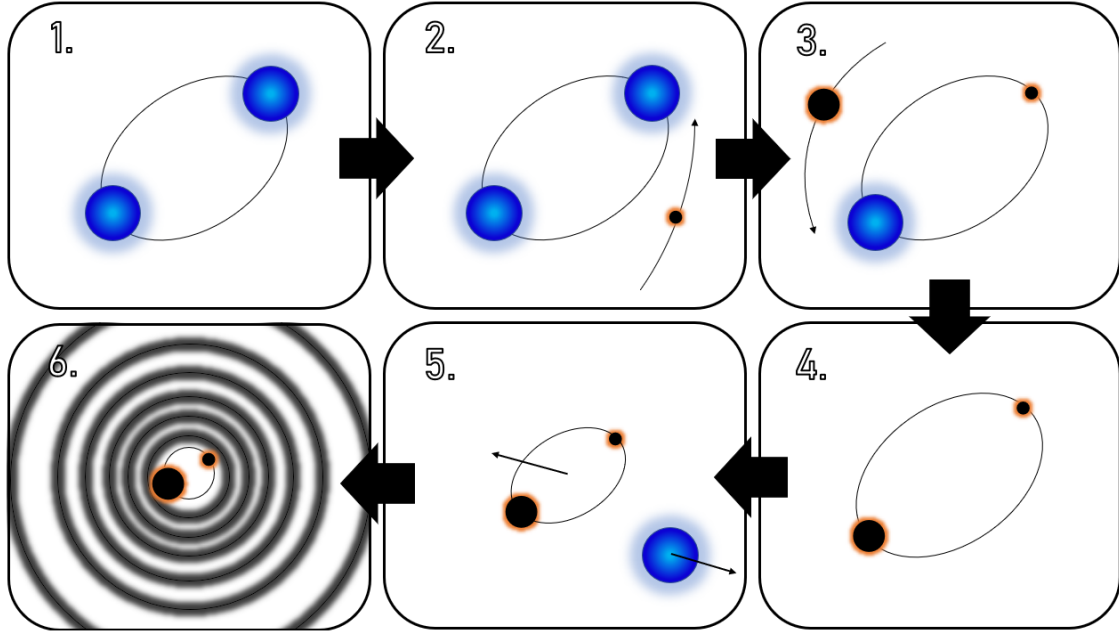


Figure 1.11: Example of a binary black hole dynamical formation channel. Blue dots represent stars, while black dots represent black holes. 1 - Binary system composed of two stars. 2 - Three-body encounter between the binary and a black hole. If the black hole is more massive than one of the two components, it can replace the secondary star via the exchange mechanism. 3 - A second exchange replaces the other star with another black hole. 4 - A binary black hole formed via three-body interactions is born. 5 - Hardening processes cause  $a$  to shrink and induce a recoil. 6 - If hardening processes have been efficient enough, the binary black hole can enter the gravitational wave regime, and its semi-major axis keeps decreasing due to gravitational wave emission, while the orbit becomes circularized. The same scheme works if the binary system in box 1 is a binary black hole: in this case, the exchange processes can introduce more massive black holes into the system. Lastly, if the merger product in box 6 does not experience a dynamical ejection from the cluster, it can create a second-generation binary black hole via three-body encounters (e.g., in box 2), establishing a loop process in which a black hole keeps growing in mass (hierarchical mergers, see section 1.4.8).

negligible eccentricity. In contrast, in the isolated formation channel, binary interactions tend to circularize the orbit even before the two stars evolve into black holes. Even if other processes, such as natal kicks, impart moderate eccentricity to the newly formed binary black hole, gravitational wave emission has enough time from the formation of the compact binary to circularize the orbit before the merger. Eccentricity, if detected in a gravitational wave event, might be used as a smoking gun to disentangle the dynamical formation of a binary black hole.

#### 1.4.7 Ionizations

In a three-body encounter, if the third star loses a fraction of its kinetic energy while the internal energy of the binary becomes more positive, the kinetic energy of the three-body center-of-mass is decreased  $E_{k,i} > E_{k,f}$  and so does the binding energy of the binary  $E_{b,i} > E_{b,f}$ . As a consequence of the dynamical interaction with the single star, the binary semi-major axis increases  $a_i < a_f$  and becomes less bound or softened. This can also cause the *ionization* of the binary, i.e. the binary

components have  $E_{\text{tot}} > 0$  and can be considered as single stars. For this to happen, the kinetic energy of the reduced particle in the three-body system must be equal to the binding energy of the binary

$$\frac{1}{2} \frac{m_3(m_1 + m_2)}{(m_1 + m_2 + m_3)} v_{\text{crit}}^2 = \frac{Gm_1m_2}{2a}. \quad (1.28)$$

From this expression, it is possible to derive (Hut & Bahcall 1983)

$$v_{\text{crit}} = \sqrt{\frac{Gm_1m_2(m_1 + m_2 + m_3)}{m_3(m_1 + m_2)a}} \quad (1.29)$$

which is the critical velocity. A single star with mass  $m_3$  can ionize a binary system if its velocity at infinity exceeds this critical value. Ionization is typically the fate of soft binaries in a star cluster.

#### 1.4.8 Hierarchical mergers

In massive clusters, such as globular and nuclear clusters, the lifespan of the most massive stars is shorter than their mass segregation timescale  $t_{\text{lifetime}} < t_{\text{MS}}$ . In these environments, massive stars cannot reach the core on time and are likely to end their lives midway, leaving behind a compact object more massive than the average star mass  $\langle m \rangle$  of the cluster<sup>8</sup>. If this remnant is not ejected from the cluster due to a natal kick, it may continue sinking into the cluster core where the density is higher, progressing even faster if bound in a binary system. Within the core, the compact objects begin interacting with each other, forming a dynamically decoupled sub-core that evolves separately from the rest of the cluster (due to the approaching of energy equipartition, see section 1.4.1). In this phase, the remaining neutron stars, which have not been ejected by their natal kicks, are dynamically expelled due to the recoil imparted by three-body interactions (Equation 1.23). If the remnant is a black hole, there is a strong probability that it will acquire a massive companion, leading to the formation of a binary black hole system through one of the processes outlined in section 1.4.3. After their formation, binary black holes may undergo repetitive three-body interactions that cause the binary to harden, potentially resulting in repeated mergers. This framework was first proposed by Miller & Hamilton (2002) as a possible growth mechanism to produce intermediate-mass black holes. The process, known as *hierarchical mergers* scenario, can be summarized as follows:

- I. Dynamical formation of a black hole binary through gravitational capture, three single black hole encounters, or binary-single interactions. The newly-formed binary black hole is most likely a hard binary.
- II. The binary black hole undergoes hardening through three-body interactions, leading to a reduction in its semi-major axis.
- III. Due to the hardening process, the binary can enter the gravitational wave regime which further reduces the orbital separation because of gravitational wave emission (see section 1.4.5). This will eventually lead to the merger of the two black holes.

---

<sup>8</sup>If the stellar population of the cluster follows a Kroupa initial mass function (Kroupa 2001), i.e.  $N(m) \propto m^\alpha$  with  $\alpha = -0.3$  if  $0.08 \leq m \leq 0.5$ ,  $\alpha = -1.3$  if  $0.5 \leq m \leq 1$ , and  $\alpha = -2.3$  if  $1 \leq m \leq 150$ , the average mass of a star in a cluster where  $m_{\text{min}} = 0.08 \text{ M}_\odot$  and  $m_{\text{max}} = 150 \text{ M}_\odot$  is  $\langle m \rangle \sim 0.6 \text{ M}_\odot$ .

IV. The merger product is a massive black hole. If the relativistic kick has not expelled it from the cluster, it will likely interact with other black holes of the core and form dynamically a  $n$ -th generation binary black hole<sup>9</sup>. If this happens, we are back to the point I.

This loop can repeat several times up to the formation of multiple generations of binary black holes. Hierarchical mergers represent a purely dynamical mechanism for generating massive black holes within the pair-instability mass gap and in the intermediate-mass black hole range. This mechanism remains unaffected by uncertainties associated with single and binary stellar evolution, such as pair-instability and common envelope physics. There are, however, several processes that can break the loop and halt the black hole growth through hierarchical mergers.

Firstly, the hardening process induces a recoil on the binary black holes when they interact with a third object (Equation 1.23). This recoil can be strong enough to eject the binary from the cluster before subsequent hardening interactions sufficiently tighten its orbit, making gravitational radiation emission efficient (Sigurdsson & Phinney 1993). Miller & Hamilton (2002) demonstrated the existence of a maximum binding energy  $E_{\text{b},\text{min}}$  above which the binary is expelled from the cluster after a three-body interaction. This implies that a binary with a semi-major axis below a critical value, defined by  $E_{\text{b},\text{min}}$ , will be expelled from the star cluster during the next three-body interaction. This critical value of the orbital separation is defined as:

$$a_{\text{ej}} = \frac{\xi m_3^2}{(m_1 + m_2)^3} \frac{G m_1 m_2}{v_{\text{esc}}^2}, \quad (1.30)$$

where  $\xi$  and  $v_{\text{esc}}$  are defined as in equation 1.24, and equation 1.10, respectively.

The second and more influential process that could impede the hierarchical mergers mechanism is the relativistic kick received by the product of a gravitational wave merger due to anisotropic gravitational wave emission. This post-merger kick can propel the newly formed black hole remnant to recoil with velocities up to thousands of  $\text{km s}^{-1}$  (Lousto et al. 2012; Healy & Lousto 2018). Higher kick velocities are typically achieved when the binary is characterized by components with large, misaligned spins, and low mass ratio (Fitchett 1983; Maggiore 2018). If the relativistic kick velocity exceeds the escape velocity of the cluster, the black hole remnant is ejected, putting a halt to its hierarchical growth. Given that escape velocities are higher for more massive clusters (equation 1.10), nuclear star clusters represent ideal environments for hosting hierarchical mergers (Arca Sedda et al. 2020; Fragione & Silk 2020; Mapelli et al. 2021a).

#### 1.4.9 Stellar collisions & runaway mergers

When the mass of a star cluster is only moderately large, its relaxation time can be relatively low and the most massive stars populating the cluster can safely reach the core within their lifetime, i.e.  $t_{\text{lifetime}} > t_{\text{MS}}$ . This is the case of massive young star clusters, i.e. young clusters with  $M_{\text{cl}} \sim 10^4 M_{\odot}$  where the relaxation timescale can be of the order of  $\lesssim 100$  Myr. These environments can achieve a large density of massive stars that have migrated in their core in the very first phases of the cluster evolution, typically within the first 10 Myr. Within the core, massive stars dynamically interact with each other causing stellar collisions. Stellar collisions can produce very massive stars and blue stragglers, with a mass  $M > 100 M_{\odot}$ . These very massive stars, which have a different chemical structure compared to normal single stars, may undergo direct collapse, leading to the formation of

<sup>9</sup>where  $n$  is the number of mergers experienced + 1, so that binary black holes that still have to merge are classified as 1-st generation binaries, while binary black holes where one of the two component is a product of one single previous merger, are classified as a 2-nd generation binary black hole.

massive black holes within the pair-instability mass gap ( $60 \lesssim M_{\text{BH}}/M_{\odot} \lesssim 120$ , see section 1.2.2). These conditions are met when the collision takes place between a massive star with a well-developed helium core, like a red supergiant star, merges with a non-evolved companion, like a main sequence or an Hertzsprung-gap star. The product of this merger is likely a massive core helium burning star with an oversized hydrogen envelope (Costa et al. 2022; Ballone et al. 2023). If the helium core of this star remains below  $\sim 30 M_{\odot}$  throughout its evolution, the star may avoid triggering pair-instability pulsations and instead undergo a direct collapse into a black hole. In the absence of significant mass loss through wind emission episodes, the entire mass of its oversized envelope will be accreted by the central black hole during the collapse process, potentially resulting in the formation of a massive black hole within the pair-instability mass range (Di Carlo et al. 2020a). After its formation, the massive black hole can dynamically interact with other members of the cluster core, form a binary black hole and merge within a Hubble time (Di Carlo et al. 2019). Figure 1.12 shows an example of dynamical formation by stellar collision of a binary black hole merger with one of the two black holes having mass within the pair-instability mass gap.

This very massive star produced by the collision is likely to be the most massive object in the cluster core. Different studies (Colgate 1967; Sanders 1970; Portegies Zwart et al. 1999; Portegies Zwart & McMillan 2002a; Portegies Zwart et al. 2004; Mapelli 2016) have shown that the most massive star in a cluster will likely dynamically interact and merge with other stars within the core along its lifetime, before evolving into black holes. If this happens, the very massive star increases its mass through repeated mergers with other stars, making more likely other interactions and mergers, and less likely to escape from the cluster (Portegies Zwart & McMillan 2002a). Hence, the majority of collisions involve one particular object, most likely a star in a binary system (due to the higher cross-section), which is the product of the first dynamical collision process in the cluster. This very massive star can reach masses  $> 1000 M_{\odot}$ , eventually ending its life in a direct collapse and giving birth to an intermediate-mass black hole. This mechanism, known as *runaway collision* scenario, may constitute a possible channel for the formation of intermediate-mass black holes. However, its efficiency strongly depends on two factors. First, the pre-collapse mass of the very massive star strongly depends on the wind mass loss that might strip the very massive star from its outer envelope, and this in turn depends on the metallicity of the star. This is partially solved if the star has low metallicity; however, the evolution of very massive stars remains a subject of debate in the literature (Costa et al. 2023b). Their proximity to the Eddington limit may lead to pulsation-induced mass loss from the star (Volpato et al. 2023). Second, the growth rate through collisions of this very massive star depends on the mass lost in the collision: up to  $\sim 25\%$  of its mass might be lost in the impact process (Gaburov et al. 2008, 2010).

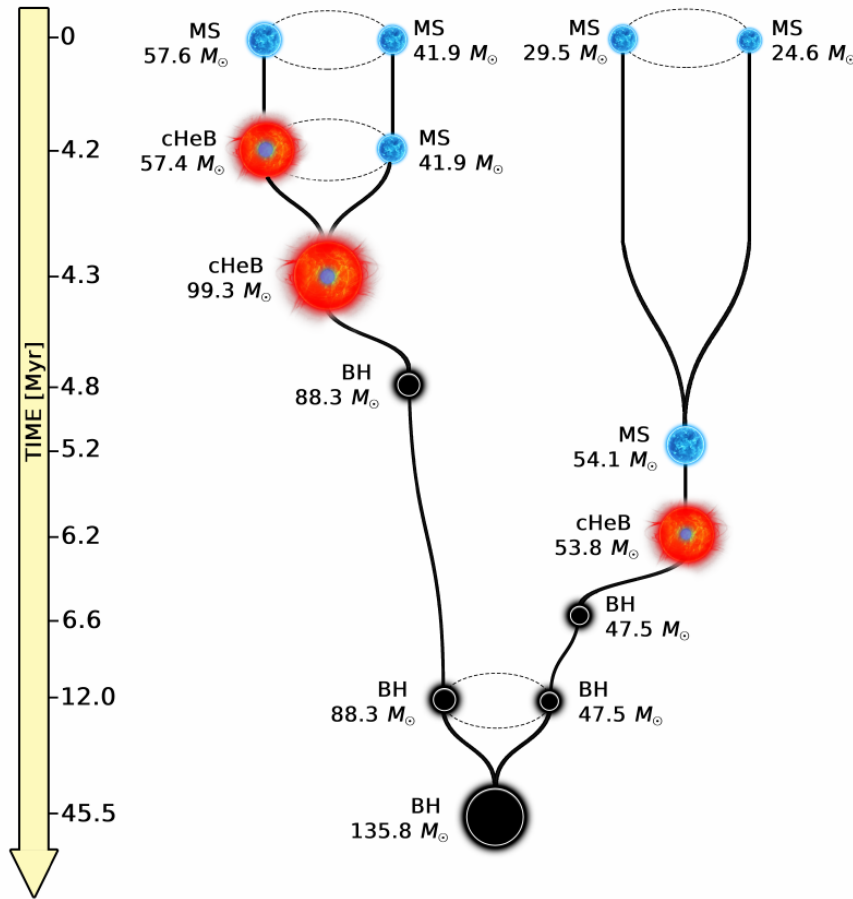


Figure 1.12: Dynamical formation history of a binary black hole merger with one of the two components coming from the direct collapse of a stellar collision product from Di Carlo et al. (2019). Image credit: Ugo N. Di Carlo.



## Chapter 2

# GW190521 formation via three-body encounters in young massive star clusters

*Based on:*

Dall’Amico M., Mapelli M., Di Carlo U.N., Bouffanais Y., Rastello S., Santoliquido F., Ballone A., Arca Sedda M., “GW190521 formation via three-body encounters in young massive star clusters”, 2021, MNRAS 508, 3045

### Abstract

GW190521 is the most massive binary black hole (BBH) merger observed to date, and its primary component lies in the pair-instability (PI) mass gap. Here, we investigate the formation of GW190521-like systems via three-body encounters in young massive star clusters. We performed  $2 \times 10^5$  simulations of binary-single interactions between a BBH and a massive  $\geq 60 M_\odot$  black hole (BH), including post-Newtonian terms up to the 2.5 order and a prescription for relativistic kicks. In our initial conditions, we take into account the possibility of forming BHs in the PI mass gap via stellar collisions. If we assume that first-generation BHs have low spins,  $\sim 0.17\%$  of all the simulated BBH mergers have component masses, effective and precessing spin, and remnant mass and spin inside the 90% credible intervals of GW190521. Seven of these systems are first-generation exchanged binaries, while five are second-generation BBHs. We estimate a merger rate density  $\mathcal{R}_{\text{GW190521}} \sim 0.03 \text{ Gpc}^{-3} \text{ yr}^{-1}$  for GW190521-like binaries formed via binary-single interactions in young star clusters. This rate is extremely sensitive to the spin distribution of first-generation BBHs. Stellar collisions, second-generation mergers and dynamical exchanges are the key ingredients to produce GW190521-like systems in young star clusters.

**keywords:** gravitational waves – black hole physics – methods: numerical – stars: black holes – stars: kinematics and dynamics – galaxies: star clusters: general

### 2.1 Introduction

Since the detection of GW150914 (Abbott &al. 2016; Abbott et al. 2016), the number of gravitational wave (GW) sources observed by the LIGO–Virgo collaboration (LVC) has increased year after year, culminating with the recent publication of the results of the first half of the third LVC observing run (Abbott &et al. 2021a; The LIGO Scientific Collaboration et al. 2021). So far, the sample of detected compact binaries includes 53 binary black hole (BBH) candidates, 2 binary neutron stars (Abbott et al. 2017; Abbott &et al. 2020) and 2 possible neutron star – black hole binary systems (Abbott et al. 2021a). Among these systems, GW190521 detains the record of the most massive

BBH ever observed, with primary mass  $m_1 = 85^{+21}_{-14} M_{\odot}$  and secondary mass  $m_2 = 66^{+17}_{-18} M_{\odot}$  in the source frame (90% credible interval, Abbott & et al. 2020; Abbott et al. 2020a). The coalescence of these two massive black holes (BHs) produced a  $\sim 140 M_{\odot}$  remnant that lies in the still unexplored intermediate mass range of the BH mass spectrum, and can thus be considered as the first intermediate-mass BH (IMBH) candidate detected with GWs (Abbott et al. 2020a). IMBHs bridge the gap between stellar-mass and super-massive BHs in the range  $10^2 \leq m_{\text{BH}}/M_{\odot} \leq 10^5$ ; their existence is pivotal to explain the nature of ultra- and hyper-luminous X-ray sources and the growth of super-massive BHs (e.g., Greene et al. 2020, for a recent review).

The primary BH of GW190521 has a 99% probability of lying in the pair-instability (PI) mass gap ( $\sim 60 - 120 M_{\odot}$ , Abbott & et al. 2020; Abbott et al. 2020a, see also Mehta et al. 2021). In this mass range, no BH is expected to form from the collapse of a single star, as a consequence of the unstable oxygen-silicon burning phase experienced by the progenitor (Heger & Woosley 2002; Woosley et al. 2007; Belczynski et al. 2016; Spera & Mapelli 2017; Woosley 2017; Marchant et al. 2019; Stevenson et al. 2019; Woosley 2019; Woosley & Heger 2021). Fishbach & Holz (2020) and Nitz & Capano (2021) interpret GW190521 as a merger event straddling the PI mass gap. In this case, the primary mass would safely be above the upper edge of the mass gap.

GW190521 shows mild evidence for precession effects (Abbott & et al. 2020). The waveform analysis reports a precessing spin parameter  $\chi_p = 0.68^{+0.25}_{-0.37}$ , and an effective spin parameter  $\chi_{\text{eff}} = 0.08^{+0.27}_{-0.36}$  (90% credible interval), favouring a precessing binary model with in-plane spin components and high spin magnitudes for both BHs. Finally, some authors also claim support for non-zero eccentricity at the time of merger (Gayathri et al. 2020; Romero-Shaw et al. 2020; Bustillo et al. 2021).

Because of its peculiar properties, the formation of GW190521 is still a matter of debate. First, the boundaries of the PI mass gap still suffer from large uncertainties, mostly related to nuclear reaction rates, stellar rotation and the fate of the outer envelope (Farmer et al. 2019, 2020; Farrell et al. 2021; Tanikawa et al. 2021; Umeda et al. 2020; Mapelli et al. 2020; Renzo et al. 2020b; Costa et al. 2021a). Assuming a recent estimate of such uncertainties, Belczynski (2020) shows that it is possible to produce a system with similar masses to GW190521 via isolated binary evolution. On the other hand, this scenario can hardly account for a strong spin misalignment. Binary evolution tends to align the spin of the two components with the orbital angular momentum vector, and the BHs that result from the direct collapse of the two stars inherit their spin orientation forming a non-precessing BBH (Gerosa et al. 2018; Bavera et al. 2020). In contrast, a dynamically active environment tends to isotropically redistribute the spin orientation of BHs (Rodriguez et al. 2016c), while also favouring the production of higher mass binaries (Hills & Fullerton 1980a).

In the hierarchical merger scenario, a BH can undergo repeated mergers with smaller BHs, as long as it is harbored in a star cluster (Miller & Hamilton 2002). This mechanism has recently been studied by several authors to explain the origin of GW190521 (Fragione et al. 2020; Anagnostou et al. 2020; Kimball et al. 2021; Mapelli et al. 2021a; Arca Sedda et al. 2021d). Hierarchical mergers can also take place inside the disc of active galactic nuclei, where BBHs such as GW190521 can form in the migration trap due to the dynamical friction exerted by the disc (McKernan et al. 2012, 2018; Bartos et al. 2017; Samsing et al. 2020; Gondán & Kocsis 2021; Secunda et al. 2020; Tagawa et al. 2021a,b). Either in the core of a dense star cluster or in the disc of a galactic nucleus, the coalescence of GW190521 might also have been caused by Kozai-Lidov oscillations (Kozai 1962; Lidov 1962) induced on the binary by the central super-massive BH (Liu & Lai 2021). Finally, several authors (Spera et al. 2019; Di Carlo et al. 2019, 2020a,c; Gerosa & Fishbach 2021) have shown that PI-mass range BHs can be formed from the collapse of a massive star with an oversized hydrogen-rich envelope and a relatively small helium core. This object could be the product of single or repeated

stellar collisions between stars with a well-developed helium core and main-sequence/Hertzsprung-gap stars (Kremer et al. 2020; Renzo et al. 2020a; Vigna-Gómez et al. 2021; González et al. 2021).

Here, we study the dynamical formation of systems like GW190521 in young star clusters (YSCs), by means of  $2 \times 10^5$  three-body simulations with post-Newtonian terms. We start from the results of the simulations by Di Carlo et al. (2019). Since it would be computationally prohibitive to study a large sample of GW190521-like systems with full  $N$ -body simulations, we extract the main properties of our single and binary BHs (mass and semi-major axis distribution) from the simulations by Di Carlo et al. (2019) and we use them to simulate the formation of GW190521-like systems with three-body encounters. In this way, we include BHs in the mass gap formed via stellar mergers.

## 2.2 Methods

### 2.2.1 $N$ -body simulations with ARWV

We simulated  $2 \times 10^5$  three-body encounters between a BBH and a single massive BH using the direct  $N$ -body code ARWV (Arca-Sedda & Capuzzo-Dolcetta 2019; Chassonney et al. 2019; Chassonney & Capuzzo-Dolcetta 2021). ARWV exploits the algorithmic regularization chain method to integrate the equations of motion (Mikkola & Aarseth 1989, 1993). For our simulations we make use of the ARWV feature to combine the logarithmic-Hamiltonian regularization (logH, Mikkola & Tanikawa 1999b,a; Preto & Tremaine 1999) with the Time-Transformed-Leapfrog method (TTL, Mikkola & Aarseth 2002). The code implements a post-Newtonian (PN) treatment up to the 2.5 order for the correction of the equations of motion in case of strong gravitational interaction (Mikkola & Merritt 2008; Memmesheimer et al. 2004). ARWV calculates the relativistic kick received by the BH remnant due to anisotropic GW emission at merger adopting the equations reported by Healy & Lousto (2018).

We integrate each three-body encounter for  $10^5$  yr. If at that time the system is still in an unstable triple configuration, the simulation is then restarted and carried on until the conclusion of the interaction. At the end of the simulation, if only a BBH is left, we calculate its merger time as (Peters 1964)

$$\begin{aligned} \frac{da}{dt} &= -\frac{64}{5} \frac{G^3 m_i m_j (m_i + m_j)}{c^5 a^3 (1 - e^2)^{7/2}} f_1(e) \\ \frac{de}{dt} &= -\frac{304}{15} e \frac{G^3 m_i m_j (m_i + m_j)}{c^5 a^4 (1 - e^2)^{5/2}} f_2(e), \end{aligned} \quad (2.1)$$

where  $G$  is the gravity constant,  $c$  the speed of light,  $m_i$  the primary mass,  $m_j$  the secondary mass,  $a$  the semi-major axis,  $e$  the orbital eccentricity and

$$\begin{aligned} f_1(e) &= \left( 1 + \frac{73}{24} e^2 + \frac{37}{96} e^4 \right) \\ f_2(e) &= \left( 1 + \frac{121}{304} e^2 \right). \end{aligned} \quad (2.2)$$

These equations only account for the effect of GW emission, they do not encode the information relative to the first and second post-Newtonian terms. For this reason, we integrate a system with equations 3.1 only after the three-body interaction is concluded and only a binary is left.

We assume that two BHs merge when their distance is  $\leq 6 G(m_i + m_j)/c^2$ , i.e. the sum of the innermost stable circular orbits of the two BHs considering non-spinning BHs.

### 2.2.2 Initial Conditions

We set our three-body scattering experiments in the massive YSCs of Di Carlo et al. (2019). This family of clusters can be frequently found in star-forming spiral, starburst and interacting galaxies, including the Milky Way (e.g., see Portegies Zwart et al. 2010b for a review). In YSCs, star formation is still at work, and they are one of the main forges of massive stars in the local Universe (Lada & Lada 2003). Several studies in the literature have already shown that YSCs are ideal birthplaces for BBH mergers (Portegies Zwart & McMillan 2000b, 2002b; Portegies Zwart et al. 2010b; Ziosi et al. 2014; Mapelli 2016; Kimpson et al. 2016; Chatterjee et al. 2017a; Banerjee 2017, 2018a,b, 2021; Di Carlo et al. 2019, 2020a,c; Kumamoto et al. 2019, 2020; Trani et al. 2021).

In the simulations of Di Carlo et al. (2019) and Di Carlo et al. (2020a), massive stars rapidly sink toward the core of the star cluster, where they may experience repeated collisions with other massive stars and thus increase their mass. This can cause stars to acquire a large hydrogen-rich envelope maintaining a relatively small helium core ( $\lesssim 32 M_{\odot}$ ). If the star concludes its life before mass loss efficiently erodes its envelope, and its core does not grow above the threshold for PI, the star avoids PI and instead collapses directly to form a BH in the  $60 - 120 M_{\odot}$  mass range. Since the direct collapse mechanism does not induce a strong recoil kick on the compact remnant, these BHs likely remain inside the YSC and can pair-up dynamically, possibly leading to the formation of BBHs (Heggie & Hut 2003).

Our sample of synthetic three-body simulations is generated considering YSCs with a metallicity  $Z = 0.002 \simeq 0.1 Z_{\odot}$ . Star clusters with lower metallicity develop BBH populations with a similar mass spectrum (e.g., Di Carlo et al. 2020c). In contrast, at higher metallicity, the formation of BHs in the PI mass gap and IMBH mass range is quenched by wind mass loss episodes experienced by the stellar progenitors along their evolution (Di Carlo et al. 2020a).

From here on, we will refer to the quantities related to the primary BH with the subscript 1, to the secondary BH with 2, and to the single BH with 3. Moreover, to distinguish the initial configuration from the outcome binaries, we call *original binary* and *intruder* respectively the BBH ( $m_1 - m_2$ ) and the single BH ( $m_3$ ) that are generated from the initial conditions and set as input to the simulation at time  $t = 0$ .

The initial conditions for BH masses are extracted from the simulations of YSCs performed by Di Carlo et al. (2019), considering the most massive clusters of their sample with  $8 \times 10^3 \leq M_{\text{cl}}/M_{\odot} \leq 3 \times 10^4$ . The simulations of Di Carlo et al. (2019) implement realistic models for stellar and binary evolution and allow the formation of BHs in the PI mass gap and in the IMBH mass range via repeated stellar mergers. This is pivotal in our study since it allows our initial BHs to be a representative sample of the BH population of a YSC. We derive three independent distributions for  $m_1$ ,  $m_2$  and  $m_3$  applying the kernel density estimation method to the BBHs and single BH populations of Di Carlo et al. (2019). We then randomly sample the BH masses from these distributions. Based on Di Carlo et al. (2019), we draw the mass of primary BHs in the  $[3.7, 438] M_{\odot}$  range, the mass of secondary BHs in the  $[3, 74] M_{\odot}$  range and the mass of the intruder in the  $[60, 378] M_{\odot}$ . Namely, we specifically require the intruder mass to be above the lower end of the PI mass gap. The main reason for this choice is that BHs in the PI mass gap are only  $\sim 1\%$  of the entire population by Di Carlo et al. (2019): if we had simulated intruders with all possible masses, including lower mass BHs, we would have needed to run  $\sim 100$  times more simulations, with a prohibitive computational cost. When calculating the merger rate of GW190521-like systems, we will correct our results accounting for the whole possible intruder mass range.

The semi-major axes  $a$  are derived from the simulations of Di Carlo et al. (2019) and Di Carlo et al. (2020a). We fit a log-normal distribution to their data with mean  $\mu_{\log(a/\text{AU})} = 1.51$  and

sigma  $\sigma_{\log(a/\text{AU})} = 0.92$ , and then we randomly sample from this distribution to generate the initial semi-major axis of our original BBHs. We set the limits of the distribution to  $[5.8 \times 10^{-2}, 10^4]$  AU, where the lower limit refers to the smallest semi-major axis in the sample of Di Carlo et al. (2019), while the upper limit is a cut-off value that we introduce to exclude soft binaries, using a 3D velocity dispersion of  $5 \text{ km s}^{-1}$  as reference value for YSCs.

YSCs have a relatively short two-body relaxation timescale of  $t_{\text{rlx}} \sim 20 \text{ Myr} (M_{\text{cl}}/10^4 M_{\odot})^{1/2} (r_h/1 \text{ pc})^{3/2}$ , where  $r_h$  is the half-mass radius (Spitzer 1987). If the cluster reaches two-body relaxation, the stellar velocities can be described with a Maxwell-Boltzmann distribution. We assume the BHs are in thermal equilibrium with the cluster population, and we randomly generate the velocity at infinity  $v_{\infty}$  from a Maxwellian distribution with a 3D velocity dispersion  $\sigma_{\infty} = 5 \text{ km s}^{-1}$ , typical of a YSC. The sampled velocity can be interpreted as the relative velocity between the intruder and the centre-of-mass of the original binary. If the BBHs are in thermal equilibrium with the rest of the cluster population, the eccentricity values  $e$  of the original binaries follow the thermal eccentricity distribution (Ambartsumian 1937; Heggie 1975). This is further confirmed by the simulations of Di Carlo et al. (2019): they find that the eccentricity distribution of their BBHs at 100 Myr is coherent with this behaviour. We thus generate the eccentricities from a uniform distribution in  $e^2$  inside the range  $[0, 1]$ .

The GW events observed so far seem to favour a slowly spinning BH population (The LIGO Scientific Collaboration et al. 2021; Abbott & et al. 2021b). Therefore, we generate the initial dimensionless spin of each BH  $\chi_i = S_i c/(G m_i^2)$ , where  $S_i$  is the magnitude of the spin vector, according to a Maxwell-Boltzmann distribution with root-mean square  $\sigma_{\chi} = 0.1$ , as already done by Bouffanais et al. (2019, 2021). Star cluster dynamics tends to isotropically redistribute the natal spin direction of the BHs via dynamical encounters, which cause BHs to lose memory of their initial spin orientation with respect to the orbital plane of the BBH. To account for this effect, we randomly draw the spin directions isotropic over the sphere. We also check the main effects of a different choice of the spin magnitudes ( $\sigma_{\chi} = 0.01, 0.2, 0.3, 0.5$ ) by overriding the spin magnitudes a posteriori, without rerunning the dynamical simulations.

For the remaining initial quantities (the impact parameter, the three orientation angles, and the phase of the binary star), we use the same formalism as Hut & Bahcall (1983). The orientation of the encounter is randomly drawn from an isotropic sphere<sup>1</sup>, where the angles  $\phi$  and  $\psi$  are sampled from a uniform distribution in  $[0, 2\pi]$ , while  $\theta$  is uniformly drawn from  $\cos \theta$  in  $[-1, 1]$ .

We set the initial single-binary distance  $D = 100a$ , so that the original binary is initially unperturbed by the intruder. The impact parameter  $b$  is drawn according to a uniform probability distribution in  $b^2$ , due to its proportionality to the surface element transverse to the incoming direction of the intruder. The values are generated in the interval  $[0, b_{\max}]$ , with the upper limit derived from the gravitational focusing expression (Sigurdsson & Phinney 1993):

$$b_{\max} = \frac{\sqrt{2 G (m_1 + m_2 + m_3) a}}{v_{\infty}}, \quad (2.3)$$

which represents the maximum impact parameter for a hard encounter as a function of the mass of each BH and the semi-major axis  $a$  of the original BBH. Per each scattering experiment, we require that  $b < D$ . Equation 3.7 assumes that the simulated interactions have maximum pericentre  $p_{\max}$

<sup>1</sup>The angles  $\phi$ ,  $\psi$  and  $\theta$  are defined as in Hut & Bahcall (1983):  $\phi$  is the angle between the pericentre of the binary orbit and the intersection of the vertical plane in which lies the initial velocity vector of the intruder;  $\psi$  is the angle that defines the orientation of the impact parameter with respect to the orbital plane direction in a surface perpendicular to the initial velocity of the intruder; the angle  $\theta$  defines the aperture included between the perpendicular versor of the binary orbital plane and the intruder initial velocity direction at infinity.

equal to the semi-major axis of the binary system. Three-body interactions with  $p_{\max} > a$  likely lead to soft encounters, in which the energy exchange between the single body and the binary is negligible, and the system configuration remains unchanged. This implies that all our simulations are hard encounters. Including softer encounters in our simulations would have requested a larger number of runs, with a much higher computational cost.

The orbital phase of the original binary  $f$  is generated in the range  $[-\pi, \pi]$  according to the prescription adopted by Hut & Bahcall (1983). For each original binary, we first derive the eccentric anomaly  $\epsilon$  from

$$\mathcal{F} = \epsilon - e \sin \epsilon. \quad (2.4)$$

In equation 2.4,  $\mathcal{F} \equiv \frac{2\pi}{T} t_p$ , where  $T$  is the orbital period of the BBH and  $t_p$  is the time elapsed since pericentre passage. We randomly sample  $\mathcal{F}$  in the range  $[0, 2\pi)$ . Finally, we retrieve the initial value of the binary phase  $f$  with:

$$\tan\left(\frac{f}{2}\right) = \left(\frac{1+e}{1-e}\right)^{1/2} \tan\left(\frac{\epsilon}{2}\right). \quad (2.5)$$

## 2.3 Results

### 2.3.1 Flybys, exchanges and ionizations

Three-body encounters are chaotic dynamical interactions that can evolve into several stable configurations. The outcome of an encounter strictly depends on the amount of energy exchanged in the process. In our simulations, we consider three possible outcomes: flybys, exchanges and ionizations. With *flyby* we refer to any simulation in which the initial and final configuration of the three BHs is conserved, i.e. where the original binary survives to the three-body encounter. In this process, the binary can acquire binding energy (hardening) or lose it (softening), according to Heggie's law (Heggie 1975). We define *ionizations* all the events in which the binding energy of each BH pair is positive at the end of the simulation. An ionization can happen only if the intruder approaches the binary with a velocity higher than the critical one (Hut & Bahcall 1983):

$$v_c = \sqrt{\frac{G m_1 m_2 (m_1 + m_2 + m_3)}{a m_3 (m_1 + m_2)}}. \quad (2.6)$$

If, at the end of the simulation, the resulting binary system is composed of different BHs with respect to the original ones, the encounter is labeled as an *exchange* and the binary is an *exchanged binary*. Exchange events are the product of resonant or prompt interactions during which the intruder replaces the primary or secondary BH of the original BBH to form an exchanged binary. The probability of an exchange to happen is higher if the intruder is more massive than one of the two binary members (Hills & Fullerton 1980a). Thus, the final exchanged binary tends to have a higher total mass than the initial one. Flybys and exchanges may induce two of the three BHs to merge during the simulation. If the binding energy between the remnant BH and the third BH is sufficiently large that the relativistic kick does not unbind the binary system, the remnant BH and the third BH form a new BBH, which, in turn, can merge again. We refer to these latter systems as *second-generation* BBHs. In contrast, if the remaining binary after the interaction does not contain a BH remnant (i.e., after an exchange or a fly-by event) it is defined as a *first-generation* BBH.

Table 2.1 reports the outcome fractions of our three-body experiments. Overall, the flybys represent  $\approx 18\%$  of all the simulations, while exchanges are the most common outcome ( $\approx 79\%$ ).

Table 2.1: Outcomes of three-body encounters for all the simulations.

$f_{\text{fb}}$	$f_{\text{ex13}}$	$f_{\text{ex23}}$	$f_{\text{ion}}$
0.178	0.521	0.274	0.027

Column 1 ( $f_{\text{fb}}$ ): fraction of flybys; column 2 ( $f_{\text{ex13}}$ ): fraction of exchanges in which the final BBH is composed of  $m_1$  and  $m_3$  (the secondary BH was kicked off); column 3 ( $f_{\text{ex23}}$ ): fraction of exchanges in which the final BBH is composed of  $m_2$  and  $m_3$  (the primary BH was kicked off); column 4 ( $f_{\text{ion}}$ ): ionization fraction.

Table 2.2: Outcomes of three-body encounters for BBH mergers only (first line) and of BBH mergers that match the masses of GW190521 (second line).

Sample	$f_{2G}$	$f_{12}$	$f_{13}$	$f_{23}$
BBH mergers	0.002	0.193	0.567	0.238
GW190521	0.006	0.009	0.971	0.014

Column 1: the considered sample can be all BBH mergers (first line) or only the mergers with component masses inside the 90% credible interval of GW190521 (second line) according to Abbott &et al. (2020). Column 2 ( $f_{2G}$ ): fraction of second-generation mergers (i.e., the merger remnant of the BBH merges with the third BH); column 3 ( $f_{12}$ ): fraction of mergers between  $m_1$  and  $m_2$ ; column 4 ( $f_{13}$ ): fraction of mergers between  $m_1$  and  $m_3$ ; column 5 ( $f_{23}$ ): fraction of mergers between  $m_2$  and  $m_3$ .

The BBH is ionized only in the  $\approx 3\%$  of the simulations. Table 2.2 focuses on the BBH mergers (i.e., all the simulated BBHs that merge within a Hubble time). Over a total of 7187 BBH mergers, 54% (25.5%) are exchanged binaries where the secondary (primary) component is kicked off the system, 20.2% are flybys and 0.3% are second-generation BBHs.

We calculate the merger timescale (eq. 3.1) at the beginning of all the simulations ( $\tau_0$ ) using the initial orbital properties of the BBHs. After the three-body simulation, we calculate again the merger timescale adopting the new orbital properties of the BBH ( $\tau_{1g}$ ), and we define this timescale as the time-span between the beginning of the three-body integration and the merger. The values of  $\tau_{1g}$  and  $\tau_0$  can be different because of the perturbations induced by the three-body encounter, which might speed up or delay the merger. In 0.25% of the simulations, we observe the merger of the first-generation BBH during the three-body simulation. About 91% of the BBHs that merge during the three-body integration (i.e.,  $\tau_{1g} < 10^5$  yr) have an initial delay time of  $\tau_0 > 10^5$  yr: their coalescence is sped up by the three-body encounter. Finally, in 0.005% of the simulations, we have a second-generation BBH merger during a timescale  $\tau_{2g}$ , defined as the time elapsed from the beginning of the simulation.

### 2.3.2 Component masses

Figure 2.1 shows the mass of the primary and secondary components of the BBH mergers. We now focus only on the BBH mergers that have both the primary and secondary mass in the 90% credible intervals of GW190521 ( $85^{+21}_{-14}$  and  $66^{+17}_{-18}$   $M_\odot$ , as reported by Abbott &et al. 2020; Abbott et al. 2020a). One every  $\sim 9$  BBH mergers (11% of the total) satisfy this criterion. As shown by Table 2.2, the vast majority of these systems are exchanged BBHs (98.5%). Most of these mergers are between  $m_1$  and  $m_3$  (97.1%), while mergers between  $m_2$  and  $m_3$  are only the 1.4% of the GW190521-like systems. Flybys and second-generation binaries contribute to 0.9% and 0.6% of the GW190521-like systems, respectively. Specifically, five over 10 second-generation BBHs lie inside the Abbott &et al. (2020) 90% credible regions for the component masses of GW190521. Their properties are

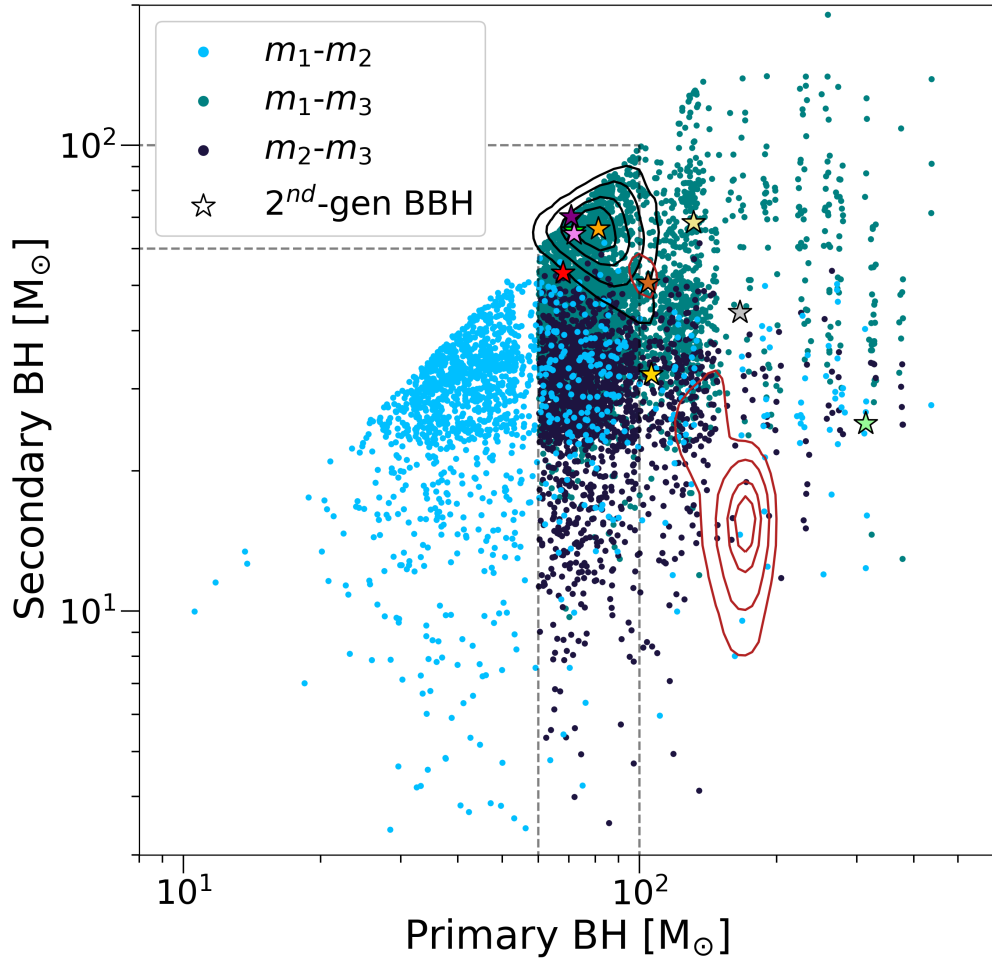


Figure 2.1: Primary and secondary masses of the simulated BBH mergers. Light blue circles are flyby BBHs, while grey (dark) blue circles are exchanged BBHs where the intruder replaced the secondary (primary) BH. The black (magenta) contour levels are the 25, 50, 75, 90% credible regions of GW190521 reported by Abbott &et al. 2020 (Nitz &Capano 2021). Coloured stars are second-generation BBHs. The lime-green, brown, purple, orange and violet stars are inside the 90% credible regions from Abbott &et al. 2020. The vertical dashed grey lines mark the lower-end of the PI mass gap, at  $60 M_\odot$ , and the lower end of the IMBH mass range, at  $100 M_\odot$ .

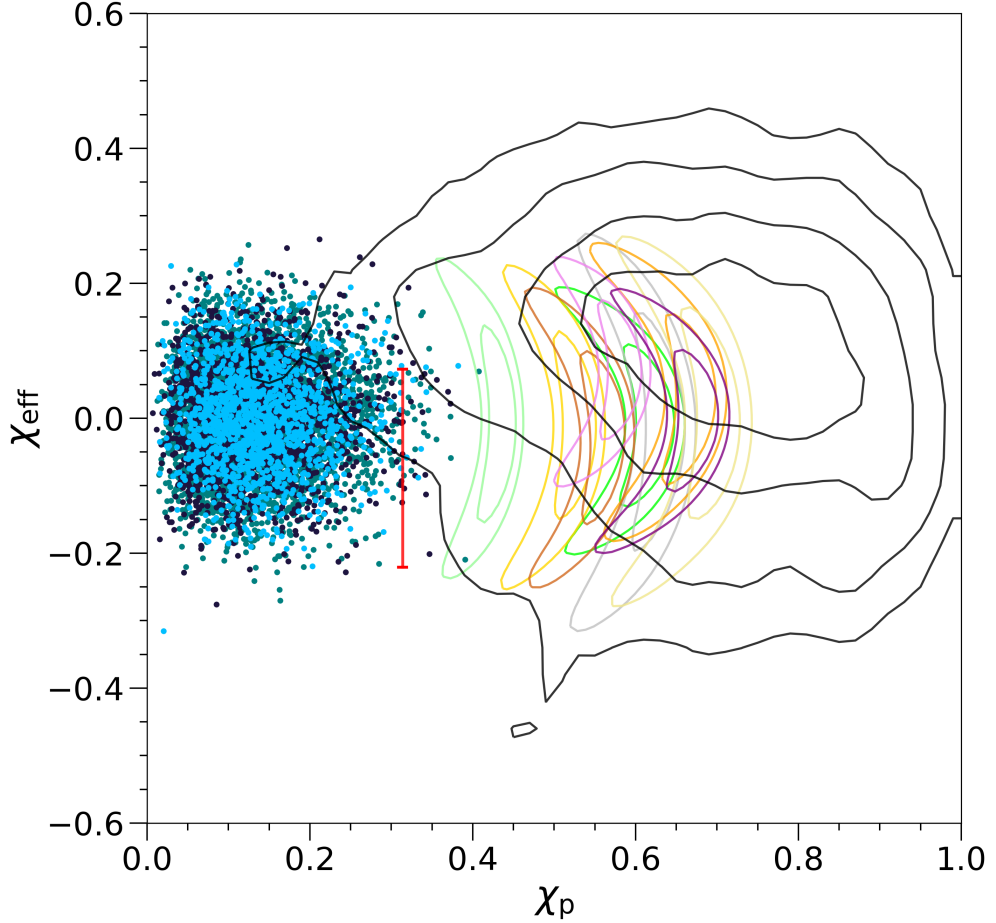


Figure 2.2: Effective spin parameter  $\chi_{\text{eff}}$  versus precessing spin parameter  $\chi_p$  for all the BBH mergers. The colours are the same as Figure 2.1. The lime-green, gray, orange, yellow, brown, light-green, violet, khaki, purple contours are the 50 and 90% credible regions for 9 out of the 10 second-generation BBHs. The red bar shows the last second-generation BBH for which  $\chi_p$  depends only on the spin of the first-generation component (see the main text for details). The black contours are the 25, 50, 75, 90% credible regions for the GW190521 spin parameters posterior reported by Abbott &et al. 2020 and Abbott et al. 2020a.

reported in Table 2.3. In four of these three-body simulations, the original binary experiences a strong encounter with the intruder BH, during which  $m_3$  extracts enough internal energy from the binary to induce it to merge. Despite the relativistic kick, the merger remnant resulting from this first coalescence forms a second-generation BBH with the intruder BH. These systems merge again in less than a Hubble time. The coalescence time of the original binary  $m_1 - m_2$  computed at the beginning of the simulation is longer than the duration of the simulation (i.e., 10<sup>5</sup> yr) for all of these mergers, meaning that the coalescence between  $m_1$  and  $m_2$  is sped up by the three-body interaction. One out of five second-generation BBHs matching the component masses of GW190521 is instead the product of an exchange event. In this simulation, the primary BH  $m_1$  is kicked out from the original binary by the intruder, which merges with the secondary BH giving rise to a massive remnant. The remnant and  $m_1$ , in turn, form a second-generation BBH that merges again in less than a Hubble time. Finally, another second-generation binary grazes the 90% contours, but lies outside the 90% credible interval of GW190521.

Nitz &Capano (2021) interpret the detection of GW190521 as the coalescence of a BBH with primary mass  $168^{+15}_{-61} M_{\odot}$  and secondary mass  $16^{+33}_{-3} M_{\odot}$ , according to the 90% credible intervals derived with a uniform in mass-ratio prior (see also Fishbach &Holz 2020; Ezquiaga &Holz 2021). Their posterior distributions for the component masses are less populated by our BBH mergers than the posterior credible region of Abbott &et al. (2020) and Abbott et al. (2020a). This may suggest that three-body encounters in YSCs could more easily create a BBH with both components in the  $60 - 100 M_{\odot}$  range than a binary straddling the PI mass gap. Indeed, even if a BBH is able to merge within the cluster, the BH remnant is likely kicked out by the relativistic recoil and cannot participate to the cluster dynamics anymore. Hence, only a dense stellar environment with an escape velocity high enough to retain multiple-generation mergers (e.g., nuclear star clusters; Arca Sedda et al. 2021a; Arca Sedda 2020a; Antonini et al. 2019; Fragione et al. 2020; Fragione &Loeb 2021; Mapelli et al. 2021b,a) is able to form an intermediate-mass ratio inspiral such as the one proposed by Nitz &Capano (2021).

### 2.3.3 Effective and precessing spins

Figure 2.2 shows the effective spin parameter  $\chi_{\text{eff}}$  as function of the precessing spin parameter  $\chi_p$  for all the BBH mergers of Figure 2.1. These quantities are computed with the following expressions:

$$\begin{aligned}\chi_{\text{eff}} &= \frac{(m_i \vec{\chi}_i + m_j \vec{\chi}_j)}{m_i + m_j} \cdot \frac{\vec{L}}{L}, \\ \chi_p &= \frac{c}{B_i G m_i^2} \max(B_i S_{i\perp}, B_j S_{j\perp}),\end{aligned}\quad (2.7)$$

where  $\vec{L}$  is the orbital angular momentum vector of the system,  $S_{i\perp}$  and  $S_{j\perp}$  are the spin angular momentum components in the orbital plane of the primary and secondary bodies of the binary,  $B_i \equiv 2 + 3q/2$  and  $B_j \equiv 2 + 3/(2q)$  with  $q = m_j/m_i$  ( $m_i \geq m_j$ ). Since dynamics randomly redistributes the initial BH spins' orientation during a three-body interaction, we compute the final spin parameters  $\chi_p - \chi_{\text{eff}}$  re-drawing the direction of each BH spin isotropically over a sphere but conserving their initial magnitude. For the BH remnants that pair up in second-generation BBHs we do not derive a single value but rather generate a full set of direction angles still sampled from an isotropic distribution. This implies that second-generation BBHs are represented in the plot as contour regions, with the exception of one system (red bar) in which the first-generation component has a higher spin magnitude than the second-generation companion, and thus dominates the  $\chi_p$  term in equation 2.7 resulting in one single  $\chi_p$  value for a set of  $\chi_{\text{eff}}$  values.

Figure 2.2 highlights two distinct populations of mergers. First-generation BBHs, which underwent exchanges and flybys, cover the parameter space at low values of the precessing spin, while second-generation BBHs are located at high  $\chi_p$ . Half of all second-generation BBH mergers (five out of ten BBHs) match both the component masses and the spin parameters of GW190521 inside the 90% credible regions reported by Abbott & et al. (2020), while only 0.1% of the first-generation BBH mergers have both component masses and spin parameters inside the 90% credible regions of GW190521 according to Abbott & et al. (2020). This is an effect of our assumption that all first-generation BH's spin magnitudes are distributed according to a Maxwellian distribution with  $\sigma_\chi = 0.1$ . Had we assumed a larger value for  $\sigma_\chi$ , we would have obtained a correspondingly higher fraction of first-generation BBHs matching GW190521's component masses and spin parameters, as reported in Table 2.4.

The intersection of the two BBH samples that lie inside the posterior regions for the component masses (Figure 2.1) and spin parameters (Figure 2.2) of GW190521 contains twelve systems. These are five second-generation BBHs (marked by the lime-green, brown, purple, orange and violet stars in Figures 2.1 and 2.2) and seven exchanged binaries where  $m_3$  replaced  $m_2$  in the original system. The merger product of all these systems is an IMBH with a mass and a dimensionless spin magnitude inside the 90% credible region of GW190521 ( $M_{\text{rem}} = 142^{+28}_{-16} M_\odot$  and  $\chi_{\text{rem}} = 0.72^{+0.09}_{-0.12}$ , Abbott & et al. 2020; Abbott et al. 2020a). Table 2.3 reports properties of the six BBHs matching GW190521, including the values of  $\tau_0$ ,  $\tau_{1g}$  and  $\tau_{2g}$ .

Table 2.3: BBH mergers with masses and spins in the 90% credible intervals of GW190521. Upper five (Lower seven) lines: second-generation BBHs (first-generation BBHs).

Name	$m_i, m_j$ [ $M_\odot$ ]	$m_{\text{rem}}^{\text{1gen}} - m_k$ [ $M_\odot$ ]	$m_{\text{rem}}^{\text{2gen}}$ [ $M_\odot$ ]	$\chi_{\text{rem}}^{\text{2gen}}$	$\tau_0$ [yr]	$\tau_{1g}$ [yr]	$\tau_{2g}$ [yr]	$e$
9721	35.4, 33.3	65.5 – 71.8	130.7	0.67	$1.1 \times 10^{-5}$	1.52	$4.1 \times 10^4$	$2.6 \times 10^{-3}$
19852	32.4, 75.8	104.3 – 50.6	149.0	0.64	$4.1 \times 10^5$	1.0	$6.13 \times 10^8$	$9.0 \times 10^{-7}$
86653	37.2, 36.9	70.5 – 70.8	135.0	0.64	$3.1 \times 10^9$	3.35	$8.2 \times 10^8$	$1.8 \times 10^{-6}$
112964	43.3, 42.0	81.1 – 66.2	139.9	0.70	$2.7 \times 10^5$	0.79	$6.5 \times 10^4$	$4.0 \times 10^{-3}$
128151	42.1, 25.2	64.3 – 71.9	129.4	0.69	$3.1 \times 10^8$	14.9	$2.9 \times 10^9$	$6.0 \times 10^{-7}$
Name	$m_1, m_3$ [ $M_\odot$ ]	$m_2$ [ $M_\odot$ ]	$m_{\text{rem}}$ [ $M_\odot$ ]	$\chi_{\text{rem}}$	$\tau_0$ [yr]	$\tau_{1g}$ [yr]	$\tau_{2g}$ [yr]	$e$
90086	73.7, 70.8	30.1	137.2	0.71	$2.2 \times 10^{11}$	$1.1 \times 10^9$	–	$1.0 \times 10^{-6}$
102042	78.2, 85.7	27.9	156.4	0.66	$1.2 \times 10^{15}$	$5.7 \times 10^8$	–	$1.6 \times 10^{-6}$
129317	62.5, 77.9	30.1	134.0	0.66	$1.1 \times 10^{11}$	$8.4 \times 10^5$	–	$1.5 \times 10^{-5}$
141880	52.0, 84.7	9.7	130.6	0.67	$3.5 \times 10^{11}$	$4.8 \times 10^8$	–	$1.3 \times 10^{-6}$
154193	68.4, 74.2	6.9	135.5	0.71	$1.6 \times 10^7$	$8.3 \times 10^9$	–	$2.7 \times 10^{-7}$
184181	48.1, 68.7	24.7	129.5	0.62	$4.0 \times 10^{10}$	$3.8 \times 10^9$	–	$2.4 \times 10^{-7}$
188838	52.1, 89.0	47.2	134.9	0.68	$9.2 \times 10^{13}$	$1.4 \times 10^9$	–	$6.4 \times 10^{-7}$

The simulations in the first five lines are second-generation BBHs, reported in Figures 2.1, 2.2 and 2.3 with the colours lime-green, brown, purple, orange and violet. Subscripts  $i, j$  in the first column and  $k$  in the second column mark the three-body configuration that triggers the first merger: simulations 9721, 86653, 112964 and 128151 have  $i = 1, j = 2$  (flyby) and  $k = 3$ , while simulation 19852 has  $i = 2, j = 3$  (exchange) and  $k = 1$ . Column 1: simulation name; column 2: mass of the components of the initial BBH; column 3: mass of the components of the second-generation BBH; column 4: mean mass of the final second-generation remnant BH; column 5: mean magnitude of the remnant spin; column 6 ( $\tau_0$ ): initial coalescence time of the original BBH at the beginning of the simulation (we calculated the merger timescale for the initial BBH according to Peters 1964 assuming that the BBH is not perturbed by dynamics); column 7 ( $\tau_{1g}$ ): effective coalescence time of the original binary as a result of the 3-body simulation; column 8 ( $\tau_{2g}$ ): coalescence time of the second-generation BBH since the beginning of the simulation; column 9 ( $e$ ): eccentricity at  $\nu_{\text{gw}} = 10 \text{ Hz}$  of the second-generation BBH. The last seven lines are exchanged first-generation BBHs that match the properties of GW190521. Column 1: simulation name; column 2: mass of the components of the exchanged binary (which is always composed of  $m_1$  and  $m_3$ ); column 3: mass of the secondary BH ejected during the exchange; column 4: mass of the final BH remnant; column 5: magnitude of the remnant spin; column 6: coalescence time of the BBH merger since the beginning of the simulation, calculated according to Peters (1964); column 7 ( $\tau_{1g}$ ): effective coalescence time of the 3-body simulation; column 9 ( $e$ ): eccentricity at  $\nu_{\text{gw}} = 10 \text{ Hz}$  of the exchanged BBH.

Table 2.4: Percentage of first-generation BBH mergers that match the main properties of GW190521 as a function of the spin prescription adopted.

$\sigma_\chi$	$P_{\text{GW190521}} [\%]$
0.01	0
0.1	0.1
0.2	2.8
0.3	3.9
0.5	4.2

Column 1 ( $\sigma_\chi$ ): root-mean square value of the Maxwell-Boltzmann distribution used to generate the dimensionless spin magnitude of each BH. Column 2 ( $P_{\text{GW190521}}$ ): percentage of first-generation BBH mergers that have  $m_1$ ,  $m_2$ ,  $\chi_{\text{eff}}$ ,  $\chi_p$ ,  $M_{\text{rem}}$  and  $\chi_{\text{rem}}$  inside the 90% credible intervals of GW190521 reported by Abbott & et al. (2020); Abbott et al. (2020a).

### 2.3.4 Merger remnants

Figure 2.3 shows the mass of the merger remnants as function of their dimensionless spin magnitudes. The values are derived from the numerical relativity fitting equations of Jiménez-Forteza et al. (2017). Specifically, to compute the remnant spin of the first-generation BBH mergers, we re-sampled the spin orientation of the progenitor BHs from an isotropic sphere. For second-generation BBHs we applied the same procedure we adopted in Figure 2.2: we randomly generated a full set of isotropic-oriented spins for the progenitor BHs, from which we then derived all the possible mass and spin magnitudes of the remnants. The error bars on the plot show all the possible masses and spins inherited by these third-generation remnants while the stars mark the mean value of the intervals.

The merger remnants inherit the orbital angular momentum of their progenitor BBH, and are therefore characterized by high spin magnitudes (Fishbach et al. 2017; Gerosa & Berti 2017). The main peak of the distribution is located at a mass of  $M_{\text{rem}} \approx 112 M_\odot$  and a spin of  $\chi_{\text{rem}} \approx 0.66$ , and is mainly produced by exchanged BBHs with components  $m_1 - m_3$ . Other two secondary peaks exist at  $\chi_{\text{rem}} \approx 0.68$ ,  $M_{\text{rem}} \approx 68 M_\odot$  and  $\chi_{\text{rem}} \approx 0.60$ ,  $M_{\text{rem}} \approx 101 M_\odot$ , and are mostly given by the contribution of flybys  $m_1 - m_2$  and exchanged BBHs with components  $m_2 - m_3$ , respectively.

The difference among these three sub-peaks is explained by the different total mass of the progenitor BBHs: flybys produce lower mass remnants than exchanged binaries, since the intruder ( $m_3$ ) is generally more massive than the two members of the original BBH  $m_1 - m_2$ . In their turn, exchanged binaries with component masses  $m_1 - m_3$  are more massive than exchanged binaries with component masses  $m_2 - m_3$ , because  $m_1 > m_2$ . This difference in the BH masses results in a difference in the remnant spin  $\chi_{\text{rem}}$ , mostly because of the different mass ratios. BBH mergers with components  $m_1 - m_2$ ,  $m_1 - m_3$  and  $m_2 - m_3$  have, on average, different mass ratios with typical values of  $\approx 0.96$ ,  $0.55$  and  $0.36$ , respectively (Figure 2.4).

The only contour region that intersects the posteriors of GW190521 is the one populated mostly by exchanged BBHs with components  $m_1 - m_3$ . Moreover, the same five second-generation BBHs that match the component masses of GW190521 lie inside the 90% credible region of  $M_{\text{rem}} - \chi_{\text{rem}}$ , along with one additional system. This result further confirms that GW190521 might have been originated either by a primary exchange system or by a second-generation BBH.

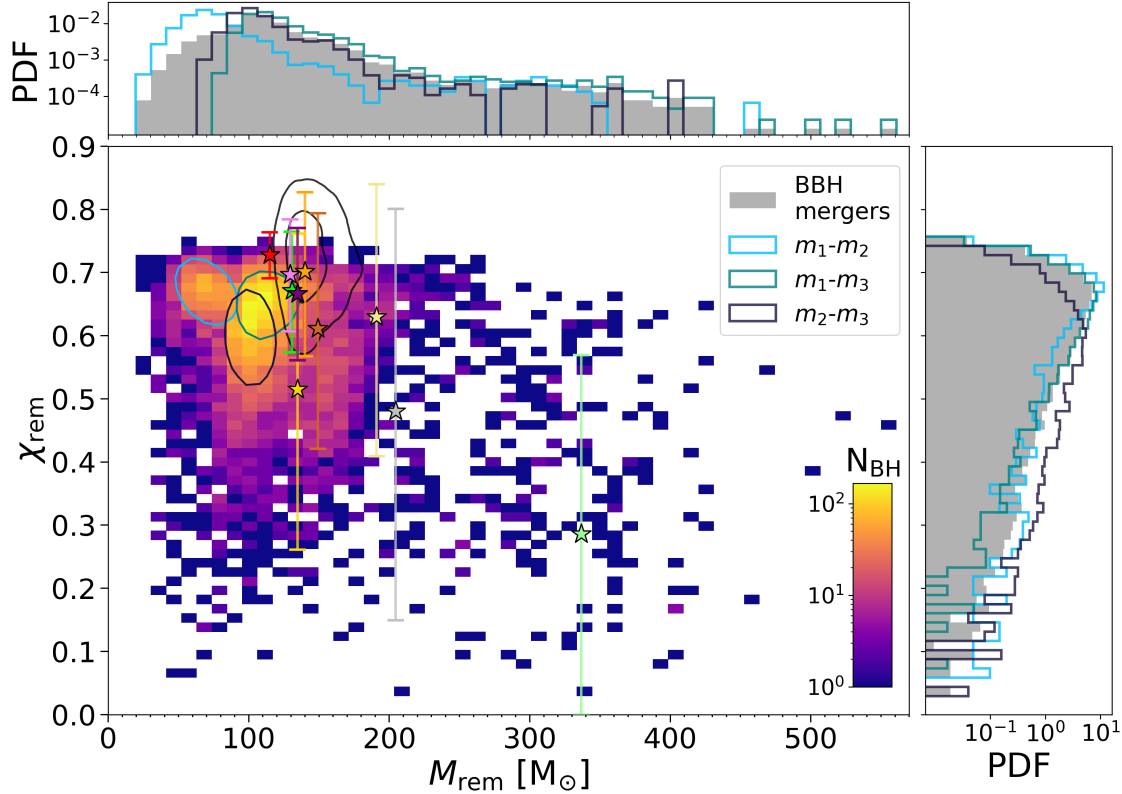


Figure 2.3: Mass of the BH remnant produced by each BBH merger as a function of its dimensionless spin magnitude. The two-dimensional filled histogram shows all first-generation BBH mergers. The light-blue, dark-blue and navy unfilled contours show the 50% credible regions for first-generation BBH mergers with components  $m_1 - m_2$ ,  $m_2 - m_3$  and  $m_1 - m_3$ , respectively. The stars mark the average values of  $M_{\text{rem}}$  and  $\chi_{\text{rem}}$  for second-generation BBH mergers, while the error bars show all the possible masses and spins inherited by these third-generation remnants (mass error bars are smaller than the markers, see the text for more details). The black unfilled contours show the 50 and 90% credible region for the posteriors of GW190521 (Abbott & et al. 2020; Abbott et al. 2020a). The values of  $M_{\text{rem}}$  and  $\chi_{\text{rem}}$  for the lime-green, brown, purple, orange, violet, and yellow stars are inside the 90% credible region of GW190521. The grey filled marginal histograms show the distributions of  $M_{\text{rem}}$  and  $\chi_{\text{rem}}$  for all simulated BBH mergers. The light-blue, dark-blue and navy unfilled marginal histograms show the distributions of  $M_{\text{rem}}$  and  $\chi_{\text{rem}}$  for first-generation BBHs with components  $m_1 - m_2$ ,  $m_2 - m_3$  and  $m_1 - m_3$ , respectively.

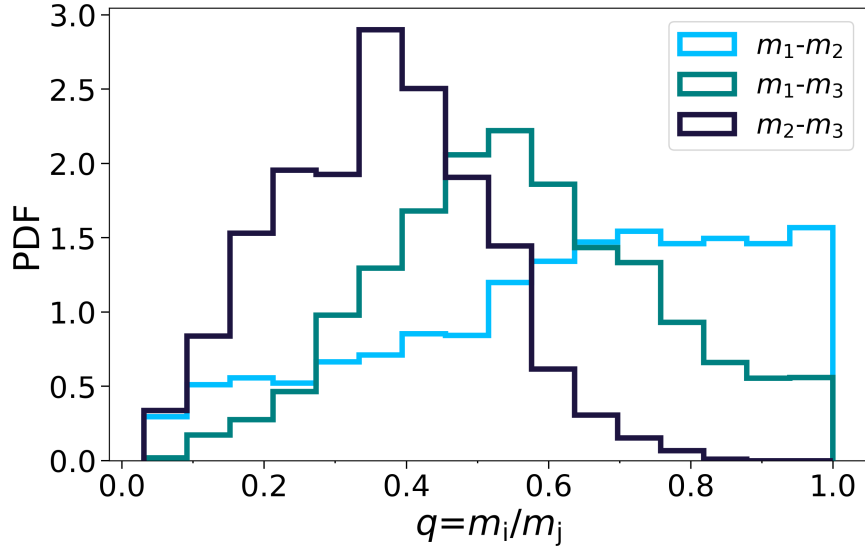


Figure 2.4: Mass ratio of the BBH mergers at the end of the simulations. The histograms show the distribution of the three different outcomes: flybys are indicated with the light-blue line, while the navy (dark) blue lines show the exchanged binaries in which the intruder replaced the secondary (primary) BH.

## 2.4 Discussion

### 2.4.1 Dynamical origin of GW190521 and merger rate density

There are at least four main features that characterize a BBH born from dynamical interactions with respect to an isolated binary.

- **Large total mass:** hierarchical BH mergers and repeated stellar collisions may produce massive BHs also inside the PI gap or even in the IMBH range (e.g., Antonini et al. 2019; Fragione et al. 2020; Arca Sedda et al. 2020; Mapelli et al. 2021a). These BHs can eventually interact with other binaries and form BBHs with higher total mass via exchange events.
- **Misaligned spins:** dynamical interactions tend to isotropically redistribute the spin orientation of the binary components, while binary evolution in the isolated channel favours the production of parallel spinning stars due to angular momentum transfer (e.g., Rodriguez et al. 2016c; Gerosa et al. 2018).
- **Low mass ratio:** binary evolution can cause several stable and unstable mass transfer episodes, which generally redistribute the mass between the two stars and lead to a mass ratio close to one (e.g., Dominik et al. 2012; Mapelli et al. 2019; Neijssel et al. 2019). On the other hand, in a dynamically active environment, exchange interactions produce lower mass ratio BBHs (e.g., Chatterjee et al. 2017b; Di Carlo et al. 2019).
- **Non-zero eccentricity in chirping regime:** dynamical interactions and resonant perturbations such as the Kozai-Lidov effect can heavily increase the eccentricity in already existing BBHs, or even produce head-on collisions (e.g. Samsing et al. 2014, 2018a; Arca Sedda et al.

2021a; Zevin et al. 2019). These systems may merge before the GW emission is able to circularize the orbit, producing a distinct feature in the waveform (e.g., Gayathri et al. 2020; Romero-Shaw et al. 2020; Holgado et al. 2021).

Our simulations indicate that GW190521 can be the result of a first-generation exchanged BBH with at least one component produced by a stellar merger, or of a second-generation BBH. The posterior distribution of its component masses, the mass of the remnant, and the combination of its  $\chi_p - \chi_{\text{eff}}$  spin parameters seem to exclude the merger of an original binary but rather favour a scenario in which a less massive BBH experienced an exchange event between the secondary and the massive intruder that increased the total mass of the system. Another interpretation is provided by the merger of a second-generation BBH. If the first-generation BH population is characterized by low spin magnitudes as suggested by The LIGO Scientific Collaboration et al. (2021), the latter scenario is even more likely because of the mild evidence for large spins in GW190521 (Abbott &et al. 2020).

Some authors (Gayathri et al. 2020; Romero-Shaw et al. 2020; Bustillo et al. 2021; Abbott et al. 2020a) interpret the detection of GW190521 as the merger of a binary system with non-zero eccentricity at the time of coalescence. We calculated the eccentricity of the simulated BBH systems when the frequency of GW emission is  $\nu_{\text{gw}} = 10$  Hz (i.e., approximately when the binary system enters the LIGO–Virgo range, Table 2.3). We find that two of the second-generation BBHs that match the properties of GW190521 have respectively  $e \sim 0.003$  and  $e \sim 0.004$  in the LIGO–Virgo range (see table 2.3). This translates into  $e \sim 0.4$  and  $e \sim 0.3$  at  $\nu_{\text{gw}} = 10^{-2}$  Hz in LISA band. All the other systems that match the properties of GW190521 have eccentricity  $\lesssim 10^{-4}$  in the LIGO–Virgo range, even if post-Newtonian corrections are accounted for.

Finally, we estimated the approximate merger rate density of GW190521-like systems from our simulations as

$$\mathcal{R}_{\text{GW190521}} \sim 0.03 \text{ Gpc}^{-3} \text{ yr}^{-1} \left( \frac{N_{190521}}{12} \right) \left( \frac{N_{\text{BBH}}}{7187} \right)^{-1} \left( \frac{\mathcal{R}_{\text{BBH}}(z=0.8)}{170 \text{ Gpc}^{-3} \text{ yr}^{-1}} \right) \left( \frac{f_{\text{YSC}}}{0.7} \right) \left( \frac{f_{\text{corr}}}{0.14} \right), \quad (2.8)$$

where  $N_{190521}$  is the number of simulated BBH mergers with the mass of the components, the effective and precessing spin parameters and the mass and spin of the remnant inside the 90% credible intervals reported by Abbott &et al. (2020) and Abbott et al. (2020a),  $N_{\text{BBH}}$  is the number of BBH mergers in our simulations,  $\mathcal{R}_{\text{BBH}}(z=0.8)$  is the BBH merger rate density at  $z \simeq 0.8$  (i.e., the median redshift value of GW190521; Abbott &et al. 2020; Abbott et al. 2020a). We calculated  $\mathcal{R}_{\text{BBH}}$  for the YSCs simulated by Di Carlo et al. (2020c) following the method described in Santoliquido et al. (2020).  $\mathcal{R}_{\text{BBH}}$  is affected by a substantial uncertainty (about one order of magnitude), mostly because of the metallicity evolution (see Santoliquido et al. 2021 for more details). Finally,  $f_{\text{YSC}}$  is the fraction of BBH mergers that originate in YSCs, according to the fiducial model of Bouffanais et al. (2021), and  $f_{\text{corr}}$  is a correction factor to compensate for the bias we introduced when we simulated only intruders with  $m_3 \geq 60 M_\odot$ . In the simulations of Di Carlo et al. (2020a), the BHs with mass inside the PI gap are only  $\sim 1\%$  of the whole BH population (considering both single and binary BHs), but the BBHs that contain at least one BH in the PI mass gap are  $\sim 10\%$  of all the BBHs. Since all BHs in the PI gap are single BHs at birth, this means that they are extremely efficient in pairing up via dynamical exchanges. In our three-body simulations, we find that 71% of all the final BBHs have at least one component in the PI mass gap. Hence  $f_{\text{corr}} = 0.14$  compensates for this spurious enhancement of BBHs in the mass gap in our simulations with respect to the ones of Di Carlo et al. (2020a).

Equation 2.8 leads to a merger rate density value of  $\mathcal{R}_{\text{GW190521}} \sim 0.03 \text{ Gpc}^{-3} \text{ yr}^{-1}$  for BBHs like GW190521 formed via three-body encounters in YSCs. This is about a factor of 2.7 lower than the median value reported in Abbott &et al. (2021c), but still inside their 90% credible interval ( $0.08^{+0.19}_{-0.07} \text{ Gpc}^{-3} \text{ yr}^{-1}$ ).

### 2.4.2 Caveats

The number of BBH mergers matching the effective and precessing spin parameters of GW190521 is strongly affected by our choice of the spin magnitude of first-generation BHs, which is drawn from a Maxwellian distribution with  $\sigma_\chi = 0.1$ . Table 2.4 shows that changing  $\sigma_\chi$  from 0.1 to 0.2 dramatically increases the fraction of first-generation BBHs that match GW190521's masses and spins. A choice of  $\sigma_\chi = 0.2$  would have produced 198 first-generation BBH mergers with the same properties as GW190521, rather than just seven binaries as derived with  $\sigma_\chi = 0.1$ . Hence, the merger rate density of GW190521-like systems is very sensitive to the spin distribution of first-generation BBHs: we obtain  $\mathcal{R}_{\text{GW190521}} \sim 0.01 \text{ Gpc}^{-3} \text{ yr}^{-1}$  if  $\sigma_\chi = 0.01$  (no first-generation BBH mergers matching GW190521) and  $\mathcal{R}_{\text{GW190521}} \sim 0.47 \text{ Gpc}^{-3} \text{ yr}^{-1}$  if  $\sigma_\chi = 0.2$ .

Moreover,  $\mathcal{R}_{\text{GW190521}}$  also depends on  $\mathcal{R}_{\text{BBH}}$ , which in turn varies with redshift. In the LIGO-Virgo sensitivity range, this translates to a merger rate density of systems like GW190521 that ranges from  $\sim 0.01 \text{ Gpc}^{-3} \text{ yr}^{-1}$  at  $z \sim 0$  up to  $\sim 0.04 \text{ Gpc}^{-3} \text{ yr}^{-1}$  at  $z \sim 1$  for our fiducial model ( $\sigma_\chi = 0.1$ ).

We simulated a single three-body interaction for each original binary. This is a conservative approach, because each simulated BBH might undergo more than one interaction after its formation and before its ejection from the YSC. However, our simulated YSCs are relatively short lived ( $\lesssim 1$  Gyr) with a low escape velocity ( $v_{\text{esc}} \sim 10 \text{ km s}^{-1}$ ), and their central density drops soon after their formation (Rastello et al. 2021b). Hence, it is reasonable to assume that each BBH cannot undergo a long chain of encounters. To further support our choice of a single encounter per binary, we calculated the value of the semi-major axis below which a binary can be ejected by a single-binary scattering (Miller & Hamilton 2002; Antonini & Rasio 2016):

$$a_{\text{ej}} = \frac{\xi m_3^2}{(m_1 + m_2)^3} \frac{G m_1 m_2}{v_{\text{esc}}^2}, \quad (2.9)$$

where  $\xi = 3$  (Quinlan 1996) is a dimensionless parameter and  $v_{\text{esc}}$  is the escape velocity from the star cluster. We estimated that  $\approx 80\%$  of our BBHs have  $a \leq a_{\text{ej}}$  at the end of the three-body simulation. Hence, most of them are ejected from the cluster after the first encounter. This also implies that most BBHs evolve unperturbed after the simulated three-body interaction. Second-generation BBHs are therefore likely ejected from the cluster, where they can freely evolve and merge in the field. If retained, the probability of experiencing a second three-body encounter with another BH is low due to the short life span of the cluster.

In our scattering experiments we considered just triple BH interactions, without stellar components. This assumption implies that our three-body encounters take place after all BHs, even the lightest ones, have formed in a star cluster ( $t \gtrsim 10$  Myr). While including three-body encounters between our BBHs and non-degenerate stars would make our simulations more realistic, it is unlikely that this kind of interactions drastically affect our results. Firstly, at  $t \gtrsim 10$  Myr, only stars with mass  $\lesssim 15 M_\odot$  remain in the cluster: it is unlikely that these stars exchange with our massive BBHs. Secondly, BHs in YSCs tend to dynamically decouple from the lighter stars and to interact mainly with each other, because of their larger mass and shorter dynamical friction timescale (Spitzer 1987; Morscher et al. 2015).

## 2.5 Summary

We studied the dynamical formation of GW190521 via three-body interactions in massive YSCs. By means of direct  $N$ -body simulations, we performed  $2 \times 10^5$  dynamical encounters between a BBH and a single BH with mass  $\geq 60 M_\odot$ , above the lower edge of the PI mass gap. Our simulations include the first post-Newtonian terms (1, 2 and 2.5) and a relativistic kick prescription for the merger remnants. We generate the mass, semi-major axis and orbital eccentricity of our BBHs from the population produced in the YSC simulations of Di Carlo et al. (2019). In this way, our sample includes also BHs with mass inside and above the PI gap, produced by stellar collisions in massive YSCs. We adopt a Maxwellian distribution with  $\sigma_\chi = 0.1$  to generate the magnitude of BH spins, while their direction is isotropic over the sphere (Bouffanais et al. 2019, 2021).

From our simulations, we extract the first- and second-generation BBH mergers that match the main properties of GW190521 ( $m_1, m_2, \chi_{\text{eff}}, \chi_p, M_{\text{rem}}, \chi_{\text{rem}}$ ) within the 90% credible interval reported by Abbott et al. (2020a). About 11% of our simulated BBH mergers lie inside the 90% credible interval of the component masses of GW190521. In contrast, only 0.17% of our simulated BBH mergers have not only the mass of the components, but also the effective and precessing spin parameters, and the final mass and spin of the BH remnant in the 90% credible intervals of GW190521, as reported by Abbott & et al. (2020). Seven of these systems are exchanged first-generation binaries where the BH intruder replaced the secondary component of the original BBH, while five are second-generation BBHs. All the systems that match the properties of GW190521 have eccentricity  $< 10^{-4}$  in the LIGO–Virgo range, with the exception of two second-generation BBHs that have respectively  $e \sim 0.003$  ( $e \sim 0.4$ ) and  $e \sim 0.004$  ( $e \sim 0.3$ ) at 10 Hz ( $10^{-2}$  Hz).

All the second-generation BBHs resulting from the simulations match the observed ranges of  $\chi_p - \chi_{\text{eff}}$  for GW190521, forming a separate population with non-negligible precessing spin parameter with respect to first-generation BBHs. Nevertheless, these systems are much rarer than exchanged binaries, which in turn represent almost all ( $\sim 98.5\%$ ) of the BBH mergers with the components in the same mass range as GW190521.

The effective and precessing spins are the most constraining parameters for GW190521-like systems in our simulations because we assumed that first-generation BHs have relatively low spins, following a Maxwellian distribution with  $\sigma_\chi = 0.1$ . If we relax this assumption, many more first-generation BBHs match the main properties of GW190521 ( $m_1, m_2, \chi_{\text{eff}}, \chi_p, M_{\text{rem}}, \chi_{\text{rem}}$ ), increasing from 0.1% of all our simulated first-generation BBH mergers for  $\sigma_\chi = 0.1$  up to  $\sim 4.2\%$  for  $\sigma_\chi = 0.5$  (Table 2.4). We do not know the exact spin distribution of massive BHs born from stellar mergers, but we can guess that high spins are possible, because the entire star collapses to BH in this scenario (Costa et al. 2021a).

If we assume relatively low spins for first-generation BHs ( $\sigma_\chi = 0.1$ ), the merger rate density of GW190521-like systems is  $\mathcal{R}_{\text{GW190521}} \sim 0.03 \text{ Gpc}^{-3} \text{ yr}^{-1}$ , within the 90% credible interval derived by Abbott & et al. (2021c) but rather on the low side. Our estimate of the merger rate density is very sensitive to the spin distribution of first-generation BBH mergers: we obtain  $\mathcal{R}_{\text{GW190521}} \sim 0.01 \text{ Gpc}^{-3} \text{ yr}^{-1}$  if  $\sigma_\chi = 0.01$  (no first-generation BBH mergers matching GW190521) and  $\mathcal{R}_{\text{GW190521}} \sim 0.46 \text{ Gpc}^{-3} \text{ yr}^{-1}$  if  $\sigma_\chi = 0.2$ . Our results imply that GW190521, if it was born in a massive YSC, is either a first-generation BBH resulting from an exchange with a massive intruder ( $\geq 60 M_\odot$ ) or a second-generation BBH merger triggered by a resonant three-body encounter.

## Acknowledgements

We thank the anonymous Referee for their useful comments which helped us improve our work. MD acknowledges financial support from Cariparo foundation under grant 55440. MM, UNDC, YB, SR, FS and AB acknowledge financial support by the European Research Council for the ERC Consolidator grant DEMOBLACK, under contract no. 770017. MAS acknowledges financial support from the Alexander von Humboldt Stiftung under the research program "Black Holes at all the scales", the Volkswagen Foundation Trilateral Partnership project No. I/97778 "Dynamical Mechanisms of Accretion in Galactic Nuclei", the Deutsche Forschungsgemeinschaft (DFG, German Research Foundation) – Project-ID 138713538 – SFB 881 ("The Milky Way System"), and the COST Action CA16104. We acknowledge the CINECA-INFN agreement for the availability of high performance computing resources and support. We also thank Roberto Capuzzo Dolcetta, Pauline Chassonney and Seppo Mikkola for making the ARWV code available to us.



# Chapter 3

## Eccentric black hole mergers via three-body interactions in young, globular and nuclear star clusters

*Based on:*

Dall'Amico M., Mapelli M., Torniamenti S., Arca Sedda M., "Eccentric black hole mergers via three-body interactions in young, globular and nuclear star clusters", 2022, ArXiv 2303.07421 pre-print, A&A accepted

### Abstract

Eccentric mergers are a signature of the dynamical formation channel of binary black holes (BBHs) in dense stellar environments and hierarchical triple systems. Here, we investigate the formation of eccentric mergers via binary-single interactions by means of  $2.5 \times 10^5$  direct  $N$ -body simulations. Our simulations include post-Newtonian terms up to the 2.5th order and model the typical environment of young (YSCs), globular (GCs), and nuclear star clusters (NSCs). Around 0.6% (1%) of our mergers in NSCs (GCs) have an eccentricity  $> 0.1$  when the emitted gravitational-wave frequency is 10 Hz in the source frame, while in YSCs this fraction drops to 0.08%. Approximately  $\sim 63\%$  of these mergers are produced by chaotic, resonant interactions where temporary binaries are continuously formed and destroyed, while  $\sim 31\%$  arise from an almost direct collision of two black holes (BHs). Lastly,  $\sim 6\%$  of these eccentric mergers occur in temporary hierarchical triples. We find that binaries undergoing a flyby generally develop smaller tilt angles with respect to exchanges. This result challenges the idea that dynamics produces perfectly isotropic spin orientations. The environment dramatically affects BH retention: 0%, 3.1%, and 19.9% of all the remnant BHs remain in YSCs, GCs, and NSCs, respectively. The fraction of massive BHs also depends on the host cluster properties, with pair-instability ( $60 \leq M_{\text{BH}}/M_{\odot} \leq 100$ ) and intermediate-mass ( $M_{\text{BH}} \geq 100 M_{\odot}$ ) BHs accounting for approximately  $\sim 44\%$  and 1.6% of the mergers in YSCs,  $\sim 33\%$  and 0.7% in GCs, and  $\sim 28\%$  and 0.4% in NSCs.

**keywords:** gravitational waves – black hole physics – methods: numerical – stars: black holes – stars: kinematics and dynamics – galaxies: star clusters: general

### 3.1 Introduction

Binary-single encounters dominate the interactions between black holes (BHs) in the core of star clusters (Heggie 1975; Hut & Bahcall 1983; Hut 1983, 1993; Banerjee et al. 2010). In this region,

BHs form a dynamically decoupled sub-core where they can mostly interact via binary-single scatter due to the large cross section of this process (e.g., Breen & Heggie 2013a,b; Samsing et al. 2014). This springs from star clusters’ tendency to evolve toward energy equipartition (Spitzer 1969; Trenti & van der Marel 2013; Spera et al. 2016; Bianchini et al. 2016), combined with dynamical friction acting on the most massive bodies of the cluster (Meylan & Heggie 1997; Fregeau et al. 2002; Gürkan et al. 2004).

Most binary black holes (BBHs) in star clusters belong to the family of hard binaries, i.e. binary systems with a binding energy larger than the average star kinetic energy of the cluster. Since hard binaries statistically tend to get harder during binary-single encounters (Heggie 1975), BBHs tend to progressively decrease their semi-major axis, or even increase their total mass if a dynamical exchange with a single BH takes place (Hills & Fullerton 1980b). Three-body interactions<sup>1</sup> between BHs are therefore a key mechanism to speed up the merger before gravitational-wave (GW) emission becomes efficient. These dynamical encounters not only efficiently produce BBH mergers (e.g., Sigurdsson & Phinney 1995; Portegies Zwart & McMillan 2000c; Banerjee et al. 2010; Tanikawa 2013; Ziosi et al. 2014; Morscher et al. 2015; Rodriguez et al. 2015, 2016a,b; Mapelli 2016; Samsing et al. 2017, 2018b; Samsing & Ilan 2018; Trani et al. 2019, 2021; Dall’Amico et al. 2021) and BH-neutron star mergers (e.g., Clausen et al. 2013; Arca Sedda 2020b, 2021), but they may also cause eccentric mergers (Gültekin et al. 2006; Samsing et al. 2014; Samsing & Ramirez-Ruiz 2017; Samsing 2018; Samsing et al. 2018a; Rodriguez et al. 2018; Zevin et al. 2019; Arca Sedda et al. 2021b; Trani et al. 2022; Codazzo et al. 2023). These are mergers in which the coalescence time of the binary is shorter than the timescale it takes for GW emission to circularize the orbit, such that the binary can merge with non-zero eccentricity in the LIGO–Virgo sensitivity band (Abbott & et al. 2019). In dynamical interactions, the energy exchange between the bodies can excite the eccentricity of a BBH and even induce it to merge. This is particularly true for three-body interactions, where the system can evolve into a chaotic regime with temporary binaries that are continuously created and destroyed. In this unstable triple configuration, the single BH can perturb the temporary binary and induce it to merge rapidly enough that GW are not sufficient to completely circularize the orbit (Samsing et al. 2014).

Isolated binaries, on the other hand, struggle to produce BBHs with non-negligible eccentricity at merger. Tidal effects, mass transfer episodes, and common envelope events usually circularize the orbit of a binary star even before it evolves into a BBH (Hurley et al. 2002). Even if supernova kicks can increase the eccentricity of the system, GW efficiently circularize the orbits by the merger time (Peters 1964). Eccentric mergers are therefore commonly associated with BBHs formed in a dynamically active environment. Eccentricity, if detected in the waveform of a merger, might be used as a tool to infer the dynamical origin of a BBH (Amaro-Seoane & Chen 2016; Chen & Amaro-Seoane 2017; Gayathri et al. 2020; Romero-Shaw et al. 2020, 2021; Zevin et al. 2021).

How often are these eccentric mergers produced by dynamical interactions? And in which environment should we expect them to be more frequent? Here, we aim to address these questions via direct  $N$ -body simulations of three-body encounters between BBHs and BHs. We performed three different sets of binary-single scattering experiments, each with different initial conditions appositely set to reproduce the properties of a class of star clusters: young star clusters (YSCs), globular clusters (GCs), and nuclear star clusters (NSCs). Our goal is to investigate the effect of the cluster properties on the interactions and to derive the influence that the hosting environment has on the outcomes and production of eccentric BBH mergers.

Three-body interactions are the fundamental mechanism at the base of hierarchical mergers, i.e. the process in which two BHs merge and their merger remnant collides with other BHs of the cluster,

---

<sup>1</sup>Hereafter, we will use the terms three-body interactions and binary-single encounters as synonyms.

giving rise to multiple-generations of BBHs (Miller & Hamilton 2002; Gerosa & Berti 2017; Fishbach et al. 2017; Rodriguez et al. 2019; Antonini et al. 2019; Doctor et al. 2020; Arca Sedda et al. 2021c; Mapelli et al. 2021a; Gerosa & Fishbach 2021; Atallah et al. 2022). Here, we discuss the impact of three-body recoil velocities on hierarchical mergers, and how this effect, combined with relativistic kicks and star cluster evaporation, could dynamically eject the BHs from the cluster.

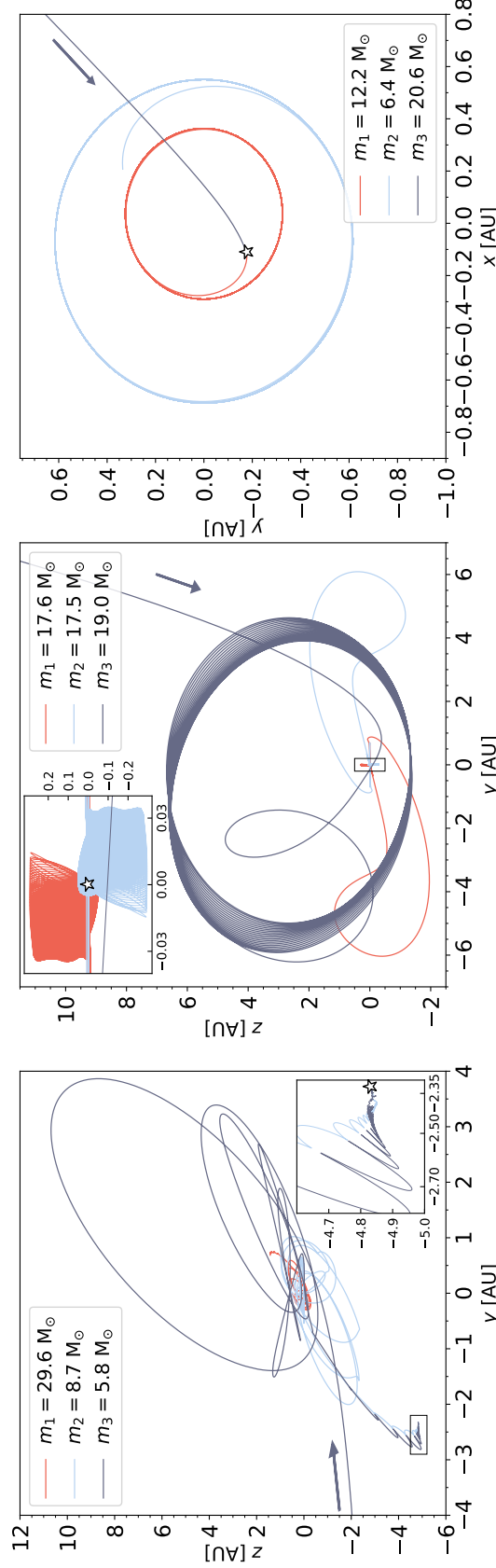


Figure 3.1: Trajectories of three eccentric mergers triggered by a three-body interaction in NSCs (left- and right-hand panels) and GCs (central panel). In the three panels, the systems are centred in the centre-of-mass of the initial BBH, while the position at which the merger takes place is marked with a white star. The trajectories of the primary and secondary BH of the initial BBH (with mass  $m_1$  and  $m_2$ ), and the intruder ( $m_3$ ) are reported in red, blue, and grey, respectively. The incoming direction of the intruder is shown with an arrow. The insets in the left-hand and central panels display a close-up view of the merger region. In the left-hand panel the view is face-on. The initial binary is shown edge-on, while in the right-hand panel the view is face-on. The initial coalescence time of these BBHs, i.e. the coalescence time of the initial binary at the beginning of the interaction, is longer than the Hubble time.

## 3.2 Methods

### 3.2.1 Direct $N$ -Body simulations

Three-body encounters are chaotic processes (Poincaré 1892; Valtonen & Karttunen 2006). Due to this nature, the orbits of the interacting bodies are highly unpredictable, and no general analytical solutions are known to exist. Potentially, even a perturbation of the Planck-scale order applied to the initial conditions can exponentially grow and lead to different final configurations of the system (Samsing & Ilan 2018; Manwadkar et al. 2020; Boekholt et al. 2020, 2021; Portegies Zwart et al. 2021; Parischewsky et al. 2021). Therefore, the most convenient approach to study the three-body problem from the perspective of BBH mergers is to use a numerical integrator over a large set of interactions, and derive the statistical properties of the encounters.

Here, we use the direct  $N$ -body code ARWV to simulate 3 different sets of three-body interactions, for a total of  $2.5 \times 10^5$  simulations between a BBH and a single BH. Each of our three sets of simulations is initialized with different initial conditions, designed to reproduce the properties of three-body encounters that take place inside YSCs, GCs, and NSCs. ARWV is an algorithmic regularization direct  $N$ -body code (Mikkola & Aarseth 1989, 1993; Arca-Sedda & Capuzzo-Dolcetta 2019; Chassonney et al. 2019; Chassonney & Capuzzo-Dolcetta 2021) that solves the equations of motion of the interacting bodies with post-Newtonian corrections up to the 2.5 order (Mikkola & Merritt 2008; Memmesheimer et al. 2004).

We integrate each system with ARWV for a minimum time of  $10^5$  yr. We stop the integration at this time only if at least one merger takes place, or if the three-body encounter is over. If none of these two conditions is satisfied (e.g., the three bodies are still interacting), we carry on the integration with ARWV for a longer time. We stop the simulation if at least one of the two aforementioned conditions is fulfilled, or if the time reaches a maximum of 1 Myr. Figure 3.1 shows three examples of our three-body simulations computed with ARWV.

Most BBH mergers do not take place during the simulation with ARWV. Therefore, we evolve the remaining binary population according to Peters (1964):

$$\begin{aligned} \frac{da}{dt} &= -\frac{64}{5} \frac{G^3 m_i m_j (m_i + m_j)}{c^5 a^3 (1 - e^2)^{7/2}} f_1(e), \\ \frac{de}{dt} &= -\frac{304}{15} e \frac{G^3 m_i m_j (m_i + m_j)}{c^5 a^4 (1 - e^2)^{5/2}} f_2(e), \end{aligned} \quad (3.1)$$

where

$$\begin{aligned} f_1(e) &= \left( 1 + \frac{73}{24} e^2 + \frac{37}{96} e^4 \right) \\ f_2(e) &= \left( 1 + \frac{121}{304} e^2 \right). \end{aligned} \quad (3.2)$$

Here,  $G$  is the gravity constant,  $c$  the speed of light,  $m_i$  the primary mass,  $m_j$  the secondary mass,  $a$  the semi-major axis, and  $e$  the orbital eccentricity. We assume that two BHs merge when their mutual distance is less than the sum of their innermost stable circular orbits for non-spinning BHs, i.e. when  $r \leq 6G(m_i + m_j)/c^2$ . All the binaries that survive after the end of the three-body integration with ARW are long-lived and circularize their orbit through GW emission, unaffected by external perturbations. Hence, we can treat them with the simplified formalism described in Eqs. 3.1, without the need for a more computationally expensive post-Newtonian formalism.

Table 3.1: Initial conditions.

Property	Initial distribution	Interval
$m_1, m_2, m_3$	Population synthesis	$[5, 60] M_\odot$
$a$	Log-normal Distribution	$[\max(a_{\text{ej}}, a_{\text{gw}}), a_{\text{hard}}]$
$e$	Thermal distribution	$[0, 1]$
$f$	Hut & Bahcall (1983)	$[-\pi, \pi]$
$v_\infty$	Maxwellian distribution	—
$b$	Uniform in $b^2$	$[0, b_{\text{max}}]$
$D$	$10^3 a$	—
$\psi$	Uniform	$[0, 2\pi]$
$\theta$	Uniform in $\cos \theta$	$[-1, 1]$
$\phi$	Uniform	$[0, 2\pi]$
$\chi_1, \chi_2, \chi_3$	Maxwellian distribution	$[0, 1]$
$\vec{\chi}_1, \vec{\chi}_2, \vec{\chi}_3$	Isotropic spin orientation	—

Column 1, initial conditions: mass of the primary and secondary BH in the initial binary ( $m_1$  and  $m_2$ ), mass of the single BH ( $m_3$ ), semi-major axis ( $a$ ), orbital eccentricity ( $e$ ), orbital phase of the binary ( $f$ ), initial relative velocity between the single BH and the BBH ( $v_\infty$ ), impact parameter ( $b$ ), initial distance ( $D$ ) of the intruder from the binary centre-of-mass, three directional angles of the interaction ( $\psi$ ,  $\theta$ , and  $\phi$ ), spin magnitude ( $\chi_1$ ,  $\chi_2$ , and  $\chi_3$ ) and direction of the three BHs ( $\vec{\chi}_1$ ,  $\vec{\chi}_2$ , and  $\vec{\chi}_3$ ). Column 2, distribution we used to sample the initial conditions. For the masses, we used the output of the population synthesis code MOBSE (Mapelli et al. 2017; Giacobbo et al. 2018). Column 3, interval we considered for each distribution.

When two BHs merge, we implement the relativistic fitting equations reported in Lousto et al. (2012) to compute the relativistic kick exerted on the BH remnant by the anisotropic GW emission at merger. Furthermore, we compute the mass of the BH remnant and the magnitude of its spin with the fitting equations presented by Jiménez-Forteza et al. (2017).

### 3.2.2 Initial conditions

Simulating a three-body interaction with spinning BHs requires 21 initial parameters for each simulation. Since covering a 21–dimension parameter space with direct  $N$ -body simulations is computationally prohibitive, we initialize three different sets of  $5 \times 10^4$ ,  $10^5$ , and  $10^5$  simulations for YSCs, GCs, and NSCs, respectively. Table 3.1 reports all the initial conditions, the distribution used to generate each of them, and the interval in which the parameters are sampled. We initialized the properties of each encounter with the same procedure as in Dall’Amico et al. (2021), except for the masses, semi-major axis, and initial intruder velocity. Here, we summarize the main features of our initial conditions.

We assume that the initial BH mass distribution does not change if the cluster is young, globular, or nuclear (Mapelli et al. 2021a), and sample the mass of all our single and binary BHs from a catalogue of synthetic BHs generated with the population-synthesis code MOBSE (Mapelli et al. 2017; Giacobbo et al. 2018; Giacobbo & Mapelli 2018b). With this method, our population is composed of first-generation BHs produced by the evolution of binary stars at metallicity  $Z = 0.1 Z_\odot$  with  $Z_\odot = 0.02$ . MOBSE implements up-to-date wind models for massive stars (Vink et al. 2001; Chen et al. 2015), the core-collapse supernova models by Fryer et al. (2012) and the (pulsational) pair-instability supernova treatment presented in Mapelli et al. (2021b). We adopted the rapid core-collapse supernova model by Fryer et al. (2012). With this choice, our BH mass spectrum ranges

between 5 and  $60 M_{\odot}$  BHs.

The semi-major axis  $a$  of the initial binaries is sampled from a log-normal distribution as

$$p(a) = \frac{1}{\sigma_{\log} \sqrt{2\pi}} \exp \left[ -\frac{(\log a - \mu_{\log})^2}{2\sigma_{\log}^2} \right] \quad (3.3)$$

with limits  $[\max(a_{\text{ej}}, a_{\text{gw}}), a_{\text{hard}}]$ , where

$$a_{\text{hard}} = \frac{G m_1 m_2}{m_* \sigma^2}, \quad (3.4)$$

$$a_{\text{ej}} = \frac{\xi m_3^2}{(m_1 + m_2)^3} \frac{G m_1 m_2}{v_{\text{esc}}^2}, \quad (3.5)$$

$$a_{\text{gw}} = \left[ \frac{32 G^2}{5 \pi \xi c^5} \frac{\sigma m_1 m_2 (m_1 + m_2)}{\rho_c (1 - e^2)^{7/2}} f_1(e) \right]^{1/5}. \quad (3.6)$$

Here  $a_{\text{hard}}$  is the limit for a binary to be considered hard (Heggie 1975),  $a_{\text{ej}}$  is the maximum semi-major axis for ejection by three-body encounters, and  $a_{\text{gw}}$  is the limit below which the semi-major axis shrinking by emission of GWs becomes dominant with respect to dynamical hardening. In the above equations,  $m_*$  is the average mass of a star in the cluster,  $\sigma$  the typical 3D velocity dispersion of the cluster,  $v_{\text{esc}} \sim 2\sigma$  the escape velocity,  $\rho_c \simeq 20 \times \rho$  the star cluster core density,  $\rho$  the average star cluster density and  $\xi \sim 3$  a numerically calibrated constant (Hills 1983b; Quinlan 1996). The mean of the log-normal distribution of the semi-major axes is computed as the average of the logarithmic limits assuming  $\rho = 10^{3.3}, 10^{3.3}, 10^5 M_{\odot} \text{pc}^{-3}$ , such that the average results in  $\mu_{\log}(a/\text{AU}) = 2.42, 1.22, 0.42$  for the case of YSCs, GCs, and NSCs, respectively. The dispersion is derived from the simulations of Di Carlo et al. (2019) and Di Carlo et al. (2020a), and set as  $\sigma_{\log}(a/\text{AU}) = 0.92$  in all three samples of simulations, as already done in Dall'Amico et al. (2021). With this prescription, all our BBHs are hard binaries for which GW emission is negligible if compared to hardening, but at the same time their semi-major axis is large enough such that previous interactions did not lead to a dynamical ejection of the binary from the cluster.

We assume that the BHs are in thermal equilibrium with the rest of the cluster core so that the initial velocity at infinity  $v_{\infty}$  of the single BH with respect to the centre-of-mass of the binary can be sampled from a Maxwell-Boltzmann distribution (Heggie 1975). For the three sets of simulations we assume a 3D velocity dispersion of 5, 20, and 50 km s<sup>-1</sup> in the case of YSCs (Portegies Zwart et al. 2010a), GCs (Pryor & Meylan 1993), and NSCs (Neumayer et al. 2020b), respectively.

We set the initial distance of the single BH from the centre-of-mass of the binary as  $D = 10^3 a$ . This guarantees that the BBH has not been perturbed by the intruder before the beginning of the integration.

The impact parameter  $b$  of the interaction is sampled from a uniform probability distribution proportional to  $b^2$  (Hut & Bahcall 1983) in the range  $[0, b_{\text{max}}]$ , with  $b_{\text{max}}$  defined as

$$b_{\text{max}} = \frac{\sqrt{2 G (m_1 + m_2 + m_3) a}}{v_{\infty}}. \quad (3.7)$$

This is the maximum impact parameter for a strong three-body interaction with a hard binary derived by Sigurdsson & Phinney (1993). As  $v_{\infty}$  and  $a$  change between YSCs, GCs, and NSCs, also the impact parameter in these three environments will be different. Equation 3.7 assumes strong gravitational focusing, i.e.  $G (m_1 + m_2 + m_3) / (v_{\infty}^2 b) \gg 1$ , and minimum intruder-binary star distance  $r_p = a$ . In section 3.6, we discuss the impact of this assumption on our results.

LIGO–Virgo observations favour a population of low-spin BHs (Abbott et al. 2021b). Therefore, we extract the magnitude of the dimensionless spin  $\chi$  of each BH from a Maxwell-Boltzmann distribution with root-mean-square  $\sigma_\chi = 0.1$  and truncated to  $\chi = 1$ . Furthermore, we isotropically sample the spin directions accounting for the fact that dynamical encounters randomize them (Rodriguez et al. 2016d).

### 3.3 Results

#### 3.3.1 Outcomes

We divide the outcomes of the interactions into five classes, as a function of the system configuration at 1 Myr since the beginning of the simulation. We classify each simulation as follows.

- **Flyby:** the final binary has the same components as the initial binary. If the encounter hardens it enough, this binary may merge during or after the simulation.
- **Exch13:** the three-body interaction ends with a binary composed of the primary BH of the initial binary and the intruder ( $m_1 - m_3$ ). If this exchanged binary merges during the simulation, we still classify the interaction as an exch13 event.
- **Exch23:** the three-body interaction ends with a binary composed of the secondary BH of the initial binary and the intruder ( $m_2 - m_3$ ). If this exchanged binary merges during the simulation, we still classify the interaction as an exch23 event.
- **Ionization:** the encounter splits the initial binary, resulting in three single BHs.
- **Triple:** the system is still in an unstable triple configuration at the end of the simulation.

The upper panel of Fig. 3.2 classifies the end states of our binary-single scattering experiments. Flybys are the most frequent end state in all three cluster types, followed by exchanges. This result is expected since these encounters generally have a larger impact parameter  $b$  than the semi-major axis of the initial binary  $a$ : if  $b \gg a$  the intruder sees the binary as a point-like object, and the interaction evolves into a flyby.

In YSCs, the number of ionizations is lower with respect to both GCs and NSCs. Vice versa, exchanges are more common in YSCs than in both GCs and NSCs. This happens because the typical dispersion velocities of YSCs are around  $5 \text{ km s}^{-1}$ , much smaller than GCs and NSCs, where the intruder can likely have a velocity higher than the critical velocity required to break-up the binary system (Hut & Bahcall 1983). At 1 Myr, unstable triples are much more numerous in YSCs than in GCs, while we find no triple systems in NSCs at the end of our simulations. In YSCs the encounter takes place later than in more dense clusters since the inter-particle distance is much larger while the dispersion velocity is lower. The intruder takes more time to reach the binary and the interaction begins at later times in the simulation, resulting in several systems that at 1 Myr are still in an unstable triple configuration.

#### 3.3.2 BBH mergers

We find that 0.1%, 2.4%, and 11.8% of the simulations produce BBHs that merge within a Hubble time (13.8 Gyr) in YSCs, GCs, and NSCs, respectively. Of these mergers, 14.8%, 4.6%, and 4% take place in the first Myr of integration with ARWV. These results, which are also reported in

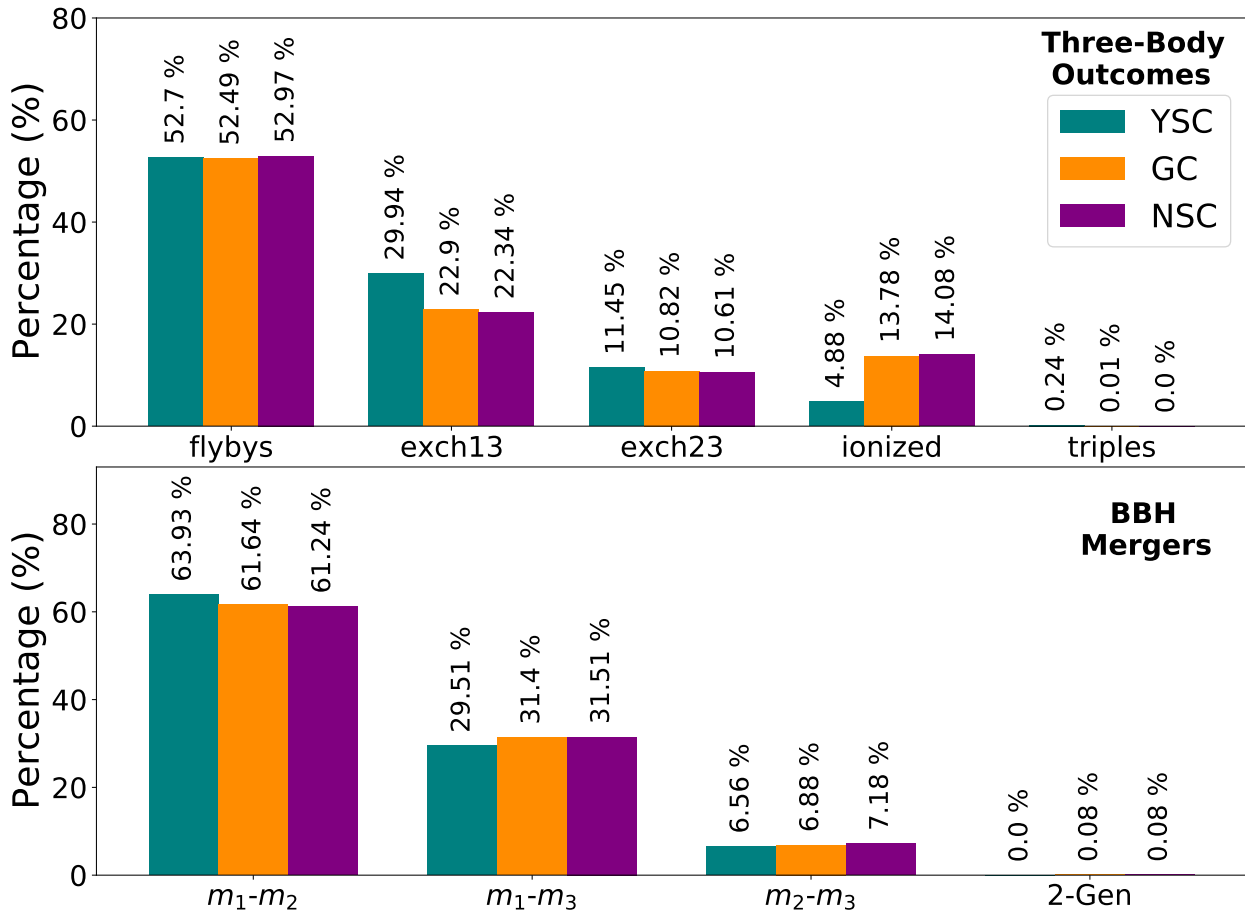


Figure 3.2: Upper panel: percentage of different interaction outcomes for each cluster type. From left to right: (i) flyby events, (ii) exchanges in which the intruder replaces the secondary BH, (iii) exchanges in which the intruder replaces the primary BH, (iv) ionizations, and (v) unstable triples. Lower panel: Percentage of BBH mergers. From left to right: (i) BBH mergers occurring after a flyby, (ii) an exchange interaction with the secondary BH replaced by the intruder, (iii) an exchange with the primary BH replaced by the intruder, and (iv) second-generation BBH mergers. In both the upper and lower panel, the colours mark the cluster type in which the interaction takes place.

Table 3.2: Percentage of peculiar events in YSCs, GCs, and NSCs.

Event	P <sup>YSC</sup> (%)	P <sup>GCs</sup> (%)	P <sup>NSC</sup> (%)
Merger	0.1	2.4	11.8
Merger $t_{\text{coal}} < 1 \text{ Myr}$	14.8	4.6	4.0
PIBH	44.3	33.3	27.7
IMBH	1.6	0.7	0.4
Merger with $e_{10 \text{ Hz}} > 0.1$	0.08	1	0.6
Retained BH remnants	0	3.1	19.9

Line 1: percentage of BBH mergers over all the three-body simulations. Line 2: percentage of BBH mergers that take place during the three-body simulation with ARWV over all the BBH mergers. Line 3: percentage of pair-instability BHs produced by the merger. Line 4: percentage of intermediate-mass BHs (IMBHs) produced by the merger. Line 5: percentage of BBH mergers with eccentricity at a GW frequency of 10 Hz  $e_{10 \text{ Hz}} > 0.1$  with respect to all BBH mergers. Line 6: percentage of BHs produced by BBH mergers that happen before star cluster evaporation and are retained inside the cluster after the three-body interaction and the GW recoil.

Table 3.2, imply that the more massive and denser the cluster is, the larger the fraction of mergers produced via three-body interactions. This happens because the minimum binding energy of a hard binary is higher in more massive clusters. As a result, BBHs in NSCs are consistently closer to the GW regime than in YSCs, making it more likely for a single interaction to push them into the GW emission regime. The lower panel of Fig. 3.2 classifies these mergers by their formation channel: flyby, exch13, or exch23, and second-generation mergers (i.e. mergers that occur between the remnant of a previous merger and the third BH). The barplot shows that flybys count for  $\sim 53\%$  of all our encounters, but they are  $\sim 61 - 64\%$  of the BBH mergers. Hence, flybys are more efficient in inducing mergers than, for example, exch23 events, which in turn are  $\sim 11\%$  of the outcomes but account only for  $\sim 7\%$  of the mergers. This happens because exchanges usually produce new BBHs with a larger total mass but also with a larger semi-major axis than BBHs involved in flyby events.

For some systems that produce a BBH merger, we find that the initial binary would have merged within a Hubble time even without the interaction. These are binaries that, if evolved as an unperurbed binary, would have produced a BBH merger without undergoing any three-body encounter. These systems are 1.6%, 11.4%, and 45.0% of the BBH mergers in YSCs, GCs, and NSCs respectively. Even for these systems, the interaction has efficiently sped up the merger. This can be seen in Fig. 3.3, which shows the coalescence time of the unperturbed binaries (if the three-body interaction would not have taken place), and the coalescence time resulting from the three-body simulation. For example, none of all the BBH mergers that take place during the simulation with ARWV within the first 1 Myr were meant to merge in less than 1 Myr if left unperurbed.

Finally, in a few cases, we find the formation of second-generation BBH mergers. In these simulations, two BHs merge during the three-body interaction, and their remnant forms a new BBH with the remaining BH, which in turn is able to reach coalescence in less than a Hubble time. We find the same percentage of second-generation mergers in GCs and NSCs, while no second-generation systems form in YSCs via three-body interactions (Fig. 3.2).

Despite the three simulation sets being initialized with the same BH mass spectrum, the total mass of the BBH mergers produced in YSCs, GCs, and NSCs differ, as shown by Fig. 3.4. This difference in the mass of BBH mergers is clearly an effect of the environment.

Mergers by dynamical exchange are slightly favoured in GCs and NSCs with respect to YSCs (Fig. 3.2). Since exchanges typically take place when the intruder is more massive than at least

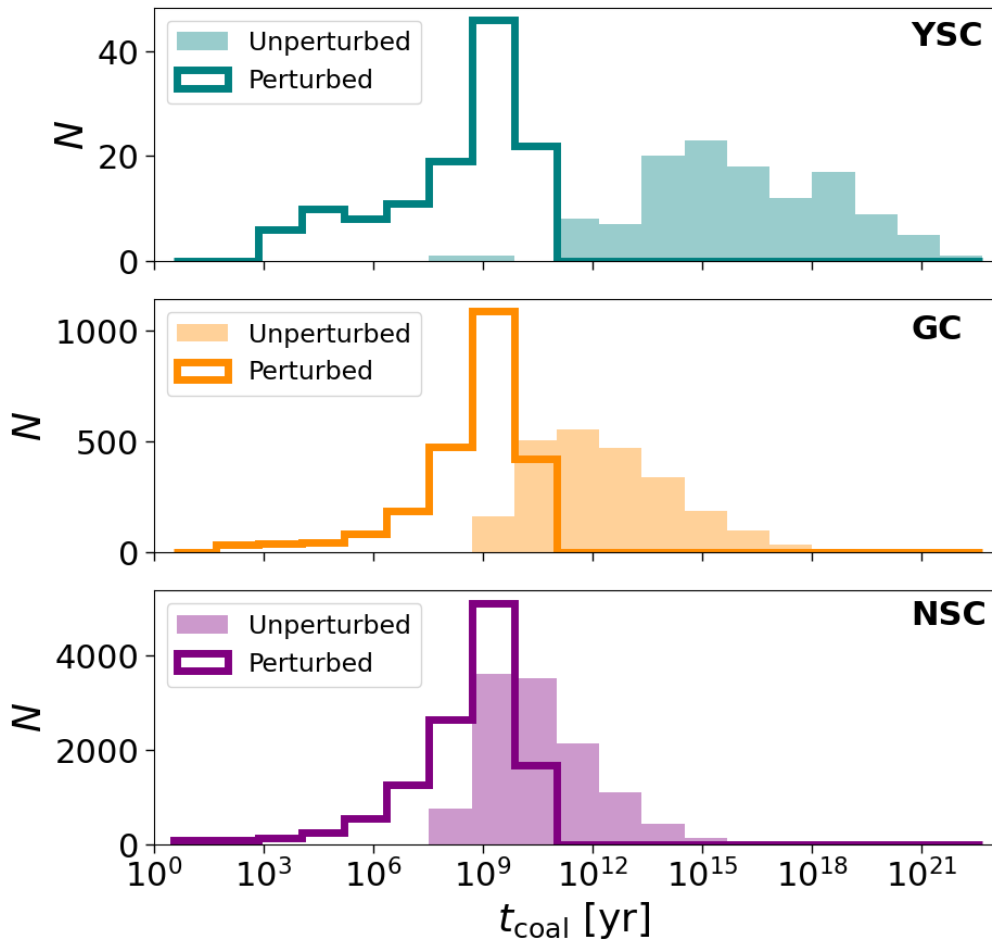


Figure 3.3: Distribution of coalescence times for unperturbed initial binaries (filled histograms), and for the same initial binaries perturbed by the three-body interaction (unfilled histograms). The upper, central, and lower panel show the case of YSCs, GCs, and NSCs, respectively.

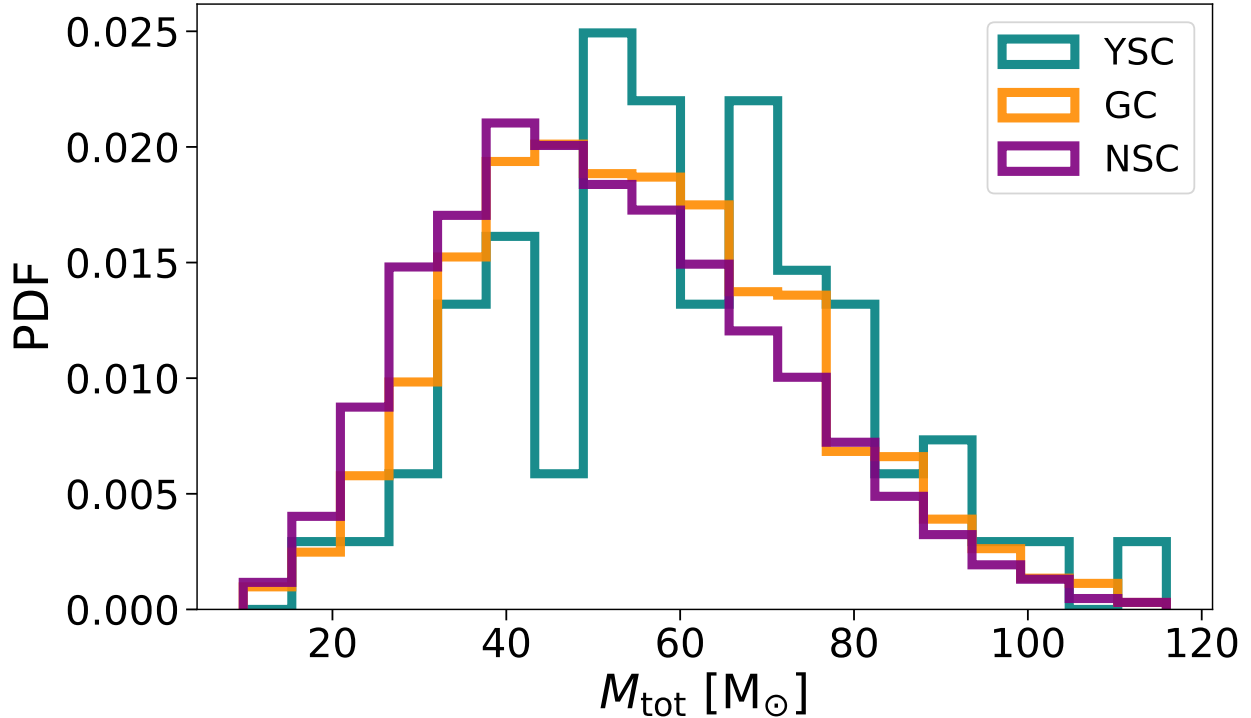


Figure 3.4: Total mass of the BBH mergers in YSCs (blue), GCs (orange), and NSCs (purple).

one of the two binary components, we should expect more massive BBH mergers in GCs and NSCs. Nevertheless, Fig. 3.4 shows that YSCs are more likely to produce massive mergers via three-body encounters than the other two sets of simulations. This happens because in YSCs only the most massive systems are able to merge within a Hubble time. In GCs and NSCs, given the larger velocity dispersions, the hard-soft boundary is shifted towards lower semi-major axis (see eq. 3.4). Therefore, GW emission can be efficient also for relatively low-mass BBHs (eq. 3.1). In YSCs, instead, given the larger semi-major axis at formation, mergers are more biased towards the most massive BBHs. In this way, NSCs and GCs are more efficient in the production of BBH mergers with low-mass components than YSCs. This is further confirmed if we look at the percentage of massive BH remnants produced by these mergers in Table 3.2: pair-instability BHs, defined as BHs with mass in the range  $60 - 100 M_{\odot}$ , are 44.3%, 33.3%, and 27.7% over all the mergers produced in YSCs, GCs, and NSCs, respectively. Intermediate-mass BHs (IMBHs, i.e. BHs with mass  $\geq 10^2 M_{\odot}$ ) are 1.6%, 0.7%, and 0.4% over all the mergers in YSCs, GCs, and NSCs, respectively. The most massive remnant produced by a merger is  $\sim 110 M_{\odot}$  in all three sets. In YSCs and GCs, the most massive remnants are produced by a flyby event, while in the NSC case the most massive remnant is produced by the merger of a second-generation BBH.

Pair-instability BHs and IMBHs form mainly via flybys, because these are the most frequent type of interaction among our simulations. Exch13 are the most likely events to create a BBH more massive than the initial binary. On the other hand, exch23 tend to produce less massive binaries than the initial ones. Nevertheless, the latter have a minor impact on the total mass distribution in Fig. 3.4, because they are rare events, representing only  $\approx 7\%$  of all mergers (Fig. 3.2). Finally, mergers of second-generation binaries are rare even among pair-instability BHs and IMBHs: they represent 0.25% and 0% of pair-instability BHs and IMBHs in GCs, 0.12% and 4% in NSCs.

### 3.3.3 Eccentric mergers

Figure 3.5 shows the eccentricity of the BBH when the emitted GW frequency is 10 Hz in the source frame (hereafter,  $e_{10\text{Hz}}$ ) as a function of the coalescence time from the beginning of the simulation. All three sets present two distinct families of mergers regarding their eccentricity. In the first one, and also the most common one, the mergers follow the relation  $t_{\text{coal}}(e)$  of eq. 3.1, such that  $e_{10\text{Hz}}$  decreases as the coalescence time of the binary increases. In these systems, the dynamical encounter ends before the merger takes place. This allows the BBH resulting from the interaction to evolve unperturbed up to the merger, such that the eccentricity evolution is ruled only by the angular momentum loss by GW emission<sup>2</sup>.

The second family of mergers is composed by systems that do not follow the relation of eq. 3.1, but rather reach the merger with  $e_{10\text{Hz}} > 10^{-3}$  in a relatively short time during the simulation with ARWV, while the dynamical interaction is still ongoing. Some of these systems even have  $e_{10\text{Hz}} > 0.1$  (insets of Fig. 3.5). In the following, we refer to the mergers with  $e_{10\text{Hz}} > 0.1$  simply as eccentric mergers. These are 0.08%, 1%, and 0.6% of all the mergers in YSCs, GCs, and NSCs, respectively (Table 3.2). The low number of eccentric mergers in YSCs might be an effect of limited statistics if compared to the other two sets of simulations. Nevertheless, the only two eccentric mergers occurring in YSCs both have  $e_{10\text{Hz}} \sim 0.1$ , while eccentric events in GCs and NSCs span eccentricities up to and beyond  $e_{10\text{Hz}} = 0.9$ . We can divide these eccentric mergers as a function of the type of interaction that triggered the coalescence:

- **Chaotic mergers** are the product of three-body interactions in which temporary binaries with brand-new orbital parameters are continuously formed and destroyed. If the eccentricity of these temporary binaries are sufficiently high, and their lifetime is longer than the perturbation timescale of the outer body, a nearly radial merger can be triggered. These are the most common interactions to produce eccentric mergers, accounting for  $\sim 63\%$  of all the eccentric events with  $e_{10\text{Hz}} > 0.1$  in GCs and NSCs. The left-hand panel of Fig. 3.1 shows one of these interactions and the subsequent eccentric merger.
- **Prompt mergers** are the second most common event to cause eccentric mergers, representing  $\sim 31\%$  of all these events in GCs and NSCs. The right-hand panel of Fig. 3.1 shows an example of an eccentric merger that follows a prompt interaction. These mergers typically follow flyby events in which the intruder significantly extracts angular momentum from the binary, driving the two components to a nearly radial orbit and inducing a prompt merger. This is for example the case of the two eccentric mergers in the YSC set. We call prompt mergers also simulations in which the intruder tangentially intersects the orbital plane of the binary and approaches one of the two components with almost anti-parallel velocity, such that they rapidly merge with a nearly head-on collision (as the simulation in the right-hand panel of Fig. 3.1). This is the case of the most eccentric mergers in our simulations. In NSCs, five head-on collisions trigger a merger with  $e_{10\text{Hz}} \sim 1$  (right-hand panel of Fig. 3.5), while in GCs the maximum value of  $e_{10\text{Hz}}$  is 0.87 (central panel Fig. 3.5).
- **Temporary triple mergers** take place when the system evolves as a hierarchical triple. Stable triple systems cannot form from three isolated unbound bodies (Naoz 2016), however temporary stable hierarchical triples can be created via three-body interactions. In this configuration, the intruder sets in an outer orbit, perturbing the initial binary and causing it to

<sup>2</sup>After 1 Myr all the mergers are forced to follow eq. 3.1, since we assumed no further dynamical interactions after the first encounter. This choice is discussed more in detail in Section 3.4.2.

merge rapidly enough that GW emission does not efficiently circularize the binary's orbit. This is the case for the system shown in the central panel of Fig. 3.1. The merger occurs only if the system remains stable for a sufficient period of time for the perturbations to be effective. Due to the low stability of these systems, temporary triple mergers are responsible only of  $\sim 6\%$  of the eccentric mergers in GCs and NSCs.

Even if flybys are the most common formation path of BBH mergers in our simulations (lower panel of Fig. 3.2), eccentric mergers come almost in the same proportion from flybys and exchanges in both GCs and NSCs. On the other hand, no second-generation BBH mergers belong to eccentric mergers. With our assumption of no further dynamical interactions beyond 1 Myr, second-generation binaries, after their formation, circularize their orbits before reaching coalescence. On the other hand, all the mergers that give birth to one of the two BHs that compose second-generation binaries are eccentric mergers. We refer to these systems as BBH progenitors of second-generation mergers. In the GC scenario, the progenitor systems of the two second-generation BBHs are both eccentric mergers with an eccentricity of 0.82 and 0.67, respectively, with the first being an almost head-on collision in a prompt event, and the latter coming from a chaotic merger. This is also true for the NSC case, where all the nine progenitors have  $e_{10\text{ Hz}} > 0.1$ , four of which merge in a head-on collision with  $e_{10\text{ Hz}} \sim 1$ .

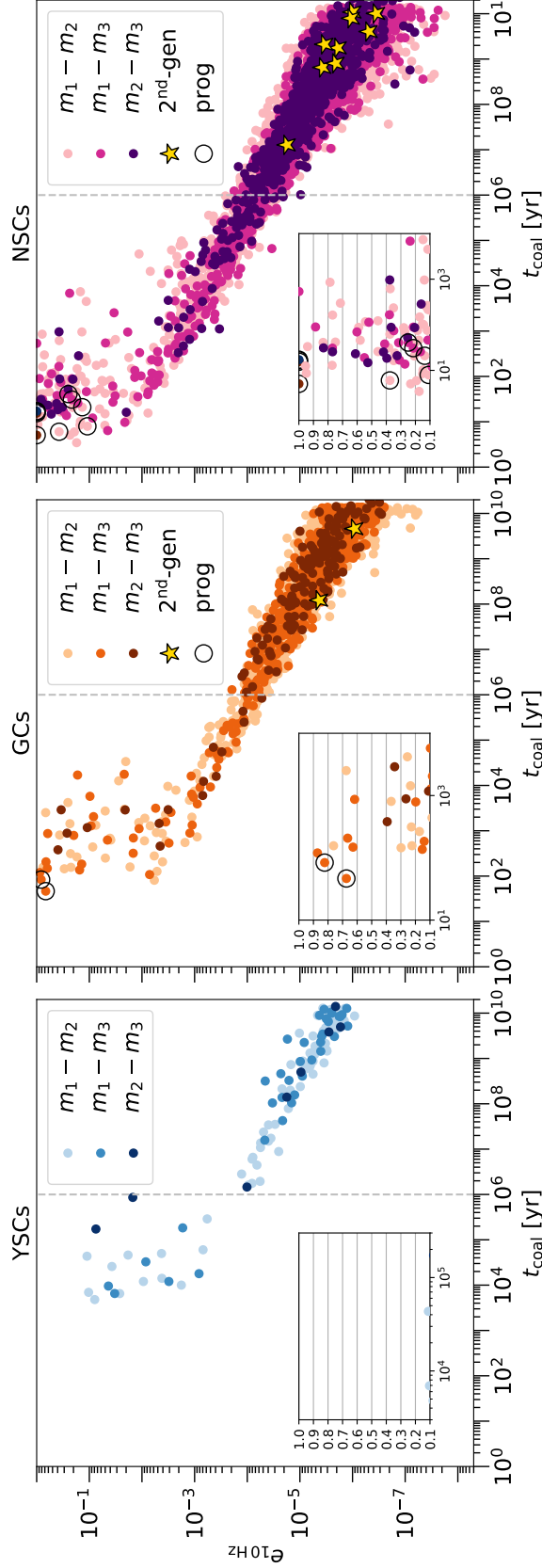


Figure 3.5: Orbital eccentricity at 10 Hz ( $e_{10\text{Hz}}$ ) as a function of the coalescence time ( $t_{\text{coal}}$ ) of BBH mergers in YSCs (left), GCSs (centre), and NSCs (right). Different colours indicate mergers through flybys and the two families of exchanges. The yellow stars show second-generation BBH mergers. The black empty dots highlight the BBH progenitors of second-generation mergers. The dashed vertical line divides the plot into two regions: up to 1 Myr we evolve the systems with ARWV, above 1 Myr all the dynamical interactions are concluded, and we stop the ARWV integration and evolve the remaining BBHs with Eqs. 3.1. The three insets show a zoom for mergers with  $e_{10\text{Hz}} > 0.1$ . Note that some of the points at  $e_{10\text{Hz}} \sim 1$  overlap.

### 3.3.4 Dynamical ejections

Our BBHs can escape from the cluster as a consequence of dynamical recoil. Three-body interactions with hard binaries tend to reduce the binary internal energy and convert it into kinetic energy of the system. This induces a recoil velocity  $v_{\text{rec}}$  both on the binary and the single object. If this velocity is larger than the escape velocity  $v_{\text{esc}}$  of the cluster, both the binary and the single object are dynamically ejected from the cluster (Heggie 1975; Hills 1975; Sigurdsson & Phinney 1993).

This has major implications for BBH mergers: on the one hand, the energy exchange speeds the merger up reducing the semi-major axis and thus the coalescence time  $t_{\text{coal}}$ ; on the other hand, it might also kick out the binary from the cluster preventing further encounters. If the ejection happens before the binary merges, the BH remnant produced by the coalescence will not be able to dynamically interact with other bodies of the cluster, and produce new binaries. This may strongly affect the efficiency of the hierarchical merger mechanism, by which repeated BH mergers produce massive BHs (e.g., Miller & Hamilton 2002; Mapelli et al. 2021a). Figure 3.6 shows the impact of these dynamical ejections on BBH mergers. Here, we assume that all the mergers that take place during the three-body encounter merge inside the cluster. Therefore, the plots report only the BBH mergers that take place after  $10^5$  yr and for which the three-body interaction is concluded. These recoil velocities span from less than  $1 \text{ km s}^{-1}$  up to  $\sim 40 \text{ km s}^{-1}$  in YSCs,  $\sim 200 \text{ km s}^{-1}$  in GCs and  $\sim 400 \text{ km s}^{-1}$  in NSCs. These differences are, once again, explained by the large binding energy of the binaries in GCs and NSCs, which translate in larger recoil kicks. In YSCs, for example, the BBHs have a larger semi-major axis than binaries in more dense clusters and the recoil velocities are lower.

In the three simulation sets, the most likely population of ejected mergers is the one produced by exch23 events. The marginal plots of Fig. 3.6 and Table 3.3 show that these BBHs generally have larger recoil velocities with respect to the other two families of mergers. The fraction of BBH mergers ejected after the three-body interaction is 6% in NSCs, 18% in GCs and 18% in YSCs. In YSCs, we must also keep into account the evaporation of the cluster, i.e. when the cluster dissolves because of stellar mass loss and tidal stripping (Spitzer 1987; Heggie & Hut 2003; Binney & Tremaine 2008). Due to evaporation, most of the BBH mergers in YSCs happen in the field even without being dynamically ejected (e.g., Rastello et al. 2021b; Torniamenti et al. 2022). If we assume a typical evaporation time  $t_{\text{evap}} \sim 1 \text{ Gyr}$  for a YSC<sup>3</sup> (Torniamenti et al. 2022), 48% of the BBH mergers happen inside the cluster, 5% take place in the field because of dynamical recoil, while the remaining 47% occur in the field because of cluster evaporation. Finally, all the eccentric mergers in GCs and NSCs merge inside the cluster. They are mostly the product of chaotic interactions that take place over a short timescale and rapidly lead to the merger of two of the three BHs.

GWs emitted from a spiraling BBH are generally irradiated anisotropically due to the asymmetry of the system. This induces linear momentum transfer on the remnant BH produced by the merger, which translates into a relativistic kick that might accelerate the remnant even up to a few thousand of  $\text{km s}^{-1}$  (Fitchett 1983; Maggiore 2018). Figure 3.7 shows this relativistic kick produced by all the BBH mergers in our three sets of simulations. All three distributions peak at  $\sim 200 \text{ km s}^{-1}$ , with velocities that are approximately one order of magnitude higher than the ones reported in Fig. 3.6. Hence, GW recoils are more efficient in ejecting BHs from their parent cluster than three-body recoils. Due to GW kicks, only 3.6% and 21.2% of the BH remnants are retained in GCs and NSCs, respectively. This fraction drops to 0 in YSCs.

---

<sup>3</sup>This evaporation timescale refers to YSCs with mass  $\sim 10^4 M_\odot$  and must be considered as an upper limit. Processes like galactic perturbations and encounters with giant molecular clouds might, in principle, accelerate the disruption of the cluster (e.g., Gieles et al. 2006).

Table 3.3: Three-body recoil velocities.

Cluster	$v_{\text{rec}}^{m_1-m_2}$ [km s $^{-1}$ ]	$v_{\text{rec}}^{m_1-m_3}$ [km s $^{-1}$ ]	$v_{\text{rec}}^{m_2-m_3}$ [km s $^{-1}$ ]
YSC	7	4	15
GC	18	18	26
NSC	33	34	55

Median recoil kicks of three-body interactions for the YSC, GC, and NSC cases. The values are referred to the distributions of the marginal plots in Fig. 3.6, and are reported for the three different types of BH couples that merge after a three-body encounter.

We can now count the overall fraction of BH remnants retained by the cluster for which 1) the relativistic recoil is below the escape velocity of the cluster, 2) the BBH progenitor is not ejected after a three-body interaction, and 3) the binary is able to merge inside the cluster before its evaporation. This fraction is 0% for YSCs, 3.1% for GCs, and 19.9% for NSCs (Table 3.2). Finally, all the second-generation BH remnants in GCs and NSCs are kicked out of the cluster due to GW recoils.

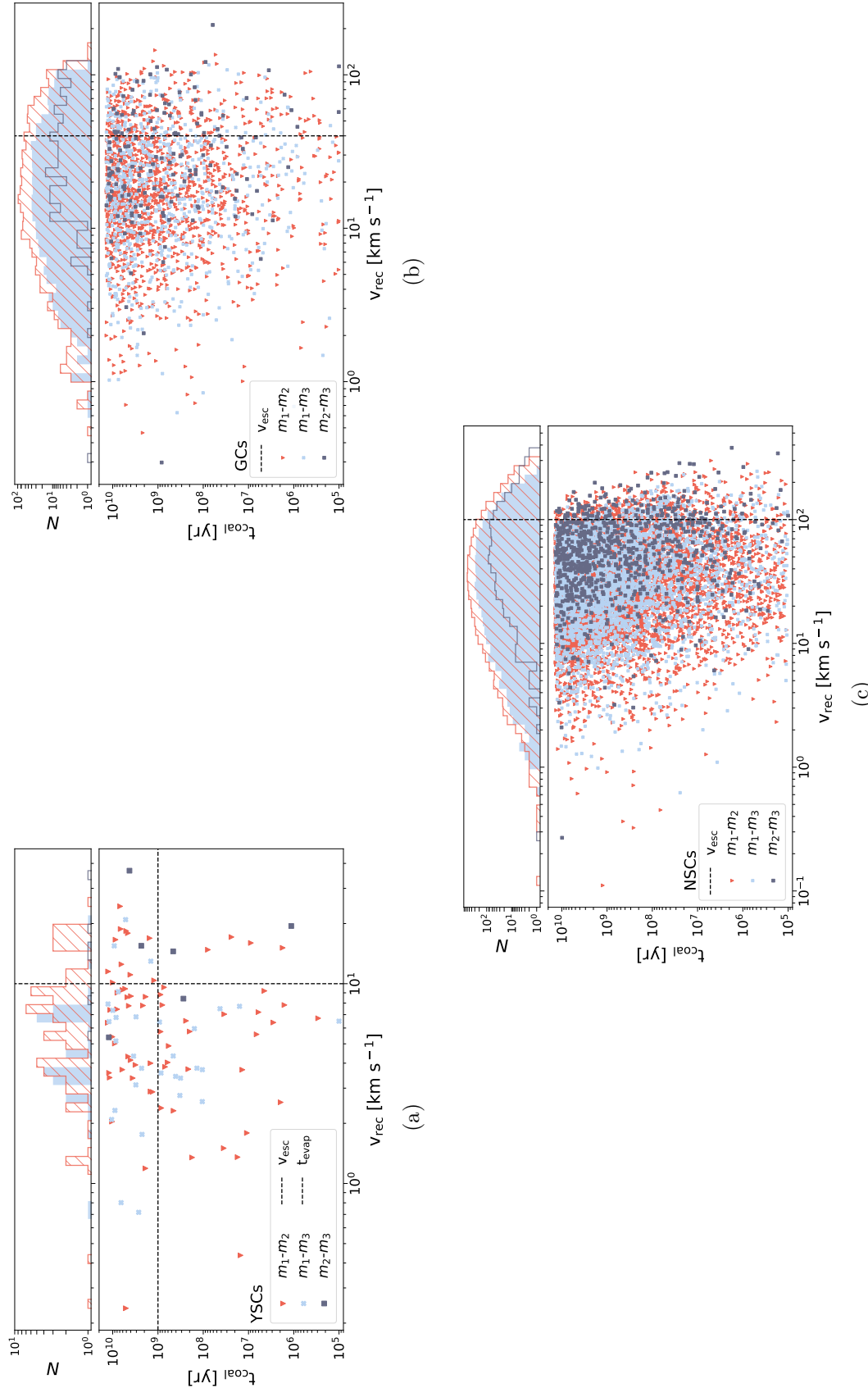


Figure 3.6: The upper-left, upper-right, and lower scatter plots display the BBH mergers that take place after the three-body interactions respectively in the YSCs, GCs, and NSCs. All the mergers that take place during the three-body interaction, i.e.  $< 10^6 \text{ yr}$ , are assumed to merge inside the cluster. The x-axis reports the recoil velocity caused by the energy exchange in the three-body encounter. The y-axis shows the coalescence time of the binary from the beginning of the simulation. Different outcomes are shown with different markers and colours. In the YSCs case, the horizontal dashed line reports the typical evaporation time of a YSC. The vertical dashed line in all the plots shows the escape velocity of the cluster. Distributions of the recoil velocities are displayed as marginal histograms. The colour legend is the same as the scatter plot.

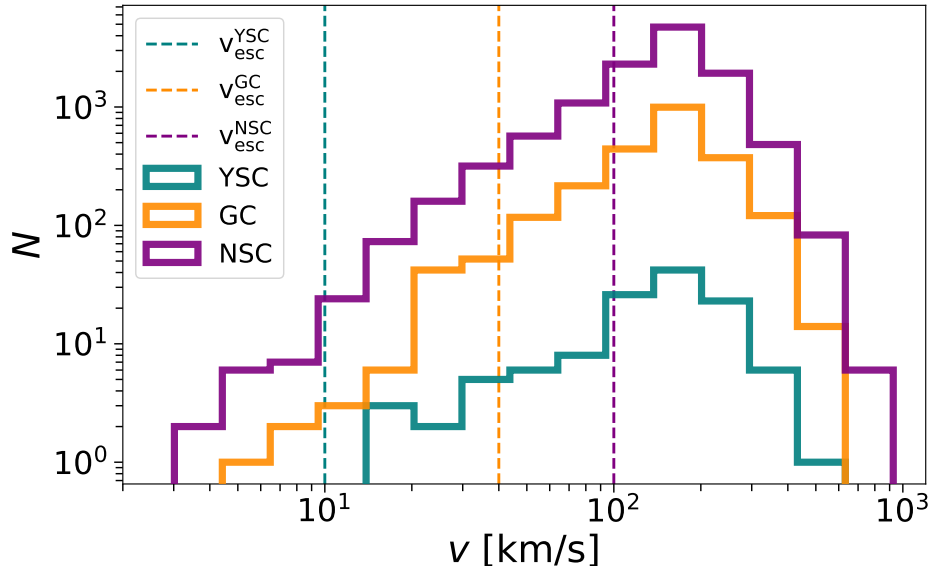


Figure 3.7: Distribution of the relativistic recoil kick of the remnants produced by the BBH mergers in YSCs, GCs, and NSCs. The dashed vertical lines represent the escape velocities of the three types of star clusters.

### 3.3.5 Orbital plane tilt

Figure 3.8 shows the tilt angle  $i$ , defined as the angle between the orbital plane of the initial binary and the orbital plane of the final binary left after the three-body interaction. These distributions show that three-body interactions are capable of inducing large tilt angles on the BBH population, in good agreement with what was found by Trani et al. 2021 (see also Banerjee et al. 2023). The magnitude of the tilt depends on the outcome of the interaction. Binaries that underwent a flyby generally experience smaller tilt angles with respect to exchanges, with the distribution that peaks at  $\sim 15^\circ$  for the former, and  $\sim 90^\circ$  for the latter. Since there is no strong correlation between the initial angle  $\theta$  (sec. 3.2.2) of the interaction and the outcome, the distributions of Fig. 3.8 are a direct product of the interactions. This means that flybys statistically induce small perturbations on the orbital plane of the initial binary if compared to exchanges. Exchanges, on the other hand, favour the production of new-born, more massive binaries with an orbital plane likely tilted with respect to the original one. This implies that the orientation of spins in dynamically-assembled BBHs might not be perfectly isotropic. Our finding is consistent with Bouffanais et al. (2019), who assume isotropic spin orientation for exchanges, but nearly aligned spins for flybys, which are less perturbed by the encounter.

## 3.4 Discussion and caveats

### 3.4.1 Merger rate density of eccentric mergers

In Section 3.3.3, we derived the fraction of eccentric mergers in YSCs, GCs, and NSCs, i.e. that have  $e_{10\text{ Hz}} > 0.1$ . Through semi-analytical simulations, Mapelli et al. (2022) were able to derive the merger rate density of BBH mergers in YSCs, GCs, and NSCs. They find  $\mathcal{R}_{\text{YSC}} = 3.0 \text{ Gpc}^{-3} \text{ yr}^{-1}$ ,  $\mathcal{R}_{\text{GC}} = 4.4 \text{ Gpc}^{-3} \text{ yr}^{-1}$ , and  $\mathcal{R}_{\text{NSC}} = 1.3 \text{ Gpc}^{-3} \text{ yr}^{-1}$  in their fiducial model. These rates refer to

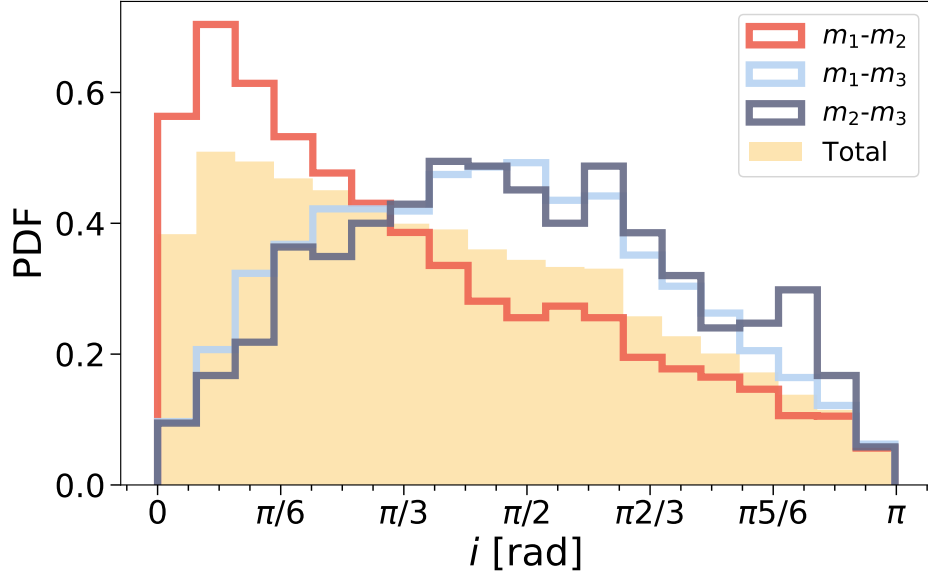


Figure 3.8: Tilt angle distributions of the BBH orbital plane in NSCs at the end of the simulation with respect to the initial binary orbital plane. Unfilled histograms are flybys (red), exch13 (blue), and exch23 (grey). The filled histogram (yellow) shows the total distribution. We do not show GCs and YSCs, because they have exactly the same behaviour.

first-generation BBH mergers. Since our first-generation BHs are drawn from the same population as Mapelli et al. (2022), we combine these rates with the fraction of eccentric mergers produced by three-body interactions in our three simulation sets. In this way, we find the following rates of eccentric mergers as a function of the type of cluster:  $\sim 2 \times 10^{-3} \text{ Gpc}^{-3} \text{ yr}^{-1}$  in YSCs,  $\sim 4 \times 10^{-2} \text{ Gpc}^{-3} \text{ yr}^{-1}$  in GCs and  $\sim 8 \times 10^{-3} \text{ Gpc}^{-3} \text{ yr}^{-1}$  in NSCs. These rates represent a rough estimate, since a more realistic evaluation requires taking into account the possible differences between the coalescence times of our eccentric mergers and the BBH merger population of Mapelli et al. (2022).

### 3.4.2 Single vs multiple three-body interactions

Our eccentric mergers (Fig. 3.5) qualitatively match the properties of eccentric mergers simulated by Samsing & Ramirez-Ruiz (2017) and Zevin et al. (2019). For example, Samsing & Ramirez-Ruiz (2017) and Samsing et al. (2018b) find that  $\sim 1\%$  of all the mergers by binary-single encounters in GCs are eccentric mergers, which is in excellent agreement with the fraction of eccentric events we find in this work. On the other hand, Samsing (2018) and Rodriguez et al. (2018) find a fraction of eccentric mergers  $\sim 5$  times higher than the one we find in our simulations. This difference is a consequence of our choice to simulate one single interaction for each binary.

Assuming a single dynamical encounter per binary is particularly well motivated in YSCs, since three-body interactions between BHs are expected to happen with a frequency of  $\sim 1$  per cluster (Di Carlo et al. 2019). In more dense clusters, it is more likely for a BBH to experience multiple interactions along its lifetime. However, as we presented in Section 3.3.3 and in Fig. 3.5, all the eccentric mergers take place while the dynamical interaction is still ongoing, meaning that in our simulations the typical timescale for an eccentric three-body merger is smaller compared to the timescale of a three-body interaction. Our results imply that even one single three-body encounter

in a BBH lifetime is sufficient to speed up the merger and to produce an eccentric event in the LIGO–Virgo band. Nevertheless, the masses, eccentricities, and fraction of ejected BHs reported in this work must be interpreted as lower limits since further interactions might produce more massive and eccentric mergers and more dynamical ejections. This is especially true for all the mergers that take place after 1 Myr in our simulations. The effects of multiple three-body interactions on the BBH population are going to be presented in a future paper.

Finally, our work does not consider the special case of an AGN disc. In AGN discs, eccentric mergers can be significantly boosted if binary-single scatters occur with small mutual inclinations (less than a few degrees). This ultimately leads to a relatively flat distribution of the spin-tilt angle in eccentric mergers (Samsing et al. 2022), which is very different from the one we find here for NSCs. The reason for this difference is that three-body interactions in star clusters require completely distinct initial conditions with respect to the AGN case. We will include AGN discs in forthcoming studies.

### 3.5 Summary

In this work, we have presented the results of  $2.5 \times 10^5$  three-body simulations performed via direct  $N$ -body integration with the ARWV code (Mikkola &Aarseth 1989; Chassonney et al. 2019). Our simulations incorporate post-Newtonian corrections up to the 2.5th order and adopt initial conditions that mimic the properties of young star clusters (YSCs), globular clusters (GCs), and nuclear star clusters (NSCs). With this approach, we aim to investigate the influence of the host environment on: 1) the outcomes of three-body encounters, 2) the populations of binary black hole (BBH) mergers produced through interactions, and 3) the production of BBH mergers with non-negligible eccentricities in the LIGO–Virgo frequency range. Our results can be summarized as follows.

- We divide the outcomes in flybys, exchanges in which the primary or the secondary BH component is replaced by the intruder, ionizations, and triples. Flybys dominate the interactions in all the simulation sets, accounting for approximately  $\sim 53\%$  of all the outcomes. YSCs differ from GCs and NSCs, with fewer ionizations (around  $\sim 5\%$  compared to  $\sim 14\%$  for GCs and NSCs) but more exchanges (about  $\sim 41\%$  compared to  $\sim 33\%$  for GCs and NSCs), and also a non-zero number of systems that are in an unstable triple configuration at the end of the simulation.
- Three-body interactions in GCs and NSCs produce a higher number of mergers compared to YSCs. Approximately 2.4% and 11.8% of the simulations in GCs and NSCs, respectively, lead to a BBH merger within a Hubble time, compared to the 0.1% of the simulations in YSCs. Flybys are the most effective pathway to produce mergers as they significantly decrease the coalescence time. Of the three types of clusters we considered, YSCs are less efficient in producing low-mass BBH mergers than both GCs and NSCs.
- Pair-instability BH remnants ( $60 - 100 M_\odot$ ) are  $\sim 44\%$ ,  $\sim 33\%$ , and  $\sim 28\%$  over all the mergers produced in YSCs, GCs, and NSCs, while IMBHs ( $> 100 M_\odot$ ) are 1.6%, 0.7%, and 0.4%, respectively. Finally, we find second-generation BBH mergers only in GCs and NSCs, accounting for 0.08% of all mergers in both sets.
- The percentage of BBH mergers with an orbital eccentricity higher than 0.1 at a GW frequency of 10 Hz in the source frame ( $e_{10\text{Hz}} > 0.1$ ) is 0.08% in YSCs, 1% in GCs and 0.6% in NSCs. In both GCs and NSCs, the most frequent interactions leading to eccentric mergers are chaotic

exchange events, accounting for approximately 63% of all eccentric mergers. These involve the creation and destruction of several temporary binaries before the merger takes place. Prompt interactions, including flybys in which the intruder extracts enough angular momentum from the binary to cause a radial merger, and head-on collisions between the intruder and one of the binary components, account for approximately 31% of eccentric events. Finally, BBH mergers in temporary stable hierarchical triples contribute to approximately 6% of all eccentric mergers in GCs and NSCs. In our simulations, all the progenitors of second-generation BBHs are eccentric mergers in both GCs and NSCs.

- The percentage of remnant BHs that are not expelled from the cluster is 0% for YSCs, 3.1% for GCs, and 19.9% for NSCs. These are BHs that are not dynamically ejected from the cluster by the three-body and GW relativistic recoil kicks, and for which the progenitor BBHs merge before the evaporation of the star cluster. In YSCs,  $\sim 50\%$  of the BBH mergers take place in the field after the cluster has evaporated. Relativistic recoil kicks due to anisotropic GW emission are the primary cause of dynamical ejections, with typical velocities that exceed  $100 \text{ km s}^{-1}$ . This strongly affects hierarchical mergers.
- Three-body interactions alter the inclination of the original orbital plane, causing tilt angles that are not isotropically distributed, but rather depend on the interaction outcome. Exchanges tend to produce new binary systems that have an isotropically-oriented orbital plane with respect to the original one, while flybys usually result in relatively minor perturbations of  $\sim 15^\circ$  on the orbital plane. This result challenges the idea that dynamics produces perfectly isotropic spin orientations.
- We estimate the merger rate density of eccentric BBH mergers to be  $\sim 2 \times 10^{-3} \text{ Gpc}^{-3} \text{ yr}^{-1}$  for YSCs,  $\sim 4 \times 10^{-2} \text{ Gpc}^{-3} \text{ yr}^{-1}$  for GCs and  $\sim 8 \times 10^{-3} \text{ Gpc}^{-3} \text{ yr}^{-1}$  for NSCs. These rates must be regarded as lower limits, as we only considered a single three-body interaction per binary in our simulations. Additional dynamical interactions during the lifetime of these binaries may lead to an increase in the number of eccentric mergers.

## Acknowledgements

We are grateful to Roberto Capuzzo Dolcetta, Pauline Chassonney, and Seppo Mikkola for making the ARWV code available to us. We thank Alessandro Trani for the useful comments. We also thank the members of the DEMOBLACK team for the helpful discussions. MD acknowledges financial support from Cariparo Foundation under grant 55440. MM and ST acknowledge financial support from the European Research Council for the ERC Consolidator grant DEMOBLACK under contract no. 770017. MAS acknowledges funding from the European Union’s Horizon 2020 research and innovation programme under the Marie Skłodowska-Curie grant agreement No. 101025436 (project GRACE-BH, PI: Manuel Arca Sedda).

## 3.6 Appendix: Impact of the maximum impact parameter

Three-body scatterings are computationally advantageous with respect to full star-cluster simulations. The price to pay is that the results depend on the choice of the initial parameters, which must convey information about the properties of the host star clusters and their binary systems. For example, to compute the upper limit of the impact parameter  $b_{\max}$  (eq. 3.7), we assumed that the

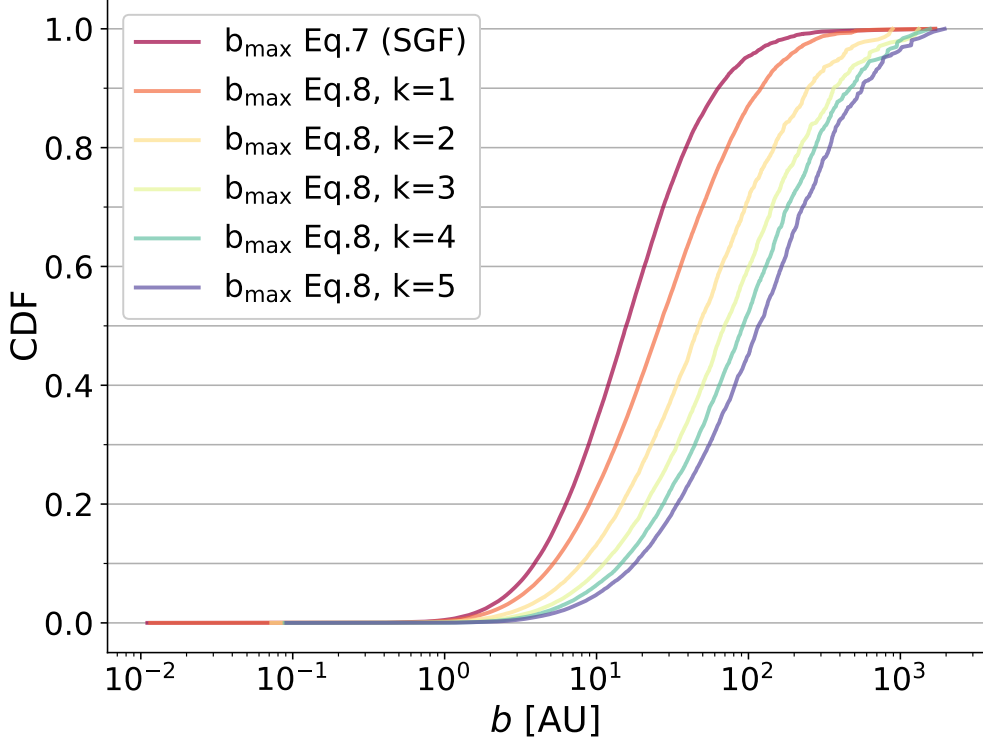


Figure 3.9: Cumulative distribution function of the impact parameter computed assuming  $b_{\max}$  from eq. 3.7, and from eq. 3.8 with  $k=1,2,3,4,5$ .

distance of closest approach  $r_p$  is equal to the semi-major axis  $a$  of the binary system and that the strong gravitational focusing limit is valid, or in other words that  $G(m_1 + m_2 + m_3)/(v_\infty^2 b) \gg 1$ . These assumptions ensure that the majority of our three-body interactions are classified as hard encounters, where significant energy exchange occurs between the single and binary BH. How critical is this assumption, and what are the effects on our results if we change this prescription? If we relax this hypothesis, the upper limit of the distribution takes the more general form

$$b_{\max}^2 = r_p^2 \left[ 1 + 2 \frac{G(m_1 + m_2 + m_3)}{r_p v_\infty^2} \right]. \quad (3.8)$$

The distance of closest approach is typically defined as  $r_p = k a$ , with  $k$  assumed as an arbitrary constant. To study how the strong gravitational focus approximation impacts our results, we have run  $5 \times 10^4$  additional three-body interactions initialized as the main NSC set, but with impact parameters generated according to eq. 3.8 with  $k = 1, 2, 3, 4, 5$ .

Figure 3.9 shows the cumulative distribution function of the impact parameter if we consider  $b_{\max}$  computed as in eq. 3.7 or eq. 3.8 with various choices for  $k$  in the NSC case. By calculating  $b_{\max}$  from eq. 3.7, it is more probable to generate interactions where the impact parameter favours closer encounters compared to the sample generated with eq. 3.8. The difference between the distributions is marginal with  $k = 1$ , but it gradually grows with increasing  $k$ . For example, there is a probability of approximately 34% for a simulation of having an impact parameter  $\leq 10$  AU in our fiducial model, while this probability decreases to 23% for  $k = 1$  and drops to 5% for  $k = 5$ .

The probability to draw an impact parameter  $b > 10^3$  AU is  $< 0.1\%$  in our fiducial model, while this fraction rises to 3% and 4% in the case of  $k = 4$  and  $k = 5$  with eq. 3.8. Assuming large values of

$k$  produces a non-negligible fraction of simulations where the impact parameter is of the same order of magnitude as the inter-particle distance in the core of a NSC. In these simulations, the single BH is likely to interact with other members of the star cluster before reaching the target binary, and the simulated interaction may not occur.

Figure 3.10 shows the outcomes of three-body interactions and BBH mergers as a function of the assumed  $b_{\max}$ . The simulation sets with larger values of  $b_{\max}$  result in fewer exchanges and ionizations while favouring more flybys, with this effect becoming more pronounced with larger values of  $k$ . For instance, in the case of  $k = 4$  and  $k = 5$ , almost 8 to 9 simulations over 10 evolve as a flyby. In contrast, our fiducial model produces flybys in almost 50 % of cases. This happens because, when the strong gravitational focus approximation is not assumed, interactions with larger impact parameters become more common. In such encounters, the single BH is more likely to perceive the binary system as a point-like object, leading more frequently to weaker energy exchanges between the binary and the single object. It also disfavours exchanges, which require closer passages between the single BH and one of the two binary components.

The lower panel of Fig. 3.10 shows that the choice of  $b_{\max}$  also affects the percentage of mergers, even if less dramatically than the percentage of flybys, exchanges and ionizations. The dependence of the percentage of BBH mergers on the choice of  $b_{\max}$  is further shown in Fig. 3.11. The fraction of BBH mergers decreases only by 1.7% from our fiducial model to the simulation set with  $k = 5$ . This plot also shows that the merger fraction linearly decreases with  $k$  as  $P_{\text{merg}} = \alpha k + \beta$ , with  $\alpha = -0.38 \pm 0.09$  and  $\beta = 11.83 \pm 0.31$ .

BBH mergers are less affected by the choice of  $b_{\max}$  because both Eqs. 3.7 and 3.8 encode the distribution of our semi-major axis, which shapes the overall impact parameter distribution through the  $b_{\max}$  dependence on  $a$ . In our approach, we sample  $a$  in a way which ensures that all our binaries are hard, while also being sufficiently large to prevent efficient gravitational-wave emission.

Different approaches are assumed in the literature to sample the parameter space of close encounters. For example, Hut & Bahcall (1983) and Zevin et al. (2019) compute  $b_{\max}$  as eq. 3.8 and set  $k = 1$  with arbitrary fixed values for  $a$ . Samsing et al. (2014) chose  $k = 5$  to ensure the sampling of distant interactions, but at the same time they keep the semi-major axis fixed at  $10^{-5}$  AU, which corresponds to very hard binaries, close to the merger. Quinlan (1996), on the other hand, fix  $a$  but varies the  $k$  parameter.

Here, we adopt a physically-motivated semi-major axis distribution, ranging from the limit between hard and soft binaries down to the threshold for efficient gravitational-wave decay. Moreover, in our models we aim to fully explore the parameter space for hard encounters. The price to pay is that we do not consider encounters with large  $k$ . Their effect is shown in Figures 3.10 and 3.11, for completeness.

Finally, Figure 3.12 shows the relative total energy variation of the binaries  $dE/E = |E_{\text{fin}} - E_{\text{in}}| / |E_{\text{fin}}|$ , where  $E_{\text{fin}}$  and  $E_{\text{in}}$  are the total binary energy at the beginning and at the end of the simulation, respectively. The peak of the distribution shifts from larger to lower values of the relative total binary energy variation, when  $k$  increases. For instance, the distribution for our fiducial model and for eq. 3.8 with  $k = 1$  peak more than one order of magnitude above the distributions obtained for  $k = 4$  and  $k = 5$ . In the former, only 2.6% and 2.7% of the binary systems yield  $dE/E < 10^{-2}$ , while this number increases to 20% and 31% for the latter.

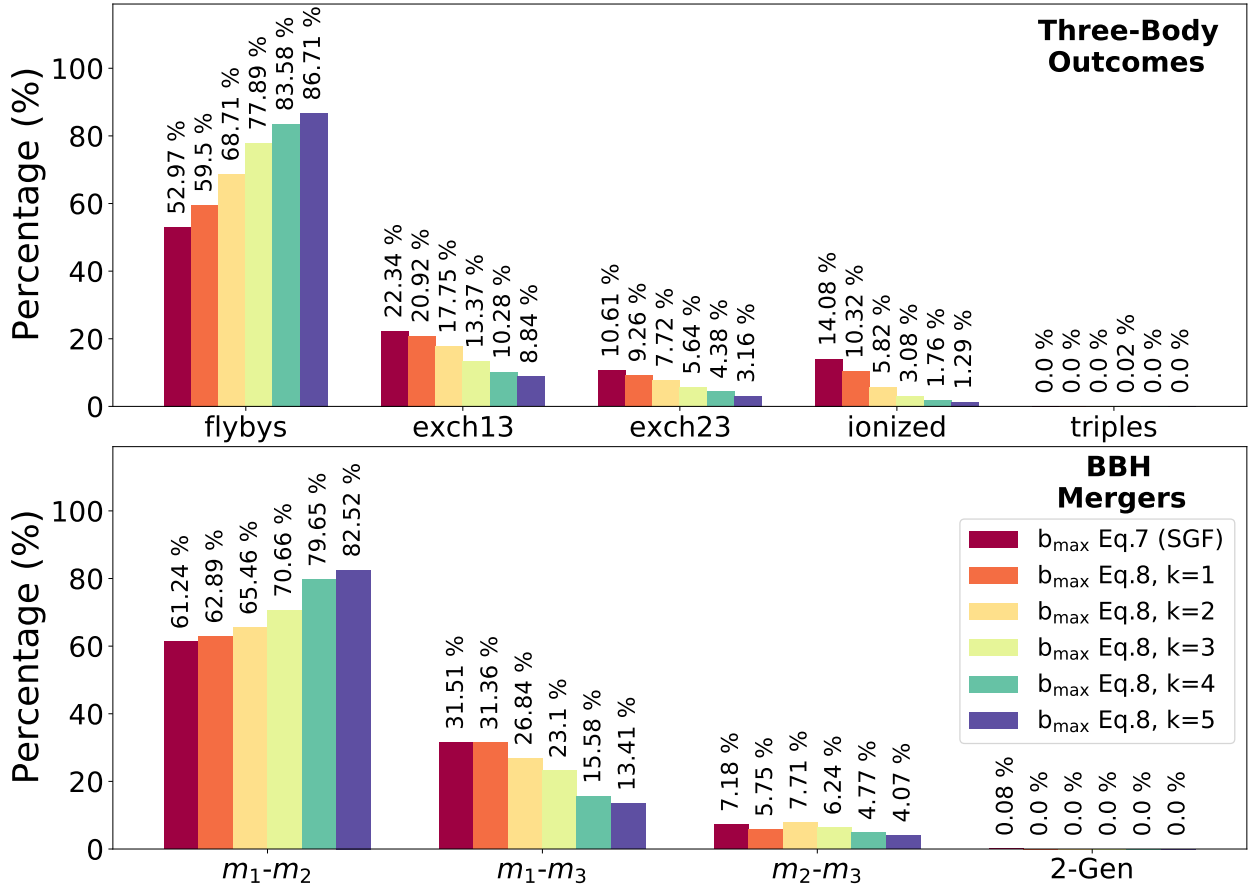


Figure 3.10: Same as Fig. 3.2 but assuming eq. 3.8 for the choice of  $b_{\max}$ . The plot shows the outcome of the three-body simulations (upper panel) and the formation channel of the BBH mergers (lower panel) for the main NSC set initialized with eq. 3.7 (dark red, fiducial model) and the smaller NSC sets initialized with eq. 3.8 assuming  $k = 1$  (orange), 2 (yellow), 3 (light-green), 4 (dark-green), and 5 (blue).

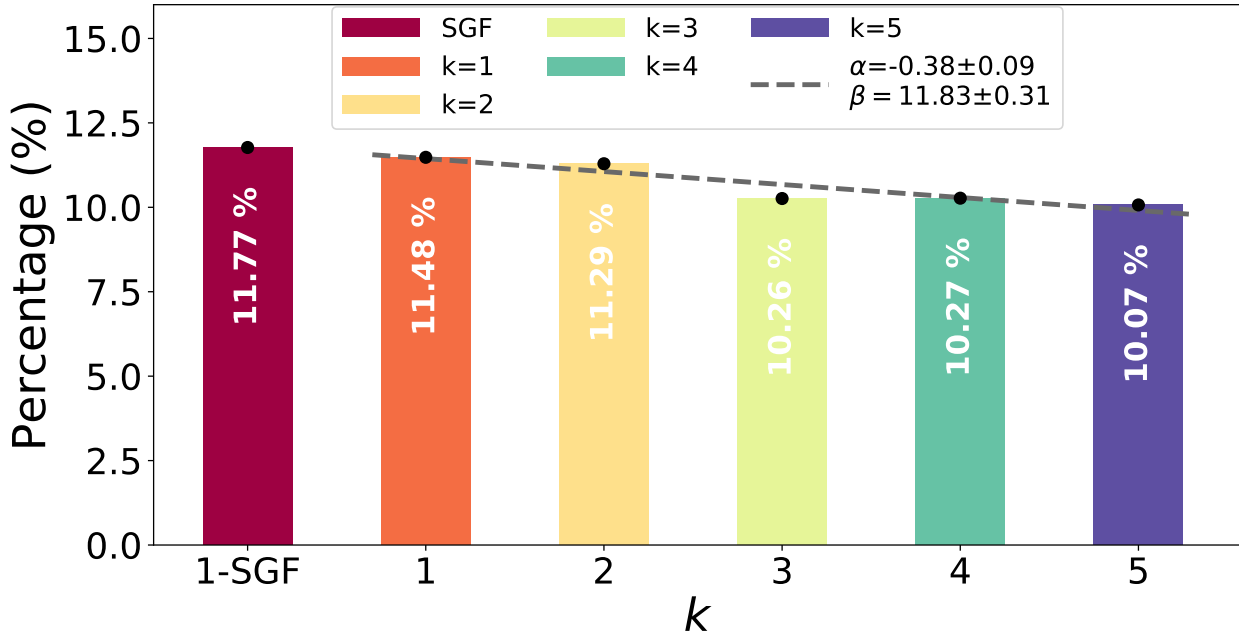


Figure 3.11: Percentage of BBH mergers over all the simulated encounters in NSCs, where  $b_{\max}$  is computed with eq.3.7 and eq.3.8 assuming  $k = 1, 2, 3, 4, 5$ . The bar colours are the same as in Figs. 3.9 and 3.10. The grey-dashed line is the linear fit to the percentage of mergers as a function of the  $k$  parameter.

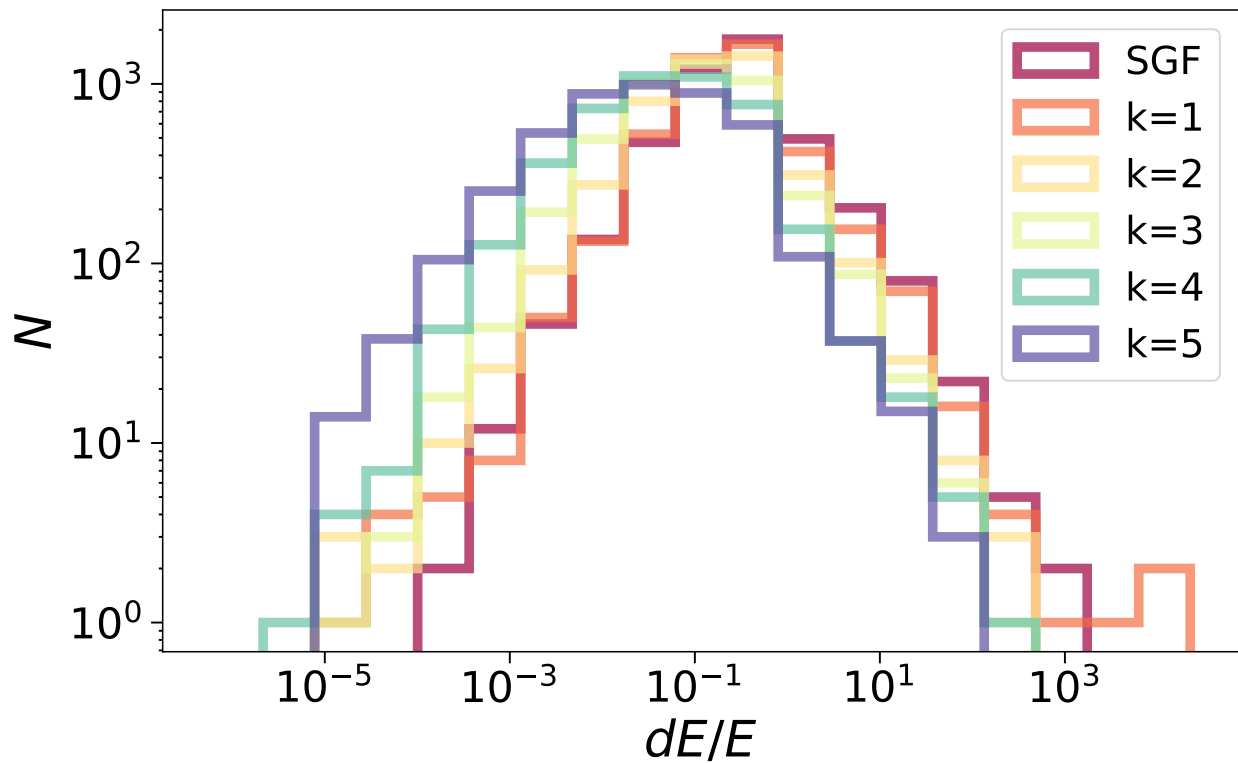


Figure 3.12: Histograms of the normalized variation of the binary total energy with respect to final binary total energy as a function of  $b_{\max}$ . The colours are the same as in Figs. 3.9, 3.10, and 3.11.



## Chapter 4

# Chemically Homogeneous Evolution: Impact on Stellar and Compact Binary Populations

*Based on:*

Dall'Amico M., "Chemically Homogeneous Evolution: Impacts on Stellar and Compact Binary Populations",  
2024, in prep.

### Abstract

Chemically homogeneous evolution strongly affects the life and death of massive stars in metal-poor binaries. In this work, we explore the effects of accretion-induced CHE on both a stellar population and its compact binary remnants. We simulated a total of  $1.2 \times 10^8$  binaries and  $5 \times 10^7$  single stars with two different CHE prescriptions and at 5 different metallicities with the state-of-the-art population synthesis code SEVN. Our simulations show that CHE efficiently enhances the formation of Wolf-Rayet stars (WRs) from the secondary stars, halting their evolution into red supergiant stars (RSGs). WRs formed through CHE are, on average, more massive, numerous, and luminous than those formed through standard stellar evolution. These stars do not give rise to neutron stars but rather favour the formation of more massive black holes. As a direct consequence, the CHE mechanism enhances the formation of binary black holes (BBHs) and black hole-neutron star (BHNS) systems, while simultaneously quenching the production of binary neutron stars (BNSs). However, the primary effect of CHE is to significantly suppress the formation of all categories of compact binary mergers at low metallicity. For instance, the number of BBH mergers drops by a factor  $\sim 12$  in our models with CHE at  $Z = 0.004$ . Finally, we find that CHE enhances the formation of asymmetric mass ratio BBH mergers. BBH mergers resulting from CHE can exhibit a mass ratio of  $\leq 0.6$ , resembling the characteristic mass ratio of dynamically assembled BBH systems.

### 4.1 Introduction

Massive stars drive the evolution of the Universe. Their strong stellar winds and supernova events serve as a primary source of mechanical feedback for the interstellar medium, playing a key role in the genesis of new stars and planets (Elmegreen & Scalo 2004; McKee & Ostriker 2007). Massive

star radiative feedback, characterized by strong UV radiation, leads to the formation of HII regions and is commonly assumed to be the main source of the reionization epoch in the early stages of the Universe (Haiman &Loeb 1997; Loeb &Barkana 2001; Schaerer 2002; Maio et al. 2011; Bromm &Larson 2004; Bromm 2013; Klessen &Glover 2023). Moreover, these stars are considered the main forge of massive elements in the Universe, shaping the chemical evolution of galaxies (Woosley &Weaver 1995; Woosley et al. 2002; Rauscher et al. 2002; Nomoto et al. 2013). In addition, massive stars are deemed progenitors of high-energy events like gamma-ray bursts, and in their final stages, they give birth to compact objects such as neutron stars and black holes (Narayan et al. 1992; Heger et al. 2003; Woosley &Heger 2006). Lastly, massive stars can actively contribute to cluster dynamics, potentially triggering catastrophic events like stellar collisions (e.g. Portegies Zwart et al. 1999; Fregeau et al. 2004; Portegies Zwart &van den Heuvel 2016; Di Carlo et al. 2020b).

Massive stars are rare and short-lived, with most of their crucial evolutionary phases lasting just a blink of an eye in the context of cosmological timescales. Despite their importance, several aspects of the evolution of massive stars remain unresolved. Mass loss episodes due to winds, pulsations, and outflows (e.g. Smith 2014), combined with rotation (e.g. Maeder 2009), magnetic fields (e.g. Donati &Landstreet 2009), and thermally induced mixing by overshooting, semiconvection, and dredge-up (e.g. Costa et al. 2023b) are crucial events that govern the evolution of massive stars but still lack a complete understanding. To add an additional layer of complexity to the problem, it is now well-established that the vast majority of massive OB stars reside in binary systems, and that over 70% of them are expected to interact with their companions (Sana et al. 2012; Moe &Di Stefano 2017). Binary interactions strongly affect the evolution of massive stars, and largely influence the production of compact binary mergers possibly detectable by ground-based interferometers (e.g. Marchant &Bodensteiner 2023; Costa et al. 2023b, and references therein).

One of the primary outcomes resulting from the interplay of stellar evolution and binary processes is chemically quasi-homogeneous evolution (CHE). In massive metal-poor stars, large rotational velocities can generate strong mixing currents, causing the star to be partially or fully mixed before the depletion of hydrogen (Eddington 1925b; Sweet 1950b). Rotational mixing transports nuclear fusion byproducts from the core to the surface, simultaneously replenishing the core with hydrogen drawn from the outer envelope, beyond the limits of convection. These mixing currents prevent the formation of a strong chemical gradient between core and envelope, inducing the star to become CHE (Maeder 1987; Langer 1992; Maeder &Meynet 2000b; Heger et al. 2000; de Mink et al. 2009; Brott et al. 2011b; Köhler et al. 2015; Szécsi et al. 2015).

CHE can be prevented if the massive star is a rapid, single rotator: angular momentum mass loss by stellar winds and magnetic braking can effectively spin down the star even before the mixing process becomes efficient (Ivanova &Taam 2003; Meynet et al. 2011). In binary systems, on the other hand, various processes such as mass transfer episodes (e.g. Packet 1981; Pols et al. 1991; Petrovic et al. 2005; Eldridge et al. 2011; van Rensbergen et al. 2011; Shao &Li 2014), tidal interactions (e.g. Zahn 1975; Hut 1981; de Mink et al. 2009; Song et al. 2016b), and stellar mergers (e.g. Podsiadlowski et al. 1992; Tyrenda et al. 2011) contribute as spin-up mechanism, potentially sustaining the formation of rapidly rotating stars that undergo CHE.

CHE has a profound impact on both the observational properties of a massive stellar population (Eldridge et al. 2011; Brott et al. 2011c; Eldridge et al. 2017; Schootemeijer &Langer 2018; Cui et al. 2018; Ramachandran et al. 2019; Stanway et al. 2020; Massey et al. 2021; Ghodla et al. 2023) and its efficiency in the production of compact binary mergers (Eldridge &Stanway 2016; de Mink &Mandel 2016; Mandel &de Mink 2016; Marchant et al. 2016; Eldridge et al. 2019; du Buisson et al. 2020; Riley et al. 2021). The overabundance of heavier elements in a CHE star's envelope reduces opacity and increases the mean molecular weight of the outer layers, leading to the formation of

more compact and luminous stars. Consequently, stars entering the CHE state evolve differently compared to their non-homogeneous counterparts. CHE stars become hotter and bluer along their evolution, evolving in pure helium stars in their post-main sequence stage and appearing as Wolf-Rayet stars (de Mink et al. 2013; Brott et al. 2011b). Due to the mixing currents that replenish the star’s core with fresh envelope hydrogen, these stars can develop a larger helium core and, at the end of their life, give birth to a massive compact object (Mandel &de Mink 2016; de Mink &Mandel 2016). Furthermore, rapidly rotating CHE stars are considered the progenitor of hypernovae and long gamma-ray bursts (Podsiadlowski et al. 2004; Yoon &Langer 2005; Yoon et al. 2006; Woosley &Heger 2006; Cantiello et al. 2007; Georgy et al. 2009; Eldridge et al. 2011).

In this work, we explore the effects of CHE on a population of binary stars with primary mass in the range  $[5, 150] \text{ M}_\odot$ . We first studied the impact of CHE on the production of Wolf-Rayet stars (WRs) and red supergiant stars (RSGs) as a function of the binary fraction and the metallicity of the stellar population, assuming a constant star formation rate. We then explored the subsequent impact of CHE on the formation of binary black holes (BBHs), binary neutron stars (BNSs), and black hole-neutron star (BHNSs) binary systems. We discuss how the properties of binary compact mergers and their formation efficiency change as a function of the CHE prescription. We model our stellar population through the state-of-the-art population synthesis code SEVN (Spera &Mapelli 2017; Spera et al. 2019; Mapelli et al. 2021b; Iorio et al. 2023). SEVN calculates stellar evolution by interpolating pre-computed sets of stellar tracks and concurrently simulates binary evolution using analytic and semi-analytic prescriptions. For the CHE mechanism, we considered only the accretion spin-up scenario, following the prescription presented by Eldridge et al. (2011). We evolved a total of  $1.2 \times 10^8$  binaries and  $5 \times 10^7$  single stars at different metallicities, including (excluding) the pre-mainsequence phase, and with different CHE prescriptions.

#### 4.1.1 Population synthesis with SEVN

We evolved our binary and single stellar populations with the stellar evolution for  $N$ -body code SEVN. SEVN is a population-synthesis code that implements single stellar evolution by interpolating pre-computed stellar tracks on the fly, while also modeling binary processes by means of analytic and semi-analytic prescriptions (Spera &Mapelli 2017; Spera et al. 2019; Mapelli et al. 2021b; Iorio et al. 2023). In this work, we adopt the latest version of SEVN<sup>1</sup>, fully described in Iorio et al. (2023). Our simulations are based on the latest stellar tracks computed with the stellar evolution code PARSEC (Bressan et al. 2012; Chen et al. 2015; Costa et al. 2019, 2021b). Here, we specifically make use of the tracks named `SEVNtracks_parsec_ov05_AGB` for stars initialized in the hydrogen main sequence, and `SEVNtracks_parsec_pureHe36` for pure helium stars. SEVN traces the evolution of individual stars by adaptively interpolating the stellar properties from the four closest stellar tracks to match the star’s zero-age-main-sequence mass and metallicity. At the end of a star’s lifetime, if a star is sufficiently massive, SEVN computes the mass of the compact remnant as in Giacobbo &Mapelli (2019) for electron-capture SNe, Fryer et al. (2012) for core-collapse SNe, and Mapelli et al. (2021b) for pulsational and pair-instability SNe. In our simulations, we specifically employed the *rapid* core-collapse SN model by Fryer et al. (2012). With this prescription, SEVN assumes that the remnant is a neutron star if its mass is less than  $3 \text{ M}_\odot$ , and a black hole otherwise. The supernova kicks applied to the compact remnants are modeled by SEVN following the approach outlined by Giacobbo &Mapelli (2020). In addition, SEVN incorporates a wide range of binary evolution processes, including stable mass transfer by Roche-lobe overflow and winds, common envelope evolution, angular momentum dissipation by magnetic braking, tidal interactions, orbital decay by gravitational-wave emission,

---

<sup>1</sup>SEVN is publicly available at [https://gitlab.com/sevn\\_codes/sevn](https://gitlab.com/sevn_codes/sevn).

dynamical hardening, chemically homogeneous evolution, and stellar mergers. For a comprehensive description of the implementation of each of these processes, we refer to Iorio et al. (2023).

In the following, we discuss only the most significant assumptions implemented in our simulations for these binary-evolution processes. We adopted the same stability criterion for Roche-lobe overflow as the fiducial model presented by Iorio et al. (2023). This model assumes a critical mass ratio,  $q_c$ , between the donor star and the accretor star, above which the mass transfer becomes unstable on a dynamical timescale. Here,  $q_c$  is defined as in Hurley et al. (2002), but for the following exception: the mass transfer is always considered stable if the donor has a radiative envelope, i.e. is a main sequence or a Hertzsprung gap star. SEVN describes the common envelope phase with the  $\alpha - \lambda$  formalism (Webbink 1984; Livio & Soker 1988; Iben & Livio 1993). Here,  $\alpha$  represents the fraction of orbital energy injected into the envelope while  $\lambda$  measures the concentration of the envelope and incorporates all the uncertainties related to the envelope structure. In our simulations, we adopted the same fiducial model as Iorio et al. (2023), where  $\alpha = 3$  and  $\lambda$  depends on the mass of the star, except for pure helium stars for which  $\lambda = 0.5$  (Claeys et al. 2014b).

SEVN manages tidal interactions by employing the analytical formalism presented by Hut (1981) and further detailed by Hurley et al. (2002). This includes the treatment of synchronization between stellar and orbital rotation, as well as the orbital circularization of the binary. Spin-down by magnetic braking is treated as in Hurley et al. (2002), and it is active only if the star has an envelope and a core with, respectively, non-zero mass. Finally, in our work we considered only the evolution of isolated binaries, therefore we do not take into account the effects of dynamical hardening.

### 4.1.2 Chemically Quasi-Homogeneous Simulations

In this work, we exclusively explored the formation of CHE stars through accretion spin-up. This scenario occurs when the most evolved star in the binary expands to its Roche radius, initiating a Roche-lobe overflow mass transfer. If the mass transfer remains dynamically stable, the companion star can efficiently accrete mass and angular momentum at a rate sufficient to effectively spin up. When the star is massive enough and sufficiently metal-poor, rotational mixing becomes extremely efficient, inducing the accretor star to evolve into the CHE state. In principle, CHE can also be achieved in tight binaries due to tidal interactions. Strong tides tend to synchronize the rotational periods of the stars with the orbital periods of the binary and, as a result, both stars rapidly spin up, possibly triggering CHE. Here, we focus our study only on the former discussed CHE case. This choice and its impact on our results are further discussed in section 4.4.

SEVN allows for the formation of CHE stars through the accretion spin-up mechanism, adopting the prescription first introduced by Eldridge et al. (2011). In this framework, a star becomes CHE if it satisfies three criteria.

1) The star must accrete enough material and angular momentum during the Roche-lobe overflow phase to be considered rapidly spinning and fully mixed. In SEVN, this is assumed when a star accretes a fraction of its initial mass through Roche lobe overflow. In principle, if a non-rotating star accretes  $\sim 10\%$  of its initial mass, the star gathers enough angular momentum to reach its critical rotation velocity (Eldridge et al. 2011). We followed Eldridge et al. (2011), and set this accretion fraction to  $M_{\text{acc}} = 5\%$  of the stellar initial mass.

2) Rotational mixing is more efficient in more massive stars (Heger et al. 2000; Maeder & Meynet 2001; Ekström et al. 2012; Georgy et al. 2013) and the minimum rotation rate required for CHE decreases with increasing mass of the star (Yoon et al. 2006). Moreover, massive stars are more likely to interact in binaries, meaning that the possibility of getting spun up by accretion is larger (Sana et al. 2012). SEVN enables the CHE only if a star is characterized by a post-accretion mass larger than

Table 4.1: Description of our models.

Name	$t_{\text{in}}$	CHE	$M_{\text{min}} [\text{M}_{\odot}]$	$M_{\text{acc}}$	$Z_{\text{max}}$
NoCHEzams	ZAMS	No CHE			
NoCHEpreMS	0.1 Myr	No CHE			
CHE10zams	ZAMS	Eldridge et al. (2011)	10	5%	0.004
CHE10preMS	0.1 Myr	Eldridge et al. (2011)	10	5%	0.004
CHE20zams	ZAMS	Eldridge et al. (2017)	20	5%	0.004
CHE20preMS	0.1 Myr	Eldridge et al. (2017)	20	5%	0.004

From left to right: name of the simulation set, initial age of the stars in the binaries at the beginning of the simulation ( $t_{\text{in}}$ ), reference for the CHE prescription adopted in the simulation (CHE), minimum mass required for a star to enter in CHE phase ( $M_{\text{min}}$ ), minimum accreted mass relative to its ZAMS mass required for a star to enter in CHE phase ( $M_{\text{acc}}$ ), and maximum metallicity required for a star to enter in CHE phase ( $Z_{\text{max}}$ ).

a given threshold  $M_{\text{min}}$ . In our models, we tested two possible mass thresholds  $M_{\text{min}} = 10, 20 \text{ M}_{\odot}$ , following the approach of Eldridge et al. (2011) and Eldridge et al. (2017).

3) Wind mass loss in massive stars strongly depends on metallicity (e.g. Vink et al. 2001). Since mass loss removes angular momentum from the star, its metallicity must be low enough to weaken the winds and prevent the star from spinning down. We set the maximum metallicity below which CHE is possible as  $Z_{\text{max}} = 0.004$  (Yoon et al. 2006; Eldridge et al. 2011).

If a star fulfills these three conditions, it is flagged as a CHE. In SEVN, its evolution proceeds with a fixed radius during the main sequence, at the end of which it directly evolves into a pure helium star. We performed a total of  $1.2 \times 10^8$  binary simulations divided into six distinct sets, summarized in table 4.1. We further simulated  $5 \times 10^7$  single stars. We explored three different prescriptions for CHE: one without CHE, one with  $M_{\text{min}} = 10 \text{ M}_{\odot}$ , and a final one with  $M_{\text{min}} = 20 \text{ M}_{\odot}$ . Each of these simulation sets has been tested by initializing the stars at their zero-age-main-sequence and 0.1 Myr from their birth. Finally, we repeated the evolution of our single and binary stars for five different metallicities  $Z = 0.04, 0.02, 0.008, 0.004, 0.001$ .

#### 4.1.3 Initial conditions

We generate the mass of the primary and single stars from a Kroupa initial mass function (Kroupa 2001) in the range  $[5, 150] \text{ M}_{\odot}$ . The secondary mass in our binary systems is sampled assuming a mass ratio distribution  $\mathcal{F}(q) \propto q^{-0.1}$  in the range  $[0.1, 1]$  (Sana et al. 2012). We discarded all the systems with at least one star less massive than  $2.2 \text{ M}_{\odot}$ , as the PARSEC stellar tracks in SEVN include only stars above this threshold. The initial period and eccentricity of our binaries are generated according to Sana et al. (2012). The period follows a distribution  $\mathcal{F}(\mathcal{P}) \propto \mathcal{P}^{-0.55}$ , with  $\mathcal{P} = \log_{10}(P/\text{days}) \in [0.15, 15]$ . The eccentricities are extracted from the distribution  $\mathcal{F}(e) \propto e^{-0.45}$  in the range  $[10^{-5}, e_{\text{max}}(P)]$ . Here, the upper limit of the eccentricity distribution is a function of the orbital period as  $e_{\text{max}}(P) = 1 - [P/(2 \text{ days})]^{-2/3}$  (Moe & Di Stefano 2017). To date, SEVN does not incorporate evolutionary tracks for rotating stars. Therefore, we initialize our binary and single populations with stars having zero initial rotation. We stop our simulations either if the binary is disrupted by a supernova kick or when only compact objects remain.

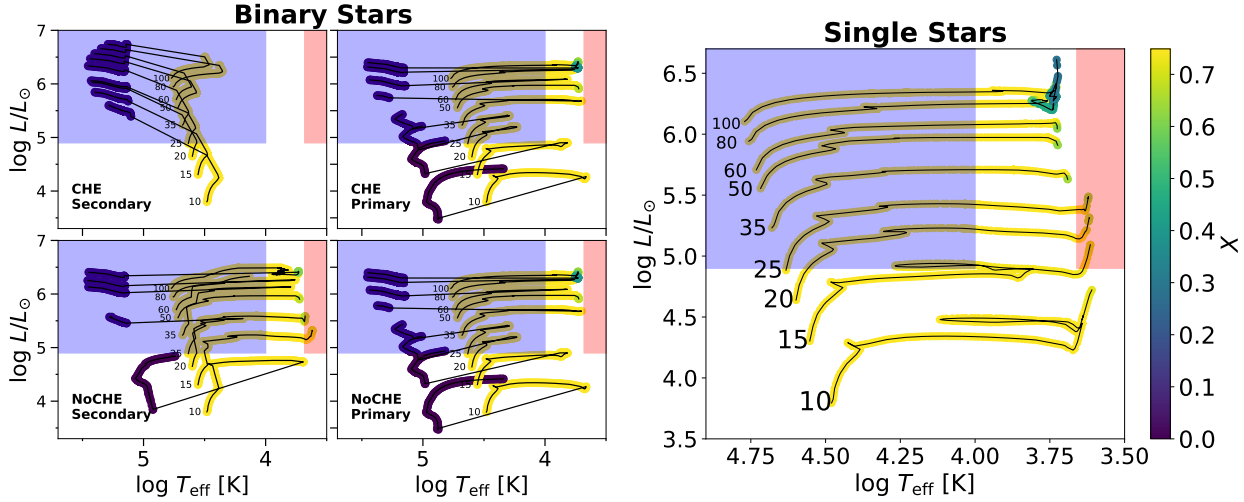


Figure 4.1: Evolutionary tracks at metallicity  $Z = 0.001$  of binary stars (left) and single stars (right) with masses of 10, 15, 20, 25, 35, 50, 60, 80, and  $100 M_{\odot}$ . The plots depict, in a clockwise order starting from the upper left panel, the evolutionary tracks for secondary stars from the CHE10zams model, primary stars from the CHE10zams model, primary stars from the NoCHEzams model, and secondary stars from the CHE10zams model. The primary and secondary stars are not part of the same binary systems. The colourmap shows the hydrogen surface abundance during the stars' evolution. The blue and red-filled regions indicate the threshold within which the luminosity and temperature are sufficient to classify a star as a WR or a RSG.

## 4.2 Results: Stellar populations

In this section, we present the results relative to our fiducial models NoCHEzams and CHE10zams. The comparison with the results relative to the other sets of simulations (table 4.1) is discussed in Section 4.6.

### 4.2.1 Wolf-Rayet & red supergiant stars

We explore the effects of CHE on a stellar population by studying the effects on the production of RSGs and WRs, as these are commonly associated with evolved stages of two distinct stellar sub-groups. RSGs are helium-burning stars with ages in the  $\sim 8 - 35$  Myr range that arise from the evolution of stars with initial mass  $\sim 8 - 30 M_{\odot}$ . WRs descend instead from the evolution of stars with a mass larger than  $\sim 30 M_{\odot}$ , and are characterized by ages lower than  $\sim 8$  Myr. Observationally, these two categories of stars lie in distinct regions on the Hertzsprung-Russell diagram, highlighted in blue and red in Figure 4.1. We categorize RSGs as stars exhibiting temperatures typical of M and K spectral type stars, defined by  $\log(T/K) \leq 3.68$  (Klencki et al. 2020). We additionally set a minimum luminosity criterion of  $\log(L/L_{\odot}) \geq 4.8$  for classifying a star as an RSG (Massey et al. 2021). This threshold limits the contamination from stars in the asymptotic giant branch (Brunish et al. 1986; Massey & Olsen 2003). We further categorized stars as RSGs only if they have a hydrogen surface abundance of  $X > 0.001$  (Eldridge et al. 2008). For WRs, we set a luminosity, temperature, and surface hydrogen abundance thresholds of  $\log(L/L_{\odot}) \geq 4.8$ ,  $\log(T/K) \geq 4$ , and  $X \leq 0.4$ , following the definition of Eldridge et al. (2008) and Massey et al. (2021).

### 4.2.2 Single stellar evolution

The right-hand panel in Figure 4.1 shows an example of evolutionary tracks for single stars at  $Z = 0.001 \sim 1/20Z_{\odot}$ . In these models, our single stellar population does not yield any WR. The mass loss is nearly negligible, and the winds lack the strength required to effectively strip the star of its hydrogen envelope, thereby preventing the formation of a WR (Conti 1975b; Chiosi et al. 1979; Chiosi & Maeder 1986). On the other hand, at higher metallicity, the larger the value of  $Z$  is, the more impactful the mass loss, and the lower the minimum mass for a star to become a WR.

We find that at  $Z = 0.004$  only massive stars with an initial zero-age-main-sequence mass  $M_{ZAMS} \geq 63$  become WRs, while at  $Z = 0.008$  WRs arise only from the evolution of stars with mass  $M_{ZAMS} \geq 42$ . At solar ( $Z = 0.02$ ) and super-solar ( $Z = 0.04$ ) metallicity, only stars with  $M_{ZAMS} \geq 29$ , and  $M_{ZAMS} \geq 23$ , respectively, produce WRs. At these latter metallicities, WR progenitors in the range  $M_{ZAMS} = 23 - 29$  also experience a relatively short RSG phase before completely expelling their envelopes.

We find that the maximum mass for a star to form a RSG does not sharply depend on metallicity, and exhibits less variability with  $Z$  compared to the minimum mass necessary to form a WR. In our single stellar evolution models, the maximum zero-age-main-sequence mass required for a star to evolve into RSG branch is  $31, 40, 51, 38, 30 M_{\odot}$  at  $Z = 0.001, 0.004, 0.008, 0.02, 0.04$ , respectively. This is intrinsically related to the Humphreys-Davidson limit, i.e. the empirical region at large luminosity and low temperature in the Hertzsprung-Russell diagram characterized by a dearth of observed stars (Humphreys & Davidson 1979). The limit is commonly associated either with super-Eddington winds resulting from radiative instability or with rotational mixing (Gilkis et al. 2021). This luminosity limit unequivocally constrains the maximum mass for a cool supergiant star. Our findings are consistent with the observations performed by Davies et al. (2018), where they studied the luminosity distributions of RSGs in the Large and Small Magellanic Clouds. They find no metallicity correlation with the Humphreys-Davidson limit, with a dearth of RSG from stars with  $M_{zams} > 30 M_{\odot}$ , in good agreement with our results.

### 4.2.3 Binary stellar evolution

Binary evolution provides an efficient pathway to produce WRs even at low metallicity. This is shown in the left-hand panels of Figure 4.1. The stellar evolutionary tracks correspond to primary and secondary stars with different initial masses of different binaries at  $Z = 0.001$ , relative to the CHE10zams and NoCHEzams models. In the evolutionary model without CHE (bottom panels), the main formation channel for WRs is envelope stripping by Roche lobe overflow. Primary stars evolve more rapidly than secondary stars, expanding beyond their Roche radius and initiating to donate mass to the secondary. By the end of this process, the envelope of the primary star is completely lost and the star evolves into a WR. This is the fate of most primary stars in our interacting binaries, and it constitutes the primary process to form WRs in metal-poor binary systems.

In contrast, not all secondary stars evolve into WRs. This occurs only when the secondary, in its turn, donates mass through Roche lobe overflow (as in the  $100, 80, 60, 20, M_{\odot}$  tracks), or when the secondary initiates a common-envelope phase and loses its outer envelope, and eventually undergoes a merger (the case of the  $10 M_{\odot}$  track). When secondary stars accrete mass from the primary, during this phase their evolution follows a nearly vertical path in the Hertzsprung-Russell diagram (e.g.  $15 M_{\odot}$  tracks). After this phase, if they do not initiate any mass transfer in turn, these secondary stars will spend the rest of the evolution with their hydrogen envelope intact. This is a direct consequence of wind weakness at low metallicity. As a result, these stars start to expand and evolve toward lower temperatures, far from the WR region, with some of them eventually becoming RSGs.

The lack of WR formation through single stellar evolution at low metallicity suggests that, at  $Z \leq 0.001$ , WRs must either be or have been part of an interacting binary system.

The upper panels of figure 4.1 show the same systems evolved with the CHE model. The main difference is the evolution of the secondary stars compared to their counterparts in the model without CHE. In these binaries, the primary star fills its Roche radius and initiates the mass transfer, at the end of which it becomes a peeled WR. If the mass transfer on the secondary fulfills the conditions presented in section 4.1.2, the secondary star becomes chemically homogeneous. This is the case of all the secondaries in the upper-left panel of Figure 4.1, which at the end of their main sequence become pure helium stars and evolve into the upper-left part of the Hertzsprung-Russel diagram. In contrast, the evolution of the primary stars remains unaffected by the CHE of the secondary. This happens because these stars have already undergone a significant portion of their evolution by the time CHE begins. In summary, CHE enhances the production efficiency of WRs in binary systems by increasing the likelihood of secondary stars evolving into WRs.

#### 4.2.4 RSG to WR ratio

Figure 4.2 shows the effect of metallicity, binary fraction, and CHE on the RSG-to-WR ratio of a stellar population. The ratio is defined as the number of RSGs over the number of WRs integrated assuming a constant star formation rate<sup>2</sup>. We tested 11 binary fractions  $f = 2N_{\text{binaries}}/N_{\text{stars}}$  ranging from  $f = 0$ , i.e. a population composed solely of single stars, up to  $f = 1$ , i.e. a population completely constituted by stars in binaries.

The plot shows that when the population is only composed of single stars, the ratio monotonically decreases with increasing metallicity. This happens because the minimum mass to form a WR decreases with  $Z$ , while the lifetime spent by a star in the WR phase increases with increasing  $Z$ . This has the overall effect of increasing the number of WRs when the metallicity increases. The number of RSGs, on the other hand, drops with increasing  $Z$ , because at high metallicity the most massive stars get stripped by their winds and evolve into WRs.

A second trend we see in the figure is that the higher the binary fraction is, the lower the overall RSG-to-WR ratio. Binary evolution produces a larger number of stripped stars by mass transfer episodes, meaning more WRs and fewer RSGs. Even a modest binary fraction can significantly reduce the ratio at low metallicity. This stems from the inefficiency of producing WRs through single stellar evolution when  $Z$  is low, because stellar winds are not strong enough to strip the stellar envelope. The binary fraction not only reduces the ratio but also alters its pattern with metallicity. While at low values of  $f$ , the ratio still exhibits a monotonically decreasing trend with  $Z$ , at  $f = 1$ , the ratio increases with rising  $Z$  up to solar metallicity, beyond which it begins to decline.

Finally, if we consider the models where CHE is active, the RSG-to-WR ratio drops when the metallicity is  $\leq 0.004$  in all the populations with  $f > 0$ . As we discussed in section 4.2.3, CHE is extremely efficient in forming WRs. CHE suppresses the evolution into RSG of a large fraction of secondary stars, which instead become WRs. This effect becomes more pronounced in stellar populations with both a large binary fraction and low metallicity.

---

<sup>2</sup>Massey et al. (2021) have shown in their study that the RSG to WR ratio is only marginally sensitive to different star formation rate models.

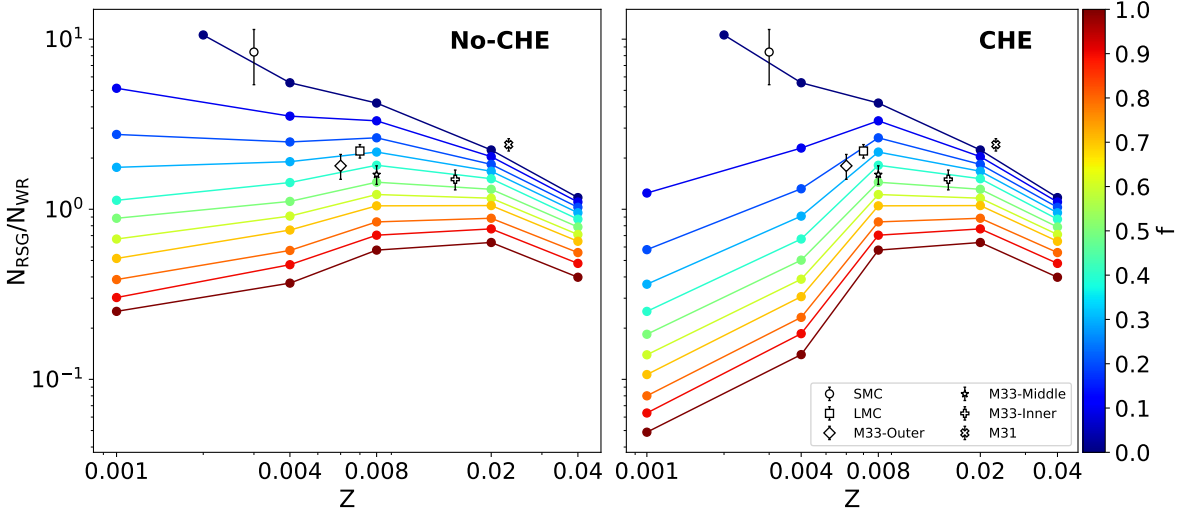


Figure 4.2: RSG and WR ratio as a function of metallicity and binary fraction. The left-hand (right-hand) side panel reports the results for the simulations evolved without (with) CHE. The markers show the ratio observed for different galaxies reported in Massey et al. (2021).

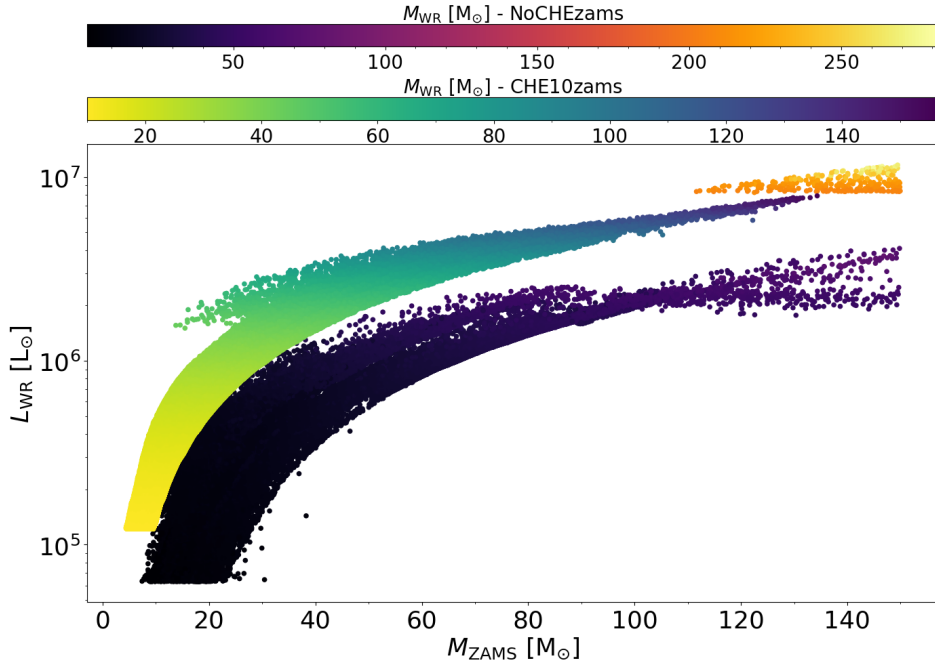


Figure 4.3: Masses of WR progenitors at their zero-age main-sequence plotted against the WR luminosity at birth. The color scales represent the WR masses at birth, with the upper color bar indicating WRs born in the NoCHEzams model and the lower color bar indicating those born in the CHE10zams model. The plot shows the results for our models at  $Z = 0.001$ .

### 4.2.5 WR luminosity

Figure 4.3 compares the luminosity and masses at the formation age of WRs born through CHE and standard binary evolution without CHE at  $Z = 0.001$ . At the same zero-age-main-sequence mass, WRs born through CHE are on average more massive and more luminous than their counterparts formed through envelope-stripping due to binary evolution processes. The median mass of a WR produced by the CHE channel is  $15 M_{\odot}$ , while the median mass for a WR formed without CHE is  $9 M_{\odot}$ . At the same time, the median luminosity of a WR formed via CHE is  $3 \times 10^5 L_{\odot}$ , while this is  $1.9 \times 10^5 L_{\odot}$  for WRs formed without CHE.

These differences arise from the nature of their formation path. In the standard formation scenario, WRs form in binary systems when one of the two stars fills its Roche lobe, starts to donate mass to the companion, and gets stripped of its outer envelope. What remains is the naked core of the previous star that has partially, or completely lost a large fraction of its mass with its envelope. In contrast, WRs formed through CHE retain their envelopes, as the outer hydrogen layers become fully mixed with the stellar interior. Consequently, WRs resulting from this mixing process exhibit larger mass and luminosity compared to their stripped, pure helium counterparts. In the plot, these two families of WRs cover two distinct regions. CHE can form WRs from progenitors with zero-age-main-sequence mass as low as  $4.4 M_{\odot}$ . Remarkably, these WRs exhibit the same luminosity as a WR formed by a  $M_{\text{ZAMS}} = 20 M_{\odot}$  progenitor through Roche lobe stripping. This large luminosity is a direct consequence of the larger mass of these WRs: a star with  $M_{\text{ZAMS}} = 4.4 M_{\odot}$  in the CHE10zams model accretes a substantial amount of mass from the companion, and once it settles into CHE it then evolves into a  $10 M_{\odot}$  WR. In contrast, the lightest WR progenitor in the NoCHEzams model has a mass of  $M_{\text{ZAMS}} = 7.4 M_{\odot}$  and, after losing its envelope by Roche lobe overflow, it creates a WR of  $2.1 M_{\odot}$ .

The maximum luminosity of a WR formed by envelope stripping in our NoCHEzams model is  $\sim 4 \times 10^6 L_{\odot}$ , corresponding to stars with  $M_{\text{ZAMS}} > 140 M_{\odot}$ . Above this luminosity limit, WRs can only be formed in our models either by CHE or by stellar mergers. The upper-right corner of Figure 4.3 is populated by massive WRs, exceeding  $200 M_{\odot}$ , which result from the merger of two stars in a binary system with an initial zero-age-main-sequence mass exceeding  $100 M_{\odot}$ . This region is occupied exclusively by stars that have not experienced CHE. In the CHE channel, the primary and secondary component of a binary both evolve into pure helium stars remaining compact. As both stars are restrained from further expansion, they cannot reach the merger.

### 4.2.6 From Wolf-Rayet and red supergiant stars to compact objects

The CHE channel not only yields WRs that are more massive and luminous but also enhances the efficiency of WR production, resulting in the formation of a larger number of WRs compared to the model without CHE. Figure 4.4 shows the stellar type and pre-SN mass plotted against their remnant mass for all the secondary stars that experienced CHE and their counterpart evolved in the NoCHEzams model. Here we focus exclusively on secondary stars, since in our simulations only secondary stars can become chemically quasi-homogeneous. The evolution of the primary star (the first star that fills its Roche lobe) is unaffected. The plot shows that at both  $Z = 0.001$  and  $0.004$  the number of WRs increases by a factor larger than 4. In addition, the production of WRs by CHE suppresses the number of RSGs: the few RSGs in pre-SN phase at  $0.004$  become instead WRs when the star experiences CHE in the CHE10zams model, and remain WR up to the pre-SN phase.

This is the main reason for the drop observed in the right panel of Figure 4.2 at  $Z \leq 0.004$ . As discussed in Section 4.2.5, WRs formed through CHE are more massive at birth than their non-CHE counterparts. Given the limited wind mass loss at low metallicity, a significant portion of their

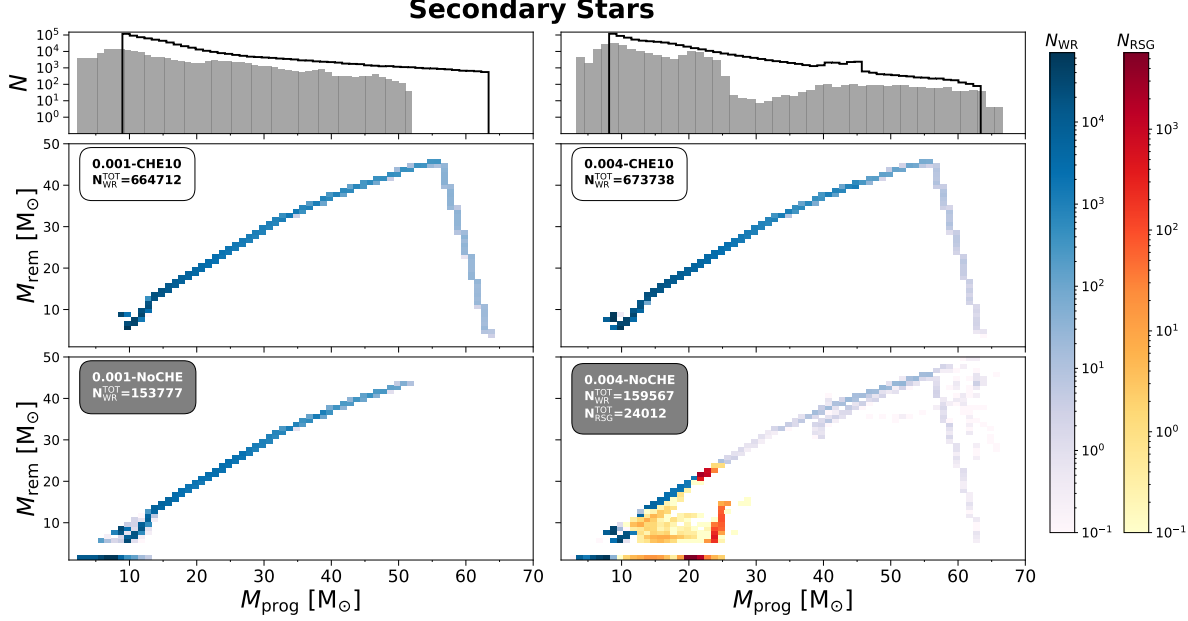


Figure 4.4: Mass of the secondary stars during the pre-SN phase plotted against the resulting compact object mass, exclusively for systems that experience CHE in the CHE10zams model. The blue and red colourmaps depict the number of WRs and RSGs per bin. The upper and lower panels respectively display the progenitor and remnant mass for both the CHE10zams and NoCHEzams models at  $Z = 0.001$  (left) and  $Z = 0.004$  (right). The upper marginal histograms show the distribution of secondary star progenitor masses for the same binaries in the NoCHEzams model (grey-filled histogram) and the CHE10zams model (black histogram).

mass is retained until their pre-SN phase. The marginal histograms in Figure 4.4 display the pre-SN masses of these stars, revealing that, on average, stars undergoing CHE exhibit larger pre-SN masses. Larger pre-SN masses imply also larger remnant masses. In our NoCHEzams model, a non-negligible fraction of stars, primarily RSGs, evolves into neutron stars right after the SN event. In contrast, in the CHE10zams model, none of the secondary stars experiencing CHE gives rise to a neutron star. CHE suppresses the formation of neutron stars in favor of the production of black holes. This has significant implications for the production of BHNSs and BNSs and their respective merger rates.

Finally, we find that pre-SN stars that experience CHE develop a larger helium core if compared to their non-CHE counterparts. Massive helium cores larger than  $\sim 32 M_{\odot}$  efficiently ignites pair-production, and lead the star to evolve as pulsational pair-instability SNe or as pair-instability SNe (Woosley et al. 2007). In the CHE10zams model, pre-SN stars with a mass in the range  $51 - 63 M_{\odot}$  evolve into pulsational-pair instability SNe, and produce less massive BHs. Above this mass range, stars explode as pair-instability SNe, and leave no remnants at all. These stars are not shown in the plot. Pre-SN stars in the NoCHEzams model, on the other hand, have smaller helium cores than their CHE counterparts, and typically require larger  $M_{\text{prog}}$  to trigger efficient pair production. This is especially true at  $Z = 0.001$ , where pulsational pair instability affects all stars in the pre-SN mass range  $51 - 103 M_{\odot}$ , without the occurrence of any pair instability SN. These stars end their life as yellow supergiants, and consequently, they are not displayed in the plot.

### 4.3 Results: Compact object binaries

In this Section, we focus our discussion on the formation of compact object binaries and compact binary mergers. Table 4.2 reports the fraction of binaries with one star undergoing CHE as a function of the simulation model and the metallicity. This fraction is larger for the CHE10zams model since we allow CHE for stars with mass as low as  $10 M_{\odot}$  in the post-accretion phase, which are less rare than stars more massive than  $20 M_{\odot}$  required instead by the CHE20zams model. Nevertheless, even with the CHE20zams prescription, approximately 1 every 20 of our secondary stars evolves into CHE, both at  $Z = 0.001$  and  $Z = 0.004$ .

Since these stars are the progenitors of compact objects, this significantly influences the formation of compact binary mergers. Table 4.2 underscores four primary implications of the CHE scenario:

- CHE enhances the formation of black holes originating from the secondary star, significantly increasing the fraction of BBH and BHNS systems. This is especially true in the CHE10zams model, where at  $Z = 0.001$  we form approximately six times more BHNSs than in the case without CHE: the number of BHNSs overcomes even that of BBHs. In the CHE20zams model, the increase of the number of BBHs and BHNSs is more moderate but still evident at both metallicities.
- The CHE10zams model suppresses the formation of BNSs. This happens because, in this model, metal-poor stars with ZAMS mass as low as  $10 M_{\odot}$  (i.e., neutron star progenitors) can become chemically homogeneous. In this model, many of the stars that would have formed a neutron star evolve instead into a CHE phase to conclude their life as black holes. On the other hand, with the CHE20zams model, where CHE star formation is permitted only for post-accretion masses exceeding  $20 M_{\odot}$ , the formation of BNSs remains almost unchanged at low metallicity ( $Z = 0.001$ ). This is because most of the neutron star progenitors do not become chemically homogeneous. At  $Z = 0.004$ , BNSs are still slightly suppressed even with the CHE20zams model. This is due to the increasing influence of mass loss at higher metallicities, causing some neutron star progenitors to lose mass below  $20 M_{\odot}$ , enter in the CHE state, and eventually evolve into black holes.
- The most striking effect present in both CHE10zams and CHE20zams models is that CHE dramatically reduces the number of all compact binary mergers. The most optimistic scenario occurs with the CHE10zams model at a metallicity of  $Z = 0.001$ , where the fraction of BBH mergers is just 1/3 of the fraction of BBH mergers produced in the NoCHEzams model. This drop in the production of mergers affects all BBHs, BHNS, and BNSs at all metallicities where CHE is active. The reason for this inefficiency in the production of mergers stems from the evolution of the binary systems when one of the two stars enters the CHE phase. When the secondary star becomes almost homogeneous, its radius remains frozen along its evolution, and the two stars in the binary hardly interact anymore. By the time the secondary starts burning helium and evolves into a WR, the primary is either a pure helium star stripped from its envelope, or has already evolved into a compact object. The binary is then composed of two compact stars that cannot trigger any mechanism to efficiently reduce their orbital separation, such as further mass transfer episodes or a common envelope phase. The binary eventually evolves into a binary of compact objects where the mutual separation is too large to allow

gravitational wave emission to become efficient. In this framework, the newborn binary compact object cannot merge within the age of the Universe.

- Finally, in the models where CHE is active, the fraction of BBH and BHNS mergers arising from a system with one CHE star is always relatively large. It ranges from a few percent of the mergers for BHNSs produced at  $Z = 0.001$  in the CHE20zams model to nearly 40% of all BBH mergers at  $Z = 0.004$  in the CHE10zams model. On the contrary, none of the BNS mergers form through the CHE channel. To form, BNS mergers typically require undergoing at least one common envelope phase (e.g. Iorio et al. 2023), a process that is not initiated when the secondary star evolves homogeneously.

In the upcoming sections we discuss the properties of the BBH and BHNS systems and their relative mergers produced in the CHE10zams and NoCHEzams models. We present a further comparison with other models in Section 4.6.

Table 4.2: Percentages of BBHs, BHNSs, and BNSs, mergers, and CHE evolution as a function of the model and the metallicity.

Z	name	P <sub>CHE</sub>	BBH			BHNS			BNS		
			P <sub>cob</sub>	P <sub>merg</sub>	P <sub>CHE</sub> <sub>merg</sub>	P <sub>cob</sub>	P <sub>merg</sub>	P <sub>CHE</sub> <sub>merg</sub>	P <sub>cob</sub>	P <sub>merg</sub>	P <sub>CHE</sub> <sub>merg</sub>
0.001	NoCHEzams	0	4.28	0.92	0	0.97	0.23	0	0.66	0.42	0
	NoCHEpreMS	0	4.28	0.92	0	0.97	0.24	0	0.66	0.41	0
	CHE10zams	14.8	5.17	0.32	22.63	5.76	0.06	19.99	0.17	0.05	0
	CHE10preMS	14.69	5.18	0.31	23.42	5.68	0.06	20.01	0.17	0.05	0
	CHE20zams	4.25	4.69	0.28	13.8	1.38	0.07	3.63	0.62	0.39	0
	CHE20preMS	4.29	4.7	0.28	14.36	1.39	0.07	3.7	0.62	0.39	0
0.004	NoCHEzams	0	3.98	0.59	0	0.94	0.18	0	0.61	0.32	0
	NoCHEpreMS	0	3.98	0.59	0	0.94	0.18	0	0.60	0.32	0
	CHE10zams	14.93	5.43	0.05	37.7	4.72	0.02	32.94	0.20	0.09	0
	CHE10preMS	14.31	5.44	0.05	39.15	4.57	0.02	32.66	0.20	0.10	0
	CHE20zams	5.85	4.86	0.04	12.96	1.67	0.02	12.3	0.45	0.22	0
	CHE20preMS	5.9	4.86	0.04	13.51	1.69	0.02	11.83	0.45	0.22	0

From left to right column: metallicity ( $Z$ ), name of the model, percentage of binaries that experience CHE in the simulation set ( $P_{C\text{HE}}$ ), percentage of compact object binaries produced in the simulation set ( $P_{\text{cob}}$ ), percentage of compact object binary mergers produced in the simulation set ( $P_{\text{merg}}$ ), and percentage of compact object binary mergers that evolve through CHE among all mergers of the simulation set ( $P_{\text{merg}}^{\text{CHE}}$ ). The latter three columns are repeated for BBHs, BHNSs, and BNSs, respectively.

### 4.3.1 Binary black holes

Figure 4.5 reports the total mass, i.e. the sum of the two binary mass components  $M_{\text{tot}} = m_1 + m_2$ , and the semi-major axis at the birth of all our BBH systems formed in the CHE10zams and in the NoCHEzams models at  $Z = 0.001$  and  $Z = 0.004$ . The plot reports the same fractions as Table 4.2, showing that the CHE channel efficiently increases the production of BBH systems at both metallicities. In the NoCHEzams model, the peak for BBHs occurs at  $M_{\text{tot}} \sim 15 M_{\odot}$  and  $a \sim 10 R_{\odot}$ . These BBHs originate from binary systems that undergo stable mass transfer during their early stages. As the secondary star evolves after the first SN, the system subsequently enters a common envelope phase, resulting in a contraction of its orbit<sup>3</sup>.

Conversely, when CHE is active, BBHs concentrate in a different region of the diagram, characterized by larger total masses and orbital separations. In the upper panels of Figure 4.5, BBHs peak at  $M_{\text{tot}} \sim 25 - 30 M_{\odot}$  and  $a \sim 10^2 R_{\odot}$ . These are all BBH systems wherein one of the two stellar progenitors evolved chemically homogeneous. CHE stars are more massive in their pre-SN phase, and produce more massive black holes which in turn form more massive BBHs. Additionally, binaries with the secondary star in the CHE stage are unable to initiate a common envelope phase and rarely undergo further mass exchange. Consequently, BBHs formed through the CHE channel exhibit larger orbital separations compared to their non-CHE counterparts. This is the primary reason why the CHE channel suppresses the formation of BBH mergers. This is clearly shown in Figure 4.6, which displays the same panels as Figure 4.5, focusing specifically on BBH mergers. In the plot, the inclusion of the CHE strongly suppresses the occurrence of BBH mergers. Nevertheless, the BBH formed through the CHE channel still cluster around a total mass of  $\sim 25 M_{\odot}$  at  $Z = 0.001$  and  $\sim 20 M_{\odot}$  at  $Z = 0.004$ . These systems exhibit a distinctive distribution of mass ratios, reported in Figure 4.7.

Generally, mass transfer tends to equally redistribute the mass of the system between the two stars, such that the final mass ratio of BBH mergers tends to 1. In contrast, when the secondary stars evolve chemically homogeneous, the mass accreted from the primary gets fully mixed within the stellar interior of the secondary star. This mass is neither redistributed within the system through subsequent mass transfer episodes nor lost during common envelope phases. The secondary retains all the accreted mass from the primary, and it eventually becomes the most massive component of the binary system. In some cases, the secondary star accretes enough mass to become more than twice as massive as the former primary star.

Figure 4.7 shows that BBH mergers formed through CHE tend to exhibit an asymmetric mass ratio within the range of 0.4 – 0.6 at both  $Z = 0.001$  and  $Z = 0.004$ . This suggests that the accretion-induced CHE channel serves as a mechanism for generating BBH mergers with low mass ratios through isolated formation, without the requirement of any dynamical interactions.

### 4.3.2 Black Hole - Neutron Star binaries

Figure 4.8 displays the orbital separation and black hole mass of all BHNS systems formed in the CHE10zams and NoCHEzams models, at both  $Z = 0.001$  and  $Z = 0.004$ . The upper panels highlight the impressive growth in the number of NSBH formed through CHE. In the CHE10zams model, the black hole companions spread along the same range of masses as in the NoCHEzams model, with the difference that here black holes easily reach  $\sim 15 - 20 M_{\odot}$  at both metallicities, while in the NoCHEzams model most of the black holes are restricted below  $\sim 10 M_{\odot}$ .

---

<sup>3</sup>This formation pathway is commonly referred to as Channel I (Broekgaarden et al. 2021; Iorio et al. 2023).

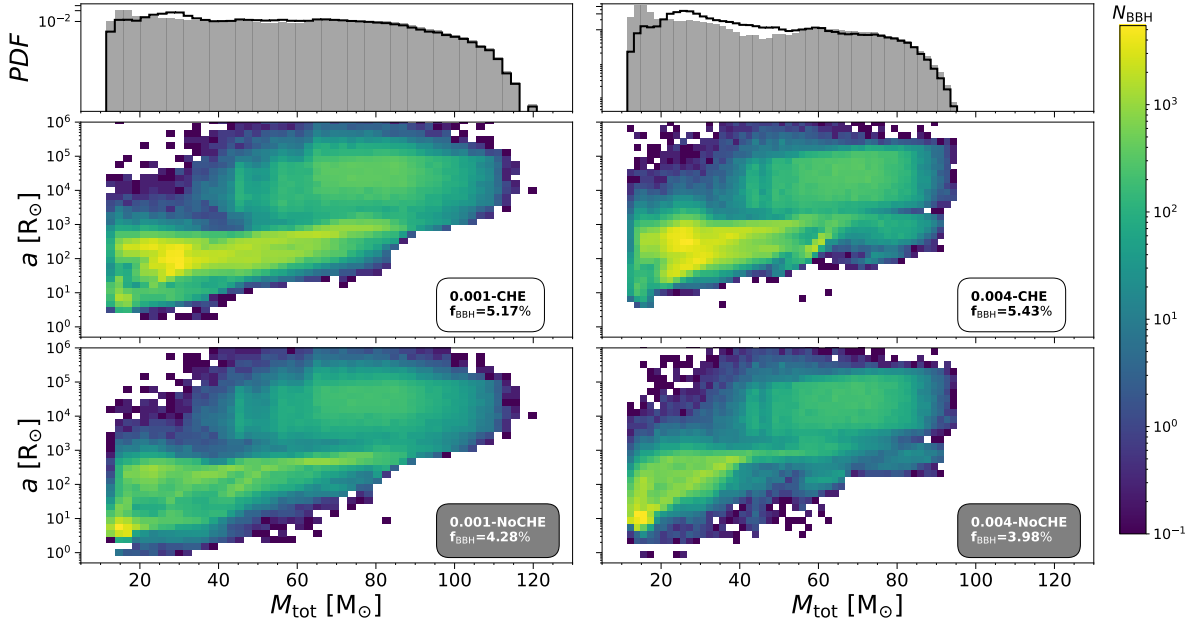


Figure 4.5: Total mass as a function of the semi-major axis for BBHs produced in the CHE10zams models (upper panels) and the NoCHEzams models (lower panels) at metallicities  $Z = 0.001$  (left panels) and  $Z = 0.004$  (right panels). The colormap represents the number of BBHs per bin. The plots also display the fraction of BBHs produced in the simulation set, as documented in Table 4.2. The two marginal histograms show the distributions of the BBHs total mass for the CHE10zams (black histograms) and the NoCHEzams (grey-filled histograms) models at  $Z = 0.001$  (left panel) and  $Z = 0.004$  (right panel).

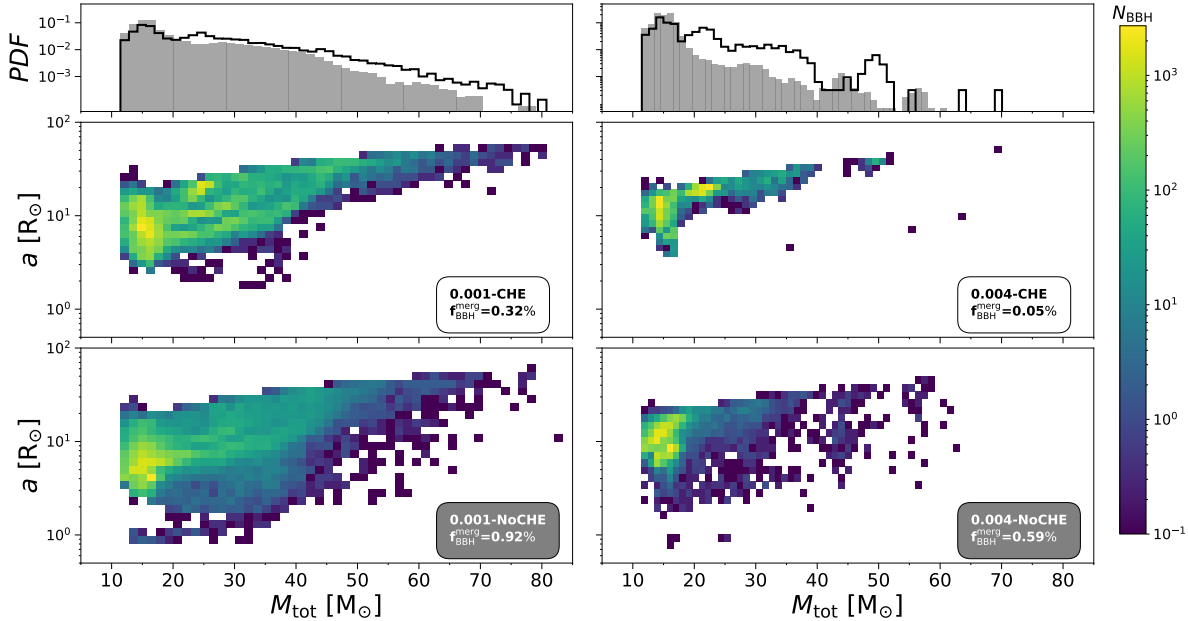


Figure 4.6: Same as Fig. 4.5 but for BBH mergers only.

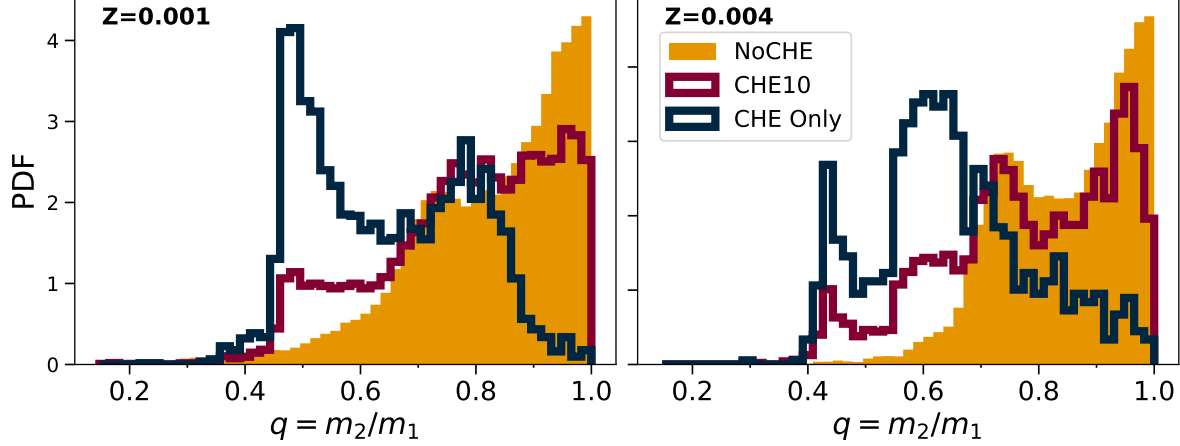


Figure 4.7: Mass ratio distribution for the BBH mergers in the NoCHEzams (orange-filled histograms) and CHE10zams (red histograms) models at  $Z = 0.001$  (left) and  $Z = 0.004$  (right). The plot shows also the distribution only of the binaries in the CHE10zams models that experienced CHE (blue histograms).

BHNS systems formed in the NoCHEzams model follow the traditional formation pathway in which the primary, stripped of its outer envelope, collapses into a black hole, while the secondary, after possibly undergoing a further mass transfer phase, evolves into a neutron star. On the contrary, in the CHE10zams model, black holes can likely have masses more large than  $15 M_{\odot}$ . In the CHE channel, the neutron star progenitor is the primary star. After accreting a substantial amount of mass from the primary star, the secondary star undergoes CHE evolution, ultimately collapsing into a more massive black hole. More massive black holes in the range  $\sim 15 - 25 M_{\odot}$  are a frequent component also of CHE-BHNS mergers, as shown in Figure 4.9. Nevertheless, BHNS formed through CHE suffer the same issue that affects CHE-BBH systems: after the initial mass transfer that triggers the secondary CHE, the two stars in the binary stop interacting and the orbital period remains frozen at large distances. This strongly suppresses the formation of BHNS mergers.

## 4.4 Discussions

### 4.4.1 Accretion vs tidally-induced CHE

In this work, we assumed that the primary mechanism for triggering CHE in a star is through accretion-induced spin-up during Roche lobe overflow. Our assumption is supported by the findings of Sana et al. (2012), who observed that up to 40% of massive stars in binaries could potentially experience spin-up through accretion from their companions. In principle, CHE can also be achieved in both stars of a tight binary system through tidal interactions. In this scenario, the binary reaches tidally locked equilibrium, where the orbital separation between the two stars is reduced by tidal forces to the point where the orbital period is equal to the rotational period of the two stars. As a result, the two stars undergo rapid spin-up, experience rotational mixing, and possibly transition into the CHE state. The main difference with our prescription is that, in general, the tidal spin-up mechanism leads to the formation of more massive BBH systems, with less extreme mass ratio. Additionally, the tidal spin-up mechanism does not hinder the formation of binary black hole mergers, as it exclusively occurs in binaries with already small orbital separations.

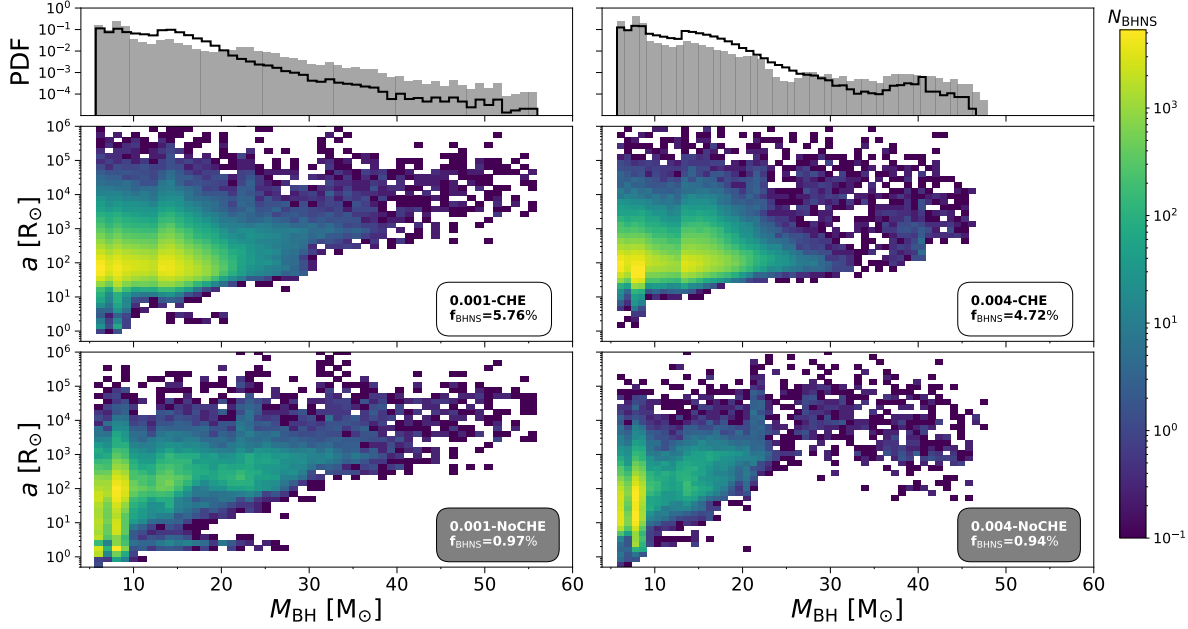


Figure 4.8: Mass of the BH as a function of the semi-major axis for BHNS systems produced in the CHE10zams models (upper panels) and the NoCHEzams models (lower panels) at metallicities  $Z = 0.001$  (left panels) and  $Z = 0.004$  (right panels). The colormap represents the number of BBHs per bin. The plots also display the fraction of BHNS systems produced in the simulation set, as documented in Table 4.2. The two marginal histograms show the distributions of the BH mass in BHNS binaries for the CHE10zams (black histograms) and the NoCHEzams (grey-filled histograms) models at  $Z = 0.001$  (left panel) and  $Z = 0.004$  (right panel).

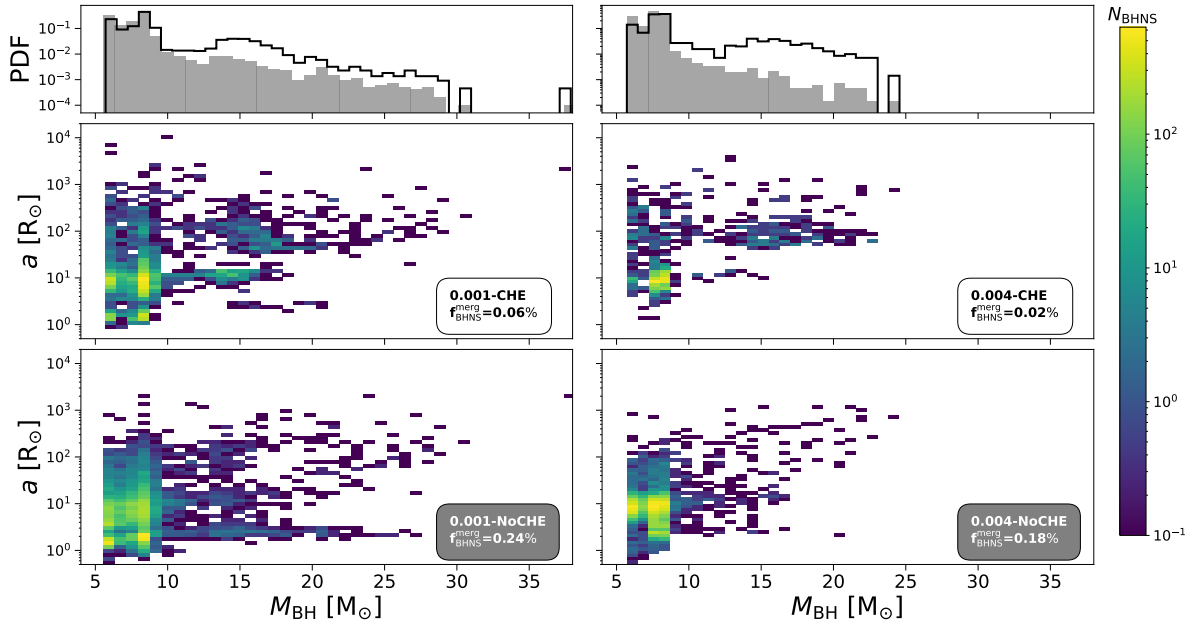


Figure 4.9: Same as Fig. 4.8 but for BHNS mergers only.

Riley et al. (2021) explored the formation of massive BBH mergers through tidal spin-up CHE. They find that only 0.2% of their binary population has at least one component that evolves through CHE. This is because only extremely tight binaries where the two stars are tidally locked can achieve CHE. These conditions are generally met when the period of the binary is smaller than 2 days and both stars are more massive than  $\sim 20 M_{\odot}$  (Song et al. 2016b). In our binary population, only 3% of the binaries have an initial orbital period below 2 days. Additionally, in our CHE10zams model at  $Z = 0.001$ , only  $\sim 19\%$  of all the binaries that evolve through CHE have the orbital period below 2 days when the secondary becomes a chemically homogeneous star. In most of these systems, at least one of the two stars in the binary is typically in the main sequence and possesses a radiative envelope, making tidal forces relatively ineffective. Hence, tidally induced CHE would have affected only a negligible fraction of our binaries. We will include the effect of CHE induced by tidal forces in a forthcoming paper.

## 4.5 Summary

In this work, we have investigated the effects of CHE both on a stellar population and on the subsequent formation of compact binary mergers. We evolved  $1.2 \times 10^8$  binaries and  $5 \times 10^7$  single stars with the state-of-the-art population synthesis code SEVN (Iorio et al. 2023). We specifically focus on the accretion spin-up scenario where CHE is triggered by a Roche-lobe overflow event. Our simulations adopt the prescription presented by Eldridge et al. (2011) and Eldridge et al. (2017), where a star enters in CHE state only if it has a post accretion mass of  $10 M_{\odot}$ , and  $20 M_{\odot}$ , respectively, a metallicity  $Z \leq 0.004$ , and has accreted at least 5% of its initial mass. Our simulations are further divided into two subsets, where we initialized the stars at zero-age-main-sequence and 0.1 Myr from their birth. Finally, we tested our stellar populations at five different metallicities:  $Z = 0.04, 0.02, 0.008, 0.004, 0.01$ .

We find that the accretion spin-up CHE mechanism suppresses the formation of RSGs, favoring instead the production of WRs from secondary stars in binary systems. The RSG to WR ratio of a stellar population decreases with a larger binary fraction, and at the same time, it drops with metallicity due to the CHE below solar metallicity.

The WRs produced by CHE are, on average, more massive, more numerous, and more luminous than WRs produced either via single or common binary evolution. These WR are secondary stars that have accreted a large fraction of mass and angular momentum from the companion. Unlike WRs generated through standard stellar evolution, these stars retain their oversized hydrogen envelope, which is then partially or completely mixed with the stellar interior by rotational mixing. In contrast, conventionally formed WRs are stripped stars that have lost their outer envelope, leading to the creation of less massive and less luminous WRs composed only by the naked core of the progenitor. CHE-assembled WRs remain more massive than their non-CHE counterparts up to the pre-SN phase, and eventually produce more massive compact remnants. In our models, CHE stars favor the production of more massive black holes with a distribution that peaks at  $\sim 15 M_{\odot}$ . Concurrently, CHE models do not produce any neutron stars.

Our simulations show that accretion-induced CHE greatly affects the formation of compact binary systems and their merger. CHE significantly enhances the formation of BBH and BHNS systems, with the latter especially growing by a factor of 6 at  $Z = 0.001$ . The enhanced efficiency in the formation of BHNS systems comes at the cost of a substantial decrease in the production of BNS systems, which number drop by a factor of 4 in the CHE models at  $Z = 0.001$ . Unlike the conventional BHNS formation channel where the primary star evolves into a black hole and the

secondary becomes a neutron star, in our CHE models, the primary experiences mass loss through mass transfer and evolves into a neutron star. Simultaneously, the secondary star enters the CHE stage, undergoes rotational mixing, and gives rise to a black hole. We find that this formation pathway can produce BHNS mergers with a black hole that is likely more massive than black holes in traditionally formed BHNS mergers that do not experience any CHE phase.

CHE completely suppresses the formation of all types of compact binary mergers. Including CHE in our models results in a reduction of approximately one-third in the total number of BBH mergers, one-fourth in BHNS mergers, and one-eighth in BNS mergers compared to their counterparts without CHE, at  $Z = 0.001$ . This suppression is even stronger for BBH and BHNS mergers at  $Z = 0.004$ . In CHE binaries, when the secondary starts evolving chemically homogeneously, the system is composed of a primary that has lost its outer envelope and a secondary that evolves at fixed radius. The two stars cannot expand anymore and the system cannot be further shrunk through additional stable or unstable mass transfer episodes. Consequently, the two stars are destined to maintain large orbital distances. Only if the binary is already sufficiently tight after the first Roche-lobe event it can successfully produce a compact binary merger.

Lastly, we find that CHE can form BBH mergers with asymmetric mass ratio, with a preference for systems with  $q = 0.5$  at  $Z = 0.001$  and  $q = 0.6$  at  $Z = 0.004$ . This result is surprising because systems with low mass ratios are typically attributed to dynamical formation processes rather than the isolated formation channel. In our CHE models the secondary gains enough mass to become the new primary star in the binary, and since the system does not experience any further mass transfers, the binary remains asymmetric up to the formation of the two compact remnants.

## 4.6 Appendix: The CHE20zams model

Here we present the results relative to the CHE20zams model. The RSG to WR ratio is presented in Figure 4.10. The CHE model shows now a milder difference with respect to the NoCHEzams model. This is because stars more massive than  $20 M_{\odot}$  are more rare than stars in the  $10 - 20 M_{\odot}$  mass range, implying that less WRs are produced through CHE. Nevertheless, Figure 4.11 shows that even with a relaxed criterion on the minimal mass for a star to enter the CHE phase, we consistently observe that CHE-produced WRs are, on average, characterized by higher luminosities and masses compared to their non-CHE counterparts. The main difference with the WRs produced by the CHE10zams is that now the minimum WR mass is  $20 M_{\odot}$ , which sets a minimum luminosity threshold at  $4 \times 10^5 L_{\odot}$ . This minimum mass limit is also visible in figure 4.12. In the plot, the minimum mass in the CHE models is lower than  $20 M_{\odot}$  as the panels report the pre-SN mass of these stars. After entering the CHE stage, the newborn WRs experience wind mass loss which decreases their total mass below  $20 M_{\odot}$ . The minimum mass during the pre-SN phase is lower for the model at  $Z = 0.004$  compared to  $Z = 0.001$ , owing to stronger wind mass losses at higher metallicities. The plot shows that even with the CHE20zams model, the production of WRs is enhanced by the CHE, while the formation of RSGs and neutron star remnants is still suppressed. Figure 4.13 shows that the formation of BBH via CHE is slightly less efficient with the CHE20zams model if compared with the CHE10zams model, but still more efficient than the NoCHEzams model. This is due to fewer secondary stars being influenced by the CHE, resulting in a reduced production of BBH systems if compared with our fiducial CHE10zams model. On the other hand, the BBH mergers population presented in figure 4.14 remains almost unaffected by the CHE20zams model as the distribution is comparable with the one relative to the CHE10zams model of Figure 4.6. The main difference is that now, only secondary stars that are already quite massive from their birth can evolve through CHE

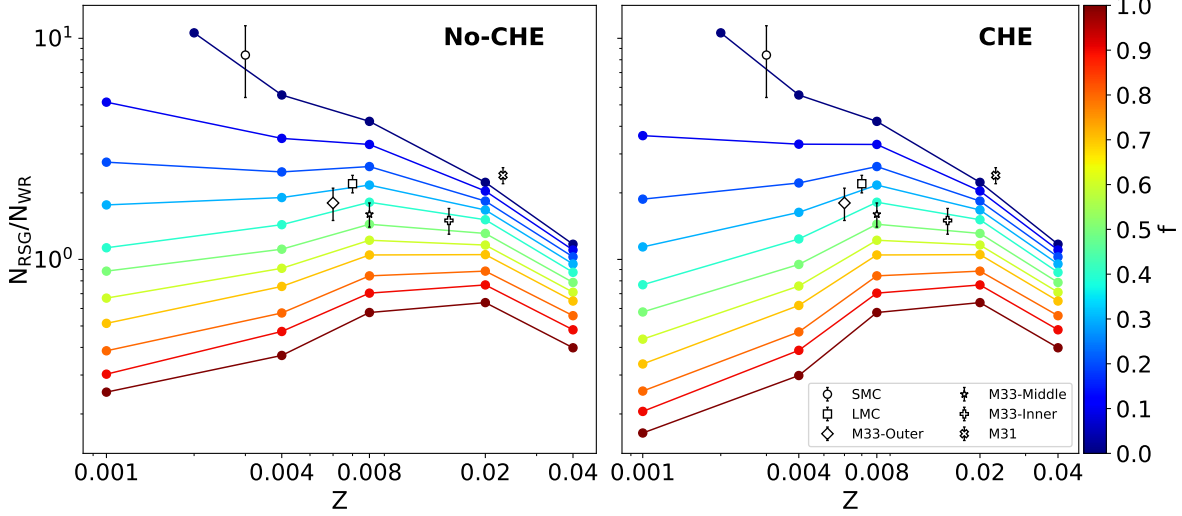


Figure 4.10: Same as figure 4.2 but for the CHE20zams model.

and produce a massive remnant. This affects also the mass ratio of the BBH mergers, which peaks at  $\sim 0.8$  with  $Z = 0.001$  and at  $\sim 0.7$  with  $Z = 0.004$ , as shown in Figure 4.15. The production of BHNS systems remains relatively efficient with the CHE20zams model; however, this efficiency is significantly lower compared to the CHE10zams model. This is shown in Figure 4.16, which also displays a clear peak in the black holes distribution at  $\sim 15 M_{\odot}$  present at both  $Z = 0.001$  and  $Z = 0.004$ . This peak arises from all the black holes produced by secondary stars more massive than  $20 M_{\odot}$  that become chemically homogeneous. Finally, Figure 4.17 shows that BHNS mergers in the CHE model are more likely to involve black holes with masses exceeding  $\sim 15 M_{\odot}$  compared to those formed without CHE. At the same time, the absence of a late common envelope phase due to CHE, as observed in the CHE10zams model, continues to suppress BHNS mergers.

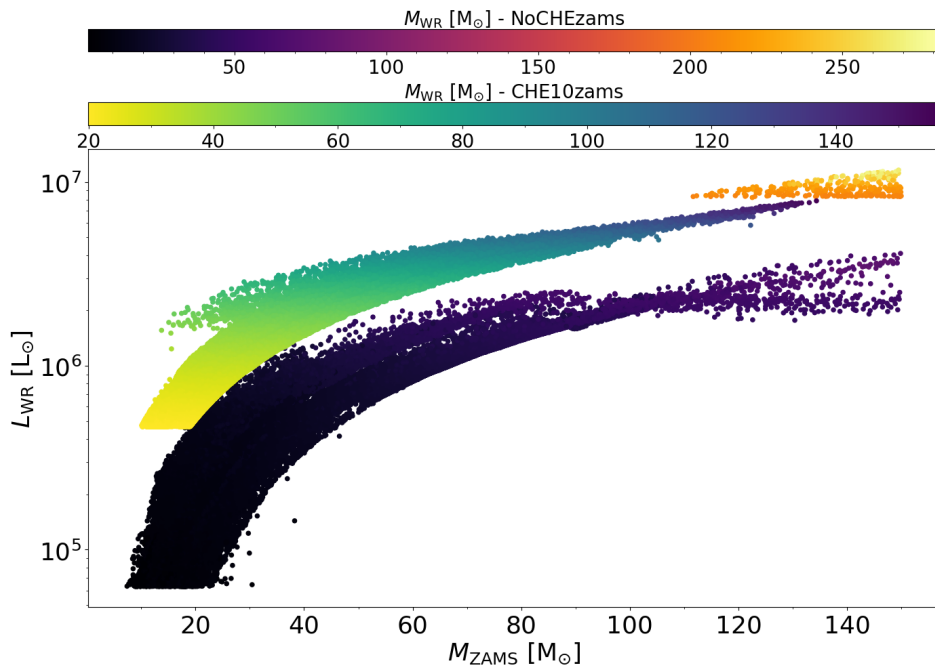


Figure 4.11: Same as figure 4.3 but for the CHE20zams model.

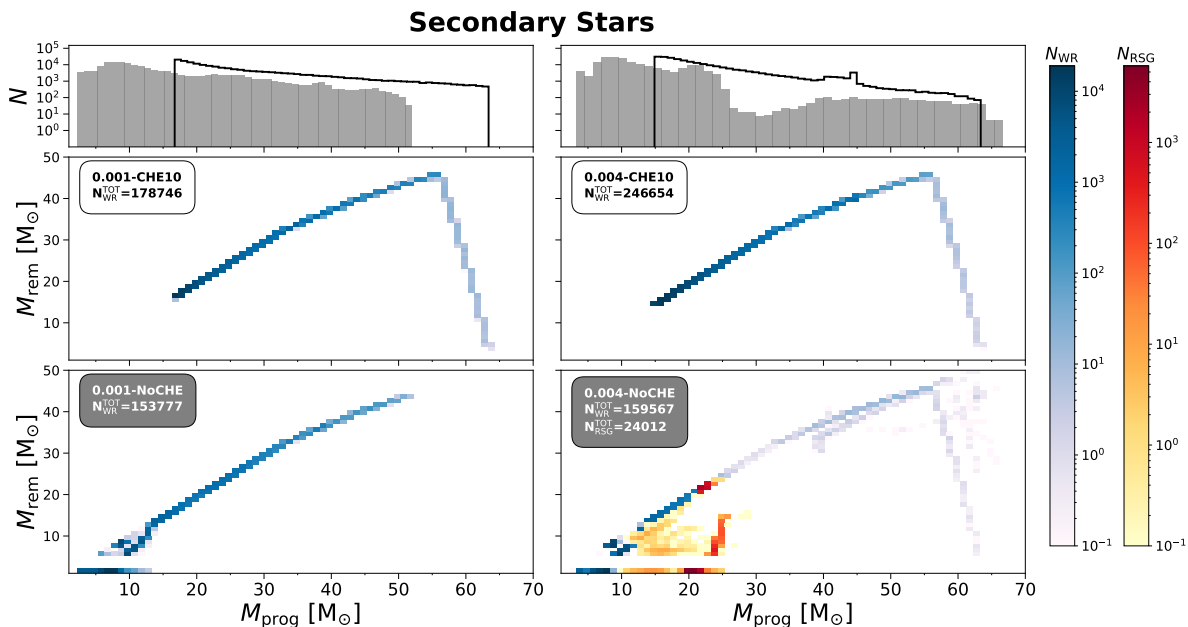


Figure 4.12: Same as figure 4.4 but for the CHE20zams model.

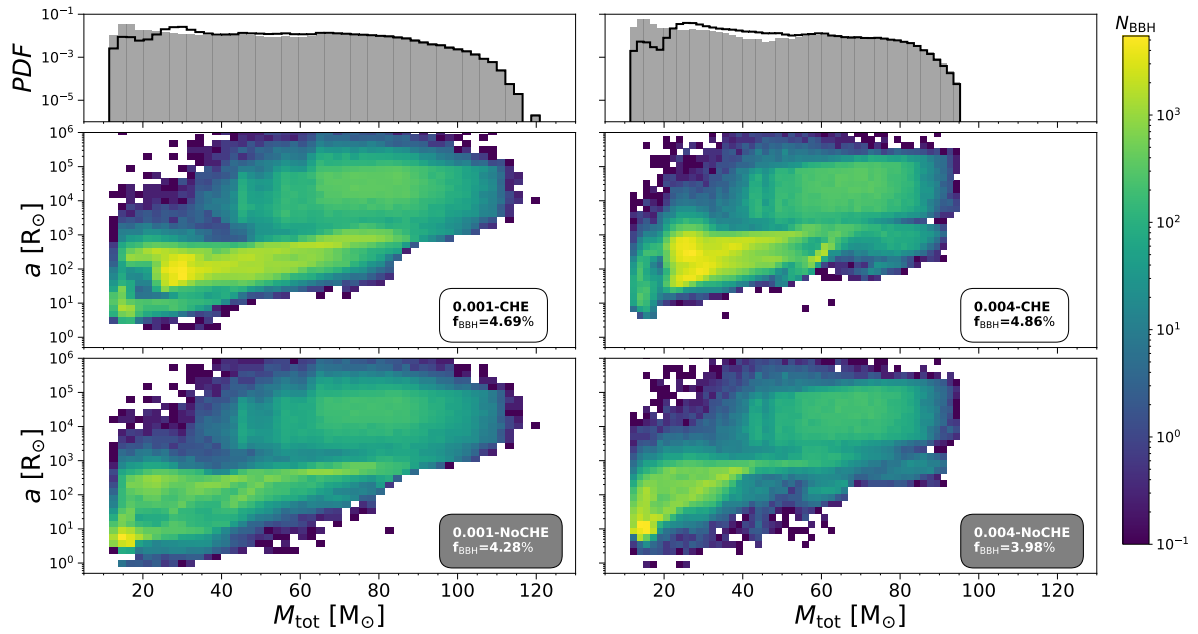


Figure 4.13: Same as figure 4.5 but for the CHE20zams model.

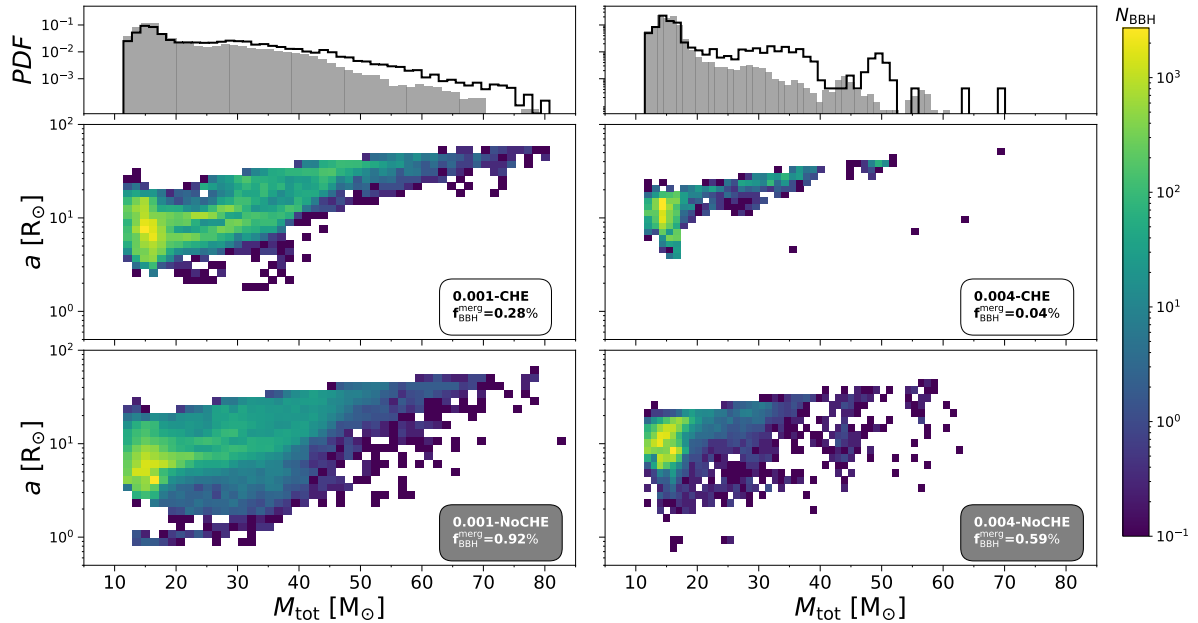


Figure 4.14: Same as figure 4.6 but for the CHE20zams model.

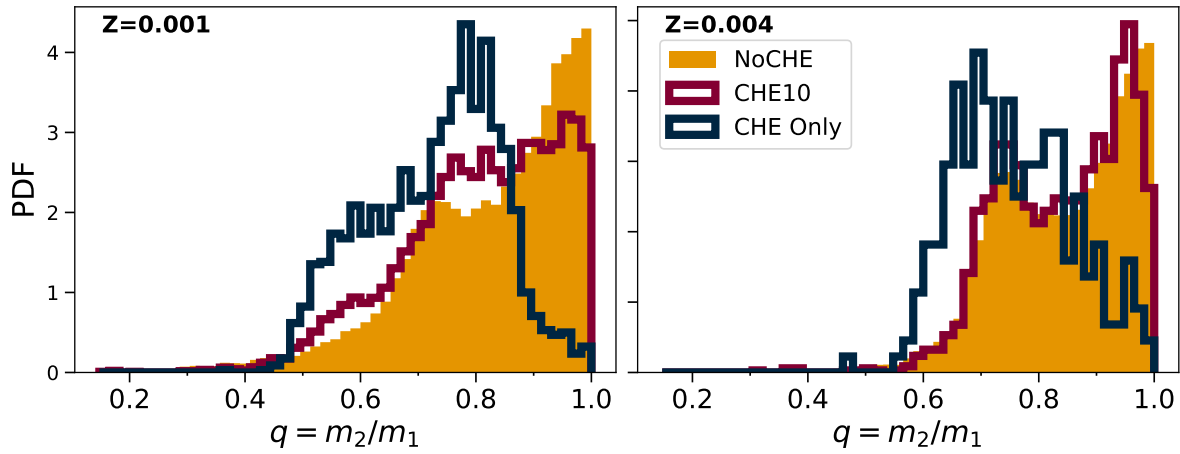


Figure 4.15: Same as figure 4.7 but for the CHE20zams model.

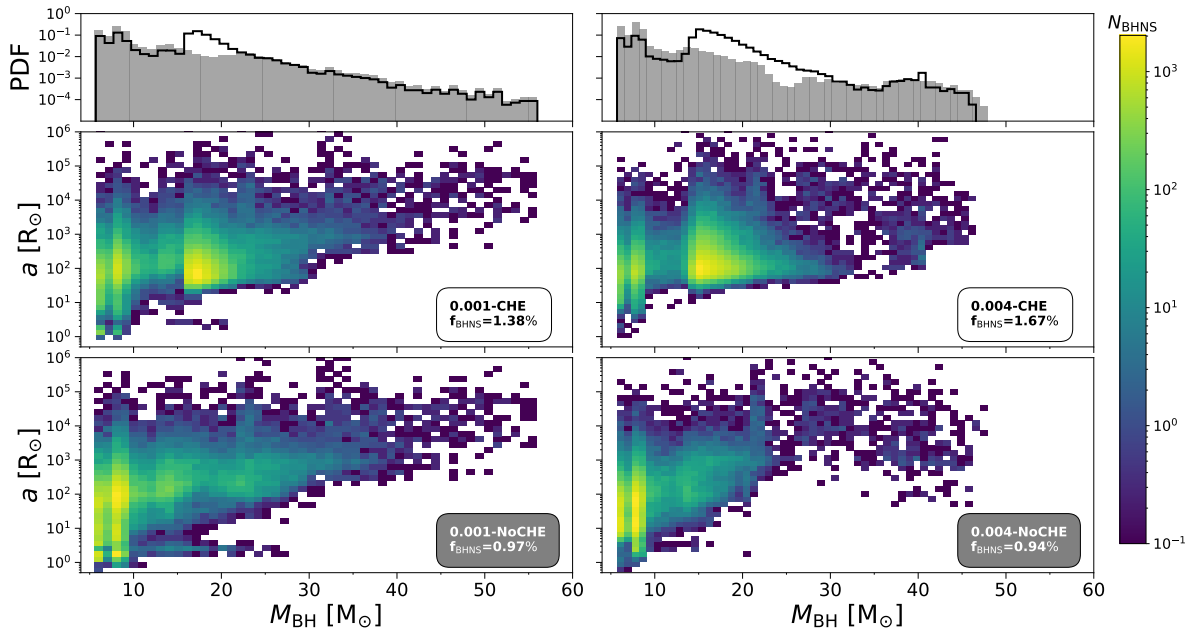


Figure 4.16: Same as figure 4.8 but for the CHE20zams model.

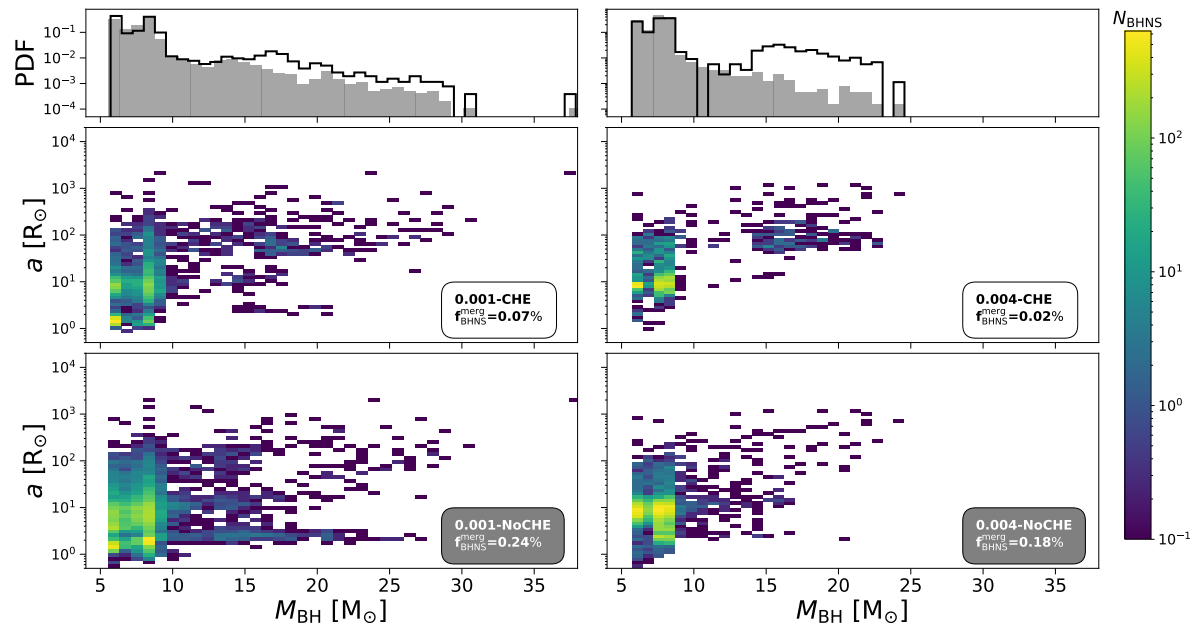


Figure 4.17: Same as figure 4.9 but for the CHE20zams model.



# Chapter 5

## Conclusions and outlook

In this thesis, I delved into the two primary formation processes of compact binary systems. First, I studied the dynamical formation channel of binary black holes (BBHs) by focusing on the chaotic three-body interactions. Next, I explored the effects of binary evolution, and specifically of the chemically homogeneous evolution (CHE), on the formation of compact binary mergers through the isolated formation channel.

In Chapter 2 I focused on GW190521, by far one of the most unique gravitational wave detections reported to date. Out of all the observed gravitational wave events, GW190521 stands on the podium as the most massive BBH ever detected, featuring a primary mass of  $m_1 \simeq 85 M_\odot$  and secondary mass  $m_2 \simeq 66 M_\odot$  in the source frame (Abbott &et al. 2020; Abbott et al. 2020a). The coalescence of these two massive black holes (BHs) produced a  $\sim 140 M_\odot$  BH remnant that lies in the still unexplored intermediate mass range of the BH mass spectrum. Moreover, the primary BH of GW190521 falls inside the so-called pair-instability mass gap: a mass range between  $\sim 60$  to  $\sim 120 M_\odot$  where no BH is expected to form from the collapse of a single star. Finally, the gravitational wave signal from GW190521 exhibits a feature compatible with either the precession effects of the two BHs, implying that their spins were misaligned, or with a non-negligible eccentricity at the merger.

What is the formation channel that best explains these physical features of such a peculiar event? And at what rate should we expect to detect similar events? In the first part of this thesis, I aimed to find an answer to these questions. I studied the dynamical formation of systems like GW190521 in young massive star clusters by means of direct  $N$ -body simulations of three-body interactions with the code ARVW (Mikkola &Aarseth 1989; Chassonney et al. 2019). The simulations include general relativistic corrections necessary to reproduce a dynamical encounter between a binary of BHs with a single BH, known as a three-body encounter. These are the most frequent dynamical interactions that can take place between BHs in the core of star clusters, and as such, are tremendously important for the formation of BH mergers.

From the simulations, I extracted the properties of the first- and second-generation BBH mergers, i.e. binaries where one of the two BHs is itself the result of a previous BH merger, and that in turn merges again creating a new, more massive BH. I compared the features of these mergers with the properties derived from gravitational wave observation of GW190521, and I finally computed the fraction of merger triggered by the three-body interaction that match GW190521. I specifically cross-match all the physical properties of our mergers compatible with the 90% credible interval of all the GW190521 properties reported by Abbott &et al. (2020), i.e. the masses  $m_1$ ,  $m_2$ , the effective and precession spin parameters  $\chi_{\text{eff}}$ ,  $\chi_p$ , and the mass and spin of the remnant  $M_{\text{rem}}$ ,  $\chi_{\text{rem}}$ .

My results show that, over all the simulations, seven of these GW190521-compatible systems are exchanged first-generation binaries where the BH intruder replaced the secondary component of

the initial binary, while five are second-generation BBHs. This translates into a merger rate density of  $\mathcal{R}_{\text{GW190521}} \sim 0.03 \text{ Gpc}^{-3} \text{ yr}^{-1}$  for GW190521-like system formed by the dynamical channel via three-body encounters in young star clusters.

In Chapter 3 of this thesis, I explored in a broader context the properties of BBH mergers produced by three-body interactions. I specifically focused on how the masses, the spins orientation, and the eccentricities at the merger vary as a function of the environment where the dynamical interaction takes place. To reach this purpose, I performed a large sample of direct  $N$ -body simulations of binary-single dynamical interactions in three different families of the environment: young, globular, and nuclear star clusters. In my simulations, BBH mergers produced by three-body encounters, exhibit distinctive features in their properties.

First, They can have larger masses if compared to BHs formed by binary interactions in the isolated channel. This is because, in the dynamical channel, multiple repeated mergers can occur, whereas massive BHs are less likely to be produced through pure stellar evolution of massive stars due to pair-instability. Specifically, mergers in nuclear and globular clusters are efficiently produced with a total merger fraction that spans from 11.8% to 2.4% of all the simulations respectively, while in young star clusters, this efficiency drops to 0.1%. This implies that even less massive BBHs can undergo coalescence within globular and nuclear clusters. Given the large escape velocities of these environments, the BH remnants are likely to be retained and interact again with other BHs. In young clusters, on the other hand, only the most massive systems can merge, and their remnant will be likely ejected from the cluster.

Secondly, dynamical interactions have the effect of randomly re-orienting the spins of the BHs, whereas in pure binary evolution, the two stars evolve with parallel spins due to tidal interactions. If the interaction leads to an exchange event, the spins' orientations are likely to be significantly misaligned. Conversely, if the three-body interaction evolves as a fly-by, the perturbation induces only a slight misalignment, typically a few degrees, in the spin orientation of the two BHs.

Finally, dynamical encounters can be so rapid that gravitational wave emission does not have sufficient time to circularize the binary's orbit before the merger, leading to two BHs merging with eccentricities  $> 0.1$ . These specific events are known as eccentric mergers. Nuclear star clusters result as the most efficient environment for the production of eccentric mergers, with approximately one of these events every  $10^3$  three-body interactions. On the other hand, in globular clusters, we find approximately one eccentric merger every  $10^4$  interactions, while in young star clusters, this number drops to one eccentric event every  $2.5 \times 10^4$  three-body encounters.

Finally, Chapter 4 explores the impacts of CHE on both the observable stellar population through traditional observational surveys and on the population of compact binary mergers detectable using gravitational wave interferometers. CHE occurs in metal-poor binary systems, typically with a metallicity of  $\leq 0.004$ , when one or both stars rapidly increase their rotational velocity up and beyond  $200 \text{ km s}^{-1}$ , causing their interior to become nearly fully mixed (e.g. de Mink et al. 2009). Due to rotational mixing, the heavy elements generated by nuclear fusion in the core of the star are evenly redistributed throughout the entire stellar interior, extending up to the mantle. As a result, the star experiences a change in opacity, and it no longer expands at larger radii. This causes the star to evolve to higher temperatures, resulting in a bluer spectrum, eventually becoming a hot and luminous object known as Wolf-Rayet star (WR).

To study the effects of CHE, I performed a large sample of binary and single evolution simulations at different metallicities with the population synthesis code SEVN (Iorio et al. 2023). I specifically focused on CHE triggered by accretion through the Roche-lobe overflow mass transfer. My results show that binarity and CHE strongly affect the red supergiant (RSG) to WR ratio of a stellar population. In particular, my findings reveal a decline in the ratio with increasing binary fraction,

and show that CHE quenches the ratio at lower metallicities. The former outcome springs from the fact that a larger fraction of binaries results in a higher number of stripped stars losing their envelopes and evolving into WRs. The latter effect arises from CHE favoring the production of WRs over RSGs, as CHE stars mix their hydrogen envelope and turn into WR. Not only WRs are more numerous in the models with CHE, but also their properties differ. WRs produced by CHE are typically more massive and more luminous than WR produced by standard stellar evolution. Furthermore, these stars produce more massive compact remnants, favoring the production of BHs over neutron stars. This significantly influences the production of compact binary systems, boosting the formation of BBH and black hole-neutron star (BHNS) systems, while concurrently suppressing the formation of binary neutron star (BNS) systems.

Yet, the most significant effect of CHE on compact binary systems is its overall quenching of the formation of all BBH, BHNS, and BNS mergers. This follows from the fact that when one of the two stars enters the CHE state, the binary remains composed of two WRs that hardly interact with each other. Consequently, they do not undergo any further binary processes that would decrease their mutual distance, and eventually produce a compact binary system with an orbital separation too large to trigger efficient gravitational wave emission. Finally, my study reveals that compact binary mergers produced through the CHE channel are likely characterized by an asymmetric mass ratio. For instance, CHE-assembled BBH mergers typically exhibit a mass ratio with a peak at  $\leq 0.6$ . In contrast, BHNS mergers formed through CHE are likely composed of BHs with masses up to  $\sim 15 M_\odot$ , whereas BHNS mergers produced through standard binary stellar evolution are more likely to peak at lower masses.

In summary, this thesis provides new insights into the understanding of compact binary merger formation, shedding light on both the dynamical and isolated formation channels. Firstly, it demonstrates that BBHs formed through chaotic dynamics might leave an indelible trace in the gravitational signal under the form of eccentricity or misaligned spins. Here, I emphasize how dynamically-assembled BBH mergers are characterized by larger masses, potentially within the pair-instability mass gap or in the intermediate-mass BH range. Additionally, I presented a real-case scenario explaining the formation history of the peculiar gravitational wave detection GW190521. Secondly, this thesis underscores the critical role of CHE not only in the formation of compact binary mergers but also in shaping the progenitor stellar population. The theoretical approach presented in this work can be used as a tool to reconstruct the formation mechanism of observed WRs. Finally, I demonstrated that CHE stands as a possible binary evolution mechanism capable of producing asymmetric BBH and BHNS mergers via the isolated formation channel.



# List of Figures

1.1	Masses in the stellar graveyard from LVK . . . . .	2
1.2	Predicted number of expected gravitational wave detections . . . . .	3
1.3	Single stellar evolution summary . . . . .	6
1.4	Evolutionary tracks of single stars in the Hertzsprung-Russell diagram . . . . .	7
1.5	Remnant mass ( $M_{\text{rem}}$ ) as a function of the zero-age main sequence mass ( $M_{\text{ZAMS}}$ ) from different metallicities from Spera & Mapelli (2017) . . . . .	9
1.6	Equipotential surfaces of the Roche potential of a binary . . . . .	12
1.7	Phases of the binary evolution in the isolated formation channel of a compact object binary . . . . .	15
1.8	Example of four kind of star clusters . . . . .	20
1.9	Summary of the dynamical evolution of a massive star and its remnant inside a star cluster . . . . .	24
1.10	Semi-major axis evolution over time caused by hardening and gravitational wave emission from Mapelli et al. (2019) . . . . .	27
1.11	Example of a binary black hole dynamical formation channel . . . . .	28
1.12	Dynamical formation history of a binary black hole merger with one of the two components coming from the direct collapse of a stellar collision product from Di Carlo et al. (2019) . . . . .	32
2.1	Primary and secondary masses of the simulated BBH mergers from Dall’Amico et al. (2021) . . . . .	41
2.2	Effective spin parameter $\chi_{\text{eff}}$ versus precessing spin parameter $\chi_p$ for all the BBH mergers from Dall’Amico et al. (2021) . . . . .	42
2.3	Mass of the BH remnant produced by each BBH merger as a function of its dimensionless spin magnitude from Dall’Amico et al. (2021) . . . . .	47
2.4	Mass ratio of the BBH mergers at the end of the simulations from Dall’Amico et al. (2021) . . . . .	48
3.1	Trajectories of three eccentric mergers triggered by a three-body interaction in NSCs and GCs, from Dall’Amico et al. (2023) . . . . .	57
3.2	Percentage of different interaction and merger outcomes for each cluster type, from Dall’Amico et al. (2023) . . . . .	62
3.3	Distribution of coalescence times for unperturbed initial binaries and for the same initial binaries perturbed by the three-body interaction, from Dall’Amico et al. (2021) . . . . .	64
3.4	Total mass of the BBH mergers in YSCs, GCs, and NSCs, from Dall’Amico et al. (2023) . . . . .	65
3.5	Orbital eccentricity at 10 Hz ( $e_{10\text{Hz}}$ ) as a function of the coalescence time ( $t_{\text{coal}}$ ) of BBH mergers in YSCs, GCs, and NSCs; from Dall’Amico et al. (2023) . . . . .	68

3.6	Three-body recoils vs coalescence time for all the BBH mergers that take place after the three-body interactions respectively in the YSCs, GCs; from Dall'Amico et al. (2023) . . . . .	71
3.7	Distribution of the relativistic recoil kick of the remnants produced by the BBH mergers in YSCs, GCs, and NSCs, from Dall'Amico et al. (2023) . . . . .	72
3.8	Tilt angle distributions of the BBH orbital plane in NSCs at the end of the simulation with respect to the initial binary orbital plane, from Dall'Amico et al. (2023) . . . . .	73
3.9	Cumulative distribution function of the impact parameter computed assuming a different prescription for $b_{\max}$ , from Dall'Amico et al. (2023) . . . . .	76
3.10	Same as Fig. 3.2 but assuming a different choice of $b_{\max}$ , from Dall'Amico et al. (2023)	78
3.11	Percentage of BBH mergers over all the simulated encounters in NSCs assuming a variant version of $b_{\max}$ , from Dall'Amico et al. (2023) . . . . .	79
3.12	istograms of the normalized variation of the binary total energy with respect to final binary total energy as a function of $b_{\max}$ , from Dall'Amico et al. (2023) . . . . .	80
4.1	Evolutionary tracks at metallicity $Z = 0.001$ of binary stars and single stars computed with SEVN; from Dall'Amico et al. (2024) . . . . .	87
4.2	RSG-to-WR ratio as a function of metallicity and binary fraction; from Dall'Amico et al. (2024) . . . . .	90
4.3	Masses of WR progenitors at their zero-age main-sequence plotted against the WR luminosity at birth; from Dall'Amico et al. (2024) . . . . .	90
4.4	Mass of the secondary stars during the pre-SN phase plotted against the resulting compact object mass; from Dall'Amico et al. (2024) . . . . .	92
4.5	Total mass as a function of the semi-major axis for BBHs produced with and without CHE,from Dall'Amico et al. (2024) . . . . .	97
4.6	Total mass as a function of the semi-major axis for BBH mergers produced with and without CHE,from Dall'Amico et al. (2024) . . . . .	97
4.7	Mass ratio distribution for the BBH mergers produced with and without CHE; from Dall'Amico et al. (2024) . . . . .	98
4.8	Mass of the BH as a function of the semi-major axis for BHNS systems produced with and without CHE; from Dall'Amico et al. (2024) . . . . .	99
4.9	Mass of the BH as a function of the semi-major axis for BHNS mergers produced with and without CHE; from Dall'Amico et al. (2024) . . . . .	99
4.10	Same as figure 4.2 but for the CHE20zams model. . . . .	102
4.11	Same as figure 4.3 but for the CHE20zams model. . . . .	103
4.12	Same as figure 4.4 but for the CHE20zams model. . . . .	103
4.13	Same as figure 4.5 but for the CHE20zams model. . . . .	104
4.14	Same as figure 4.6 but for the CHE20zams model. . . . .	104
4.15	Same as figure 4.7 but for the CHE20zams model. . . . .	105
4.16	Same as figure 4.8 but for the CHE20zams model. . . . .	105
4.17	Same as figure 4.9 but for the CHE20zams model. . . . .	106

# List of Tables

1.1	Indicative properties of open clusters, globular clusters, nuclear clusters, and young massive star clusters . . . . .	22
2.1	Outcomes of three-body encounters for all the simulations, from Dall'Amico et al. (2021) . . . . .	40
2.2	Outcomes of three-body encounters for BBH mergers only and of BBH mergers that match the masses of GW190521, from Dall'Amico et al. (2021) . . . . .	40
2.3	BBH mergers with masses and spins in the 90% credible intervals of GW190521, from Dall'Amico et al. (2021) . . . . .	45
2.4	Percentage of first-generation BBH mergers that match the main properties of GW190521 as a function of the spin prescription adopted; from Dall'Amico et al. (2021) . . . . .	46
3.1	Initial conditions adopted in Dall'Amico et al. (2023) . . . . .	59
3.2	Percentage of peculiar events in YSCs, GCs, and NSCs from Dall'Amico et al. (2023) . . . . .	63
3.3	Three-body recoil velocities from Dall'Amico et al. (2023) . . . . .	70
4.1	Models employed for our simulations (Dall'Amico et al. 2024) . . . . .	86
4.2	Percentages of BBHs, BHNSs, and BNSs, mergers, and CHE evolution as a function of the model and the metallicity; from Dall'Amico et al. (2024) . . . . .	95

# Bibliography

- Aasi, J., Abadie, J., Abbott, B. P., et al. 2015, Classical and Quantum Gravity, 32, 115012
- Abbott, B. P., Abbott, R., Abbott, T. D., et al. 2016, ApJ, 818, L22
- Abbott, B. P., Abbott, R., Abbott, T. D., et al. 2017, Phys. Rev. Lett., 119, 161101
- Abbott, B. P., Abbott, R., Abbott, T. D., et al. 2017, ApJ, 848, L13
- Abbott, B. P. & al. 2016, Phys. Rev. Lett., 116, 061102
- Abbott, B. P. & et al. 2019, ApJ, 883, 149
- Abbott, B. P. & et al. 2020, ApJ, 892, L3
- Abbott, B. P., LIGO Scientific Collaboration, & Virgo Collaboration. 2019, Physical Review X, 9, 031040
- Abbott, D. C. & Conti, P. S. 1987, ARA&A, 25, 113
- Abbott, R., Abbott, T. D., Abraham, S., et al. 2021a, ApJ, 915, L5
- Abbott, R., Abbott, T. D., Abraham, S., et al. 2020a, ApJ, 900, L13
- Abbott, R., Abbott, T. D., Acernese, F., et al. 2021b, arXiv e-prints, arXiv:2111.03606
- Abbott, R. & et al. 2020, Phys. Rev. D, 102, 043015
- Abbott, R. & et al. 2020, , 125, 101102
- Abbott, R. & et al. 2021a, arXiv e-prints, arXiv:2108.01045
- Abbott, R. & et al. 2021b, ApJ, 913, L7
- Abbott, R. & et al. 2021c, arXiv e-prints, arXiv:2105.15120
- Abbott, R., LIGO Scientific Collaboration, & Virgo Collaboration. 2020b, ApJ, 896, L44
- Abbott, R., LIGO Scientific Collaboration, & Virgo Collaboration. 2021c, Physical Review X, 11, 021053
- Abbott, R., LIGO Scientific Collaboration, VIRGO Collaboration, & KAGRA Collaboration. 2023, Physical Review X, 13, 011048
- Acernese, F. e. a. 2015, Classical and Quantum Gravity, 32, 024001

- Adhikari, R. X., Arai, K., Brooks, A. F., et al. 2020, Classical and Quantum Gravity, 37, 165003
- Akmal, A., Pandharipande, V. R., & Ravenhall, D. G. 1998, , 58, 1804
- Amaro-Seoane, P. & Chen, X. 2016, MNRAS, 458, 3075
- Ambartsumian, V. A. 1937, , 14, 207
- Anagnostou, O., Trenti, M., & Melatos, A. 2020, arXiv e-prints, arXiv:2010.06161
- Anders, E. H., Jermyn, A. S., Lecoanet, D., & Brown, B. P. 2022, ApJ, 926, 169
- Antonini, F., Gieles, M., & Gualandris, A. 2019, MNRAS, 486, 5008
- Antonini, F. & Rasio, F. A. 2016, ApJ, 831, 187
- Arca Sedda, M. 2020a, ApJ, 891, 47
- Arca Sedda, M. 2020b, Communications Physics, 3, 43
- Arca Sedda, M. 2021, ApJ, 908, L38
- Arca-Sedda, M. & Capuzzo-Dolcetta, R. 2019, MNRAS, 483, 152
- Arca Sedda, M., Li, G., & Kocsis, B. 2021a, A&A, 650, A189
- Arca Sedda, M., Li, G., & Kocsis, B. 2021b, A&A, 650, A189
- Arca Sedda, M., Mapelli, M., Benacquista, M., & Spera, M. 2021c, arXiv e-prints, arXiv:2109.12119
- Arca Sedda, M., Mapelli, M., Spera, M., Benacquista, M., & Giacobbo, N. 2020, ApJ, 894, 133
- Arca Sedda, M., Rizzato, F. P., Naab, T., et al. 2021d, arXiv e-prints, arXiv:2105.07003
- Aso, Y., Michimura, Y., Somiya, K., et al. 2013, , 88, 043007
- Atallah, D., Trani, A. A., Kremer, K., et al. 2022, arXiv e-prints, arXiv:2211.09670
- Ballone, A., Costa, G., Mapelli, M., et al. 2023, MNRAS, 519, 5191
- Banerjee, S. 2017, MNRAS, 467, 524
- Banerjee, S. 2018a, MNRAS, 473, 909
- Banerjee, S. 2018b, MNRAS, 481, 5123
- Banerjee, S. 2021, MNRAS, 500, 3002
- Banerjee, S., Baumgardt, H., & Kroupa, P. 2010, MNRAS, 402, 371
- Banerjee, S., Olejak, A., & Belczynski, K. 2023, arXiv e-prints, arXiv:2302.10851
- Bartos, I., Kocsis, B., Haiman, Z., & Márka, S. 2017, ApJ, 835, 165
- Baumgardt, H., De Marchi, G., & Kroupa, P. 2008, ApJ, 685, 247
- Bavera, S. S., Fragos, T., Qin, Y., et al. 2020, A&A, 635, A97

- Belczynski, K. 2020, ApJ, 905, L15
- Belczynski, K., Heger, A., Gladysz, W., et al. 2016, A&A, 594, A97
- Benacquista, M. J. & Downing, J. M. B. 2013, Living Reviews in Relativity, 16, 4
- Bianchini, P., van de Ven, G., Norris, M. A., Schinnerer, E., & Varri, A. L. 2016, MNRAS, 458, 3644
- Binney, J. & Tremaine, S. 2008, Galactic Dynamics: Second Edition
- Boekholt, T. C. N., Moerman, A., & Portegies Zwart, S. F. 2021, , 104, 083020
- Boekholt, T. C. N., Portegies Zwart, S. F., & Valtonen, M. 2020, MNRAS, 493, 3932
- Böker, T. 2010, in Star Clusters: Basic Galactic Building Blocks Throughout Time and Space, ed. R. de Grijs & J. R. D. Lépine, Vol. 266, 58–63
- Bondi, H. & Hoyle, F. 1944, MNRAS, 104, 273
- Borhanian, S. & Sathyaprakash, B. S. 2022, arXiv e-prints, arXiv:2202.11048
- Bouffanais, Y., Mapelli, M., Gerosa, D., et al. 2019, ApJ, 886, 25
- Bouffanais, Y., Mapelli, M., Santoliquido, F., et al. 2021, MNRAS, 507, 5224
- Breen, P. G. & Heggie, D. C. 2013a, MNRAS, 432, 2779
- Breen, P. G. & Heggie, D. C. 2013b, MNRAS, 436, 584
- Bressan, A., Marigo, P., Girardi, L., et al. 2012, MNRAS, 427, 127
- Broekgaarden, F. S., Berger, E., Neijssel, C. J., et al. 2021, MNRAS, 508, 5028
- Bromm, V. 2013, Reports on Progress in Physics, 76, 112901
- Bromm, V. & Larson, R. B. 2004, ARA&A, 42, 79
- Brott, I., de Mink, S. E., Cantiello, M., et al. 2011a, A&A, 530, A115
- Brott, I., de Mink, S. E., Cantiello, M., et al. 2011b, A&A, 530, A115
- Brott, I., Evans, C. J., Hunter, I., et al. 2011c, A&A, 530, A116
- Brunish, W. M., Gallagher, J. S., & Truran, J. W. 1986, AJ, 91, 598
- Brunish, W. M. & Truran, J. W. 1982, ApJS, 49, 447
- Bustillo, J. C., Sanchis-Gual, N., Torres-Forné, A., & Font, J. A. 2021, , 126, 201101
- Cantiello, M., Yoon, S. C., Langer, N., & Livio, M. 2007, A&A, 465, L29
- Carr, B. J. 1975, ApJ, 201, 1
- Chandrasekhar, S. 1931, ApJ, 74, 81
- Chandrasekhar, S. 1943, ApJ, 97, 255

- Chassonney, P. & Capuzzo-Dolcetta, R. 2021, MNRAS, 504, 3909–3921
- Chassonney, P., Capuzzo-Dolcetta, R., & Mikkola, S. 2019, arXiv e-prints, arXiv:1910.05202
- Chatterjee, S., Rodriguez, C. L., Kalogera, V., & Rasio, F. A. 2017a, ApJ, 836, L26
- Chatterjee, S., Rodriguez, C. L., & Rasio, F. A. 2017b, ApJ, 834, 68
- Chen, X. & Amaro-Seoane, P. 2017, ApJ, 842, L2
- Chen, Y., Bressan, A., Girardi, L., et al. 2015, MNRAS, 452, 1068
- Chiosi, C. & Maeder, A. 1986, ARA&A, 24, 329
- Chiosi, C., Nasi, E., & Bertelli, G. 1979, A&A, 74, 62
- Claeys, J. S. W., Pols, O. R., Izzard, R. G., Vink, J., & Verbunt, F. W. M. 2014a, A&A, 563, A83
- Claeys, J. S. W., Pols, O. R., Izzard, R. G., Vink, J., & Verbunt, F. W. M. 2014b, A&A, 563, A83
- Clausen, D., Sigurdsson, S., & Chernoff, D. F. 2013, MNRAS, 428, 3618
- Codazzo, E., Di Giovanni, M., Harms, J., Dall’Amico, M., & Mapelli, M. 2023, , 107, 023023
- Colgate, S. A. 1967, ApJ, 150, 163
- Conti, P. S. 1975a, Memoires of the Societe Royale des Sciences de Liege, 9, 193
- Conti, P. S. 1975b, Memoires of the Societe Royale des Sciences de Liege, 9, 193
- Corral-Santana, J. M., Casares, J., Muñoz-Darias, T., et al. 2016, A&A, 587, A61
- Costa, G., Ballone, A., Mapelli, M., & Bressan, A. 2022, MNRAS, 516, 1072
- Costa, G., Bressan, A., Mapelli, M., et al. 2021a, MNRAS, 501, 4514
- Costa, G., Bressan, A., Mapelli, M., et al. 2021b, MNRAS, 501, 4514
- Costa, G., Chruścińska, M., Klencki, J., et al. 2023a, arXiv e-prints, arXiv:2311.15778
- Costa, G., Chruścińska, M., Klencki, J., et al. 2023b, arXiv e-prints, arXiv:2311.15778
- Costa, G., Girardi, L., Bressan, A., et al. 2019, MNRAS, 485, 4641
- Crowther, P. A., Dessart, L., Hillier, D. J., Abbott, J. B., & Fullerton, A. W. 2002, A&A, 392, 653
- Cui, Z., Wang, Z., Zhu, C., et al. 2018, PASP, 130, 084202
- Dall’Amico, M., Mapelli, M., Di Carlo, U. N., et al. 2021, MNRAS, 508, 3045
- Dall’Amico, M., Mapelli, M., Torniamenti, S., & Arca Sedda, M. 2023, arXiv e-prints, arXiv:2303.07421
- Davies, B., Crowther, P. A., & Beasor, E. R. 2018, MNRAS, 478, 3138
- de Jager, C., Nieuwenhuijzen, H., & van der Hucht, K. A. 1988, A&AS, 72, 259

- de Mink, S. E., Cantiello, M., Langer, N., et al. 2009, A&A, 497, 243
- de Mink, S. E., Langer, N., Izzard, R. G., Sana, H., & de Koter, A. 2013, ApJ, 764, 166
- de Mink, S. E. & Mandel, I. 2016, MNRAS, 460, 3545
- Dewi, J. D. M. & Pols, O. R. 2003, MNRAS, 344, 629
- Di Carlo, U. N., Giacobbo, N., Mapelli, M., et al. 2019, MNRAS, 487, 2947
- Di Carlo, U. N., Mapelli, M., Bouffanais, Y., et al. 2020a, MNRAS, 497, 1043
- Di Carlo, U. N., Mapelli, M., Bouffanais, Y., et al. 2020b, MNRAS, 497, 1043
- Di Carlo, U. N., Mapelli, M., Giacobbo, N., et al. 2020c, MNRAS, 498, 495
- Doctor, Z., Wysocki, D., O'Shaughnessy, R., Holz, D. E., & Farr, B. 2020, ApJ, 893, 35
- Dominik, M., Belczynski, K., Fryer, C., et al. 2012, ApJ, 759, 52
- Donati, J. F. & Landstreet, J. D. 2009, ARA&A, 47, 333
- du Buisson, L., Marchant, P., Podsiadlowski, P., et al. 2020, MNRAS, 499, 5941
- Eddington, A. S. 1925a, The Observatory, 48, 73
- Eddington, A. S. 1925b, The Observatory, 48, 73
- Eggleton, P. P. 1983, ApJ, 268, 368
- Einstein, A. 1916, Sitzungsberichte der Königlich Preussischen Akademie der Wissenschaften, 688
- Ekström, S., Georgy, C., Eggenberger, P., et al. 2012, A&A, 537, A146
- El-Badry, K., Rix, H.-W., Quataert, E., et al. 2023, MNRAS, 518, 1057
- Eldridge, J. J., Izzard, R. G., & Tout, C. A. 2008, MNRAS, 384, 1109
- Eldridge, J. J., Langer, N., & Tout, C. A. 2011, MNRAS, 414, 3501
- Eldridge, J. J. & Stanway, E. R. 2016, MNRAS, 462, 3302
- Eldridge, J. J., Stanway, E. R., & Tang, P. N. 2019, MNRAS, 482, 870
- Eldridge, J. J., Stanway, E. R., Xiao, L., et al. 2017, , 34, e058
- Elmegreen, B. G. & Scalo, J. 2004, ARA&A, 42, 211
- Espinosa Lara, F. & Rieutord, M. 2011, A&A, 533, A43
- Ezquiaga, J. M. & Holz, D. E. 2021, ApJ, 909, L23
- Farmer, R., Renzo, M., de Mink, S. E., Fishbach, M., & Justham, S. 2020, ApJ, 902, L36
- Farmer, R., Renzo, M., de Mink, S. E., Marchant, P., & Justham, S. 2019, ApJ, 887, 53

- Farrell, E., Groh, J. H., Hirschi, R., et al. 2021, MNRAS, 502, L40
- Ferrarese, L. & Ford, H. 2005, Space Sci. Rev., 116, 523
- Fishbach, M. & Holz, D. E. 2020, ApJ, 904, L26
- Fishbach, M., Holz, D. E., & Farr, B. 2017, ApJ, 840, L24
- Fitchett, M. J. 1983, MNRAS, 203, 1049
- Fragione, G. & Loeb, A. 2021, MNRAS, 502, 3879
- Fragione, G., Loeb, A., & Rasio, F. A. 2020, ApJ, 902, L26
- Fragione, G. & Silk, J. 2020, MNRAS, 498, 4591
- Fragos, T., Andrews, J. J., Ramirez-Ruiz, E., et al. 2019, ApJ, 883, L45
- Fragos, T. & McClintock, J. E. 2015, ApJ, 800, 17
- Fregeau, J. M., Cheung, P., Portegies Zwart, S. F., & Rasio, F. A. 2004, MNRAS, 352, 1
- Fregeau, J. M., Joshi, K. J., Portegies Zwart, S. F., & Rasio, F. A. 2002, ApJ, 570, 171
- Fryer, C., Benz, W., Herant, M., & Colgate, S. A. 1999, ApJ, 516, 892
- Fryer, C. L., Belczynski, K., Wiktorowicz, G., et al. 2012, ApJ, 749, 91
- Gaburov, E., Gualandris, A., & Portegies Zwart, S. 2008, MNRAS, 384, 376
- Gaburov, E., Lombardi, James C., J., & Portegies Zwart, S. 2010, MNRAS, 402, 105
- Gayathri, V., Healy, J., Lange, J., et al. 2020, arXiv e-prints, arXiv:2009.05461
- Georgiev, I. Y., Puzia, T. H., Hilker, M., & Goudfrooij, P. 2009, MNRAS, 392, 879
- Georgy, C., Ekström, S., Eggenberger, P., et al. 2013, A&A, 558, A103
- Georgy, C., Meynet, G., Walder, R., Folini, D., & Maeder, A. 2009, A&A, 502, 611
- Gerosa, D. & Berti, E. 2017, , 95, 124046
- Gerosa, D., Berti, E., O'Shaughnessy, R., et al. 2018, , 98, 084036
- Gerosa, D. & Fishbach, M. 2021, Nature Astronomy, 5, 749
- Gessner, A. & Janka, H.-T. 2018, ApJ, 865, 61
- Ghodla, S., Eldridge, J. J., Stanway, E. R., & Stevance, H. F. 2023, MNRAS, 518, 860
- Giacobbo, N. & Mapelli, M. 2018a, MNRAS, 480, 2011
- Giacobbo, N. & Mapelli, M. 2018b, MNRAS, 480, 2011
- Giacobbo, N. & Mapelli, M. 2019, MNRAS, 482, 2234
- Giacobbo, N. & Mapelli, M. 2020, ApJ, 891, 141

- Giacobbo, N., Mapelli, M., & Spera, M. 2018, MNRAS, 474, 2959
- Gieles, M., Heggie, D. C., & Zhao, H. 2011, MNRAS, 413, 2509
- Gieles, M., Portegies Zwart, S. F., Baumgardt, H., et al. 2006, MNRAS, 371, 793
- Giersz, M., Heggie, D. C., & Hurley, J. R. 2008, MNRAS, 388, 429
- Gilkis, A., Shenar, T., Ramachandran, V., et al. 2021, MNRAS, 503, 1884
- Gondán, L. & Kocsis, B. 2021, MNRAS, 506, 1665
- González, E., Kremer, K., Chatterjee, S., et al. 2021, ApJ, 908, L29
- Goodman, J. & Hut, P. 1993, ApJ, 403, 271
- Gräfener, G. & Hamann, W. R. 2008, A&A, 482, 945
- Greene, J. E., Strader, J., & Ho, L. C. 2020, ARA&A, 58, 257
- Gültekin, K., Miller, M. C., & Hamilton, D. P. 2006, ApJ, 640, 156
- Gürkan, M. A., Freitag, M., & Rasio, F. A. 2004, ApJ, 604, 632
- Haiman, Z. & Loeb, A. 1997, ApJ, 483, 21
- Han, Z., Podsiadlowski, P., & Eggleton, P. P. 1994, MNRAS, 270, 121
- Harris, W. E. 2010, arXiv e-prints, arXiv:1012.3224
- Healy, J. & Lousto, C. O. 2018, , 97, 084002
- Heger, A., Fryer, C. L., Woosley, S. E., Langer, N., & Hartmann, D. H. 2003, ApJ, 591, 288
- Heger, A., Langer, N., & Woosley, S. E. 2000, ApJ, 528, 368
- Heger, A. & Woosley, S. E. 2002, ApJ, 567, 532
- Heggie, D. & Hut, P. 2003, The Gravitational Million-Body Problem: A Multidisciplinary Approach to Star Cluster Dynamics
- Heggie, D. C. 1975, MNRAS, 173, 729
- Hills, J. G. 1975, AJ, 80, 809
- Hills, J. G. 1983a, AJ, 88, 1269
- Hills, J. G. 1983b, AJ, 88, 1269
- Hills, J. G. & Fullerton, L. W. 1980a, AJ, 85, 1281
- Hills, J. G. & Fullerton, L. W. 1980b, AJ, 85, 1281
- Holgado, A. M., Ortega, A., & Rodriguez, C. L. 2021, ApJ, 909, L24
- Humphreys, R. M. & Davidson, K. 1979, ApJ, 232, 409

- Hunter, I., Dufton, P. L., Smartt, S. J., et al. 2007, A&A, 466, 277
- Hurley, J. R., Tout, C. A., & Pols, O. R. 2002, MNRAS, 329, 897
- Hut, P. 1981, A&A, 99, 126
- Hut, P. 1983, ApJ, 268, 342
- Hut, P. 1993, ApJ, 403, 256
- Hut, P. & Bahcall, J. N. 1983, ApJ, 268, 319
- Iben, Icko, J. & Livio, M. 1993, PASP, 105, 1373
- Iorio, G., Mapelli, M., Costa, G., et al. 2023, MNRAS, 524, 426
- Ivanova, N. & Chaichenets, S. 2011, ApJ, 731, L36
- Ivanova, N., Justham, S., Chen, X., et al. 2013, A&A Rev., 21, 59
- Ivanova, N., Podsiadlowski, P., & Spruit, H. 2002, MNRAS, 334, 819
- Ivanova, N. & Taam, R. E. 2003, ApJ, 599, 516
- Janka, H.-T. 2012, Annual Review of Nuclear and Particle Science, 62, 407
- Jiménez-Forteza, X., Keitel, D., Husa, S., et al. 2017, , 95, 064024
- Jones, S., Röpke, F. K., Fryer, C., et al. 2019, A&A, 622, A74
- Khlopov, M. Y. 2010, Research in Astronomy and Astrophysics, 10, 495
- Kimball, C., Talbot, C., Berry, C. P. L., et al. 2021, ApJ, 915, L35
- Kimpson, T. O., Spera, M., Mapelli, M., & Ziosi, B. M. 2016, MNRAS, 463, 2443
- King, I. R. 1966, AJ, 71, 64
- Kippenhahn, R., Weigert, A., & Weiss, A. 2013, Stellar Structure and Evolution
- Klencki, J., Nelemans, G., Istrate, A. G., & Chruslinska, M. 2021, A&A, 645, A54
- Klencki, J., Nelemans, G., Istrate, A. G., & Pols, O. 2020, A&A, 638, A55
- Klessen, R. S. & Glover, S. C. O. 2023, ARA&A, 61, 65
- Köhler, K., Langer, N., de Koter, A., et al. 2015, A&A, 573, A71
- Kormendy, J. & Ho, L. C. 2013, ARA&A, 51, 511
- Kozai, Y. 1962, AJ, 67, 591
- Kremer, K., Spera, M., Becker, D., et al. 2020, ApJ, 903, 45
- Kroupa, P. 2001, MNRAS, 322, 231
- Kroupa, P. & Boily, C. M. 2002, MNRAS, 336, 1188

- Kruckow, M. U., Tauris, T. M., Langer, N., et al. 2016, A&A, 596, A58
- Kumamoto, J., Fujii, M. S., & Tanikawa, A. 2019, MNRAS, 486, 3942
- Kumamoto, J., Fujii, M. S., & Tanikawa, A. 2020, MNRAS, 495, 4268
- Lada, C. J. & Lada, E. A. 2003, ARA&A, 41, 57
- Langer, N. 1992, A&A, 265, L17
- Lattimer, J. M. & Prakash, M. 2004, Science, 304, 536
- Lee, H. M. 1995, MNRAS, 272, 605
- Lidov, M. L. 1962, , 9, 719
- Limongi, M. & Chieffi, A. 2018, ApJS, 237, 13
- Liu, B. & Lai, D. 2021, MNRAS, 502, 2049
- Livio, M. & Soker, N. 1988, ApJ, 329, 764
- Loeb, A. & Barkana, R. 2001, ARA&A, 39, 19
- Lombardi, James C., J., Rasio, F. A., & Shapiro, S. L. 1996, ApJ, 468, 797
- Lousto, C. O., Zlochower, Y., Dotti, M., & Volonteri, M. 2012, , 85, 084015
- MacLeod, M. & Ramirez-Ruiz, E. 2015, ApJ, 803, 41
- Madau, P. & Rees, M. J. 2001, ApJ, 551, L27
- Maeder, A. 1987, A&A, 178, 159
- Maeder, A. 1992, A&A, 264, 105
- Maeder, A. 1999, A&A, 347, 185
- Maeder, A. 2009, Physics, Formation and Evolution of Rotating Stars
- Maeder, A. & Meynet, G. 2000a, ARA&A, 38, 143
- Maeder, A. & Meynet, G. 2000b, ARA&A, 38, 143
- Maeder, A. & Meynet, G. 2001, A&A, 373, 555
- Maggiore, M. 2018, Gravitational Waves: Volume 2: Astrophysics and Cosmology
- Maggiore, M., Van Den Broeck, C., Bartolo, N., et al. 2020, , 2020, 050
- Maio, U., Khochfar, S., Johnson, J. L., & Ciardi, B. 2011, MNRAS, 414, 1145
- Manchester, R. N., Hobbs, G. B., Teoh, A., & Hobbs, M. 2005, AJ, 129, 1993
- Mandel, I. & de Mink, S. E. 2016, MNRAS, 458, 2634
- Manwadkar, V., Trani, A. A., & Leigh, N. W. C. 2020, MNRAS, 497, 3694

- Mapelli, M. 2016, MNRAS, 459, 3432
- Mapelli, M., Bouffanais, Y., Santoliquido, F., Arca Sedda, M., & Artale, M. C. 2022, MNRAS, 511, 5797
- Mapelli, M., Dall'Amico, M., Bouffanais, Y., et al. 2021a, MNRAS, 505, 339
- Mapelli, M., Giacobbo, N., Ripamonti, E., & Spera, M. 2017, MNRAS, 472, 2422
- Mapelli, M., Giacobbo, N., Santoliquido, F., & Artale, M. C. 2019, MNRAS, 487, 2
- Mapelli, M., Santoliquido, F., Bouffanais, Y., et al. 2021b, Symmetry, 13, 1678
- Mapelli, M., Spera, M., Montanari, E., et al. 2020, ApJ, 888, 76
- Marchant, P. & Bodensteiner, J. 2023, arXiv e-prints, arXiv:2311.01865
- Marchant, P., Langer, N., Podsiadlowski, P., Tauris, T. M., & Moriya, T. J. 2016, A&A, 588, A50
- Marchant, P., Renzo, M., Farmer, R., et al. 2019, ApJ, 882, 36
- Massey, P., Neugent, K. F., Dorn-Wallenstein, T. Z., et al. 2021, ApJ, 922, 177
- Massey, P. & Olsen, K. A. G. 2003, AJ, 126, 2867
- McKee, C. F. & Ostriker, E. C. 2007, ARA&A, 45, 565
- McKernan, B., Ford, K. E. S., Bellovary, J., et al. 2018, ApJ, 866, 66
- McKernan, B., Ford, K. E. S., Lyra, W., & Perets, H. B. 2012, MNRAS, 425, 460
- McQuillan, A., Mazeh, T., & Aigrain, S. 2014, ApJS, 211, 24
- Mehta, A. K., Buonanno, A., Gair, J., et al. 2021, arXiv e-prints, arXiv:2105.06366
- Memmesheimer, R.-M., Gopakumar, A., & Schäfer, G. 2004, , 70, 104011
- Meylan, G. & Heggie, D. C. 1997, A&A Rev., 8, 1
- Meynet, G., Eggenberger, P., & Maeder, A. 2011, A&A, 525, L11
- Mikkola, S. & Aarseth, S. 2002, Celestial Mechanics and Dynamical Astronomy, 84, 343
- Mikkola, S. & Aarseth, S. J. 1989, Celestial Mechanics and Dynamical Astronomy, 47, 375
- Mikkola, S. & Aarseth, S. J. 1993, Celestial Mechanics and Dynamical Astronomy, 57, 439
- Mikkola, S. & Merritt, D. 2008, AJ, 135, 2398
- Mikkola, S. & Tanikawa, K. 1999a, MNRAS, 310, 745
- Mikkola, S. & Tanikawa, K. 1999b, Celestial Mechanics and Dynamical Astronomy, 74, 287
- Miller, M. C. & Hamilton, D. P. 2002, MNRAS, 330, 232
- Miller, M. C. & Lauburg, V. M. 2009, ApJ, 692, 917

- Moe, M. & Di Stefano, R. 2017, ApJS, 230, 15
- Morscher, M., Pattabiraman, B., Rodriguez, C., Rasio, F. A., & Umbreit, S. 2015, ApJ, 800, 9
- Naoz, S. 2016, ARA&A, 54, 441
- Narayan, R., Paczynski, B., & Piran, T. 1992, ApJ, 395, L83
- Neijssel, C. J., Vigna-Gómez, A., Stevenson, S., et al. 2019, MNRAS, 490, 3740
- Neumayer, N., Seth, A., & Böker, T. 2020a, A&A Rev., 28, 4
- Neumayer, N., Seth, A., & Böker, T. 2020b, A&A Rev., 28, 4
- Ng, K. K. Y., Franciolini, G., Berti, E., et al. 2022, ApJ, 933, L41
- Ng, K. K. Y., Vitale, S., Farr, W. M., & Rodriguez, C. L. 2021, ApJ, 913, L5
- Nguyen, C. T., Costa, G., Girardi, L., et al. 2022, A&A, 665, A126
- Nitz, A. H. & Capano, C. D. 2021, ApJ, 907, L9
- Nomoto, K. 1984, ApJ, 277, 791
- Nomoto, K., Kobayashi, C., & Tominaga, N. 2013, ARA&A, 51, 457
- Nomoto, K. & Kondo, Y. 1991, ApJ, 367, L19
- O'Connor, E. & Ott, C. D. 2011, ApJ, 730, 70
- Oppenheimer, J. R. & Volkoff, G. M. 1939, Physical Review, 55, 374
- Packet, W. 1981, A&A, 102, 17
- Parischewsky, H. D., Ceballos, G., Trani, A. A., & Leigh, N. W. C. 2021, arXiv e-prints, arXiv:2108.06335
- Peters, P. C. 1964, Physical Review, 136, 1224
- Petrovic, J., Langer, N., & van der Hucht, K. A. 2005, A&A, 435, 1013
- Podsiadlowski, P., Joss, P. C., & Hsu, J. J. L. 1992, ApJ, 391, 246
- Podsiadlowski, P., Mazzali, P. A., Nomoto, K., Lazzati, D., & Cappellaro, E. 2004, ApJ, 607, L17
- Poincaré, H. 1892, Les méthodes nouvelles de la mécanique céleste
- Pols, O. R., Cote, J., Waters, L. B. F. M., & Heise, J. 1991, A&A, 241, 419
- Portegies Zwart, S. F., Baumgardt, H., Hut, P., Makino, J., & McMillan, S. L. W. 2004, Nature, 428, 724
- Portegies Zwart, S. F., Boekholt, T. C. N., Por, E., Hamers, A. S., & McMillan, S. L. W. 2021, arXiv e-prints, arXiv:2109.11012
- Portegies Zwart, S. F., Makino, J., McMillan, S. L. W., & Hut, P. 1999, A&A, 348, 117

- Portegies Zwart, S. F. & McMillan, S. L. W. 2000a, ApJ, 528, L17
- Portegies Zwart, S. F. & McMillan, S. L. W. 2000b, ApJ, 528, L17
- Portegies Zwart, S. F. & McMillan, S. L. W. 2000c, ApJ, 528, L17
- Portegies Zwart, S. F. & McMillan, S. L. W. 2002a, ApJ, 576, 899
- Portegies Zwart, S. F. & McMillan, S. L. W. 2002b, ApJ, 576, 899
- Portegies Zwart, S. F., McMillan, S. L. W., & Gieles, M. 2010a, ARA&A, 48, 431
- Portegies Zwart, S. F., McMillan, S. L. W., & Gieles, M. 2010b, ARA&A, 48, 431
- Portegies Zwart, S. F. & van den Heuvel, E. P. J. 2016, MNRAS, 456, 3401
- Preto, M. & Tremaine, S. 1999, AJ, 118, 2532
- Pryor, C. & Meylan, G. 1993, in Astronomical Society of the Pacific Conference Series, Vol. 50, Structure and Dynamics of Globular Clusters, ed. S. G. Djorgovski & G. Meylan, 357
- Punturo, M., Abernathy, M., Acernese, F., et al. 2010, Classical and Quantum Gravity, 27, 194002
- Quinlan, G. D. 1996, , 1, 35
- Quinlan, G. D. & Shapiro, S. L. 1990, ApJ, 356, 483
- Ramachandran, V., Hamann, W. R., Oskinova, L. M., et al. 2019, A&A, 625, A104
- Rastello, S., Mapelli, M., Di Carlo, U. N., et al. 2021a, MNRAS, 507, 3612
- Rastello, S., Mapelli, M., Di Carlo, U. N., et al. 2021b, MNRAS, 507, 3612
- Rauscher, T., Heger, A., Hoffman, R. D., & Woosley, S. E. 2002, ApJ, 576, 323
- Reitze, D., Adhikari, R. X., Ballmer, S., et al. 2019, in Bulletin of the American Astronomical Society, Vol. 51, 35
- Remillard, R. A. & McClintock, J. E. 2006, ARA&A, 44, 49
- Renzo, M., Cantiello, M., Metzger, B. D., & Jiang, Y. F. 2020a, ApJ, 904, L13
- Renzo, M., Farmer, R. J., Justham, S., et al. 2020b, MNRAS, 493, 4333–4341
- Ricker, P. M. & Taam, R. E. 2012, ApJ, 746, 74
- Riley, J., Mandel, I., Marchant, P., et al. 2021, MNRAS, 505, 663
- Rodriguez, C. L., Amaro-Seoane, P., Chatterjee, S., et al. 2018, , 98, 123005
- Rodriguez, C. L., Chatterjee, S., & Rasio, F. A. 2016a, , 93, 084029
- Rodriguez, C. L., Haster, C.-J., Chatterjee, S., Kalogera, V., & Rasio, F. A. 2016b, ApJ, 824, L8
- Rodriguez, C. L., Morscher, M., Pattabiraman, B., et al. 2015, , 115, 051101

- Rodriguez, C. L., Zevin, M., Amaro-Seoane, P., et al. 2019, , 100, 043027
- Rodriguez, C. L., Zevin, M., Pankow, C., Kalogera, V., & Rasio, F. A. 2016c, ApJ, 832, L2
- Rodriguez, C. L., Zevin, M., Pankow, C., Kalogera, V., & Rasio, F. A. 2016d, ApJ, 832, L2
- Romero-Shaw, I., Lasky, P. D., & Thrane, E. 2021, ApJ, 921, L31
- Romero-Shaw, I., Lasky, P. D., Thrane, E., & Calderón Bustillo, J. 2020, ApJ, 903, L5
- Rosswog, S., Korobkin, O., Arcones, A., Thielemann, F. K., & Piran, T. 2014, MNRAS, 439, 744
- Samsing, J. 2018, , 97, 103014
- Samsing, J., Askar, A., & Giersz, M. 2018a, ApJ, 855, 124
- Samsing, J., Bartos, I., D’Orazio, D. J., et al. 2020, arXiv e-prints, arXiv:2010.09765
- Samsing, J., Bartos, I., D’Orazio, D. J., et al. 2022, Nature, 603, 237
- Samsing, J. & Ilan, T. 2018, MNRAS, 476, 1548
- Samsing, J., MacLeod, M., & Ramirez-Ruiz, E. 2014, ApJ, 784, 71
- Samsing, J., MacLeod, M., & Ramirez-Ruiz, E. 2017, ApJ, 846, 36
- Samsing, J., MacLeod, M., & Ramirez-Ruiz, E. 2018b, ApJ, 853, 140
- Samsing, J. & Ramirez-Ruiz, E. 2017, ApJ, 840, L14
- Sana, H., de Mink, S. E., de Koter, A., et al. 2012, Science, 337, 444
- Sánchez-Janssen, R., Côté, P., Ferrarese, L., et al. 2019, ApJ, 878, 18
- Sanders, R. H. 1970, ApJ, 162, 791
- Santoliquido, F., Mapelli, M., Bouffanais, Y., et al. 2020, ApJ, 898, 152
- Santoliquido, F., Mapelli, M., Giacobbo, N., Bouffanais, Y., & Artale, M. C. 2021, MNRAS, 502, 4877
- Schaerer, D. 2002, A&A, 382, 28
- Scholz, R. D., Kharchenko, N. V., Piskunov, A. E., Röser, S., & Schilbach, E. 2015, A&A, 581, A39
- Schootemeijer, A. & Langer, N. 2018, A&A, 611, A75
- Secunda, A., Bellovary, J., Mac Low, M.-M., et al. 2020, ApJ, 903, 133
- Sesana, A., Haardt, F., & Madau, P. 2006, ApJ, 651, 392
- Shao, Y. & Li, X.-D. 2014, ApJ, 796, 37
- Sigurdsson, S. & Phinney, E. S. 1993, ApJ, 415, 631
- Sigurdsson, S. & Phinney, E. S. 1995, ApJS, 99, 609

- Sirianni, M., Nota, A., De Marchi, G., Leitherer, C., & Clampin, M. 2002, ApJ, 579, 275
- Smith, N. 2014, ARA&A, 52, 487
- Soberman, G. E., Phinney, E. S., & van den Heuvel, E. P. J. 1997, A&A, 327, 620
- Song, H. F., Meynet, G., Maeder, A., Ekström, S., & Eggenberger, P. 2016a, A&A, 585, A120
- Song, H. F., Meynet, G., Maeder, A., Ekström, S., & Eggenberger, P. 2016b, A&A, 585, A120
- Spera, M. & Mapelli, M. 2017, MNRAS, 470, 4739
- Spera, M., Mapelli, M., Giacobbo, N., et al. 2019, MNRAS, 485, 889
- Spera, M., Mapelli, M., & Jeffries, R. D. 2016, MNRAS, 460, 317
- Spitzer, Lyman, J. 1969, ApJ, 158, L139
- Spitzer, L. 1987, Dynamical evolution of globular clusters
- Stanway, E. R., Eldridge, J. J., & Chrimes, A. A. 2020, MNRAS, 497, 2201
- Stevenson, S., Sampson, M., Powell, J., et al. 2019, ApJ, 882, 121
- Sweet, P. A. 1950a, MNRAS, 110, 548
- Sweet, P. A. 1950b, MNRAS, 110, 548
- Szécsi, D., Langer, N., Yoon, S.-C., et al. 2015, A&A, 581, A15
- Taam, R. E. & Sandquist, E. L. 2000, ARA&A, 38, 113
- Tagawa, H., Kocsis, B., Haiman, Z., et al. 2021a, ApJ, 907, L20
- Tagawa, H., Kocsis, B., Haiman, Z., et al. 2021b, ApJ, 908, 194
- Tang, J., Bressan, A., Rosenfield, P., et al. 2014, MNRAS, 445, 4287
- Tanikawa, A. 2013, MNRAS, 435, 1358
- Tanikawa, A., Hattori, K., Kawanaka, N., et al. 2023, ApJ, 946, 79
- Tanikawa, A., Kinugawa, T., Yoshida, T., Hijikawa, K., & Umeda, H. 2021, MNRAS, 505, 2170
- Tauris, T. M., Langer, N., & Podsiadlowski, P. 2015, MNRAS, 451, 2123
- Tauris, T. M. & van den Heuvel, E. P. J. 2006, in Compact stellar X-ray sources, Vol. 39, 623–665
- The LIGO Scientific Collaboration, the Virgo Collaboration, the KAGRA Collaboration, et al. 2021, arXiv e-prints, arXiv:2111.03606
- Thorne, K. S. & Zytkow, A. N. 1977, ApJ, 212, 832
- Tolman, R. C. 1939, Physical Review, 55, 364
- Torniamenti, S., Rastello, S., Mapelli, M., et al. 2022, MNRAS, 517, 2953

- Trani, A. A., Rastello, S., Di Carlo, U. N., et al. 2022, MNRAS, 511, 1362
- Trani, A. A., Spera, M., Leigh, N. W. C., & Fujii, M. S. 2019, ApJ, 885, 135
- Trani, A. A., Tanikawa, A., Fujii, M. S., Leigh, N. W. C., & Kumamoto, J. 2021, MNRAS, 504, 910
- Trenti, M. & van der Marel, R. 2013, MNRAS, 435, 3272
- Tylenda, R., Hajduk, M., Kamiński, T., et al. 2011, A&A, 528, A114
- Umeda, H., Yoshida, T., Nagele, C., & Takahashi, K. 2020, ApJ, 905, L21
- Valtonen, M. & Karttunen, H. 2006, The Three-Body Problem
- van Rensbergen, W., de Greve, J. P., Mennekens, N., Jansen, K., & de Loore, C. 2011, A&A, 528, A16
- Vesperini, E., McMillan, S. L. W., & Portegies Zwart, S. 2009, ApJ, 698, 615
- Vigna-Gómez, A., MacLeod, M., Neijssel, C. J., et al. 2020, , 37, e038
- Vigna-Gómez, A., Toonen, S., Ramirez-Ruiz, E., et al. 2021, ApJ, 907, L19
- Vink, J. S., de Koter, A., & Lamers, H. J. G. L. M. 2001, A&A, 369, 574
- Vink, J. S., Muijres, L. E., Anthonisse, B., et al. 2011, A&A, 531, A132
- Volpato, G., Marigo, P., Costa, G., et al. 2023, ApJ, 944, 40
- von Zeipel, H. 1924, MNRAS, 84, 665
- Wang, C., Langer, N., Schootemeijer, A., et al. 2022, Nature Astronomy, 6, 480
- Webbink, R. F. 1984, ApJ, 277, 355
- Wei, D., Schneider, F. R. N., Podsiadlowski, P., et al. 2023, arXiv e-prints, arXiv:2311.07278
- Wongwathanarat, A., Janka, H. T., & Müller, E. 2013, A&A, 552, A126
- Woosley, S. E. 2017, ApJ, 836, 244
- Woosley, S. E. 2019, ApJ, 878, 49
- Woosley, S. E., Blinnikov, S., & Heger, A. 2007, Nature, 450, 390
- Woosley, S. E. & Heger, A. 2006, ApJ, 637, 914
- Woosley, S. E. & Heger, A. 2021, ApJ, 912, L31
- Woosley, S. E., Heger, A., & Weaver, T. A. 2002, Reviews of Modern Physics, 74, 1015
- Woosley, S. E. & Weaver, T. A. 1995, ApJS, 101, 181
- Yoon, S. C. & Langer, N. 2005, A&A, 443, 643
- Yoon, S. C., Langer, N., & Norman, C. 2006, A&A, 460, 199

- Zahn, J. P. 1974, in Stellar Instability and Evolution, ed. P. Ledoux, A. Noels, & A. W. Rodgers, Vol. 59, 185
- Zahn, J. P. 1975, *A&A*, 41, 329
- Zevin, M., Romero-Shaw, I. M., Kremer, K., Thrane, E., & Lasky, P. D. 2021, *ApJ*, 921, L43
- Zevin, M., Samsing, J., Rodriguez, C., Haster, C.-J., & Ramirez-Ruiz, E. 2019, *ApJ*, 871, 91
- Zhang, S. N., Cui, W., & Chen, W. 1997, *ApJ*, 482, L155
- Ziosi, B. M., Mapelli, M., Branchesi, M., & Tormen, G. 2014, *MNRAS*, 441, 3703
- Zorotovic, M., Schreiber, M. R., Gänsicke, B. T., & Nebot Gómez-Morán, A. 2010, *A&A*, 520, A86